This electronic thesis or dissertation has been downloaded from the King's Research Portal at https://kclpure.kcl.ac.uk/portal/

Unravelling the Mechanics of Growth and Remodelling in the Human Myocardium A Computational Modelling Approach

Hager, Sandra

Awarding institution:
King's College London

The copyright of this thesis rests with the author and no quotation from it or information derived from it may be published without proper acknowledgement.

END USER LICENCE AGREEMENT

Unless another licence is stated on the immediately following page this work is licensed

under a Creative Commons Attribution-NonCommercial-NoDerivatives 4.0 International

licence. https://creativecommons.org/licenses/by-nc-nd/4.0/

You are free to copy, distribute and transmit the work

Under the following conditions:

- Attribution: You must attribute the work in the manner specified by the author (but not in any way that suggests that they endorse you or your use of the work).
- Non Commercial: You may not use this work for commercial purposes.
- No Derivative Works - You may not alter, transform, or build upon this work.

Any of these conditions can be waived if you receive permission from the author. Your fair dealings and other rights are in no way affected by the above.

Take down policy

If you believe that this document breaches copyright please contact librarypure@kcl.ac.uk providing details, and we will remove access to the work immediately and investigate your claim.

Download date: 12. Jan. 2025

Unravelling the Mechanics of Growth and Remodelling in the Human Myocardium: A Computational Modelling Approach

Doctoral Thesis

Author:
Sandra Priska Hager

Supervisors:
David Nordsletten, PhD
Jack Lee, PhD

A thesis submitted in fulfillment of the requirements for the degree of Doctor of Philosophy in the

School of Biomedical Engineering and Imaging Sciences
King's College London

October 5, 2023

Abstract

Growth and Remodelling (G&R) is a typical response of the heart in response to changes in cardiac load or from maladaptive pathophysiological alterations. One broadly accepted theory to explain cardiac G&R phenomena is sarcomerogenesis, which is thought to take one of two forms: (1) concentric hypertrophy (i.e. fibre thickening) or (2) eccentric hypertrophy (i.e. fibre lengthening), caused by either parallel or serial additions of the sarcomere fibres inside myocytes. The question that remains is: What may be potential growth drivers for observed hypertrophy patterns in the heart?

The complexity of G&R in the heart can vary between diseases and patients and is still not entirely understood. In the presented thesis, we focused on understanding cardiac G&R in two cases of pathological growth (hypertrophic cardiomyopathy and aortic stenosis) and one case of reverse growth following aortic valve replacement. An overall approach to analysing these cases of G&R is the theory of kinematic growth by Rodriguez et al.[201], this framework is capable to introduce growth and potential residual stresses within the grown domain. Yet, the interplay between growth and residual stress is not well understood, in later chapters, we assess how these two components of G&R act together and referred to this as the compatibility component of growth. In the case of hypertrophic cardiomyopathy (HCM), for instance, growth patterns appear more complex than in other diseases, with spatial heterogeneous and anisotropic hypertrophy observed without a change in loading condition. In a later chapter, we go into detail about what type of hypertrophy may be an underlying reason for the distinctive phenotypical HCM growth pattern, by investigating three independent test cases. In contrast, the mechanical drivers for reverse growth are apparent in the case of aortic valve replacement (AVR). Following AVR procedure, the heart reacts in two distinctive ways: (1) reverse growth or (2) adverse growth. In a subsequent chapter, we analysed the underlying growth pattern in both of these cases to identify commonalities across patients, by employing either a forward or inverse modelling approach.

In summary in this thesis, we analysed three key objectives of G&R in the heart. Firstly, we investigated the impact of kinematic G&R on the compatibility of the domain, by comparing perturbations of the kinematic G&R problem with each other. Secondly, three individual hypotheses of regional hypertrophy in HCM were studied to understand the mode of growth observed. And the third objective was the classification of G&R modes noticed in AVR with positive (reverse growth) or negative (adverse growth) outcomes.

Acknowledgments

This thesis represents the culmination of four years of rigorous work in the field of Cardio Biomechanics. It was during these years that I experienced numerous sleepless nights driven by my unwavering commitment and relentless pursuit to comprehend intricate mechanisms within the heart. Despite the challenges, this journey has been an unforgettable adventure, rich with rewards, primarily due to the invaluable help, guidance, and friendships that have graced my path.

First and foremost, my profound gratitude to my primary supervisor, Dr. David Nordsletten, whose unwavering support and guidance have been instrumental throughout this remarkable journey. His consistent encouragement, coupled with his innate curiosity to explore observed behaviours through simulations, ignited a spark within me to perform at my very best during my PhD. Furthermore, he consistently pushed me to think beyond conventional boundaries, urging me to embrace questions and motivating me.

I must also express my deep appreciation to my secondary supervisor, Dr. Jack Lee, whose invaluable guidance and continuous encouragement have been pivotal throughout the entire process.

My sincere thanks extend to the esteemed members of my Thesis Progression Committee: Prof. Alistair Young (KCL), Prof. Krishna Garikipati (UMICH), and Dr. Jorge Cardoso (KCL), whose constant feedback and unwavering support have been a cornerstone of my journey.

I extend gratitude to my examiners, Prof. Martyn Nash and Dr. Coleen Witzenburg, for their insightful discussions during my examination and for offering valuable suggestions to enhance my thesis.

To my esteemed colleagues within my lab group - Dr. Maximilian Balmus, Dr. Adela Capilnasiu, Dr. Renee Miller, Dr. Will Zhang, Dr. Marc Hirschvogel, Dr. Daniel Fovargue, Dr. Ayşe Sıla Dokumacı, Dr. David Marlevi, Mia Bonini, Javiera Jilberto Vallejos, John Sayut, Brandon Hardy, Anna Wittgenstein, Omar Darwish, and Sarah Hammoudi - your collective presence has turned this experience into an extraordinary adventure that I would never want to miss. And a big thank you to Mia, Javi, John, Brandon and Will who were a big part on the other side of the Atlantic Ocean and with some of them I experienced new places in Europe.

A heartfelt appreciation goes to Max, whose support has been essential for navigating the challenges of a pandemic and maintaining my sanity, and for being an integral part of my life and sharing so many 'rubber duck' moments with me. Here's to a lifelong friendship!

I'm deeply thankful for the incredible individuals I've had the privilege to interact with at King's during this period. Dr. Emily Chan, with whom I share a love for amazing food and had many unforgettable Zoom face-mask meetings; Dr. Esther Puyol Anton, a colleague par excellence, who can't be replaced; Dr. Aditi Roy, Dr. Hao Xu, Dr. Aven Suinesiaputra, Yiyang Xu, who helped with lifting my spirits, often through Dim Sum delights; Dr. Anna Mira, Dr. Weiwei Jin, Dr. James Bland, Rob O'Shea, whose lunch break discussions have been unparalleled, accompanied by a treasure trove of stories; Dr. Laura Dal Toso, the purveyor of delightful baked treats; Dr. Gavin Wheeler, Elsa-Marie Otoo, and Jonathan Jackson - my sincere gratitude to all of you.

I extend my appreciation to my technical college teacher at HTBLuVA Waidhofen/Ybbs, DIng. Wolfgang Diewald, for sparking my interest and building up the foundation of my knowledge in mechanics.

I'm thankful to Prof. Gerhard Holzapfel, who introduced me to the field of Biomechanics during my Bachelor's and Master's degrees at TU Graz and encouraged me to pursue a PhD in this field.

My thanks go to the friends I've made beyond King's during these years, who have added a vibrant dimension to my life. I hope they remain an enduring part of my heart: Max, Jules Lipton, Alexander Preidler, Thomas Miller (my personal ramen provider and so much more), Gayathri, and Ranjeev.

I'm also grateful to my friends at the Krav Maga Club London, who provided a sense of balance as I worked on my thesis, Kristin, Charlotte, Yoke, Oisin, Diana, Louise, Andy and Glenn. A special shout-out to my instructor for being otterly amazing.

Heartfelt appreciation goes to one of my oldest friends, Dr. mont. Irmgard Weißensteiner, an enduring inspiration and a steadfast friend from my college days.

Finally, none of these achievements would have been possible without the unwavering support and love of my family, despite them being 'Gfrasta'. My deepest thanks to my mum, Monika, whose unwavering support has fueled my pursuits and has always encouraged me to give my best. I'm grateful to my stepdad, Klaus, who has been a staunch supporter of my research. I also would like to dedicate this to my late dad, Karl, I hope he would be proud to see his little girl become a Doktor. To my two brothers, Karl and Maximilian, your presence in my life brings immense joy. And a heartfelt thank you also to my uncle Johannes for his remarkable character.

"You don't use science to show you're right, you use science to become right."

– Randall Munroe

Publications

Sandra P. Hager, Will Zhang, Renee Miller, Jack Lee, David A. Nordsletten, (In Submission). Assessment of Incompatible Growth in Cardiac Applications.

Sandra P. Hager, Will Zhang, Renee M. Miller, Jack Lee, David A. Nordsletten (2021). An Exploratory Assessment of Focused Septal Growth in Hypertrophic Cardiomyopathy. *In Functional Imaging and Modeling of the Heart*, 12738:328–339. Springer International Publishing

Sandra P. Hager, Will Zhang, Marc Hirschvogel, Javiera Jilberto Vallejos, Jack Lee, David A. Nordsletten (In Submission). Computational Study of Growth & Remodelling following AVR.

Sandra P. Hager, Will Zhang, Marc Hirschvogel, Javiera Jilberto Vallejos, Jack Lee, David A. Nordsletten (In Submission). Identification of Growth & Remodelling processes following AVR via clinical data.

Contents

List of abbreviations

AAA	Abdominal aortic aneurysms
AG	Adverse growth
AS	Aortic stenosis
AVR	Aortic valve replacement
BC	Boundary condition
BP	Blood pressure
BiV	Biventricular
COM	Centre of mass
CON	Concentric
CMR	Cardiovascular magnetic resonance
CS	Coordinate system
CT	Computed tomography
CVD	Cardiovascular disease
DT-CMR	Cardiovascular Magnetic Resonance
ECC	Eccentric
ECG	Electrocardiogram-gated
ECG-CT	Electrocardiogram-gated cardiac computed tomography
EDP	End-diastolic pressure
EDPVR	End-diastolic pressure-volume relation
EDV	End-diastolic volume
EF	Ejection fraction
ECHO	Echocardiography
ESP	End-systolic pressure
ESV	End-systolic volume
FEM	Finite element method
G&R	Growth and Remodelling
HCM	Hypertrophic cardiomyopathy
HF	Heart failure
ISO	Isotropic
LA	Long-axis
LM	Lagrange multiplier
LV	Left ventricle
LVEF	Left ventricular ejection fraction
LVOT	Left ventricular outflow tract
LVOTO	Left ventricular outflow tract obstruction
MRI	Magnetic resonance imaging
MULF	Modified Updated Lagrangian Formulation
$\mathcal{J}$	Objective function

PCA	Principal component analysis
PV	Pressure-volume
PVR	Pressure-volume relationship
RG	Reverse growth
RV	Right ventricle
SA	Short-axis
SAVR	Surgical aortic valve replacement
SSA	Statistical shape analysis
SV	Stroke volume
TAVR	Transcatheter aortic valve replacement
TMVR	Transcatheter mitral valve replacement
UVC	Universal Ventricular Coordinates

List of Figures

List of Tables

1 Introduction

Worldwide, a rise in cardiovascular diseases (CVDs) is observed, with 550 million people living with a heart or circulatory condition diagnosed[36]. CVDs are defined as heterogeneous, chronic diseases that gradually progress throughout life[68]. Changes in lifestyle, genetic mutations, hormonal alterations and increasing survival rates following cardiovascular events have gradually raised the population of people living with CVDs[36,102]. Simultaneously the number of premature deaths due to heart and circulatory diseases has increased, in 2019 globally 19 million deaths could be accounted for CVDs[68,36].

Growth and remodelling (G&R) is a typical response of the heart in response to changes in cardiac load or from maladaptive pathophysiological alterations. One case where a complex remodelling process pattern is noticed is in the context of hypertrophic cardiomyopathy (HCM). Here regional, spatial heterogeneous and anisotropic hypertrophy in the heart is observed, without any persistent change in the loading condition. An alternative case of G&R in the heart is observed in aortic valve replacement (AVR), where growth either results in a positive (reverse growth) or a negative (adverse growth) outcome. The challenge in looking at these types of G&R is that there is still a lack of understanding of what drives these growth patterns. In this thesis, we are going to investigate some ideas and attempt to identify characteristics of hypertrophy patterns by combining imaging data and the kinematic growth theory[201].

Medical imaging modalities such as computed tomography (CT), magnetic resonance imaging (MRI) and echocardiography (ECHO) provide a powerful tool to track alterations in the morphology and function of the heart. Acquiring longitudinal cardiac images of patients, particularly those experiencing pathophysiological G&R, enables a time tracking of the structural changes of the heart. While capable of providing anatomical information in the heart, imaging data are currently incapable of providing mechanical information such as the internal stress and strain states in the myocardium. Computational modelling approaches aspire to make predictions about stress levels and furthermore predict the stress development driven by growth processes over time.

Established G&R approaches, such as the phenomenological kinematic growth approach[201] and the constrained mixture model[114], are typically driven by constitutive

G&R relations motivated by observed changes in cardiomyocytes. Longitudinal imaging data combined with established G&R approaches intend to model cardiovascular alterations, due to heart failure (HF) introduced by mechanical loading [80,194] and hormonal growth drivers [58], prestrain in the heart [81], myocardial infarction [149] and reverse growth [145,146]. Despite mentioned studies being able to track or predict the G&R process in the myocardium, compatibility and characteristics of growth patterns introduced by kinematic growth are not addressed in previous studies.

The presented thesis focuses on three objectives related to G&R in the heart. The first objective was to determine the relation between compatibility components and the kinematic growth theory. As a result, we simulated perturbations of G&R tests and compared the solutions of the deformation gradient with the results from the gold standard. The second objective focuses on identifying underlying drivers to simulate a phenotypical HCM growth pattern. Hypertrophy patterns in HCM are more complex by resulting in regional, spatially heterogeneous and anisotropic G&R in the heart. In this thesis, we discuss three different hypotheses that may be underlying reasons for a phenotypical HCM growth pattern, such as fibre disarray, spatial heterogeneity and inflammation processes. The third objective was to utilise the kinematic growth theory in relation to model G&R in AVR with different patient outcomes (reverse growth or adverse growth). This study was split into two different types of modelling G&R in the sense of solving it as a forward problem or in the sense of an inverse approach. The forward problem was addressed by establishing a workflow to mimic G&R in a pre-AVR model by applying a defined kinematic growth tensor to predict a post-AVR model and further comparing some cardiac metrics with the post-AVR imaging data. Whereas with the inverse approach, the aspiration was to identify the growth tensor and analyse the introduced growth pattern for commonalities, spatial heterogeneity, and anisotropy in the individuals and across patients.

This chapter is a review to give the reader a clear picture of the challenges of G&R in cardiac applications. First, the architecture (Section 1.1) and the function of the heart (Section 1.2) were reviewed to have an understanding of the physiological state before G&R. Next, clinical applications of G&R and the alterations associated with growth are discussed in Section 1.3. This section introduces the modes of G&R observed in the heart and links them to growth patterns noticed in different cardiac conditions. With a differentiation between positive (reverse growth) and negative (adverse growth) outcomes of G&R in the heart. An effective way to track cardiac alterations due to G&R processes in medical imaging modalities. Section 1.4 gives an overview of cardiac imaging modalities and their applications in computationally modelling the biomechanics in the heart. The following section (Section 1.5) gives an overview of computational applications of G&R and reviews studies applying the discussed theories within a cardiac setting. Section 1.6 provides an overview on the objectives of G&R addressed in this work.

1.1 Heart Architecture

The heart is split up into the left (high-pressure) and the right (low-pressure) system, see Figure 1.1. The location of the heart within the chest cavity is ensured by a surrounding double-walled, tough fibrotic, fluid-filled layer sac anointed the pericardium that is fixed to the diaphragm[172]. Each side of the heart consists of an atrium and a ventricle with a separating wall between the atria (the interatrial septum) and the ventricles (the interventricular septum)[205]. To ensure a predominantly one-way flow through the heart, one valve separates the atria and ventricle while another valve is positioned at the outflow of the left ventricle (LV) and right ventricle (RV) towards the aorta or pulmonary artery, respectively. The valves consist of up to three thin fibrous layers of tissue that are covered with endothelial cells[205]. Between the left atrium and the LV is the bicuspid mitral valve (MV), with stringlike tendons that connect the cusps with the papillary muscles of the LV. The inflow to the RV is regulated by the tricuspid valve (TV), with three cusps that are attached with tendons to the RV. The exit towards the pulmonary trunk is controlled, by the pulmonary valve (PV). The opening and closing of the heart valves ensure a one-way passage of the blood through the heart during a cardiac cycle.

Oxygen-poor blood enters the right atrium through the venae cavae and gets transported into the right ventricle via the TV and pumped into the pulmonary circulation system through the PV[118]. Whilst in the lungs pulmonary gas exchange takes place, where oxygen is exchanged for carbon dioxide[238]. Coming from the pulmonary veins, oxygenated blood enters the left atrium and gets pushed through the MV into the LV. The LV further ejects the blood via the AV into the systemic circulation. Defined anatomical landmarks are the base, indicating the cut surface between the atria and the ventricles, the apex, defined as the lowermost point of each ventricle and the septum, the wall separating the RV and LV[172].

The heart wall consists of three distinct layers, the endocardium, myocardium and epicardium. During a cardiac cycle, the functionality of the heart depends on the interaction of physiological parameters in a hierarchical multiscale order. The core elements of the heart contain various cell types varying from the specific region in the heart, with a combination of myocytes and connective tissue[118]. The myocardial mass contains approximately 70% myocytes and smaller cells, such as vascular smooth muscle, endothelial cells and fibroblasts that permit the heart muscle to contract in a pump-like motion to transport the blood through the pulmonary and systemic circulation.

Myocytes contribute to the contractile force of the heart to eject blood through the atria and ventricles. A single cardiac myocyte (Figure 1.2E) can contain more than a single nucleus[172,254] and has a length of 100μm and a diameter of 25μm[116]. Cardiomyocytes are composed of bundles of myofibrils which contain myofilaments[116]. The basic

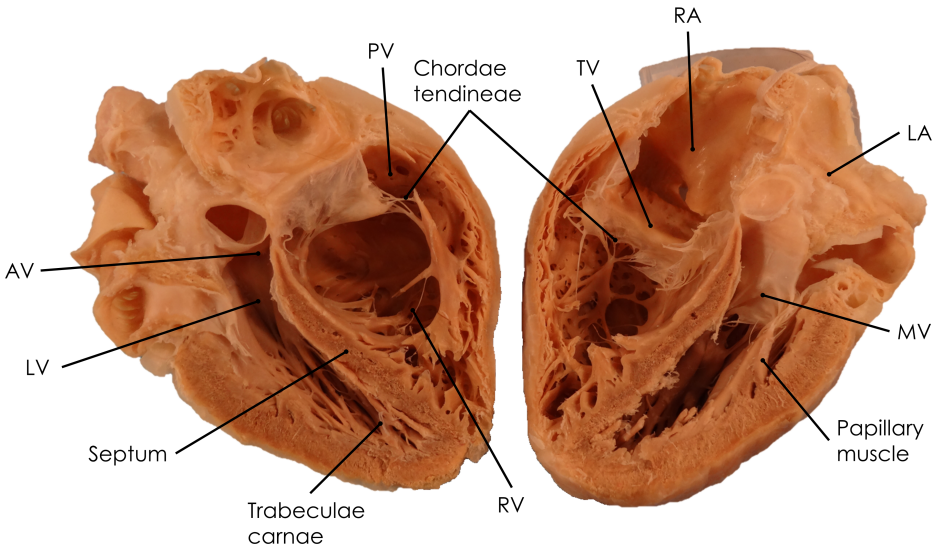

Figure 1.1 Image of a plastinated human heart (adapted with permission from Visible Heart Laboratories, University of Minnesota/©Medtronic[228]) with a sagittal cut through the heart along the long-axis and indication of the primary structures, such as the ventricles, atria, valves and endocardial muscular structures (e.g. trabeculae carnae). AV: aortic valve, LA: left atrium, LV: left ventricle, MV: mitral valve, PV: pulmonary valve, RA: right atrium, RV: right ventricle, TV: tricuspid valve. With permission from Miller et al.[172].

contractile subunit of myocytes are sarcomeres. A single sarcomere (Figure 1.2G) is built up by actin (thin filaments) and myosin (thick filaments) proteins which represent approximately half of the cell volume and are defined as the distance between two Z-lines. Due to chemical interactions, excitation-contraction processes take place by a sliding of cross-bridges between actin past the myosin filaments, which leads to a shortening of the sarcomeres. To centre the large myosin filaments within the sarcomeres a large, filamentous protein (Titin) connects the myosin filaments with the Z-lines.

Cardiomyocytes are aligned via intercalated discs in series in order to form supracellular myofibres. Whereas parallel aligned cardiac myocytes are grouped in a sheet-like structure (Figure 1.2B) by the surrounding collagen (perimysial collagen) connective tissue to achieve the local structural arrangement of the myocytes[172], displayed in Figure 1.2C and D. Myofibres and laminar sheet orientation contribute to the locally observed orthogonal coordinate system of the myocardium. The local microstructure coordinate system is defined by the orientation of the myofibres, sheets and the resulting sheet-normal direction. On the tissue scale, the orientation of the cardiac fibres is aligned with a helical angle measured to the local circumferential direction. Displayed in Figure 1.2A, the fibre alignment within the heart varies transmurally from the endocardium to the epicardium. The fibre helical angle changes in the LV from 60° to -60° and in the RV from 90° to -25°[171].

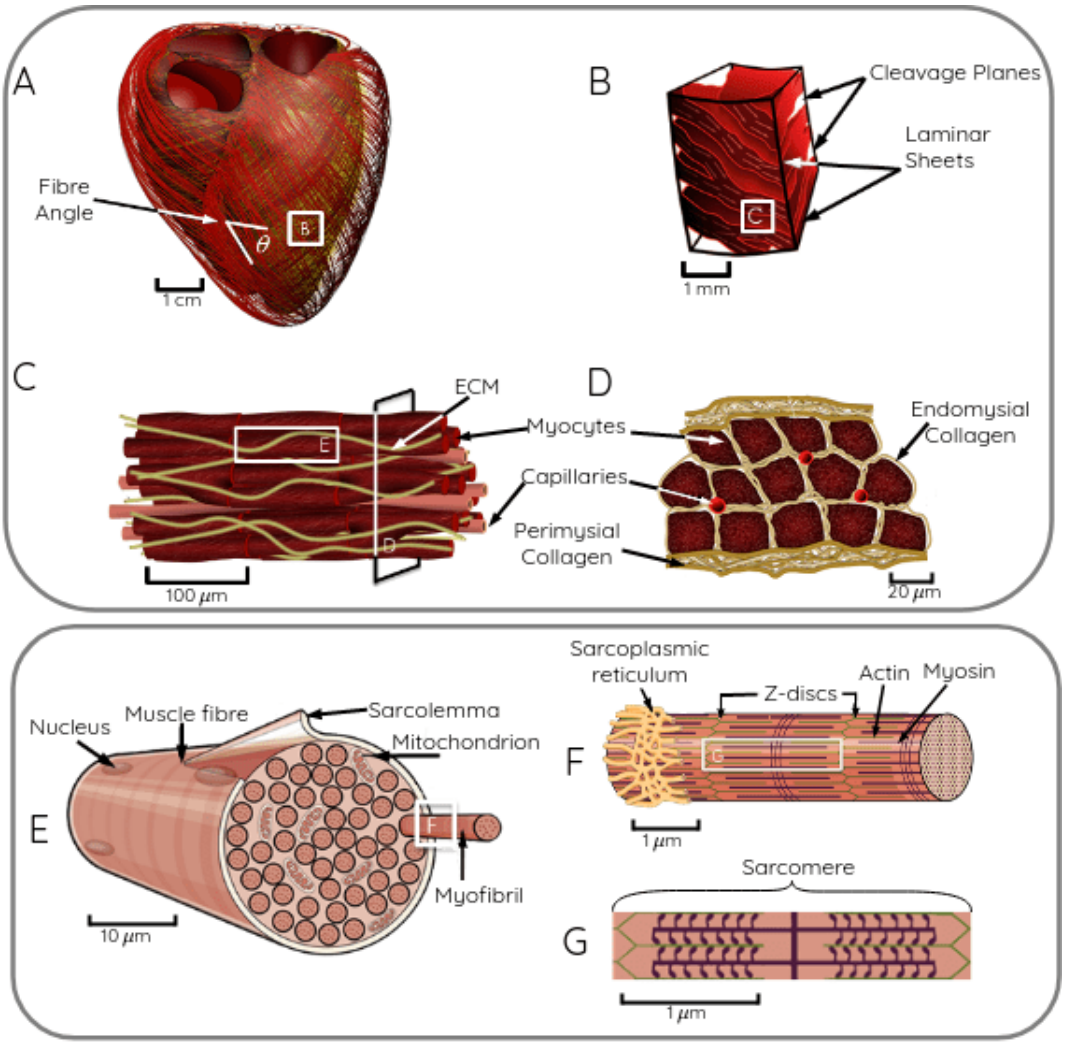

Figure 1.2 Illustration of multiscale cardiac structure. (A) Biventricular anatomy with fibre orientation, (B) tissue block illustrating laminar structure, (C) local structural arrangement of myocytes, capillaries and ECM, (D) myocytes and capillaries in endomysial and perimysial collagen, (E) myofibre cut to view internal structures, (F) moyfibril illustrating individual components, (G) sarcomere made of actin (thin) and myosin (thick) filaments, (H) bonds between multiple collagen fibrils from collagen fibres, (I) collagen fibril formed from staggered collagen molecules, (J) three amino polypeptide strands from a single collagen molecule. (E and F reproduced from Anatomy and Physiology under Creative Commons Attribution License 4.0 from OpenStax. ©2016)

1.2 Whole-Heart Function and the Cardiac cycle

The cardiac cycle can be split up into four distinct phases that describe mechanical and electrical events during every heartbeat. Starting with the ventricular filling phase (diastole), the ventricles expand and the pressure within the chambers drops below the pressure in the atria. Normal pressure levels in the RV during filling is 3–7mmHg[135]. Whereas the diastolic blood pressure (BP) in the LV during normal cardiac functionality is $\leq 80 mmHg$[111]. As a result of the pressure gradient between the left atria and the left ventricle, the MV and TV open and blood gets pushed from the atria into the ventricle which leads to a pressure rise in the ventricle. The pressure-volume (PV) curve for the left ventricle and the end of the ventricular filling is defined by the end-diastolic volume (EDV) and the end-diastolic pressure (EDP), see Figure 1.3B. In reference to the pressure, volume changes over time with respect to the electrocardiogram, the Wiggers diagram is shown in Figure 1.3A.

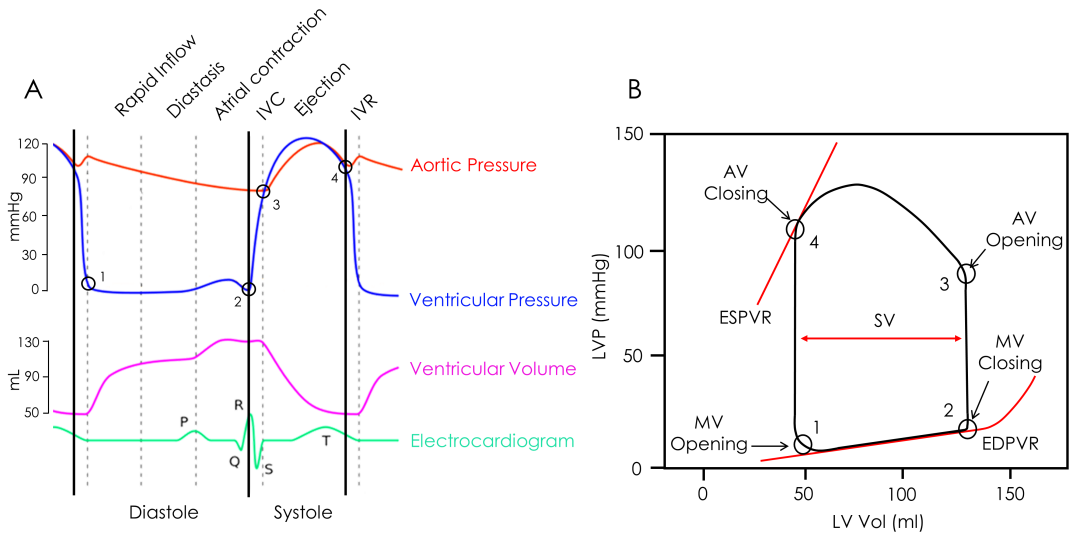

Figure 1.3 (A) The Wiggers diagram illustrates the LV and aortic pressures along with the ventricular volume and a representative electrocardiogram. Each phase discussed in the text is delineated by dashed lines, whereas diastole and systole are shown by solid lines. (B) An example pressure-volume loop for the LV is shown, highlighting three functional metrics: SV, EDPVR and ESPVR. Valve opening and closing times are drawn in both figures as open circles. It should be noted that these traces represent pressures and volumes in the LV. Analogous traces and curves can be drawn for the RV and both atrial chambers. (©2016, Springer Nature. From Miller et al.[172] with permission.)

The ventricular filling phase transitions into the isovolumetric contraction stage, with the atria repolarizing, relaxing and filling with blood for the rest of the heart cycle. The ventricle starts contracting which leads to a sharp rise of the pressure within the ventricle and results to a steep pressure gradient between the atria and ventricles that controls the MV and TV closure. After the closing of the MV, the LV and RV continue

contracting with a constant blood volume (isovolumetric) within the chamber.

During the ventricular ejection phase (systole), the pressure rise resulting from the contraction exceeds the pressure within the aortic root and pulmonary trunk, driving the AV and PV to open. The systolic pressure in the RV during ejection in a normal healthy heart is 20–30mmHg[135] and for the LV $\leq$120mmHg[111]. During ejection phase, blood enters the aorta until the pressure in the LV drops below the pressure in the aorta and initiates the closing of the AV.

At the same time, the atria start to fill with blood. During the ejection phase, not all blood is expelled from the ventricle which leads to an end-systolic volume (ESV) while the volume ejected from the LV is referred to as stroke volume (SV). The percentage of EDV versus the SV defines one of the most important parameters for cardiac health, the ejection fraction (EF). Within certain cardiac diseases, the EF may fall into a range below 50 %. At end systole, the metric of the end-systolic volume (ESV) and the end-systolic pressure (ESP) are acquired which are further used to define the cardiac workload.

The last phase of the cardiac cycle is the isovolumetric relaxation of the ventricular chambers. As a result of the relaxation the pressure in the ventricle decreases continuously while the pressure in the atria rises due to filling until the pressure exceeds the ventricular pressure, and the cycle repeats.

Throughout the cardiac cycle, the myocardium experiences force alterations caused by contraction and relaxation processes in the tissue and pressure changes within the cavity chamber. Inside the healthy heart, these forces are balanced and the tissue is in an equilibrium state. On the contrary, CVDs are linked to structural or functional changes within the heart thought to be driven by an unbalanced force or strain state.

1.3 Clinical Applications of Growth and Remodelling

G&R is a typical response of the heart when subjected to alterations in cardiac loads, such as valve stenosis, valve replacement, or genetic mutations of the sarcomeric proteins, for example in hypertrophic cardiomyopathy (HCM) (Figure 1.4). Standard growth patterns in the heart are associated with establishing a new baseline homeostatic level while simultaneously striving to maintain consistent cardiac output. On the right-hand side of Figure 1.4, the black Pressure-Volume curve of the LV represents the behaviour of a healthy heart, while the red curve represents either aortic stenosis (top) or HCM (bottom).

Figure 1.5 illustrates different G&R modes observed in the human heart and the changes in heart function during a cardiac cycle.

Concentric hypertrophy (CON), an increase in wall thickness and can frequently

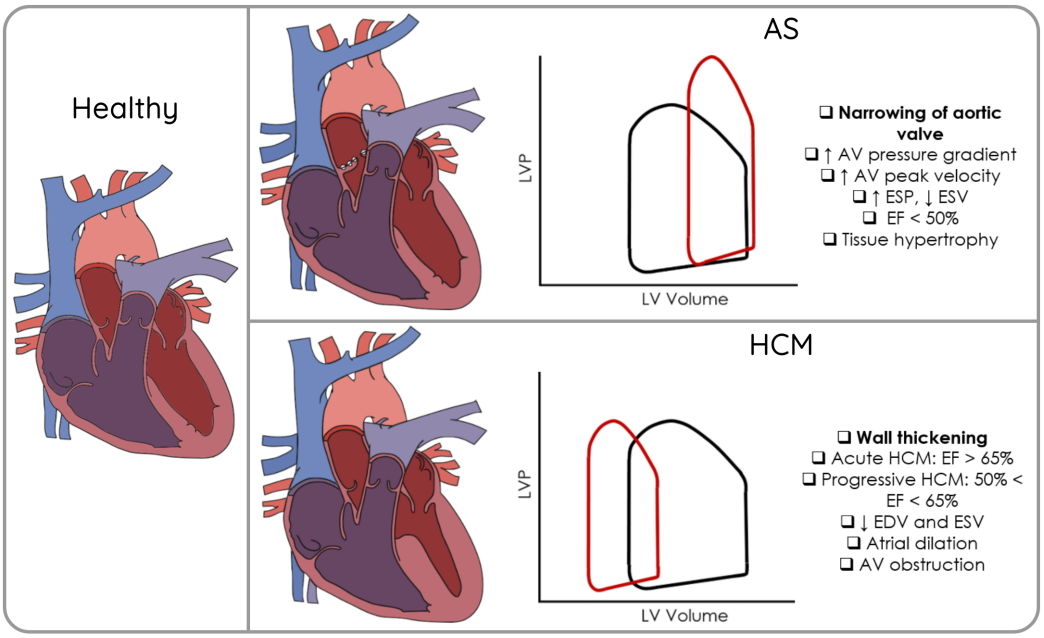

Figure 1.4 Summary of cardiac geometries and pressure-volume loops for a healthy heart (visualised by the black PV-loop) and the two discussed cardiac pathologies: hypertrophic cardiomyopathy (HCM) and aortic stenosis (AS), individually displayed in red. Adapted from Miller et al. [172]

be seen in pathological conditions with chronic increases in afterload, e.g. aortic stenosis, systemic hypertension, myocardial infarction, athletic heart with physiological left ventricle hypertrophy (LVH), subaortic stenosis, hypertrophic cardiomyopathy, infiltrative cardiac processes (e.g. Amyloidosis, Fabry disease, Danon disease) or hyperthyroidism [23,75,32]. A reduced SV is often observed in these types of CVDs. Elevated pressure levels (pressure overload) are proportionally linked to an increase in the hoop stress of the ventricle. In this case, it is hypothesised that growth is introduced as a systolic stress correction, to normalise the wall stress [95]. In addition to the morphological changes of the heart, a high concentration of interstitial and perivascular accumulation of fibrillar collagen (type I and type III) may be observed [192].

Eccentric hypertrophy (ECC), is a dilation of the ventricle and is associated with an increase in the preload and an increase in SV. Pathological conditions affiliated with this are for example aortic regurgitation, mitral regurgitation, dilated cardiomyopathy, and ventricular septal defect [32]. An increase of the passive stretches or stresses of the myocytes during diastole (volume overload) is thought to drives the cells to elongate and establish a new homeostatic equilibrium, assumed to be a stretch-correction [221].

The following section goes into detail about changes induced by specific CVDs and treatment methods.

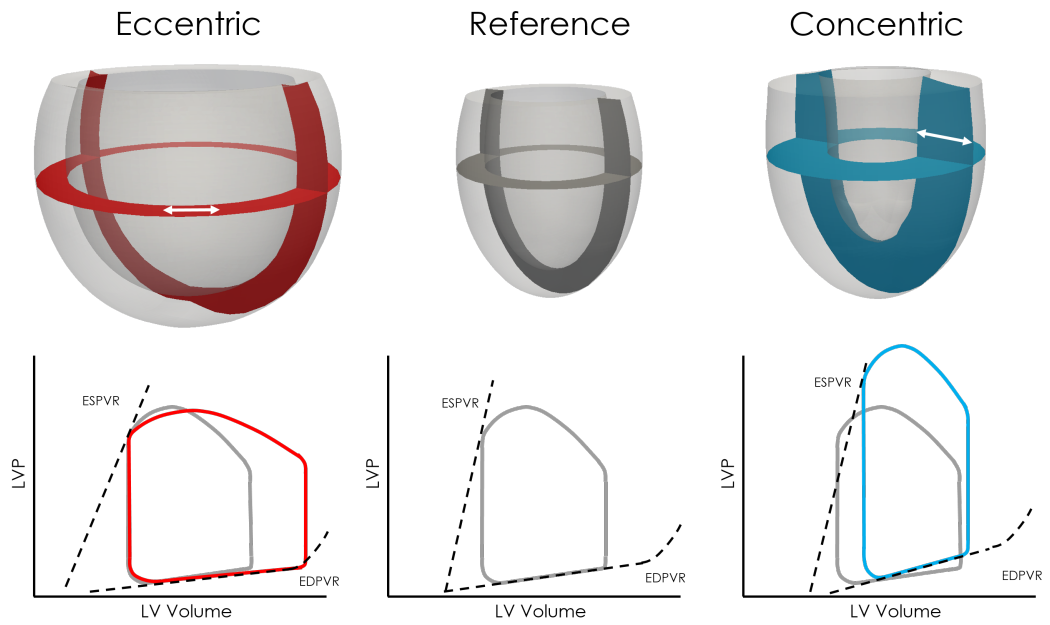

Figure 1.5 Eccentric growth (left) applied to an idealised left ventricular geometry (centre) results in cavity dilation along with elevated SV and decreased contractility, as shown by the changes in the pressure-volume loop and ESPVR. Concentric growth (right), however, results in wall thickening and is often accompanied by an increase in ESP as well as global elastance, illustrated by a steeper EDPVR. (©2016, Springer Nature. From Miller et al. [172] with permission.)

1.3.1 Aortic Stenosis

61% of valvular heart diseases affect the aortic valve [38]. AS is the narrowing of the aortic valve most commonly caused by calcium deposition in the valve leaflets, congenital aortic valve diseases or rheumatic fever [103]. Figure 1.6 shows a comparison between characteristics and diagnostic entities in a healthy (A) and calcified (B) aortic valve. The aortic valve is typically composed of three thin fibrous leaflets (Figure 1.6A1), during the progress of calcific AS, the leaflets undergo fibrosis and calcification (Figure 1.6B1) which leads to alterations of the biomechanical properties. Examining histological samples of the valve leaflets calcium deposits and inflammatory processes occur within the outermost layer, referred to as fibrosa (Figure 1.6B2). A combination of echocardiography and additional medical imaging methods (cardiac magnetic resonance (CMR) or computed tomography) enables identifying the stage of AS (Figure 1.6B3). Patients with severe AS typically exhibit peak aortic jet velocity of $\geq$ 4m/s, a mean pressure gradient of $\geq$ 40mmHg and an aortic valve orfice area (AVOA) $\leq$ 1cm^2. Using CMR may provide a powerful tool in the future, due to the four-dimensional flow tracking flow pattern in the ventricle and aorta may be identified and applied to intervention methods (Figure 1.6B4). A potential use for CMR data is to identify myocardial fibrosis, which is often not reversible and associated with an increase of mortality in patients with severe AS (Figure 1.6B4).

Degenerative AS is linked to an increase of mechanical stress and a decrease in shear

stress within the ventricular cavity and results in damage to the integrity of the endocardial lining[203]. Inflammation processes are commonly seen in the early stages of AS and are accompanied by symptoms, such as chest discomfort, syncope, dyspnea and diastolic HF[203]. Likewise, a higher risk for atrial fibrillation and stroke is observed in patients with AS[10]. Alterations introduced by AS are a large transvalvular pressure gradient during systole between the LV and the aorta, an increase of afterload, hypertrophy of the LV, left atria expansion due to mitral regurgitation, decreased stroke volume and a lowered left ventricular ejection fraction (LVEF) <50%[116,203,47,198].

G&R associated with AS may become an adverse type of growth in the heart and introduces fibrosis, cell death and HF. Hypertrophy pattern in AS, appears highly complex with regional variation of growth in the heart and heterogeneity across patients. Lee et al.[147], studied the association of late gadolinium enhancement in MRI related to AS and could prove that advanced LV hypertrophy results in a decrease of LV function and compliance. In a clinical setup, the American Society of Echocardiography (ASE) guidelines is used to calculate LV mass. For this calculation, the LV is approximated by a 2:1 long-axis/short-axis ellipsoid with a symmetric distribution of hypertrophy. However, in patients with AS an asymmetric pattern with regional hypertrophy and bulging of the basal interventricular septum is observed and also referred to as regional or sigmoid septum. Experimental studies in cultured cells suggest that transgenic animals have many different individual stimuli that can drive hypertrophy and indicate signalling cascades[104,249]. Grossman et al.[95] introduced a phenomenological concept from experimental data, where he computed estimations of the wall stresses within AS and compared them to a baseline group. Their study focused on the identification of mechanical drivers within AS, and the results indicated that hypertrophy may be driven by systolic wall stress to produce a new steady-state to normalise wall stresses in the LV. Various studies focussing on hypertrophy patterns in AS, utilise stress as the driving stimuli[50,156,173] However, it is not clear what underlying drivers are associated with growth in AS. Hypotheses are that for example, elevated systolic myocardial stress[240], elevated wall shear stresses[156] or fibre stress[173] could play a significant role in understanding AS.

1.3.1.1 Aortic Valve Replacement

The typical method to manage AS is an aortic valve replacement (AVR), to reduce the mean pressure gradient between the aorta and ventricle to normal physiological levels. The traditional method used in patients with severe AS has been surgical aortic valve replacement (SAVR), involving an incision in the chest to access the heart and remove the diseased aortic valve. The diseased valve is then replaced with a mechanical prostheses (Figure 1.7A1), heterograft bioprostheses, homograft bioprostheses (Figure 1.7A2), or pulmonary autograft[227,69,71].

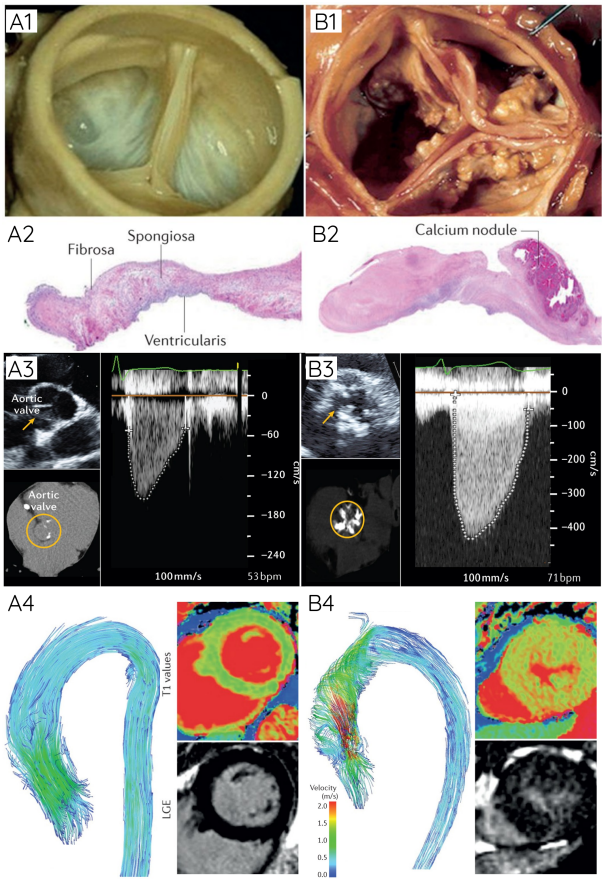

Figure 1.6 Characteristics and diagnostic entities representing a healthy (A) and calcified stenosed (B) aortic valve. From the top: post-mortem tissue specimens, showing the smooth unaffected native valve (A1) compared to the apparent calcium deposits in AS (B1). Histopathological data shows a similar native trilaminar structure in the native valve (A2) compared to calcific nodules present in AS (B2). The effect on flow is also apparent in Doppler echocardiography where native velocities (A3) are severely elevated in the stenosed case, and where calcium deposits are detectable on CT short-axis views (B3). Similar effects on flow can be observed by means of 4D Flow MRI with elevated post-stenotic velocities shows in the stenosed patient (A4 vs. B4). Similarly, high-fidelityMRI (using T1-mapping and late gadolinium enhancement (LGE) sequences) showcase signs of myocardial fibrosis in AS compared to the native equivalent (A4 vs. B4). (©2016, Springer Nature. Adapted from Lindman et al. [151] with permission.)

Consequently, due to the high mortality of SAVR for certain risk patient groups, transcatheter aortic valve replacement (TAVR) emerged over the last decade as an alternative to replace the diseased heart valve [72,254]. Figure 1.7B illustrates the less invasive approach of TAVR compared to SAVR, where either a balloon-expandable (Figure 1.7B1) or a self-expanding (Figure 1.7B2) valve is deployed via transfemoral balloon catheterization in the area of the calcified aortic valve [254,202].

AVR allows the restoration of normal blood flows through the aortic valve orifice. Right after surgery, the heart undergoes immediate changes such as a pressure gradient drop and an increase in EF. On a long time scale, reverse growth processes are observed, within the heart to adapt to the new loading conditions. Fairbairn et al. [60] gives an overview of adaptation processes following TAVR procedures and compared the outcomes of the study with reverse growth after SAVR. Indicated in the results that TAVR is a comparable alternative to SAVR related to reverse growth and lower pressure gradients and myocardial fibrosis levels are observed after TAVR.

G&R following AVR appears to be heterogeneous. It is observed that across patients different types of G&R can be observed, such as reverse growth (beneficial) or adverse growth (harmful). The correction of AS with SAVR or TAVR with reverse growth

results in a large decline of LV mass during the first 6 to 12 months[206,27]. An approach to assess the changes following AVR was done by Treibel et al.[225]. The focus of their study was the identification regression of focal fibrosis, diffuse fibrosis and myocardial cellular hypertrophy in the Post-AVR heart. Results from this study suggested that diffuse fibrosis and myocardial hypertrophy are able to regress following AVR while focal fibrosis remains and contributes to the material stiffness. Additionally indicated the study that the onset of symptoms and identified markers of long-term outcomes following AVR do not correlate. Regression of LV hypertrophy is further related to changes in the electrical conduction within the patients[212]. A challenge of computationally modelling AVR is the identification of the G&R mode of reverse growth which can be observed as a response to AVR. Moreover, we are interested in identifying if it is possible to identify a common growth pattern in patient cohorts.

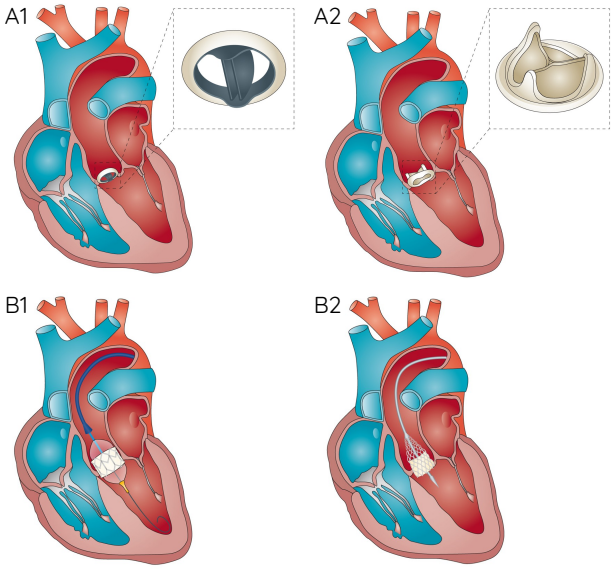

Figure 1.7 Long-axis cut of heart with different types of aortic valve replacement (AVR). Surgical aortic valve replacement (SAVR) via open-heart surgery with a bileaflet mechanical valve (A1) compared to a bioprosthetic valve (A2). Transcatheter aortic valve replacement (TAVR) with balloon-expandable valve (B1) or self-expanding valve (B2).(©2016, Springer Nature. Adapted from Lindman et al.[151] with permission.)

1.3.2 Hypertrophic Cardiomyopathy

Hypertrophy in the LV may be also driven by mutations on the intracellular level without a clear alteration of the loading conditions of the heart. Among these is the genetic CVD hypertrophic cardiomyopathy (HCM), observed in nearly 1 in 200 people[211]. Where 11 or more genes can be affected by dominant mutations within the encoding of the sarcomere proteins or the adjacent Z-discs and further lead to regional growth in the myocardium with LV wall thickness of $\geq$13 mm[160,123] (Figure 1.8). Even in familial lines, the growth pattern introduced by HCM appears heterogeneous throughout HCM hearts. One-third of HCM patients show hypertrophy that is non-obstructive (left ventricular outflow tract (LVOT) resting gradient is <30mmHg), eg. apical, reverse curve or sigmoidal growth. Another third is defined as latent-obstructive (LVOT gradient is <30mmHg at rest and $\geq$30mmHg during contraction). The remaining third of HCM growth patterns are obstructive (LVOT resting gradient is $\geq$30mmHg). Common patterns are left ventricular outflow tract obstruction, mid-ventricular obstruction or left

ventricular apical aneurysm[123].

HCM can be observed within the heart on different spatial levels. Beginning on the intracellular scale, the two most commonly mutated genes are within the thick myofilament proteins and linked to alterations of the actin-myosin interaction, are the genes MYBPC3 and MYH7 with a mutation prevalence of 25% and 20% respectively[157]. Some mutations of MYH7 are linked to an increase of the mechanical contraction force of myocytes in vitro and indicate a higher calcium sensitivity resulting in an increase of tension and ATPase activity[2]. Histological phenotypes on the microscale of HCM tissue involve myocyte hypertrophy and disarray with interstitial fibrosis[157].

The clinical diagnosis of HCM involves an electrocardiogram, where pathological changes can be observed and the type of HCM may be identified. Additionally, standard and Doppler echocardiography combined with the use of contrast agents (e.g. late gadolinium enhancement (LGE)) are exploited to gain structural and functional information about the state of the heart. Therapies to treat HCM include medications such as beta, calcium channel blockers[93] or mavacamenten to reduce contractility. Yet, patients with interventricular hypertrophy and LVOT obstruction may have to be treated through alcohol septal ablation or have parts of the septum removed via surgical myectomy. Alcohol ablation is a minimal-invasive treatment in which alcohol gets injected into the tissue and induces necrosis and later scar tissue in the affected area. An additional side effect is the reorganization of tissue causing a change to local electrical conductances, which may lead to ventricular tachycardias[164] or arrhythmias[185]. In contrast, cardiac myectomy is an open-heart surgery in which hypertrophic tissue is cut from the affected region of the heart.

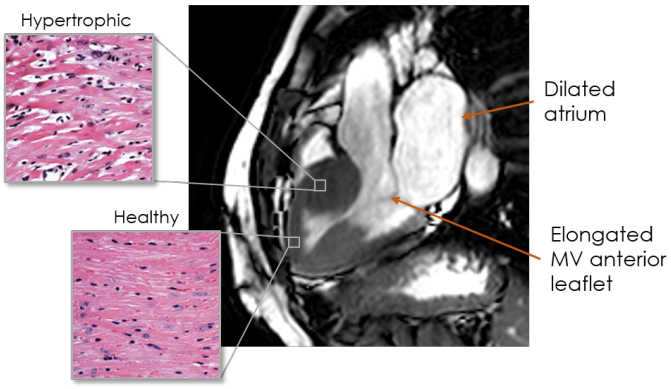

Figure 1.8 Long-axis MR image of an HCM heart showing a hypertrophic septum, an elongated anterior mitral valve (MV) leaflet, tending towards obstruction of the outflow tract, and a dilated atrium. Insets show histology images of healthy and hypertrophic myocardial tissue (adapted with permission from Miller et al.[172] and Wolf et al.[243], Copyright (2005) National Academy of Sciences, U.S.A.) illustrating the disarray observed in HCM hypertrophic myocardium with H&E staining. Blue: nucleus, red: cytoplasma, varying red: collagen fibres and ECM.

G&R in HCM is observed highly heterogeneous across patients and within the heart. The regional hypertrophy pattern makes it challenging in modelling or predicting the

phenotypical HCM pattern. One way to investigate growth patterns in HCM may be to introduce types of eccentric or concentric remodelling in the affected area to increase the thickness of the wall. Another way might be to investigate the combination of the underlying microstructure and heterogeneous remodelling drivers across the heart. Or an underlying reason could be the impact of inflammation and swelling in the heart. Typically at the start of HCM progress hypertrophy is noticed without any apparent change in loading. Hence, finding or identifying growth drivers with conventional medical assessment becomes difficult. Pre-clinical studies suggest that the use of mavacamten, an allosteric inhibitors of cardiac β myosin, reduces hypercontractility and introduces G&R and regression of the cardiomyocyte disarray and myocardial fibrosis[175,92,216].

A role for computational modelling

A key challenge is to understand in what way various cardiac pathological conditions influence G&R mechanisms in HCM. Computational and mathematical modelling modalities may be able to give an insight into how the heart might react during disease progression or following surgical intervention. This allows us to perturb various problem parameters in order to understand their impact and understand the underlying mechanisms of G&R. Computational methods provide additional information on in-vivo processes without any further use of animal experiments to establish or test treatment methods for patients. Furthermore, computational simulations are a powerful tool to assess stress states inside cardiac tissue additionally as structural information from imaging modalities.

1.4 Cardiac Imaging Modalities & Computational Modeling

Medical imaging modalities enable the identification of structural and functional characteristics of the healthy and diseased heart. During a cardiac cycle, the heart undergoes periodically large deformations. Especially during the ventricular filling and ventricular ejection phase, the heart ventricle fills is in a passive filling state while

Pathological changes in the heart are assessed by initially analysing the cardiac motion during the cardiac cycle, besides Alternations induced by G&R mechanisms may lead are commonly studied via longitudinal medical imaging data to assess the progression of growth in the myocardium.

1.4.1 Computed Tomography

Computed Tomography (CT) is an imaging technique used to produce high spatial resolution images. Involved in the image acquisition is a rotating X-ray source and a bank of detectors collecting the X-rays that did not get absorbed by the patient

tissue.

The introduction of electrocardiography gated CT images has also enabled high-spatial resolution images over time, providing functional parameters of the heart throughout the cardiac cycle. Strocchi et al. [217] utilised cardiac CT imaging data for model generation of the four-chamber heart geometry and further simulated ventricular systolic motion and the impact of the pericardium on the heart's deformation. Besides the cardiac motion, cardiac CT can be used to assess various CVDs (e.g. calcification in AS) within the LV, RV, atria or valves. In their study, Krishnamurthy et al. [128] employed biventricular (BiV) geometries segmented from cardiac CT images at end-diastole from patients with HF and calculated the unloaded reference geometry and material properties for the passive and active cardiac muscle. Cutugno et al. [45], utilised electrocardiogram-gated cardiac computed tomography (ECG-CT) images from patients with different degrees of severity and further conducted a statistical shape analysis (SSA). The results of the model of the left heart chamber correlated with the clinical and functional data of the patients. By employing an SSA, anatomical shape information due to cardiac G&R can be identified by means of a statistical tool in its principal variations in 3D. Wisneski et al. [240] addressed by utilising that low myocardial stress correlates with a low EF and is associated with eccentric LV hypertrophy from AS patients. A study by Alharbi et al. [4], used CT images to make predictions about the outcome of transcatheter mitral valve replacement (TMVR). In the study the focus was analysing 3D flow patterns in the LV and predicting pressure gradient at the outflow tract to correctly identify LVOT obstruction. Ooms et al. [191], used segmented CT imaging data to computationally model TMVR and combined in later stages with 3D printing for intervention planning. The benefit of high-resolution CT data, enables to incorporate geometrical features within the LV that are commonly neglected in computational modelling, such as papillary muscles and trabeculae. Including these features and analysing cardiac hemodynamics, Lantz et al. [139] identified flow patterns and potential vortex formation inside the LV.

1.4.2 Magnetic Resonance Imaging

Magnetic Resonance Imaging (MRI) uses a combination of magnetic fields and electromagnetic radiation for multislice imaging instead of ionising radiation for cardiac CT. The general concept in MRI is based on sending out radio frequencies and changing the energy state and net magnetical alignment of the hydrogen nuclei in the patients tissue with respect to an applied external magnetic field. Cardiac MRI (CMR) images are typically acquired using a time-resolved (cine) MRI technique to track changes in heart structures over a cardiac cycle. Real-time imaging of the heart may be combined with breath-held segmented data or ECG. Despite, utilising rapid imaging sequences and accelerated parallel imaging methods for real-time imaging, MRI proves to have a low spatial and temporal resolution compared to CT imaging. One method to overcome the

drawbacks of CMR is a retrospective reconstruction of data over multiple heartbeats during normal breathing. Nevertheless, utilising Diffusion Tensor Cardiovascular Magnetic Resonance imaging (DT-CMR) supports the use of MRI as a noninvasive imaging modality to identify a healthy cardiac fibre architecture[224] or pathological G&R in the myocardium due to CVDs, such as fibre disarray in HCM[122,65]. By utilising cardiac MRI data Wang et al.[234] was able to model the passive diastolic mechanics and further study the underlying structure in healthy and pathological cardiac conditions. Asner et al.[18], used 3D-tagged MRI data to estimate the passive and active material properties of the heart on a patient-specific basis. A different approach for the estimation of myocardial tissue properties *in vivo* with respect to HF was done by Wang et al.[235]. By solving an inverse problem the LV passive and contractile material parameters were related to changes due to HF were estimated. By employing various passive cardiac material laws to tag 3D MRI data, Hadjicharalambous et al.[100] could justify the use of a reduced form of the Holzapfel-Ogden law. The increasing usage of *in vivo* data in finite element methods (FEM) to predict G&R makes it increasingly important to generate a load-free reference state. Wang et al.[237] utilised principal component analysis, to estimate the geometry of the load-free geometry and passive myocardial properties from MRI and catheter pressure data. As shown by Gomez et al.[86], RV fibre structure is an additional compensatory mechanism in pressure overload with the suggestion that longitudinal aligned myocardial fibres in the RV contribute to an increase of the RV ejection fraction. Combining the structural and time information from 4D flow CMR allowed[232] an evaluation of LV hypertrophy in AS by studying the influence of wall shear stresses introduced by changes in haemodynamics. To model adverse growth processes in the LV following myocardial infarction, Li et al.[149] used cine magnetic resonance and late gadolinium enhanced images. For the classification into reverse growth and adverse growth, the invariants of the kinematic growth tensor were studied as supposed drivers of G&R within the LV. Lee et al.[145], employed MRI images and manually segmented the LV geometry to model reverse growth following mechanical unloading. The predicted results showed high compatibility with experimental studies.

1.4.3 Echocardiography

Echocardiography defines a subcategory of ultrasound (US) specified on cardiac scans to visualise the heart and surrounding structures. The benefit of using US comes from its portability and low costs, compared to CT or MRI imaging modalities. A 2D image is generated by a transducer transmitting ultrasound waves through the patient where the waves interact with layers between different tissues and the echo return time gets mapped to calculate an image[37]. The image data contained in a standard echo provides information about the size of chambers, cavity volume, sphericity index and wall thickness. The parameters were subsequently utilised to validate the predicted pressure-volume relationship (PVR) and the subject-specific variability. By

estimating the cardiac contraction in highly spatially resolved data, Finsberg et al. [66] compared computed and measured strains and volumes from four-dimensional (4D) echocardiographic images. Albatat et al. [3], utilised 4D echocardiographic images of patients with cardiac resynchronisation therapy (CRT) to analyse regional left ventricular fibre stresses to predict success rates of CRT implantation in patients with HF. Usyk et al. [229], studied the septal strain distribution in patients with regional septal dysfunction. The study investigated different hypotheses, such as myofibre disarray and lower sarcomeres to determine the relative importance of these mechanisms in a three-dimensional computational model. Mojumder et al. [173], used 3D echo measurements to assess mechanical stimuli during pressure overload that may be drivers for G&R in this situation. Here the authors could identify that one most likely factors for growth during AS may be the myocyte stress introduced by the elevated pressure levels. Another study focusing on the identification of mechanical stimuli for G&R was performed by Peirlinck et al. [194]. By combining machine learning and the kinematic growth theory, the results suggested stretch being a primary stimulus for myocyte lengthening during the progress of HF. Milićević et al. [170], combined parametric and echocardiography-based LV shell elements to predict hypertrophy progression associated with changes. In this case, hypertrophy was related to the distance between the endocardium and the epicardium of the LV.

1.5 Computational Applications of G&R

This section gives a general overview of the literature on biomechanical modelling of G&R applied to the cardiac system, several review studies focus on a more detailed description [8,183,144,242]. Lee [142] introduced the theory of finite elastic and plastic strains contributing to the kinematics of a deformed body. The underlying concept was the introduction of two coupled thermodynamic systems, thermoelasticity at finite strain and irreversible processes such as dissipation and absorption of plastic work, to define elastic-plastic deformations for finite strains.

1.5.1 Kinematic Growth Theory

Rodriguez et al. [201] extended the theory from Lee [142] of two thermodynamic systems from the application in plasticity G&R in tissues via a kinematic mechanics approach. The theory of kinematic growth assumes that the deformation gradient $\boldsymbol{F}$ at time $t = s$, $\boldsymbol{F}(s)$, depicts the kinematic pathway from the reference frame to the physical frame via a multiplicative split into an inelastic growth deformation $\boldsymbol{F}_g(s)$ and a purely elastic deformation $\boldsymbol{F}_e$, see Figure 1.9B. The benefit of this approach is its simplicity and straightforward implementation, and the need for few material parameters.

By virtue of its advantages, this method is widespread as a computational application for modelling biological tissue, especially modelling cardiac G&R. Yet, the kinematic

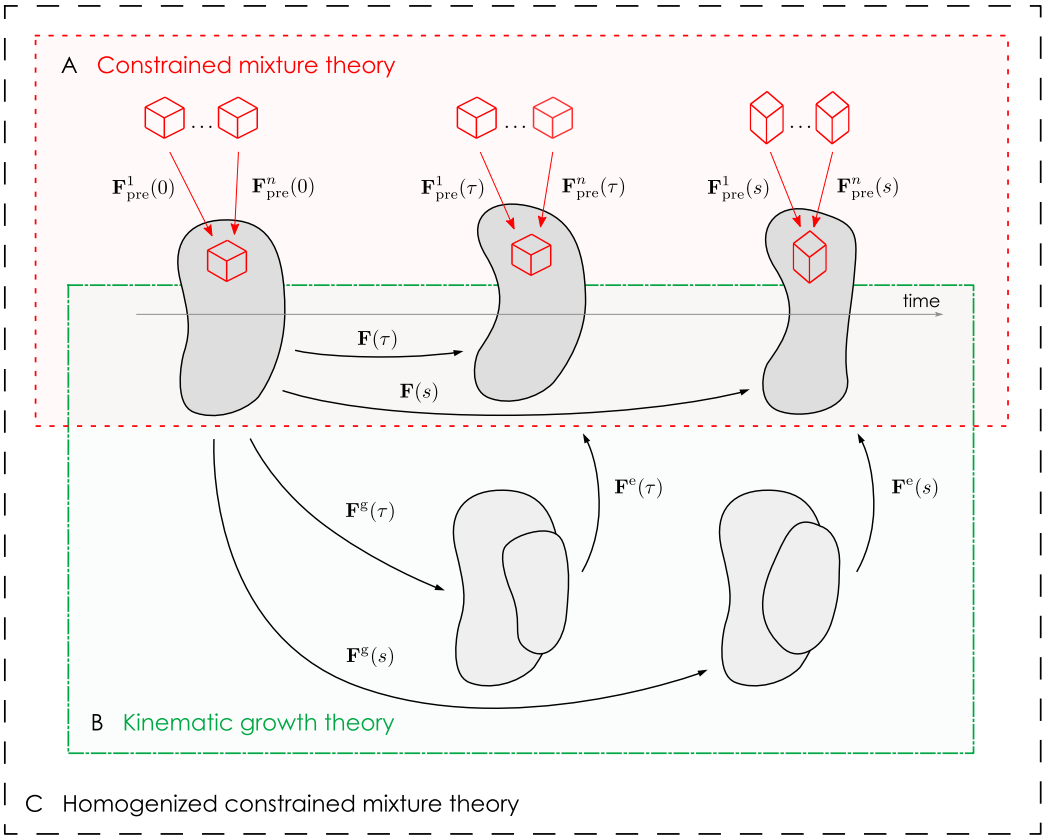

Figure 1.9 Summary of G&R theories. (A) is the constrained mixture theory, a body is composed of n individual constituents, each consisting of multiple mass increments which were deposited with a pre-stretch $\boldsymbol{F}_{pre_n}(t)$ at different times. The elastic pre-stretch depends on the individual stress-free natural configuration of each constituent. All constituents undergo the same elastic deformation together, despite having been deposited with different pre-stretches at different times. (B) In kinematic growth theory, the deformation gradient $\boldsymbol{F}$ is multiplicative split into an elastic part $\boldsymbol{F}_e$ and a part governing the growth deformation $\boldsymbol{F}_g$. The intermediate configuration may be incompatible if growth violates restrictions imposed by boundary conditions or is inhomogeneous in general. (C) The homogenized constrained mixture theory combines the kinematic growth and the constrained mixture approach in such a way that the benefits from both are inherited[46]. From Miller et al. [172]

growth theory does not account for all alterations due to growth in the tissue, such as growth of the fibres or changes in mechanical properties.

Applications of the kinematic growth theory are based on the recreation of growth patterns observed in diseases and their manifestation over time. Alterations in the heart commonly affect the myocardial volume or the underlying fibre network due to G&R processes[82]. An approach to model growth in arteries was done by Kuhl and Holzapfel[133]. The study investigated three different hypotheses of constitutive equations for growth and established Cauchy stresses as the primary driver of growth in arteries. Motivated by micromechanical alterations, models were developed focusing on fibre realignment along maximum principal strain directions to normalise strain levels[132,168]. Current G&R models enable a description of adaptations to supraphysiological loading conditions within the cardiac tissue. However, applying kinematic growth in a clinical setting to determine patient-specific treatment methods remains poorly understood. Peirlinck et al.[193] gives an overview of G&R models along with their future opportunities, such as drug development, HF, and ventricular assist devices. Costabal et al.[43] and Peirlinck et al.[194] performed a multiscale characterisation of heart failure introduced by volume overload in porcine hearts. During an eight-week period, a change in myocyte length was observed while the radial dimensions of the cardiac myocytes remained the same. Witzenburg and Holmes[241] performed simulations utilising a rapid compartmental model to predicted ventricular dilation and thickening in patients with aortic constriction over time. The motivation behind this study was to improve the computational costs of the anatomical realistic finite-element model by Kerckhoffs et al.[121] by reducing the model to a zero-dimensional model. Besides the morphological alterations of the heart, growth further influences the heart's electrical conduction system. Studies that combined kinematic growth models with electrophysiological models investigated changes in left bundle branch block[120] or cardiac resynchronization therapies[141,16]. Another field G&R models may be beneficial is the field of reverse growth, where the heart undergoes mechanical unloading due to intervention. Klepach et al.[124] suggested that removing an infarcted region of a LV may not reduce heterogeneous G&R driving forces after intervention, due to newly introduced kinematic heterogeneities from the curvature of the stitching region.

A reversible growth model for the LV was proposed and applied to MRI data to predict key features of end-diastolic pressure-volume relationship during growth and experimentally validated[145]. Above multiscale G&R models primarily focus on micromechanical growth drivers, however, a number of diseases indicate contributions to G&R related to changes in myocardial stiffness, ischemic diseases, valvular diseases, and hormone activity. Estrada et al.[58] combined mechanical and hormonal drivers to a case of transverse aortic constriction and suggested the application for surgical or drug intervention treatment.

1.5.2 Constrained Mixture Theory

A specification of the general mixture theory was developed by Humphrey and Rajagopal[114] to acknowledge the continuous turnover of constituents in the tissue (e.g. fibrillar collagen, muscle cells, etc.), referred to as the constrained mixture theory. G&R in biological tissue is associated with achieving a preferred state of homeostasis by rearranging and adding new constituents within the tissue to the existing ones, the rate of growth is defined by the change in mechanical and chemical stimuli. As indicated in Figure 1.9A, new constituents are deposited in a pre-deformed state ($\boldsymbol{F}_{pre_n}$) to comply with the existing tissue stretch level. Despite the fact that the constrained mixture theory accounts for constituent turnover, this approach has high computational costs and requires past configurations to model G&R. Consequently, this approach has mainly been used in the context of computational G&R modelling within arterial vessels[231].

1.5.3 Structural Adaptation Theory

Arts et al.[15] introduced the importance of reorientation of the microstructure within a simplified mechanical left ventricular model and further applied this theory on the cell level[14] within CircAdapt model[13]. As a next step Kroon et al.[129] computationally modelled the reorganization of microstructure based on Arts et al.[14] as a compensation mechanism to minimise shear strain between fibres and sheets that have a high impact on the shear properties of passive ventricular myocardium[54]. Subsequently, Pluijmert et al.[195] utilised the ratio of cavity-to-wall volume which defines the mean level of active wall stress[12] to their determination of the biventricular (BiV) cardiac functional models. Albeit, the structural adaptation theory recognises reorientation within the cardiac tissue, the combination with G&R models has to be still established to assess remodelling in volumetric growth. A general overview of structural adaptation can be found in Bovendeerd[33].

1.5.4 Fully Structural Theory

A major drawback of the previous theories and the fundamental theory behind these approaches is the use of a multiplicative split assuming a bijective motion during growth. As stated by Cowin[44] growth with a change in mass cannot be described by a one-to-one motion within a system and has to be extended from a closed system, utilised in the kinematic growth theory to an open system to address the mass influx to guarantee growth, resulting in a non-bijective motion. A challenge yet to be resolved is how this change in mass can be addressed with the commonly utilised kinematic growth theory. An early approach to address this drawback was investigated by Lanir[137],[138] for fibrous tissue. Here a one-dimensional G&R theory was proposed and further extended to mimic growth within three-dimensional bodies. In these particular studies, a multi-scale approach was utilised that addressed the evolving tissue structure over

time by adapting the number of fibres within a fibre bundle inside the domain (Fully Structural Theory). Considering that the total number of fibre bundles does not change within the tissue this theory can be considered as affine on a global scale, resulting in a bijective growth motion[138]. However, at the current stage, the Fully Structural Theory is restricted to collageneous tissue such as tendons and ligaments and has not been extended to multi-composite tissues, such as the heart.

1.5.5 Hybrid Theories

By combining the kinematic growth and the constrained mixture approach, a temporally homogenized constrained mixture model for G&R was first introduced by Cyron et al.[46] (Figure 1.9C). This enables one to utilise the advantages of both of the classical theories, such as the biologically motivated micromechanical foundation of the constrained mixture approach and the simple computational implementation as well the low computational cost of the kinematic growth approach. An application of the homogenized constrained mixture approach to soft tissue in the vasculature was done by Braeu et al.[35].

1.6 Thesis Outline

The aim of this thesis is to understand G&R patterns in the human heart. As described in Chapter 2, G&R in the heart appears to be a highly heterogeneous process with high variability in patients and across patient cohorts. Utilising the kinematic growth theory by Rodriguez et al.[201] may enable us to understand the underlying mechanisms of growth patterns in the heart. To achieve this task, this work was divided into three essential milestones. The first milestone before applying G&R to cardiac applications was to focus on the identification of certain perturbations of problem parameters and their impact on the final morphological state. The second contribution of this work was the investigation of regional growth in the heart. The third milestone of the thesis, emphasises reverse growth following surgical intervention.

Chapter 2: Prior to studying G&R in the heart, we review the fundamentals of cardiac mechanics and material laws. Based on the concept of cardiac mechanics we demonstrate the transition to G&R approaches where the focus lies on the kinematic growth approach[201].

Chapter 3: G&R is a complex mechanism that can be observed on multiple scales without the heart, from the changes in the cell up to visible hypertrophy pattern on the organ level. In this chapter, we focus on compatibility within the kinematic growth framework to study the potential implications of compatibility on the constitutive G&R law. Different perturbations of G&R problems were simulated and analysed to understand compatibility. The results indicated that the degree of complexity of the growth

tensor, e.g. spatial heterogeneity or anisotropy in simplified growth problems produced a compatible state regardless of the choice of material law. In these simplified tests, the solutions to the G&R problems with varying material laws converged to the same solution.

Chapter 4: The purpose of this chapter is to understand the underlying reason for the highly heterogeneous G&R pattern that can be observed in phenotypical growth in HCM. Local septal hypertrophy is observed in approximately 75% of HCM patients[187,112]. Consequently, we investigated three conceptual theories of septal hypertrophy, including fibre disarray, spatial heterogeneity of the applied growth tensor and spatial heterogeneity with an isotropic growth tensor to introduce a phenotypical HCM pattern in a region of the septum. Additionally, we studied the compatibility states of the different growth scenarios in a Neo-Hookean and a reduced Holzapfel-Ogden material. Ultimately, we observed that a regional isotropic kinematic growth tensor resulted in a phenotypic growth pattern observed in HCM.

Chapter 5: Different studies suggest that G&R following aortic valve replacement is a highly heterogeneous process. Yet, we still do not understand if the heart undergoes a specific type of G&R, such as concentric or eccentric growth after unloading. The milestone we are studying in this chapter is the understanding of growth patterns that may be associated with G&R after aortic valve replacement (AVR). Consequently, we applied a calculated kinematic growth tensor to the Pre-AVR model utilising a forward approach to achieve a modelled Post-AVR and compare it to the Post-AVR data. The workflow was designed to account for the unloading and mass reduction as the consequence of the surgical intervention. Additionally, a comparison shape comparison between the modelled Post-AVR and the Post-AVR state was executed. Subsequently, it could be identified that reverse growth following AVR is associated with kinematic growth tensors of the form concentric or isotropic reverse growth.

Chapter 6: A major challenge of applying G&R in cardiac applications, especially working with *in vivo* data is the definition of the kinematic growth tensor. This approach proposes a direction of growth by being defined via the microstructure of the heart. However, we can not be certain that growth is aligned with the structure of the myocardium. This chapter utilises inverse modelling to identify certain properties of the kinematic growth tensor $\boldsymbol{F}_g$ without any assumptions about the entries of the tensor. Consequently, the concept of universal ventricular coordinates was utilised to extract the displacement field $\boldsymbol{u}$ between a Pre-AVR and Post-AVR model, generated from twelve patient-specific cases. Based on $\boldsymbol{u}$ the growth tensor was computed and different tensor-specific metrics were analysed over a data set. It could be observed that cases with a positive response to AVR underwent reverse growth in the free wall and growth in regions of the septum. Additionally, we noticed a heterogeneous G&R pattern within the LV in both, reverse growth and adverse growth.

Chapter 7: The final chapter of the thesis summarises conclusions established by the milestones targeted and also gives an outlook on the future perspectives of computational modelling of G&R with the application in the heart.

2 Cardiac Mechanics and Kinematic Growth

Natural and pathophysiological processes are well–known to cause alterations in the morphology and biomechanical properties of the heart. A more detailed look into this growth and remodelling (G&R), its application fields, different G&R frameworks and future perspectives are presented in a number of literature reviews [183,242,8,76]. The cardiac system can undergo different types of G&R during life, physiological types include G&R in the developing embryonic heart [220] and growth induced by exercise (athlete's heart) [197]. However, investigating maladaptive G&R and reverse growth following treatment provides insight into how the heart reacts to certain growth drivers. Better understanding and knowledge of these G&R drivers could be utilised to provide more accurate diagnostic tools and further help patient-specific intervention planning to predict long–term outcomes.

This chapter reviews the important equations utilised throughout this thesis presenting the mathematics behind the kinematic growth theory and also to overview of some of the common constitutive laws The kinematic growth theory provides us with a powerful tool to simulate growth but additionally may introduce incompatibilities and residual stresses. Research on these incompatibilities is still sparse. In a later section, we introduce a metric that may assist us in identifying introduced incompatibilities in the continuum body. We studied different potential drivers for incompatibility, such as material laws, properties of the kinematic growth tensor (spatial heterogeneity/anisotropy), and the complexity of the geometry. By virtue of G&R processes being over a long time scale, we are assuming that short-time changes in regional stress or strain levels are not governing the kinematic growth tensor.

The rest of this section is structured as follows, a general review of significant kinematic properties (Section 2.1), stresses (Section 2.2) and equilibrium condition (Section 2.3) that are associated with deformation in the heart neglecting growth mechanisms is presented. Next, the kinematic G&R framework, introduced in Section 2.4.1, is incorporated in the established kinematic setup resulting in a reformulation of the previous equations (Section 2.4). And at the end, an overview of the employed material equations to describe the myocardium is presented (Section 2.5).

2.1 Kinematics in Cardiac Mechanics

This section aims to give a brief general overview of the basic kinematics of large deformations. For a more detailed description, the reader is referred to [108,31,88]. Later on, these concepts will be expanded to incorporate G&R. The use of kinematic equations enables the tracking of a body's evolution over space and time driven by deformation processes (see Figure 2.1). Across all the studies in the later chapters of this thesis, the space dimension is assumed to be in 3D ($d = 3$). The undeformed body is defined as the reference configuration $\Omega_0 \subset \mathbb{R}^d$ with the initial material point coordinates denoted as $\mathbf{X} \in \Omega_0$. The deformed configuration of the body at the current time frame is specified in $\Omega_t \subset \mathbb{R}^d$ with the spatial coordinates $\boldsymbol{x} \in \Omega_t$. The relation between the particle position in the reference configuration $\mathbf{X}$ and the position in the current configuration $\boldsymbol{x}$ is characterised by a displacement field $\boldsymbol{u} : \Omega_0 \times [0, T] \to \mathbb{R}^d$ and a bijective map [108] $\boldsymbol{\chi} : \Omega_0 \times [0, T] \to \Omega_t$, where

$$\boldsymbol{x}(\mathbf{X}, t) = \boldsymbol{\chi}(\mathbf{X}, t) = \boldsymbol{u}(\mathbf{X}, t) + \mathbf{X} \quad \forall \mathbf{X} \in \Omega_0, \ \forall t \in [0, T]. \tag{2.1}$$

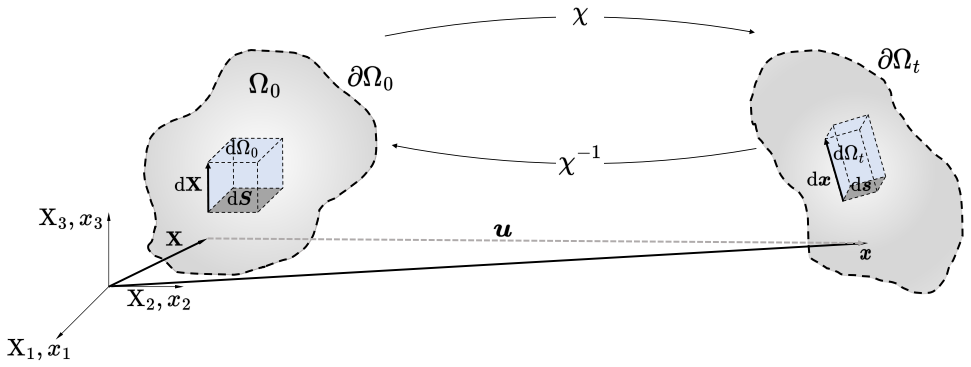

Figure 2.1 Kinematics within deformed bodies, with the reference domain Ω_0, bounded by $\partial\Omega_0$, and the physical domain Ω_t, bounded by $\partial\Omega_t$ that are linked via the bijective map $\boldsymbol{\chi}$.

All the physical variables which are ascribed to the system and which vary spatially can be described with respect to either the reference or the current (deformed) configuration. These descriptions are commonly referred to as either Lagrangian or Eulerian, respectively.

2.1.1 Deformation Gradient

For the characterisation of large deformations the deformation gradient $\boldsymbol{F}$ is used to describe local, relative deformations and stress or strain relations of a point and its surrounding due to motion and is obtained by the spatial derivative $\boldsymbol{\chi}$, such that

$$\boldsymbol{F}(\mathbf{X},t) = \frac{\partial \boldsymbol{\chi}}{\partial \mathbf{X}} = \frac{\partial \boldsymbol{x}}{\partial \mathbf{X}} = \nabla_{\mathbf{X}} \boldsymbol{u}(\mathbf{X},t) + \mathbf{I}. \tag{2.2}$$

Where the subscript of the gradient operator ($\nabla_{\mathbf{X}}$) refers to the reference domain of the continuum body[28]. The vectors $\mathrm{d}\boldsymbol{x}$ and $\mathrm{d}\mathbf{X}$ (shown in Figure 2.1) denote infinitesimal vector elements in the spatial domain and the material domain and are linked via $\mathrm{d}\boldsymbol{x} = \boldsymbol{F}\mathrm{d}\mathbf{X}$, with $\boldsymbol{F}$ being a linear transformation map.

The deformation gradient encompasses information on changes in vector length and orientation of a line element over time. Additional quantities are introduced to define the change in length of a line element, e.g. strain tensors. Assuming that a general measure for deformation is the change of a line element, considering the squared magnitude (L_2 norm) of a tangent vector $\mathrm{d}\boldsymbol{x}$ in the spatial domain that can be related back to its undeformed configuration $\mathrm{d}\mathbf{X}$ by

$$||\mathrm{d}\boldsymbol{x}||_2^2 = \mathrm{d}\boldsymbol{x}^T\mathrm{d}\boldsymbol{x} = (\boldsymbol{F}\mathbf{X})^T(\boldsymbol{F}\mathbf{X}) = \mathbf{X}^T\boldsymbol{F}^T\boldsymbol{F}\mathbf{X} = \mathbf{X}^T\boldsymbol{C}\mathbf{X}. \tag{2.3}$$

The term $\boldsymbol{C} = \boldsymbol{F}^T\boldsymbol{F}$ in Equation 2.3 is known as either the right Cauchy-Green tensor or the Green deformation tensor[134]. Similarly, the square norm of $d\mathbf{X}$ can be expressed in terms of $d\boldsymbol{x}$ as:

$$||\mathrm{d}\mathbf{X}||_2^2 = \mathrm{d}\mathbf{X}^T\mathrm{d}\mathbf{X} = (\boldsymbol{F}^{-1}\boldsymbol{x})^T(\boldsymbol{F}^{-1}\boldsymbol{x}) = \boldsymbol{x}^T\boldsymbol{F}^{-T}\boldsymbol{F}^{-1}\boldsymbol{x} = \boldsymbol{x}^T\boldsymbol{b}^{-1}\boldsymbol{x}. \tag{2.4}$$

Where $\boldsymbol{B}^{-1} = \boldsymbol{F}^{-T}\boldsymbol{F}^{-1}$ is the inverse of the left Cauchy-Green tensor $\boldsymbol{B}$. Letting $\mathrm{d}V$ and $\mathrm{d}v$ denote infinitesimal volume elements in the material and spatial frame respectively, a change of volume $\mathrm{d}v$ from $\mathrm{d}V$ can be related by

$$\mathrm{d}v = J\mathrm{d}V, \tag{2.5}$$

$$\text{with } J = \det \boldsymbol{F} > 0. \tag{2.6}$$

Certain types of motion may show volume-preserving characteristics in which case, $J = 1$. The relation between the deformed and undeformed infinitesimal surfaces is given by Nanson's formula[108]

$$\mathrm{d}\boldsymbol{s} = J\boldsymbol{F}^{-T}\mathrm{d}\boldsymbol{S}. \tag{2.7}$$

Where $\mathrm{d}\boldsymbol{S}$ and $\mathrm{d}\boldsymbol{s}$ denote infinitesimal material surface elements.

2.1.2 Tensor Invariants

According to a defined coordinate system, different components are utilised to define a second-order tensor and will change when the axes are rotated, an important exemption here is the identity matrix $\boldsymbol{I}$ and its multiples $\alpha\boldsymbol{I}$[31]. However, eigenvalues or eigenvectors of a tensor are independent of the choice of coordinate basis. In the case of a positive definite symmetric tensor, such as $\boldsymbol{C}$ and $\boldsymbol{B}$, the eigenvalues λ_i with $i = 1, 2, 3$ and resulting eigenvectors are real and positive and form a mutually orthogonal basis[108]. For generalisation purposes, let $\boldsymbol{A}$ be a second-order tensor that

satisfies positive definite symmetry where the principal scalar invariants of $\boldsymbol{A}$ are defined by

$$I_1(\boldsymbol{A}) = A_{ii} = \mathrm{tr}\boldsymbol{A} = \lambda_1 + \lambda_2 + \lambda_3, \tag{2.8}$$

$$I_2(\boldsymbol{A}) = \boldsymbol{A} : \boldsymbol{A} = \lambda_1\lambda_2 + \lambda_1\lambda_3 + \lambda_2\lambda_3, \tag{2.9}$$

$$I_3(\boldsymbol{A}) = \det \boldsymbol{A} = \lambda_1\lambda_2\lambda_3, \tag{2.10}$$

$$I_a(\boldsymbol{A}) = \boldsymbol{A} : \mathbf{e}_a \otimes \mathbf{e}_a = \mathbf{e}_a \cdot \boldsymbol{A}\mathbf{e}_a = \mathbf{E}_a \cdot \mathbf{E}_a, \tag{2.11}$$

$$I_{ab}(\boldsymbol{A}) = \mathbf{A} : \mathrm{sym}(\mathbf{e}_a \otimes \mathbf{e}_b) = \mathbf{E}_a \cdot \mathbf{E}_b. \tag{2.12}$$

Where $\mathbf{e}_a$ and $\mathbf{e}_b$ denote unit vectors in the direction a and b in the physical frame and $\mathbf{E}_a$ and $\mathbf{E}_b$ are the associated unit vectors in the reference domain. The $\otimes$, indicates that here the structural tensor is being utilised. For the remainder of this thesis, when we refer to I_1, I_2, I_3, I_a and I_{ab} it is $I_1(\boldsymbol{C})$, $I_2(\boldsymbol{C})$, $I_3(\boldsymbol{C})$, $I_a(\boldsymbol{C})$ and $I_{ab}(\boldsymbol{C})$ specifically.

2.1.3 Distortional Quantities in Kinematics

Incompressible and nearly incompressible materials can respond to bulk and shear deformation quite differently compared to each other. For this type of incompressible or nearly incompressible materials, a multiplicative decomposition of the deformation gradient into a volumetric (dilatational) and volume-preserving (distortional) component can be considered[108,31], resulting in

$$\bar{\boldsymbol{F}} = J^{-1/d}\boldsymbol{F}, \tag{2.13}$$

$$\bar{\boldsymbol{C}} = J^{-2/d}\boldsymbol{C}, \tag{2.14}$$

$$\bar{\boldsymbol{B}} = J^{-2/d}\boldsymbol{B}. \tag{2.15}$$

Where the terms $J^{-1/d}$ and $J^{-2/d}$ are associated with the volume change provoked by deformation. Whereas $\bar{\boldsymbol{F}}$, $\bar{\boldsymbol{C}}$ and $\bar{\boldsymbol{B}}$ are directly related to distortional (isochoric) deformations.

2.2 Stress Tensors

Deformation enforces the interaction of neighbouring material points in the interior of a body as a consequence internal stresses. Stress in the current configuration is defined as the force experienced per unit area, referred to as the Cauchy stress tensor $\boldsymbol{\sigma}$. The Cauchy stress tensor characterises the relationship between the traction force $\boldsymbol{t}$ and the surface normal $\boldsymbol{n}$ by

$$\boldsymbol{t}(\boldsymbol{x}, t, \boldsymbol{n}) = \boldsymbol{\sigma}(\boldsymbol{x}, t)\boldsymbol{n}. \tag{2.16}$$

In contrast to $\boldsymbol{\sigma}$ being defined in the physical frame, the first Piola-Kirchhoff stress tensor $\boldsymbol{P}$ (PK1) is defined by a traction force vector $\boldsymbol{T}$ measured per unit surface area

in the reference configuration $\boldsymbol{N}$, such as

$$\boldsymbol{T}(\mathbf{X}, t, \boldsymbol{N}) = \boldsymbol{P}(\mathbf{X}, t)\boldsymbol{N}. \tag{2.17}$$

Utilising Nanson's formula (Equation 2.7) it is possible to find the relation between the Cauchy stress tensor and the PK1, the passage from $\boldsymbol{\sigma}$ to $\boldsymbol{P}$ is defined as the push forward Piola transformation

$$\boldsymbol{P}(\mathbf{X}, t) = J\boldsymbol{\sigma}(\boldsymbol{x}, t)\boldsymbol{F}^{-T}. \tag{2.18}$$

An alternative to the introduced stresses $\boldsymbol{\sigma}$ and $\boldsymbol{P}$ is the second Piola-Kirchhoff stress tensor $\boldsymbol{S}$ (PK2). That is not linked to a physical interpretation of the surface traction and is described via

$$\boldsymbol{S} = J\boldsymbol{F}^{-1}\boldsymbol{\sigma}\boldsymbol{F}^{-T} = \boldsymbol{F}^{-1}\boldsymbol{P} = \boldsymbol{S}^{T}. \tag{2.19}$$

Cauchy and Piola-Kirchhoff stress tensors represent useful measurements in computational mechanics where they are utilised to define constitutive equations in solids.

2.3 Balance Principles

A deformable continuum body that undergoes finite motion has to satisfy a fundamental set of balance principles (equilibrium concepts), i.e. conservation of mass, the momentum balance principles and balance of energy at all times[108,31]. These conditions ensure that an isolated mechanical system remains in an equilibrium state during deformation.

2.3.1 Conservation of Mass

Assuming a mechanical system is closed, the system has a constant mass m over time within a continuum body, and no mass can be produced or destroyed, and neither can it leave or enter the system through the surface boundary. However, the volume of a closed system can change. Let $V \subseteq \Omega_0$ be an arbitrary volume in the material configuration that can be further mapped to $v \subseteq \Omega_t$ in the spatial frame with the bijective map $\boldsymbol{\chi}$. Thus m can be defined in both configurations, via

$$m = \int_V \rho_0(\mathbf{X})\mathrm{d}V = \int_v \rho_t(\boldsymbol{x}, t)\mathrm{d}v = \text{const} > 0. \tag{2.20}$$

Where ρ_0 and ρ_t are the mass density in the reference and physical frame respectively. The relationship between mass change from the material and the physical frame can be also defined in terms of the reference domain alone, such that

$$\int_V [\rho_0(\mathbf{X}) - \rho_t(\boldsymbol{\chi}(\mathbf{X}, t), t)J(\mathbf{X}, t)]\mathrm{d}V = 0. \tag{2.21}$$

As V is any a subset of Ω_0, for a solid mechanics problem the continuity mass equation with respect to the Lagrangian coordinates can be described as

$$\rho_0(\mathbf{X}) = \rho_t(\boldsymbol{\chi}(\mathbf{X}, t), t)J(\mathbf{X}, t), \tag{2.22}$$

and holds for all $\mathbf{X} \in \Omega_0$. Assuming no change of the density over time (*e.g.* $\rho = \rho_t = \rho_0$), the conservation of mass reduces to the common incompressibility condition,

$$J - 1 = 0, \tag{2.23}$$

to ensure the incompressibility constraint of the material.

2.3.2 Conservation of Linear Momentum

The conservation of linear momentum is described by Cauchy's law of motion. For the application of Newton's law of motion within the continuum mechanic framework. Subsequently, is the linear momentum equation utilised to link the mass to the velocity distribution in a continuum body[5]. The definition of the balance of linear momentum in the physical description is the sum of all forces acting on the surface and the volume of a continuum body is equal to its mass multiplied by its acceleration. Formally, this can be written as the entirety of forces on an arbitrary volume $v \subseteq \Omega_t$ with the boundary surface γ the rate change be

$$\int_\gamma \boldsymbol{t}(\boldsymbol{x}, t, \boldsymbol{n})\mathrm{d}\gamma + \int_v \boldsymbol{b}(\boldsymbol{x}, t)\mathrm{d}v = \frac{\mathrm{d}}{\mathrm{d}t}\int_v \rho_t \mathbf{v}(\boldsymbol{x}, t)\mathrm{d}v. \tag{2.24}$$

Where the Cauchy traction vector $\boldsymbol{t}$ is measured per unit surface area in the physical frame, $\boldsymbol{b}$ is a spatial vector field called the body force and $\boldsymbol{v}$ is the spatial velocity field. Applying the integral form of Cauchy's stress theorem and utilising the divergence theorem on the surface integral term of Equation 2.24 enables the transformation of the surface integral into a volume integral, stated as following

$$\int_\gamma \boldsymbol{t}(\boldsymbol{x}, t, \boldsymbol{n})\mathrm{d}\gamma = \int_\gamma \boldsymbol{\sigma}(\boldsymbol{x}, t)\boldsymbol{n}\mathrm{d}\gamma = \int_v \nabla_{\boldsymbol{x}} \cdot \boldsymbol{\sigma}(\boldsymbol{x}, t)\mathrm{d}v. \tag{2.25}$$

The time-derivative term of Equation 2.24 can be reformulated by considering the volume transformation rule and the mass continuity equation ($\rho_0 = \rho_t J$) such as

$$\begin{aligned} \frac{\mathrm{d}}{\mathrm{d}t}\int_v \rho_t \mathbf{v}(\boldsymbol{x}, t)\mathrm{d}v &= \int_{V_0} \frac{\mathrm{d}}{\mathrm{d}t}(\rho_t \mathbf{v} J)\mathrm{d}V \\ &= \int_{V_0} \frac{1}{J}\frac{\mathrm{d}}{\mathrm{d}t}(\rho_t J\mathbf{v})J\mathrm{d}V \\ &= \int_v \frac{1}{J}\frac{\mathrm{d}}{\mathrm{d}t}(\rho_0 \mathbf{v})\mathrm{d}v. \end{aligned} \tag{2.26}$$

Where ρ_0 is defined as the reference density. By substituting the surface and time-derivative integral with Equation 2.25 and 2.26, respectively, Cauchy's first equation of motion can be defined such that

$$\int_v \left(\nabla_{\boldsymbol{x}} \cdot \boldsymbol{\sigma}(\boldsymbol{x}, t) + \boldsymbol{b}(\boldsymbol{x}, t) - \frac{1}{J} \frac{\mathrm{d}}{\mathrm{d}t}(\rho_t \mathbf{v} J) \right) \mathrm{d}v = \mathbf{0}. \tag{2.27}$$

Noting this momentum balance holds for any arbitrary volume $v \subset \Omega_0$, examining the limit as $|v| \to 0$, we arrive at Cauchy's first equation

$$\nabla_{\boldsymbol{x}} \cdot \boldsymbol{\sigma}(\boldsymbol{x}, t) + \boldsymbol{b}(\boldsymbol{x}, t) - \frac{1}{J} \frac{\partial}{\partial t}(\rho_t \mathbf{v} J) = \mathbf{0}. \tag{2.28}$$

Considering an incompressible material, where $J - 1 = 0$, the conservation of linear momentum reduces to

$$\nabla_{\boldsymbol{x}} \cdot \boldsymbol{\sigma}(\boldsymbol{x}, t) + \boldsymbol{b}(\boldsymbol{x}, t) - \rho_t \frac{\partial \mathbf{v}}{\partial t} = \mathbf{0}. \tag{2.29}$$

For solid mechanical problems, it may be advised to describe the mechanical problem rather in the material instead the spatial frame, e.g.

$$\int_{\gamma_0} \boldsymbol{\sigma} J \boldsymbol{F}^{-T} \boldsymbol{N} \mathrm{d}\Gamma + \int_{V_0} J \boldsymbol{b} \mathrm{d}V = \int_{V_0} \frac{\mathrm{d}}{\mathrm{d}t}(\rho_t \mathbf{v} J) \mathrm{d}V, \tag{2.30}$$

where $\boldsymbol{\sigma} = J^{-1} \boldsymbol{F} \boldsymbol{S} \boldsymbol{F}^T$ resulting in

$$\int_{\gamma_0} \boldsymbol{F} \boldsymbol{S} \boldsymbol{N} \mathrm{d}\Gamma + \int_{V_0} J \boldsymbol{b} \mathrm{d}V = \int_{V_0} \frac{\mathrm{d}}{\mathrm{d}t}(\rho_t \mathbf{v} J) \mathrm{d}V. \tag{2.31}$$

Reformulating the global form of the linear momentum equation in the reference frame (Equation 2.31) to the local point-wise formulation leads to

$$\nabla_{\mathbf{X}} \cdot (\boldsymbol{F} \boldsymbol{S}) + J \boldsymbol{b} - \frac{\mathrm{d}}{\mathrm{d}t}(\rho_t \mathbf{v} J) = \mathbf{0}. \tag{2.32}$$

For incompressible material ($J = 1$) the momentum term of Equation 2.32 changes to

$$\nabla_{\mathbf{X}} \cdot (\mathbf{F}\mathbf{S}) + \boldsymbol{b} - \rho_t \frac{\mathrm{d}\mathbf{v}}{\mathrm{d}t} = \mathbf{0}. \tag{2.33}$$

2.3.3 Conservation of Angular Momentum

The rotational equilibrium of a continuum body implies that the sum of traction on a body and the momentum of the body on an arbitrary point vector $\boldsymbol{r}(\boldsymbol{x})$ within the domain are in equilibrium with each other, e.g.

$$\int_\gamma \boldsymbol{r}(\boldsymbol{x}) \times \boldsymbol{t}(\boldsymbol{x}, t, \boldsymbol{n}) \mathrm{d}\gamma + \int_v \mathbf{r}(\boldsymbol{x}) \times \boldsymbol{b}(\boldsymbol{x}, t) \mathrm{d}v = \frac{\mathrm{d}}{\mathrm{d}t} \int_v \boldsymbol{r}(\boldsymbol{x}) \times (\rho_t \mathbf{v}(\boldsymbol{x}, t)) \mathrm{d}v. \tag{2.34}$$

Applying Gauss' theorem to the symmetric Cauchy stress tensor of the surface integral in Equation 2.34 enables conversion to a volume integral, such as[31]

$$\int_{\gamma} \boldsymbol{r} \times \boldsymbol{t} \mathrm{d}\gamma = \int_{\gamma} \boldsymbol{r} \times \boldsymbol{\sigma} \boldsymbol{n} \mathrm{d}\gamma = \int_{v} (\boldsymbol{r}(\boldsymbol{x}) \times \nabla_{\boldsymbol{x}} \cdot \boldsymbol{\sigma} + \boldsymbol{\varepsilon} \boldsymbol{\sigma}^{T}) \mathrm{d}v, \tag{2.35}$$

where $\boldsymbol{\varepsilon} = \varepsilon_{ijk} \mathbf{e}_i \otimes \mathbf{e}_j \otimes \mathbf{e}_k$ denotes a third-order permutation tensor with

$$\boldsymbol{\varepsilon}_{ijk} = \begin{cases} 1 & \text{if permutation } \{i,j,k\} \text{ is even} \\ -1 & \text{if permutation } \{i,j,k\} \text{ is odd} \\ 0 & \text{if permutation } \{i,j,k\} \text{ has repeated indices.} \end{cases} \tag{2.36}$$

By utilising Cauchy's first equation of motion (Equation 2.34 and 2.35) and the fact that v is an arbitrary volume the permutation term in the global and local form vanishes

$$\int_{\Omega_t} \boldsymbol{\varepsilon} \boldsymbol{\sigma}^{T} \mathrm{d}v = \mathbf{0}, \tag{2.37}$$

$$\boldsymbol{\varepsilon} \boldsymbol{\sigma}^{T} = \mathbf{0}, \tag{2.38}$$

and holds for each point $\boldsymbol{x}$ for time t. Due to the conservation of angular momentum, the symmetry of $\boldsymbol{\sigma} = \boldsymbol{\sigma}^{T}$ follows that the permutation term in Equation 2.38 must be zero for the components

$$\sigma_{32} - \sigma_{23} = 0 \qquad \sigma_{13} - \sigma_{31} = 0 \qquad \sigma_{21} - \sigma_{12} = 0. \tag{2.39}$$

2.4 Kinematic Growth Approach

This section is an extension of the established equations from Section 2.1. During a cardiac cycle, the heart is constantly exposed to alterations in the loading condition[172]. CVDs can trigger chronic overload within the ventricle cavity, and in order to cope with the elevated blood pressure (BP), G&R can be induced, leading to changes in the underlying fibre microstructure and mass of the myocardial tissue. The kinematic G&R approach utilised throughout this thesis has its fundaments in a classical continuum mechanics approach for finite strains in plasticity[142]. The idea behind modelling G&R is a multiplicative split of the deformation gradient $\boldsymbol{F}$, into a purely inelastic deformation $\boldsymbol{F}_g$, associated with growth and an elastic part described by $\boldsymbol{F}_e$[201], such that

$$\boldsymbol{F}(\mathbf{X}, t) = \boldsymbol{F}_e(\mathbf{X}_g, t) \cdot \boldsymbol{F}_g(\mathbf{X}, t). \tag{2.40}$$

This theory is based on the assumption that a point in the material frame $\mathbf{X} \in \Omega_0 \subset \mathbb{R}^3$ is first mapped to a point in a fictitious new growth state following point-wise defor-

mation (e.g. growth or shrinking), $\mathbf{X}_g \in \Omega_g \subset \mathbb{R}^3$, see Figure 2.2. The grown state can be an incompatible frame, this can be indicated by disconnected or overlapping volume in the deformed fictitious domain[87]. Incompatibility can arise due to inhomogeneous growth patterns or imposing boundary conditions (BC) on the growth problem. Compatibility of the spatial configuration is "restored" by an elastic deformation $\boldsymbol{F}_e$ applied to the intermediate configuration with $\boldsymbol{x} \in \Omega_t \subset \mathbb{R}^3$.

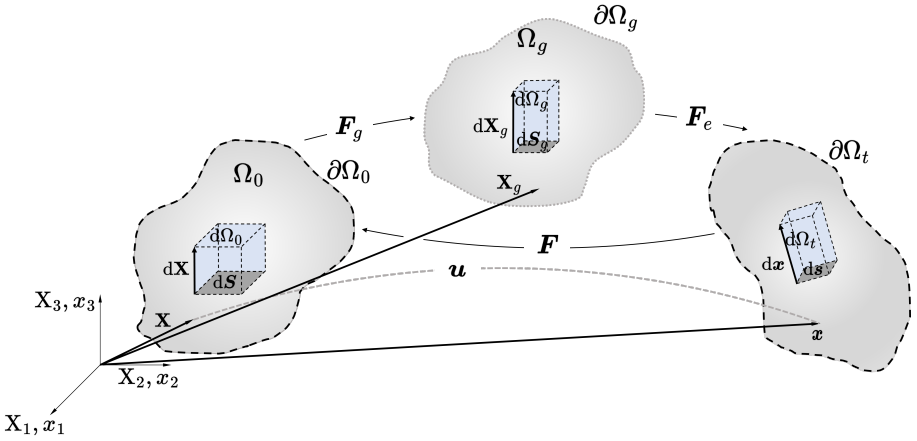

Figure 2.2 Kinematics within deformed bodies, with the reference domain Ω_0, bounded by $\partial\Omega_0$, the physical domain Ω_t, bounded by $\partial\Omega_t$ and the virtual growth domain Ω_g, bounded by $\partial\Omega_g$ that are linked via the deformation gradient $\boldsymbol{F}$, the growth deformation gradient $\boldsymbol{F}_g$ and the elastic deformation gradient $\boldsymbol{F}_e$.

2.4.1 Special case of compatible G&R

Assuming the special case of compatible G&R, the material undergoes growth, resulting in a change in the underlying domain. Let's also consider that the material does not undergo remodelling, meaning that the material's stress-strain response, or strain energy stays constant. Similarly, there are no changes to underlying parameters and materials. In this case, we can think of growth as a transformation which maps our material reference domain, Ω_0, to a new state, Ω_g. In the case of compatible growth, and assuming that the mapping is bijective, this transformation takes the form

$$\mathbf{X}_g = \boldsymbol{\chi}_g(\mathbf{X}) = \boldsymbol{u}_g(\mathbf{X}) + \mathbf{X}. \tag{2.41}$$

Where $\mathbf{X}_g \in \Omega_g$, $\mathbf{X} \in \Omega_0$ and $\boldsymbol{u}_g$ is a displacement mapping points between reference domains. Here, we assume that time-scales for growth are significant slower than those of the solid, making $\boldsymbol{u}_g$ effectively quasi-static with respect to the solid mechanical system. In this case, the material behaviour is still governed by Cauchy's first law and the conservation of mass as defined in the physical domain in Sections 2.3.1-2.3.3. However, in this case the equations, as written in the reference state, and the constitutive law must also be adapted to account for the material growth.

The effective growth of the tissue means that further loading and deformation of the

body generates stresses with respect to deformations from Ω_g to the physical domain Ω_t. Hence, whereas the original problem defined the main kinematic and kinetic tensors as

$$\boldsymbol{F} = \frac{\partial \boldsymbol{x}}{\partial \mathbf{X}}, \quad \boldsymbol{C} = \boldsymbol{F}^T\boldsymbol{F}, \quad \boldsymbol{P} = \frac{\partial \psi(\boldsymbol{F})}{\partial \boldsymbol{F}} \tag{2.42}$$

with growth, we now examine these quantities on the newly grown domain

$$\boldsymbol{F}_e = \frac{\partial \boldsymbol{x}}{\partial \mathbf{X}_g}, \quad \boldsymbol{C}_e = \boldsymbol{F}_e^T\boldsymbol{F}_e, \quad \boldsymbol{P}_e = \frac{\partial \psi(\boldsymbol{F}_e)}{\partial \boldsymbol{F}_e}. \tag{2.43}$$

As before, we can define

$$\boldsymbol{x} = \boldsymbol{u}_e(\mathbf{X}, t) + \mathbf{X}_g. \tag{2.44}$$

Where now $\boldsymbol{u}_e$ maps the grown reference state to the current physical domain under load (and $\boldsymbol{v}_e$ the corresponding velocity). Note, that since growth is effectively quasi-static with respect to kinetics of the body, $\boldsymbol{v} = \boldsymbol{v}_e$. Just as before, we can derive the same balance laws of mass and momentum from the grown domain, e.g. for an incompressible body (after growth),

$$\nabla_{\mathbf{X}_g} \cdot \boldsymbol{P}_e + \boldsymbol{b}_e - \frac{\partial(\rho \boldsymbol{v}_e J_e)}{\partial t} = \mathbf{0} \quad \text{on } \Omega_g \tag{2.45}$$

$$J_e - 1 = 0. \quad \text{on } \Omega_g \tag{2.46}$$

Where $\nabla_{\mathbf{X}_g}$ is the gradient operator with respect to $\mathbf{X}_g$, and $\boldsymbol{b}_e = J_e\boldsymbol{b}$ is the jacobian-weighted body force.

This form requires a more formal construction of Ω_g, and it can be helpful to cast the problem in terms of the original reference domain, Ω_0. By the chain rule, we know

$$\boldsymbol{F} = \frac{\partial \boldsymbol{x}}{\partial \mathbf{X}} = \frac{\partial \boldsymbol{x}}{\partial \mathbf{X}_g}\frac{\partial \mathbf{X}_g}{\partial \mathbf{X}} = \boldsymbol{F}_e\boldsymbol{F}_g. \tag{2.47}$$

Where $\boldsymbol{F}_g = \nabla_{\mathbf{X}}\mathbf{X}_g$ (with determinant $J_g = \det(\boldsymbol{F}_g)$) is given by the known growth map between Ω_0 and Ω_g. This identity enables us to further conclude that

$$J = J_e J_g. \tag{2.48}$$

Similarly, the PK2 tensor, $\boldsymbol{P}_e$ can be computed with respect to deformation quantities defined in the original reference domain, e.g.

$$\tilde{\boldsymbol{P}} = \left.\frac{\partial \psi(\boldsymbol{F}_e)}{\partial \boldsymbol{F}_e}\right|_{\boldsymbol{F}_e = \boldsymbol{F}\boldsymbol{F}_g^{-1}} \tag{2.49}$$

e.g. for a neo-Hookean material,

$$\boldsymbol{P}_e = \frac{1}{J_e^{2/3}}\left(\boldsymbol{F}_e - \frac{\boldsymbol{C}_e : \boldsymbol{I}}{3}\boldsymbol{F}_e^{-T}\right), \quad \tilde{\boldsymbol{P}} = \left(\frac{J_g}{J}\right)^{2/3}\left(\boldsymbol{F}\boldsymbol{F}_g^{-1} - \frac{\boldsymbol{C} : \boldsymbol{C_g}}{3}\boldsymbol{F}^{-T}\boldsymbol{F}_g^{T}\right), \tag{2.50}$$

Finally, we note that (using Nanson's formula and the Divergence theorem),

$$\nabla_{\mathbf{X}_g} \cdot \boldsymbol{P}_e = \nabla_{\mathbf{X}} \cdot (J_g \tilde{\boldsymbol{P}} \boldsymbol{F}_g^{-T}). \tag{2.51}$$

Combining the momentum and mass balance equations (Equations 2.45 and 2.46) we obtained a saddle point system in the form of:

$$J_g \nabla_{\mathbf{X}} \cdot \left(J_g \tilde{\boldsymbol{P}} \boldsymbol{F}_g^{-T}\right) + J\boldsymbol{b} - \frac{\partial(\rho \boldsymbol{v} J)}{\partial t} = \mathbf{0} \quad \text{on } \Omega_0 \tag{2.52}$$

$$J - J_g = 0. \quad \text{on } \Omega_0. \tag{2.53}$$

This system of equations is now set up to run on the reference domain which means no explicit formation of Ω_g is needed to solve kinetics in the grown state.

We refer to this case as compatible, that is where $\boldsymbol{u} = \boldsymbol{u}_e$, which is equivalent to an effective elastic deformation gradient $\boldsymbol{F}_e = \boldsymbol{I}$. As most material models a structured such that $\tilde{\boldsymbol{P}}(\boldsymbol{I}) = \mathbf{0}$, meaning the new reference state remains devoid of residual stresses.

2.4.2 Generalisation of Kinematic Growth

G&R in biological tissue is primarily associated with the microstructure of the tissue and the evolution of the cell, a result of this is the definition of the growth tensor $\boldsymbol{F}_g$ in a general formulation, i.e.

$$\boldsymbol{F}_g = \vartheta_{\text{iso}} \boldsymbol{I} + (1 - \vartheta_{\text{ani}}) \boldsymbol{a}_0 \otimes \boldsymbol{a}_0. \tag{2.54}$$

Where ϑ_{iso} and ϑ_{ani} are the isotropic and anisotropic stretch ratio, respectively. And, $\boldsymbol{a}_0$ is a unit vector along the microstructural orientation in the reference frame.

The previous section introduces some of the key formalisms required for simulating growth. However, it is often difficult to define constitutive equations that yield deformation fields. These deformation fields can be complex and need not follow simple relations. Further, based on Equation 2.54, the absolute displacement is not strictly necessary for forward modelling. Instead, only the growth tensor, $\boldsymbol{F}_g$ is needed to encapsulate changes. This has more direct meaning and influence, providing insights into how local vectors should be altered due to growth. This has motivated the formation of constitutive equations and tensorial forms for $\boldsymbol{F}_g$.

The simplest case of growth in tissue can be assumed to be purely isotropic with

($\vartheta_{\text{ani}} = 1$ and $\vartheta_{\text{iso}} \equiv \vartheta$)

$$\boldsymbol{F}_g = \vartheta \boldsymbol{I}. \tag{2.55}$$

The evolution of ϑ could be driven by density ρ, a pressure expressed in terms of the trace of PK2 ($\text{tr}\boldsymbol{S}_e$) or Mandel stress $\boldsymbol{\Sigma}_e$ (i.e., $\text{tr}((\boldsymbol{F}_e^T \cdot \boldsymbol{F}_e)\boldsymbol{S}_e)$[8]. Commonly the form of the evolution of the stretch ratio is given by

$$\dot{\vartheta} = f(\vartheta, \mathbf{a}_0, \boldsymbol{\Sigma}_e, \boldsymbol{F}_e, ...). \tag{2.56}$$

The simplest denotation for the development of the stretch ratio over time is a linear dependency on stress[97,154], such that

$$\dot{\vartheta} = k(\vartheta)\text{tr}\boldsymbol{\Sigma}_e, \tag{2.57}$$

where

$$k(\vartheta) = \begin{cases} \frac{1}{\tau_+}\left(\frac{\vartheta_{\max}-\vartheta}{\vartheta_{\max}-1}\right)^{\gamma_+}, & \text{tr}\boldsymbol{\Sigma}_e \geq 0 \\ \frac{1}{\tau_-}\left(\frac{\vartheta-\vartheta_{\min}}{1-\vartheta_{\min}}\right)^{\gamma_-}, & \text{tr}\boldsymbol{\Sigma}_e < 0 \end{cases} \tag{2.58}$$

with the restriction of $\vartheta_{\max} > 1$ and $\vartheta_{\min} < 1$ for hypertrophy or atrophy, respectively. While in here, γ_+/γ_- regulates the nonlinearity and τ_+/τ_- governs the speed of the G&R process. G&R problems that are mechanically driven generally depend on the tissue's strain or stress state[97]. Assuming a strain-driven problem the strain ratio $\dot{\vartheta}(\vartheta, \boldsymbol{F}_e)$ is associated with the terms of the elastic deformation, in analogy to finite strain damage. Whereas growth driven by stress $\dot{\vartheta}(\vartheta, \boldsymbol{\Sigma}_e)$ is primarily linked to finite strain plasticity[97].

In consideration of the evident orthotopic nature of the underlying microstructure in the heart, the growth tensor $\boldsymbol{F}_g$ (Equation 2.54) might be described with the anisotropic term via

$$\boldsymbol{F}_g = \vartheta_{\boldsymbol{f}} \mathbf{e}_{\boldsymbol{f}} \otimes \mathbf{e}_{\boldsymbol{f}} + \vartheta_{\boldsymbol{s}} \mathbf{e}_{\boldsymbol{s}} \otimes \mathbf{e}_{\boldsymbol{s}} + \vartheta_{\boldsymbol{n}} \mathbf{e}_{\boldsymbol{n}} \otimes \mathbf{e}_{\boldsymbol{n}}. \tag{2.59}$$

Where $\mathbf{e}_f$ is the unit vector along the myofibre direction, $\mathbf{e}_s$ is the unit vector along the sheet direction and $\mathbf{e}_n$ is the unit vector associated with the normal-myofibre direction. Whereas $\vartheta_i > 1$ with $i = \boldsymbol{f}, \boldsymbol{s}, \boldsymbol{n}$ is defined as the stretch ratio for growth in the respective structural direction, atrophy ($\vartheta_i < 1$) or no growth ($\vartheta_i = 1$). The G&R patterns in the heart are essentially dependent on the type of disease and the evolution over time.

A case of ballooning of the ventricle can be observed for example in regurgitation cases. In patients with this condition, the valve closure is incomplete, allowing blood to leak back into the ventricle and introducing a state of volume overload. To compensate for the chronic overstretching of the myocytes during end-diastole, the myocardium starts thinning and the ventricle long axis significantly increases, referred to as eccentric growth or dilation. Utilising the kinematic growth approach, the Equation 2.59 can

be set up in the way that solely the fibre-associated term of $\boldsymbol{F}_g$ is activated, such that

$$\boldsymbol{F}_{g,\text{ecc}} = \vartheta_{\boldsymbol{f}} \mathbf{e}_{\boldsymbol{f}} \otimes \mathbf{e}_{\boldsymbol{f}} + \mathbf{e}_{\boldsymbol{s}} \otimes \mathbf{e}_{\boldsymbol{s}} + \mathbf{e}_{\boldsymbol{n}} \otimes \mathbf{e}_{\boldsymbol{n}}, \tag{2.60}$$

with $\vartheta^{\boldsymbol{f}} > 1$ for hypertrophy or $\vartheta^{\boldsymbol{f}} < 1$ in case of atrophy. The general in computational G&R modelling relies on the assumption that sarcomeres within the myocytes start aligning in a serial manner to reduce the stretch to the cells that they are exposed to leading to a new equilibrium state.

The general form of the evolution equation for $\dot{\vartheta}$ (Equation 2.57) might be rewritten as

$$\dot{\vartheta} = k(\vartheta)(\lambda_{\text{myo,e}} - \lambda_{\text{myo,crit}}), \quad \text{with} \quad \lambda_{\text{myo,e}} = \frac{1}{\vartheta}\sqrt{\boldsymbol{f}_0 \cdot \boldsymbol{C}\boldsymbol{f}_0}. \tag{2.61}$$

Where $\lambda_{\text{myo,crit}}$ is associated with the critical stretch of the myocyte cells and $\lambda_{\text{myo,e}}$ is the stretch of the cardiac cells.

Another commonly observed growth pattern in cardiac tissue is an increase in the heart wall that may be caused by an obstruction of the outflow tract resulting in elevated pressure levels during end-systole (higher after-load) within the ventricle cavity (pressure overload). Here the free sarcomeres inside cardiomyocytes supposedly begin to align in parallel to the already engaged sarcomeres resulting in radial growth of the fibres, specified as concentric growth or wall thickening on the macro-scale. Applying this hypothesis to the kinematic growth approach results in a formulation of the growth tensor $\mathbf{F}_g$ such that

$$\boldsymbol{F}_{g,\text{con}} = \mathbf{e}_{\boldsymbol{f}} \otimes \mathbf{e}_{\boldsymbol{f}} + \vartheta_{\perp}(\mathbf{e}_{\boldsymbol{s}} \otimes \mathbf{e}_{\boldsymbol{s}} + \mathbf{e}_{\boldsymbol{n}} \otimes \mathbf{e}_{\boldsymbol{n}}), \tag{2.62}$$

with $\vartheta_{\perp} > 1$ as the stretch growth ratio in sheet and sheet-normal direction. The evolution of $\vartheta_{\perp}$ may be defined by a hydrostatic stress measure[97] to generate a stress-driven equilibrium, e.g.

$$\dot{\vartheta} = k(\vartheta)(\boldsymbol{S}_e : \boldsymbol{C}_e - \Sigma_{\text{crit}}). \tag{2.63}$$

Other versions of the stress-driven evolution of the strain growth ratio are for example introduced by Kerckhoffs et al.[121]. The strain ratio in this thesis is defined by the ratio between the reference and the final grown model, in this work, the evolution over time was neglected.

Unlike the compatible case, now that $\boldsymbol{F}_g$ is defined by constitutive forms, it is no longer guaranteed that our reference state remains compatible. This manifests as residual stresses present in the grown reference state, shifting the local stress-strain curve actively during further loading. While residual stresses are present within most biological systems, the questions regarding how they respond to growth and how they are manifested in typical growth models remains poorly understood.

2.4.3 Residual Stresses

G&R processes are commonly linked with residual stresses, which are introduced as a consequence of various changes in tissue constituents over time[172,169,107]. Residual stresses are the remaining stress in a body after all external loads have been removed (unloaded configuration)[215]. Within a G&R setting, residual stresses are linked to different factors that may introduce incompatibilities, such as heterogeneity or anisotropy of the growth tensor $\mathbf{F}_g$, the complexity of the material law or geometry[183]. Throughout this thesis, we are taking an *a posteriori* approach to specify the state of compatibility in a load-free continuum body. Supposed that $\boldsymbol{F}_g$ introduces a compatible grown state in a body without any external load, then no additional residual stress are considered to be introduced in the body and the elastic deformation $\boldsymbol{F}_e = \boldsymbol{I}$ and associated with

$$\boldsymbol{F}_e = \boldsymbol{F} \cdot \boldsymbol{F}_g^{-1} = \boldsymbol{I}. \tag{2.64}$$

The following metric was utilised to determine if a grown body is compatible or incompatible,

$$e_{inc} = \frac{||\boldsymbol{F}\boldsymbol{F}_g^{-1} - \boldsymbol{I}||}{||\boldsymbol{F}|| \cdot ||\boldsymbol{F}_g^{-1}|| + \sqrt{\mathrm{tr}\boldsymbol{I}}}. \tag{2.65}$$

Where $e_{inc} \geq 0$ is associated with the degree of incompatibility following growth. In the case $e_{inc} = 0$, the system is compatible, which means the kinematic growth tensor is the same as the deformation gradient $\boldsymbol{F}$. Whereas the upper bound for incompatibility is represented by $e_{inc} \leq 1$.

2.5 Constitutive Laws

The focal point in the previous section was on describing finite deformations and addressing a set of equations governing the behaviour of a continuum body during G&R. These equations may be described by functions of $\boldsymbol{\sigma}$, $\boldsymbol{P}$ or $\boldsymbol{S}$. The difficulty is that the stress tensor has to be defined empirically. To complete the picture, mathematical models are developed to characterise the behaviour of a material referred to as a constitutive model or material model. Simulating material behaviour in the field of nonlinear continuum mechanics is commonly based on the concept of strain.

2.5.1 Finite Hyperelasticity

Constitutive models for hyperelastic materials suggest the existence of a Helmholtz free-energy function Ψ defined per unit reference volume. Defining the Helmholtz free-energy function as $\Psi = \Psi(\boldsymbol{F})$ results in a scalar-valued ($\Psi : \mathbb{R}^{d\times d} \to \mathbb{R}$) function dependent on the tensor variable $\boldsymbol{F}$, assumed to be continuous and referred to as strain-energy function or stored-energy function. For convenience reasons, it is assumed that the strain-energy function vanishes in the reference configuration for many solids, the

myocardium included, without any external mechanical loading conditions. In this case the deformation gradient $\boldsymbol{F} = \boldsymbol{I}$ (global minimum at the thermodynamic equilibrium) and allows stating a normalization condition, such that

$$\Psi = \Psi(\boldsymbol{I}) = 0. \tag{2.66}$$

Principally, it assumed that the reference configuration is a stress–free and energy–free state, but this may not always be true, as there may be residual stresses already induced. As indicated earlier, G&R is commonly associated with a rise in residual stress. Within a finite strain setup, the scalar-valued function Ψ must further satisfy the growth condition, $\Psi \geq 0$.

This thesis utilises constitutive models which range from homogeneous, isotropic and incompressible materials to heterogeneous, anisotropic, and compressible materials to mimic the material behaviour of cardiac tissue in a healthy and diseased state. In light of this, the PK2 tensor for the solid may be defined via[108]

$$\boldsymbol{S} = 2\frac{\partial \Psi}{\partial \boldsymbol{C}}, \tag{2.67}$$

and further, split into an elastic and hydrostatic part $\boldsymbol{S} = \boldsymbol{S}_e + \boldsymbol{S}_p$. The elastic term of PK2 ($\boldsymbol{S}_e$) is meant to account for the distortional stresses. In contrast, the hydrostatic term consists of the stresses resisting volumetric deformations, where $\boldsymbol{S}_p = JP\boldsymbol{C}^{-1}$.

The generalised form of the constitutive equations for hyperelastic material is defined as

$$\Psi = \Psi_{\text{iso}} + \Psi_{\text{ani}} + \Psi_{\text{vol}}. \tag{2.68}$$

With a split of the strain-energy function into a distortional (Ψ_{ani}), isotropic (Ψ_{iso}) or volumetric (Ψ_{vol}) term. The last component of Equation 2.68 is dependent if we assume, compressibility, nearly-incompressibility or incompressibility of the hyperelastic material. Assuming an incompressible hyperelastic material would include

$$\Psi_{\text{vol}} = -p(J-1). \tag{2.69}$$

Here, p denotes the hydrostatic pressure, which also acts as a Lagrange multiplier to enforce incompressibility. Whereas, compressibility of the material would be ensured by adding

$$\Psi_{\text{vol}} = 1/2\kappa(J-1)^2. \tag{2.70}$$

2.5.1.1 Cardiac Hyperelastic Constitutive Equations in Literature

Numerous specific forms of hyperelastic models have been covered in literature to model the mechanical and elastic properties of cardiac tissue. Within the scope of this study

models with different degrees of complexity and functional forms inside the theory of finite elasticity are investigated for biomechanical modelling, here we are reviewing the distortional parts of the strain energy function of these models.

Constitutive equations with polynomial forms are utilised to model the isotropic mechanical behaviour ($\Psi_{\texttt{iso}}$) of the extracellular matrix (ECM) including laws such as the isotropic hyperelastic neo-Hookean law (`neo`)

$$\Psi_{\texttt{neo}} = C_1(\bar{I}_1 - 3). \tag{2.71}$$

with C_1 as material parameter. More structurally accurate models incorporate the underlying material architecture. Starting with the Holzapfel-Ogden-Gasser law (`hog`)[109], commonly employed in literature to model the arterial tissue

$$\Psi_{\texttt{hog}} = \Psi_{\texttt{neo}} + \Psi_{\texttt{ani}}. \tag{2.72}$$

Where the isotropic term is commonly represented by a neo-Hookean material and the second term includes the anisotropic properties of the material

$$\Psi_{\texttt{ani}} = \sum_{i\in\{\boldsymbol{f}_1,\boldsymbol{f}_2\}} \frac{k_{1_i}}{2k_{2_i}} \left[\exp\left[k_2(I_i-1)^2\right]-1\right]. \tag{2.73}$$

Here k_{1_i}[kPa] and k_{2_i}[-] are material parameters associated to the individual fibre family $\boldsymbol{f}_1$ or $\boldsymbol{f}_2$.

In comparison to aortic tissue, cardiac tissue exhibits an orthogonal microstructure defined via the orientation of fibres, sheets and the normal-sheet direction. One orthogonal model utilised in literature to describe the passive material properties of the myocardium is the Holzapfel-Ogden (`ho`) law:

$$\begin{aligned}\Psi_{\texttt{ho}} = \frac{k_1}{2k_2}\left[\exp^{k_2(I_1-3)}-1\right] + \sum_{i\in\{\boldsymbol{f},\boldsymbol{s}\}} \frac{k_{1_i}}{2k_{2_i}}\left[\exp^{k_{2_i}(I_i-1)^2}-1\right] \\ + \frac{k_{1_{\boldsymbol{fs}}}}{2k_{2_{\boldsymbol{fs}}}}\left[\exp^{k_{2_{\boldsymbol{fs}}}I_{\boldsymbol{fs}}^2}-1\right].\end{aligned} \tag{2.74}$$

With $\boldsymbol{f}$ and $\boldsymbol{s}$ denoting the fibre and sheet direction. To assess the insensitivity of the `hog` to volumetric deformation introduced by the use of the isochoric invariant to model compressible material a modified variant of the `hog` was also investigated, referred to as iso-Nolan formulation of the Holzapfel-Ogden law (`maho`), defined by

$$\begin{aligned}\Psi_{\texttt{maho}} = \frac{k_1}{2k_2}\left[\exp^{k_2(\bar{I}_1-3)}-1\right] + \sum_{i\in\{\boldsymbol{f},\boldsymbol{s}\}} \frac{k_{1_i}}{2k_{2_i}}\left[\exp^{k_{2_i}(I_i-1)^2}-1\right] \\ + \frac{k_{1_{\boldsymbol{fs}}}}{2k_{2_{\boldsymbol{fs}}}}\left[\exp^{k_{2_{\boldsymbol{fs}}}I_{\boldsymbol{fs}}^2}-1\right].\end{aligned} \tag{2.75}$$

Where Ψ_{vol} accounts for compressibility, with κ being the bulk modulus of the material.

3 Assessment of Incompatible G&R in Cardiac Applications

The mechanics of growth and remodelling (G&R) processes in living tissue are still not entirely understood. Hypertrophy in the cardiac tissue, such as arteries and within the myocardium is a complex mechanism with various drivers, such as changes in mechanical loading (e.g. hypertension[248,53,11]), hormonal (e.g. hyperthyroidism[23]) or genetic pathogenesis (e.g. hypertropic[83,211,160] or dilated cardiomyopathy[74,166]). Hypertrophy in the heart is typically thought to occur as concentric, increase in thickness of the myocardium volume, or eccentric growth phenotypes, with an increase of the cavity volume as an attempt to reach a new mechanical balanced state. The theory of kinematic growth[201] is commonly used in literature to introduce remodelling in the heart and identify potential mechanical growth drivers[81,194,43]. Additionally, further computational studies focused on addressing incompatibility of the kinematic growth tensor linked to the rise in residual stresses during growth[81,96,188,253].

However, previous studies neglect the impact of a number of factors, such as constitutive G&R laws, anisotropy, compressibility and spatial heterogeneity. The interplay between these factors with respect to incompatibility during growth still not understood. Within the scope of this study, we investigate perturbations of these factors and their influence on the final grown state. The results indicated that some of the factors have a strong influence on the grown configuration while others result at the same grown body. In conclusion, we could identify that in simplified G&R problems the choice of constitutive G&R laws was irrelevant as long the domain could deform freely without any restrictions on the continuum body. Whereas incompatibility started to become more apparent in cases with complex kinematic growth tensors, e.g. regional heterogeneity where the results started to be different from each other.

This chapter is a review of an article which is in submission:
Sandra P. Hager, Will Zhang, Renee Miller, Jack Lee, David A. Nordsletten. "Assessment of Incompatible G&R in Cardiac Applications".

3.1 Introduction

Based on the Framingham heart study, 45% of cardiovascular deaths involve cardiac growth and remodelling (G&R) in the left ventricle[91]. Clinically, cardiac G&R manifests as a change in size, mass and geometry along with other alterations in the cardiac tissue, such as scarring (after myocardial infarction[149]), fibrosis, inflammation (myocarditis), atrophy or ventricular aneurysms[22,207]. Observed alterations at the macroscale of the heart are either physiological or pathological. Typical cases of adaptations related to G&R in the cardiac tissue are, for example, hypertrophy due to frequent physical activity or persistent aerobic exercise training[59,64,165,57]. Other physiological types of cardiac G&R are embryonic and fetal hypertrophy during postnatal development[85,1] and pregnancy[174,155,165]. Maladaptive hypertrophy is commonly linked to changes in the loading condition[70,204], interventional therapies (causing reverse growth), such as valve replacement surgery[127,225], transaortic myectomy[182,233], catheter ablation[177,56] or medication[136,22,41,244]. Cardiac dysfunction[213,180,29], malignant arrhythmias[22,106], and heart failure (HF)[115,223,214] are related complications to the pathological change of mass and reorganization of the myocardial fibre architecture. Beyond adaptional G&R, a genetic manifestation of heterogeneous growth can be observed in the heart for example in the case of hypertrophic cardiomyopathy (HCM).

A common theory for geometrical adaptations of the heart involves the elongation of the fibres in the heart wall (eccentric growth) and is linked to an increase in preload. Alternatively, an increase of the wall thickness (concentric growth) associated with a radial increase of the fibres[208,94] compensates for high levels of afterload, see Figure 3.1.

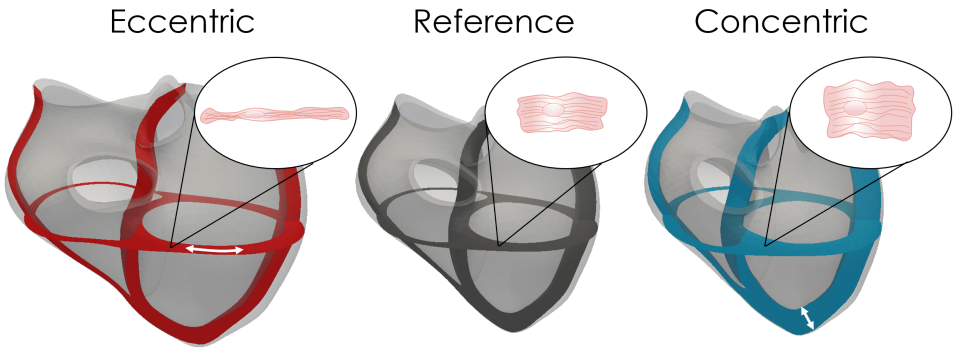

Figure 3.1 Eccentric hypertrophy (left) applied to a biventricular model (centre) results in dilation of the cavities and a decreased wall thickness of the myocardium. In this case, compared to the physiological cells (reference inset), the myocytes respond to high strain values in an elongation along the fibre direction (left inset). Concentric hypertrophy (right) results in a growth pattern with an increased wall thickness due to growth in the radial direction of the myocytes (right inset).

By utilising medical imaging modalities, such as computed tomography (CT)[117,119],

magnetic resonance imaging[67,6] or echocardiography[178,152,239] it is possible to track over a period of time the progress of G&R mechanisms. Examining growth patterns in imaging data suggests that growth is a highly heterogeneous process in the heart.

Computational models of growth may be able to close the gap between understanding growth patterns from imaging data and underlying mechanisms in G&R. Several review papers give an overview of the different methods, types, and challenges in modelling growth[183,131,219,8]. The underlying theory is based on the idea of a multiplicative decomposition of the deformation gradient, which was initially introduced to describe elastic-plasticity[142]. Based on this concept Rodriguez et al.[201] introduced one of the first G&R models, which splits the deformation tensor into an elastic and an inelastic (growth-related) part. A generalization of the original theory is the constrained mixture approach evolved, in which the growth within the tissue is dependent on the individual constituents instead of a continuum which was used in the initial hypothesis[114]. This provides a powerful tool to investigate growth, yet it introduces the challenge of knowing a significant amount of data that may prove difficult to acquire via standard medical imaging. Current models of G&R in the cardiovascular system are typically designed to achieve homeostasis of either stress or strain by applying G&R in the form of eccentric or concentric growth[98,97,121]. In those papers, the applied growth is orientated along the myocardium's internal microstructure (fibre, sheet and sheet-normal direction). Extension of these existing G&R models to include patient-specific imaging data have empowered a description of adverse growth and reverse growth due to surgery, medication or exercise[145,16,194,61]. Different hypotheses on growth drivers, eg. hormonal signal pathways, two mechanical drivers appear to model G&R in the heart fairly well. One is strain data collected from imaging data and the other one is pressure levels within the LV cavity[80,98,97].

Even though computational modelling enables simulations of morphological changes in the heart, they are also introducing uncertainties in the way of incompatibility and residual stress. Destructive experiments are at the moment the only way to analyse growth introduced residual stresses[188,190,189,252]. Research on how G&R models introduce incompatibility and residual stresses is sparse. Oftentimes, constitutive laws governing G&R are determined, based on local strains or stresses. These fields introduce naturally a kind of heterogeneity in the system depending on how heterogeneous these fields are inside the heart. This may manifest in growth behaviours that are straightforward to understand and have minimal residual effects. Or it might introduce significant residual effects. Genet et al.[81] proposed a computational method to introduce physiological residual stress fields in a patient-specific left ventricular model related to the heterogeneity of G&R. The first study that linked G&R models with introducing residual stresses was performed by Skalak et al.[215]. The study focused on determining the compatibility state of a given strain field with incompatible growth introducing residual stresses during volumetric growth. A different approach to identi-

fying the load-free left ventricular geometry was done by Wang et al. [237]. Their study proposes a method to estimate a load-free geometry and material parameters for the passive myocardium via principal component analysis (PCA). An additional challenge of the multiplicative decomposition of the deformation gradient, uncertainties related to the system's uniqueness rise [154,140,87], whereby different growth tensors may result in the same minimum energy state.

The objective of the presented paper is to explore compatibility in different test cases. Analysing different tests helps us to gain insight into compatibility and how perturbations of problem parameters may impact the solution of the problem. The test cases focused on the impact of heterogeneity, anisotropy and continuity of the kinematic growth tensor as well as on the choice of constitutive law (incompressible, compressible) within varying degrees of complexity for the geometry. Understanding compatibility in kinematic growth enables us to understand G&R patterns and residual stresses associated with growth. The results indicated that in tests in which growth was not restricted, compatibility was seen in all material laws. Whereas with the increasing complexity of the G&R problem, incompatibility became more apparent in the results.

In Section 3.2, we review cardiac mechanics and the kinematic growth theory and further introduce a metric to measure compatibility. Furthermore, we give an overview of all the performed tests to investigate compatibility in this study. Section 3.3, includes the results of the conducted tests related to the change in morphology, the correlation plots to the gold standard solution and in the cardiac applications the compatibility analysis. The following Section 3.4 discusses the results from the performed tests related to different parameters of the G&R problem. Section 3.5 gives a conclusion on the findings of this study.

3.2 Methods

In this section we establish a general understanding for the perturbations that we introduced and investigated in our study. In Section 3.2.1, we introduce the basic kinematics and notation used throughout the paper. In Section 3.2.2, we outline the hyperelastic models which we've chosen for the representation of our solids. In Section 3.2.3, we introduce the kinematic concepts of G&R which are alternated to understand the underlying dependence on the grown state. In Section 3.2.6, we present the integration of growth in a mechanical finite elasticity problem. Section 3.2.7 gives an overview of the kinematic growth tests performed in this work to analyse compatible and incompatible kinematic growth tensors.

3.2.1 Kinematics and Notation

First of all, we briefly review the classical kinematics and the individual notations in nonlinear continuum mechanics, for details see Bonet and Wood [31], Holzapfel [108]. In continuum mechanics, body motion is described by the motion of defined material points from a reference configuration, $\Omega_0 \subset \mathbb{R}^3$, to the current physical state, $\Omega_t \subset \mathbb{R}^3$ at time point $t \in [0, T]$, see Figure 3.2. The coordinate position defines the material points in the Lagrangian reference domain, $\mathbf{X} \in \Omega_0$ while the displacement field tracks the relative movement over time, $\boldsymbol{u} : \Omega_0 \times [0, T] \rightarrow \mathbb{R}^3$. Resulting from the relation between reference and physical domain, $\boldsymbol{x}(\mathbf{X}, t) = \boldsymbol{u}(\mathbf{X}, t) + \mathbf{X}$, where the displacement field links the current and reference configuration. The deformation gradient characterises the change in shape of the reference body over time, $\boldsymbol{F}(\mathbf{X},t) = \nabla_{\mathbf{X}} \boldsymbol{u}(\mathbf{X},t) + \boldsymbol{I}$, and volume change through the use of its determinant, $J = \det \boldsymbol{F} > 0$. Throughout this work, we will assume our solids to be incompressible, i.e. $J = 1$. As an important strain measure, the left and right Cauchy-Green tensors are defined as $\boldsymbol{b} = \boldsymbol{F}\boldsymbol{F}^{\boldsymbol{T}}$ and $\boldsymbol{C} = \boldsymbol{F}^{\boldsymbol{T}}\boldsymbol{F}$, respectively.

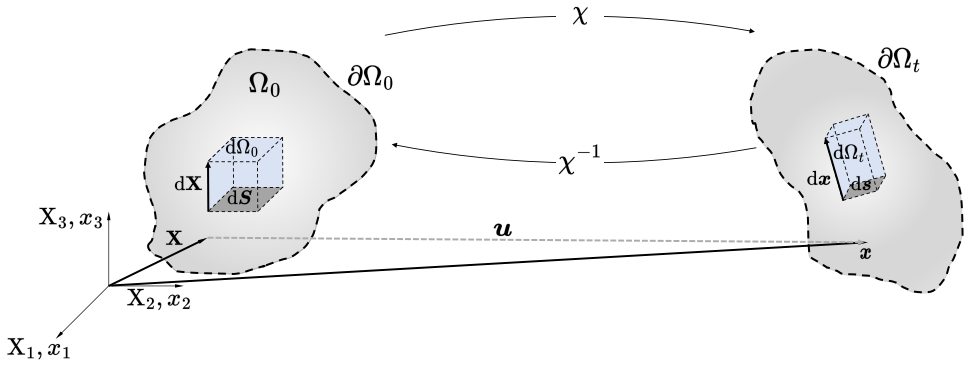

Figure 3.2 Kinematics within deformed bodies, with the reference domain Ω_0, bounded by $\partial\Omega_0$, and the physical domain Ω_t, bounded by $\partial\Omega_t$ that are linked via the bijective map $\boldsymbol{\chi}$.

To ensure that the stress state is independent of the material coordinates, consequently, the invariants of the strain tensor $\boldsymbol{C}$ are utilised

$$I_1 = \mathrm{tr}\boldsymbol{C} \qquad I_2 = \boldsymbol{C} : \boldsymbol{C} \qquad I_3 = \det \boldsymbol{C}. \tag{3.1}$$

Utilising an incompressible or nearly incompressible material requires a separation of the volumetric and the isochoric components of the deformation. Terms with $J^{-1/3}\boldsymbol{I}$ and $J^{-2/3}\boldsymbol{I}$ are associated with volume-changing deformations and are characterised by the modified invariants

$$\bar{I}_1 = J^{-2/3} I_1 \qquad \bar{I}_2 = J^{-4/3} I_2 \qquad \bar{I}_3 = 1. \tag{3.2}$$

Subsequently $\boldsymbol{F}$ was replaced with $\bar{\boldsymbol{F}} = J^{-1/3}\boldsymbol{F}$ and $\boldsymbol{C}$ with $\bar{\boldsymbol{C}} = J^{-2/3}\boldsymbol{C}$. In anticipation of the orthotropic material models which we use to describe myocardium, we also

introduce a set of three normalised orthogonal directions, $\mathbf{e}_{\boldsymbol{f}}$, $\mathbf{e}_{\boldsymbol{s}}$ and $\mathbf{e}_{\boldsymbol{n}}$, which indicate the fibre, sheet and normal directions, respectively. Here, $\mathbf{e}_a$ with $a \in \boldsymbol{f}, \boldsymbol{s}, \boldsymbol{n}$ indicates the orientation of a unit vector along the myofibres ($\boldsymbol{f}$), sheets ($\boldsymbol{s}$) and sheet-normals ($\boldsymbol{n}$), see Fig. 3.3[110]. In this paper, the orientation of the fibre field was defined by a rule-based method[55,26]. The relation of the fibre direction in the reference and the deformed configuration is defined through $\mathbf{E}_a = \boldsymbol{F}\mathbf{e}_a \in a = \boldsymbol{f}, \boldsymbol{s}, \boldsymbol{n}$.

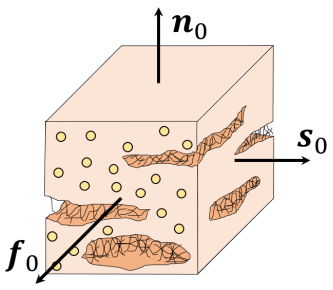

Figure 3.3 The layered myocardial organization with myocytes oriented along the fibre axis $\boldsymbol{f}_0$. Collagen fibres guarantee the connectivity of the sheet bundles and generate a distinctive organization referred to as the sheet axis $\boldsymbol{s}_0$. Orthonormal to the base, which is spanned by the fibres and the sheets, is the sheet-normal direction defined $\boldsymbol{n}_0$.

Using these, we introduce an additional six invariants, I_a, and I_{ab}, defined as,

$$I_a = \boldsymbol{C} : \mathbf{e}_a \otimes \mathbf{e}_a, \quad a \in \boldsymbol{f}, \boldsymbol{s}, \boldsymbol{n}. \tag{3.3}$$

The general version of Equation 3.3 result in

$$I_{ab} = \boldsymbol{C} : \mathrm{sym}(\mathbf{e}_a \otimes \mathbf{e}_b), \quad a, b \in \boldsymbol{f}, \boldsymbol{s}, \boldsymbol{n}, \tag{3.4}$$

with $\mathrm{sym}(\boldsymbol{A}) = 1/2(\boldsymbol{A} + \boldsymbol{A}^T)$ as the symmetric transformation for a tensor, $\mathbf{A}$.

3.2.2 Hyperelastic Material Models

In this work, we consider a wide range of material laws for the representations of muscle tissue, with different levels of model complexity to understand the impact of the material law on the compatibility state. This includes, in ascending order of complexity: the neo-Hookean (`neo`); the Holzapfel-Ogden-Gasser (`hog`)[109]; the Holzapfel-Ogden (`ho`)[110]; and the modified Holzapfel-Ogden (`maho`)[184] constitutive law. In highly simplified G&R studies of the heart, using an isotropic `neo` material as matrix tissue[98,97] may also lead to comparable deformations in the geometric model, such as the more complex material law. The generalised form of the constitutive equations for incompressible hyperelastic material is defined as

$$\Psi = \Psi_{\mathrm{iso}} + \Psi_{\mathrm{ani}} - p(J-1). \tag{3.5}$$

Here, p is the hydrostatic pressure, which also acts as a Lagrange multiplier, enforcing incompressibility, while Ψ_{iso} and Ψ_{ani} denote potential isotropic and anisotropic terms of our material laws, respectively. In this work, we describe the contribution of the

extracellular matrix by using a neo-Hookean `neo` material law, i.e.

$$\Psi_{\texttt{neo}} = C_1(\bar{I}_1 - 3), \tag{3.6}$$

where $C_1 > 0$ denotes the shear modulus.

Another model commonly used in cardiac applications in arteries is the Holzapfel-Ogden-Gasser model`hog` material law. It accounts for anisotropic material behaviour in a fibre-reinforced material with two mean fibre directions ($\boldsymbol{f_1}, \boldsymbol{f_2}$), which results in a description of the material behaviour, such as

$$\Psi_{\texttt{hog}} = \Psi_{\texttt{neo}} + \Psi_{\text{ani}}, \tag{3.7}$$

with

$$\Psi_{\text{ani}} = \sum_{i \in \{\boldsymbol{f_1}, \boldsymbol{f_2}\}} \frac{k_{1_i}}{2k_{2_i}} \left[\exp\left[k_{2_i}(I_i - 1)^2\right] - 1\right]. \tag{3.8}$$

The parameters $k_{1,i} > 0$ denote stress-like parameters and $k_{2,i} > 0$ denote dimensionless parameters representing the progressive recruitment of collagen fibres.

A common material law to describe myocardial tissue utilised in this study was the orthotropic Holzapfel-Ogden material law `ho`

$$\begin{aligned}\Psi_{\texttt{ho}} = \frac{k_1}{2k_2}\left[\exp^{k_2(I_1-3)} - 1\right] + \sum_{i \in \{\boldsymbol{f}, \boldsymbol{s}\}} \frac{k_{1_i}}{2k_{2_i}}\left[\exp^{k_{2_i}(I_i-1)^2} - 1\right] \\ + \frac{k_{1_{\boldsymbol{fs}}}}{2k_{2_{\boldsymbol{fs}}}}\left[\exp^{k_{2_{\boldsymbol{fs}}} I_{\boldsymbol{fs}}^2} - 1\right].\end{aligned} \tag{3.9}$$

The first term of Equation 3.9 denotes the isotropic term of the material. Here the second term describes the contribution to the strain energy from the fibres and the sheets. Whereas, the last term accounts for the shear behaviour of the material.

Extending Equation 3.9 with a volumetric term enables the problem to model compressible anisotropic behaviour accurately. For this purpose, Nolan et al.[184] adapted the established Holzapfel-Ogden material law referred to as modified Holzapfel-Ogden (`maho`), such that

$$\begin{aligned}\Psi_{\texttt{maho}} = \Psi_{\text{vol}} + \frac{k_1}{2k_2}\left[\exp^{k_2(\bar{I}_1-3)} - 1\right] + \sum_{i \in \{\boldsymbol{f}, \boldsymbol{s}\}} \frac{k_{1_i}}{2k_{2_i}}\left[\exp^{k_{2_i}(I_i-1)^2} - 1\right] \\ + \frac{k_{1_{\boldsymbol{fs}}}}{2k_{2_{\boldsymbol{fs}}}}\left[\exp^{k_{2_{\boldsymbol{fs}}} I_{\boldsymbol{fs}}^2} - 1\right],\end{aligned} \tag{3.10}$$

with

$$\Psi_{\text{vol}} = \frac{1}{2}\kappa(J-1)^2, \tag{3.11}$$

with κ denoting the bulk modulus of the material. Finally, with the knowledge of the

strain-energy function, the second Piola Kirchhoff stress tensor can be calculated for each of the material laws, with

$$\bar{\boldsymbol{S}} = 2\frac{\partial \psi}{\partial \bar{\boldsymbol{C}}}, \tag{3.12}$$

and further, through push-forward operation results in the Cauchy stress tensor, $\boldsymbol{\sigma} = J^{-1}\bar{\boldsymbol{F}}\bar{\boldsymbol{S}}\bar{\boldsymbol{F}}^T$.

3.2.3 Kinematic and Constitutive Equation of Growth

The kinematic growth approach outlines one of the traditional models for computational modelling of G&R[201,114]. This type of approach enables a simple material characterisation and provides a method for using phenomenological rate equations to mimic the growth process. Combined with the theory of the multiplicative decomposition of the deformation gradient[142], an accepted assumption for G&R models is the existence of a stress-free intermediate grown reference configuration, mathematically verified by Goodbrake et al.[87]. In practice, kinematic growth is achieved through the multiplicative decomposition of the deformation gradient $\boldsymbol{F}$ into an elastic and inelastic deformation gradient, see Figure 3.4, such that

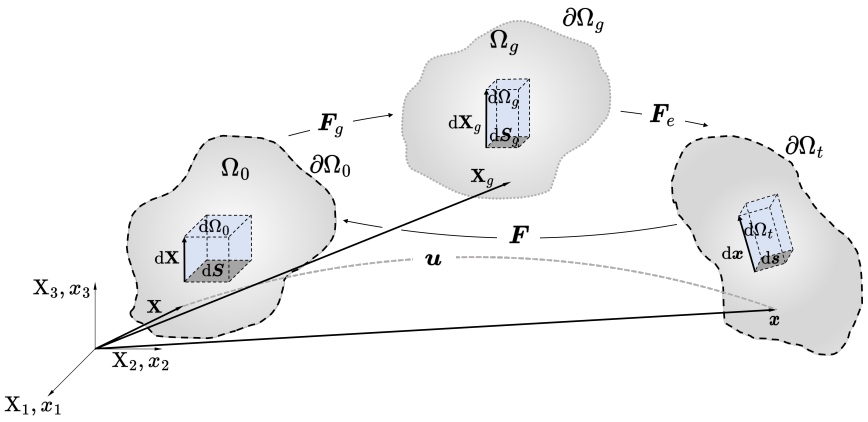

Figure 3.4 Schematics of multiplicative decomposition of $\boldsymbol{F}$ into an elastic ($\boldsymbol{F}_e$) and inelastic deformation gradient ($\boldsymbol{F}_g$).

$$\boldsymbol{F} = \boldsymbol{F}_e \cdot \boldsymbol{F}_g \tag{3.13}$$

and

$$J = J_e J_g. \tag{3.14}$$

Here, $\boldsymbol{F}_g$ denotes the kinematic growth tensor, which defines a mapping between the stress-free reference configuration, $\Omega_X \subset \mathbb{R}^3$, and the intermediate grown zero-stress configuration, $\Omega_Y \subset \mathbb{R}^3$[142,201]. J is the Jacobian of the deformation gradient and can be split into its elastic J_e and growth-related J_g components. The applied kinematic growth tensor can take different forms to introduce volumetric growth such as isotropic

or anisotropic dependent on the entries of the tensor. Despite its anisotropy properties, the determinant J_g addresses if the body is growing ($J_g > 1$) or atrophy ($J_g < 1$). Whereas, $\boldsymbol{F}_e$ contains the state deformation which contributes to the elastic-strain energy.

3.2.4 Kinematic Growth Modes observed in the Heart

In structures with an underlying microstructure, such as arteries and the heart, $\boldsymbol{F}_g$ is assumed to be a diagonal tensor. Where the components of the kinematic growth tensor represent the direction of growth. In the case of arteries, growth is defined along $\boldsymbol{r}$, $\boldsymbol{\theta}$ and $\boldsymbol{z}$ representing the alignment along the radial, circumferential and axial directions, respectively. With stress as an assumed mechanical stimuli for growth, $\dot{\boldsymbol{F}}_g = \text{diag}(\dot{\lambda}_{g,\boldsymbol{r}}, \dot{\lambda}_{g,\boldsymbol{\theta}}, \dot{\lambda}_{g,\boldsymbol{z}})$ [218]. Whereas G&R in the heart is defined along the fibre, sheet or sheet normal direction. A popular theory for growth processes in the heart is sarcomergenesis [246]. Where stretch of the cardiomyocytes results in an addition of free sarcomeres to aligned sarcomeres in the myocytes. The general form of the kinematic tensor, as follows

$$\boldsymbol{F}_g = \vartheta_{\boldsymbol{f}} \mathbf{e}_{\boldsymbol{f}} \otimes \mathbf{e}_{\boldsymbol{f}} + \vartheta_{\boldsymbol{s}} \mathbf{e}_{\boldsymbol{s}} \otimes \mathbf{e}_{\boldsymbol{s}} + \vartheta_{\boldsymbol{n}} \mathbf{e}_{\boldsymbol{n}} \otimes \mathbf{e}_{\boldsymbol{n}}. \tag{3.15}$$

Here, ϑ^a, with $a = \boldsymbol{f}, \boldsymbol{s}, \boldsymbol{n}$ describes the growth ratio in fibre, sheet or sheet normal direction. Two types of G&R can commonly be observed in the heart, one describing a thickening of the heart wall (concentric) and the other one resulting in a dilation (eccentric) of the ventricle. In an attempt to model these changes two types of growth modes within the heart were introduced to adapt to mechanical, genetic or hormonal stimuli. The theory of sarcomerogenesis was successfully applied by Göktepe et al. [98] and Menzel and Kuhl [169] in cardiac applications with strain or stress as a mechanical stimulus to introduce either eccentric or concentric growth in an LV model.

The hypothesis behind concentric G&R is founded on the assumption that sarcomeric addition is occurring to compensate for high strain levels in the radial direction of the fibres. Here, free sarcomeres start adding in parallel to the existing aligned sarcomeres, which results in a description of the growth tensor as

$$\boldsymbol{F}_{g,\text{con}} = \mathbf{e}_{\boldsymbol{f}} \otimes \mathbf{e}_{\boldsymbol{f}} + \vartheta_{\perp}(\mathbf{e}_{\boldsymbol{s}} \otimes \mathbf{e}_{\boldsymbol{s}} + \mathbf{e}_{\boldsymbol{n}} \otimes \mathbf{e}_{\boldsymbol{n}}), \tag{3.16}$$

where $\vartheta_{\perp} > 1$ corresponds to the amount of growth in the radial direction to compensate for an increase of afterload.

In contrast, eccentric growth patterns, where the heart undergoes dilation may be driven by high strain levels in the longitudinal direction of the fibres. As an adaptation process free sarcomeres are added in serial to existing ones, resulting in a growth tensor

of the form

$$\boldsymbol{F}_{g,\mathrm{ecc}} = \vartheta_{\boldsymbol{f}} \mathbf{e}_{\boldsymbol{f}} \otimes \mathbf{e}_{\boldsymbol{f}} + \mathbf{e}_{\boldsymbol{s}} \otimes \mathbf{e}_{\boldsymbol{s}} + \mathbf{e}_{\boldsymbol{n}} \otimes \mathbf{e}_{\boldsymbol{n}}. \tag{3.17}$$

Eccentric growth is assumed to be an adaptive process to compensate for volumetric overloads inside the cavity. Earlier studies represent different approaches based on ordinary differential equations to define the $\vartheta_{\boldsymbol{f}}$ and $\vartheta_{\perp}$ parameters for the G&R law[121 98].

3.2.5 Compatibility in the Kinematic G&R Framework

In this work, we take an *a posteriori* approach to analyse compatibility in a continuum body. In the way of examining incompatibility in the final grown state under zero load. Assuming that the intermediate configuration after growth, in an unloaded body, is applied results in a compatible state, then

$$\boldsymbol{F}_e = \boldsymbol{F} \cdot \boldsymbol{F}_g^{-1} = \boldsymbol{I}. \tag{3.18}$$

This means the deformation gradient is solely defined by the inelastic part ($\boldsymbol{F}_g$) and an additional elastic deformation is not present. To enable a direct comparison between the simulations, we introduced a metric for assessing the compatibility or incompatibility of the grown state The following metric was utilised to determine if a grown body is compatible or incompatible,

$$e_{inc} = \frac{||\boldsymbol{F}\boldsymbol{F}_g^{-1} - \boldsymbol{I}||}{||\boldsymbol{F}|| \cdot ||\boldsymbol{F}_g^{-1}|| + \sqrt{\mathrm{tr}\boldsymbol{I}}}. \tag{3.19}$$

Where $e_{inc} \geq 0$ is associated with the degree of incompatibility following growth. In the case $e_{inc} = 0$, the system is compatible, which means the kinematic growth tensor is the same as the deformation gradient $\boldsymbol{F}$. Whereas the upper bound for incompatibility is represented by $e_{inc} \leq 1$. Subsequently, we want to understand the impact of the $\boldsymbol{F}_g$ on the compatibility state in the grown zero-load state.

3.2.6 Kinematic Growth in Finite Elasticity

In the case of incompatible growth, the continuum body introduces stresses with respect to the intermediate grown domain Ω_g to the physical domain Ω_t. In problems without growth, the kinematics can be described via the kinematic and kinetic tensors, such that

$$\boldsymbol{F} = \frac{\partial \boldsymbol{x}}{\partial \mathbf{X}}, \quad \boldsymbol{C} = \boldsymbol{F}^T \boldsymbol{F}, \quad \boldsymbol{P} = \frac{\partial \Psi(\boldsymbol{F})}{\partial \boldsymbol{F}}. \tag{3.20}$$

Assuming a body, which undergoes growth, these quantities have to be reformulated onto the intermediate grown domain, resulting in

$$\boldsymbol{F}_e = \frac{\partial \boldsymbol{x}}{\partial \mathbf{X}_g}, \quad \boldsymbol{C}_e = \boldsymbol{F}_e^T \boldsymbol{F}_e, \quad \boldsymbol{P}_e = \frac{\partial \Psi(\boldsymbol{F}_e)}{\partial \boldsymbol{F}_e}. \tag{3.21}$$

The balance laws of mass and momentum of the grown domain, in an incompressible body following growth, lead to

$$\nabla_{\mathbf{X}_g} \cdot \boldsymbol{P}_e + \boldsymbol{b}_e - \frac{\partial(\rho \boldsymbol{v}_e J_e)}{\partial t} = \mathbf{0} \quad \text{on } \Omega_g \tag{3.22}$$

$$J_e - 1 = 0, \quad \text{on } \Omega_g \tag{3.23}$$

where $\nabla_{\mathbf{X}_g}$ is the gradient operator with respect to $\mathbf{X}_g$, and $\boldsymbol{b}_e = J_e \boldsymbol{b}$ is the jacobian-weighted body force.

Similarly, we can describe the first Piola-Kirchhoff stress tensor, $\boldsymbol{P}_e$ computed with respect to deformation quantities defined in the original reference domain, e.g.

$$\tilde{\boldsymbol{P}} = \left. \frac{\partial \Psi(\boldsymbol{F}_e)}{\partial \boldsymbol{F}_e} \right|_{\boldsymbol{F}_e = \boldsymbol{F}\boldsymbol{F}_g^{-1}}. \tag{3.24}$$

In the case of a neo-Hookean material, the equations can be formulated as follows

$$\boldsymbol{P}_e = \frac{1}{J_e^{2/3}} \left(\boldsymbol{F}_e - \frac{\boldsymbol{C}_e : \boldsymbol{I}}{3} \boldsymbol{F}_e^{-T} \right), \quad \tilde{\boldsymbol{P}} = \left(\frac{J_g}{J} \right)^{2/3} \left(\boldsymbol{F}\boldsymbol{F}_g^{-1} - \frac{\boldsymbol{C} : \boldsymbol{C_g}}{3} \boldsymbol{F}^{-T} \boldsymbol{F}_g^T \right). \tag{3.25}$$

Utilising Nanson's formula combined with the Divergence theorem, we can state that

$$\nabla_{\mathbf{X}_g} \cdot \boldsymbol{P}_e = \nabla_{\mathbf{X}} \cdot (J_g \tilde{\boldsymbol{P}} \boldsymbol{F}_g^{-T}) \tag{3.26}$$

Combining the established relations with Equation 3.22 and 3.23, it is possible to define the strong form of the balance laws of mass and momentum, e.g.

$$J_g \nabla_{\mathbf{X}} \cdot \left(J_g \tilde{\boldsymbol{P}} \boldsymbol{F}_g^{-T} \right) + J\boldsymbol{b} - \frac{\partial(\rho \boldsymbol{v} J)}{\partial t} = \mathbf{0} \quad \text{on } \Omega_0 \tag{3.27}$$

$$J - J_g = 0, \quad \text{on } \Omega_0 \tag{3.28}$$

The equation is now set up to run on the reference domain which means no explicit formation of Ω_g is needed to solve kinetics in the grown state.

3.2.6.1 Boundary conditions

Unless mentioned otherwise, the models' centre of mass (COM) is always fixed [130]. This boundary condition (BC) allows the model to grow freely without constraining the growth process and introducing additional stresses. The COM is constrained against rotation and translation of the system via Neumann boundary condition. The COM

can be uniquely ensured if and only if the net force f and net torque h acting on Ω are zero. In this case the forces f and h satisfy the compatibility conditions

$$\int_{\Omega} f \mathrm{d}\boldsymbol{x} + \int_{\partial\Omega} h \mathrm{d}s = 0, \tag{3.29}$$

$$\int_{\Omega} f \times \boldsymbol{x} \mathrm{d}\boldsymbol{x} + \int_{\partial\Omega} h\boldsymbol{x} \mathrm{d}s = 0. \tag{3.30}$$

The constraint was enforced by the use of a Lagrange multiplier and is in parallel solved to the G&R problem.

3.2.7 Kinematic Growth Tests

Utilising the kinematic growth theory enables the modelling of G&R processes. However, this type of modelling may introduce incompatibilities or residual stresses. Research on the effect of G&R on incompatibility and residual stress is still sparse. The focus of this section of the methods is to introduce test cases to assess the impact of perturbation of Equation 3.27 and 3.28 with respect to compatibility in a new zero load state. The main focus of these tests was to address the impact of the material law, heterogeneity of G&R and the application in the heart.

The first objective was to understand the impact of the material law on kinematic growth. The second test cases are built up to understand the influence of heterogeneous or homogeneous growth in G&R. And the third test case addresses the application in a complex cardiac application, in this case, a patient-specific model.

Previous papers proposed and verified a G&R law for cardiac application by using a `neo` material law to describe the properties of the myocardium. The classification of the baseline elasticity with a Neo-Hookean material places the focus on the analysis of the impact of growth on the body[98,97], consequently, we chose this material law as a reference for our results. The types of growth tensors that we considered varied on whether the problem in question was a simple benchmark problem or a cardiac model. For the former, we used *ad hoc* definitions meant to illustrate some specific underlying property. Whereas, for the latter, we focused exclusively on the eccentric and concentric G&R models modelled by Equation 3.16 and 3.17.

Block test: This test enables us to understand the impact of growth in a highly simplified G&R problem. Within this test setup, we can address the influence of material laws and kinematic growth tensor properties in a system where an analytical solution could be potentially calculated. With respect to material law, we investigate constitutive laws with varying complexity, from isotropic material such as neo-Hookean, to anisotropic material laws utilised to arterial walls or the passive behaviour of the myocardium. The laws defined in Section 3.2.2 were either applied as a compressible or nearly incompressible material model. Regarding the growth tensor, we studied anisotropic and isotropic

forms of the tensor and furthermore considered the spatial alignment of growth with the microstructure in the arterial and cardiac models.

This model consists of a cuboid with the dimensions $1 \times 1 \times 1$ that was discretized by 2 hexahedral elements ($\mathbb{Q}^2 - \mathbb{Q}^1$) in each spacial direction, leading to 8 elements in total. For each variation of the test case, the displacement solution was defined on a quadratic mesh with 125 nodes. In contrast, the scalar pressure field solution was mapped onto a linear mesh of the same geometry with 27 nodes. This problem was introduced as a simplified case of a G&R problem that enabled us to analyse the concept of incompatibility following growth. For this purpose, we analysed solutions of different perturbations of the choice of constitutive laws, growth tensors and growth tensor alignment, see Figure 3.5.

Block test

Constitutive law	Incompressibility	Compressibility
Form of growth tensor	Isotropic	Anisotropic
Orientation of growth tensor	Aligned to microstructure	Aligned to model CS

Figure 3.5 Perturbations of different G&R problems were applied to a block test to understand the impact of various specifications on the grown configuration. A variation of material laws from isotropic to complex anisotropic was applied in either its incompressible or compressible form in the G&R problem. Either an anisotropic or isotropic growth tensor was applied. Additionally, the alignment of the growth tensor related to the orientation of the microstructure in arterial or myocardial models was analysed.

In the case of isotropic growth, the volume was increased fourfold, while the density was kept constant.

Alternatively, anisotropic growth was applied by setting the main diagonal entries of the growth tensor to $\lambda_{g_1} = 2.0, \lambda_{g_2} = 4.0$ and $\lambda_{g_3} = 3.0$, which resulted in a volume increase of approximately threefold of the initial volume. Furthermore, we wanted to inspect whether the G&R pattern has any dependence on the coordinate system and the relative orientation of the fibres. Consequently, we repeated the tests while rotating the growth tensor along the fibre and main coordinate directions.

For this purpose, the growth tensor was rotated along the fibre or global coordinate orientation ($x/y/z$-direction).

Heterogeneous Growth test: In this test, we wanted to study the impact of a spatially inhomogeneous growth tensor. Furthermore, we also wanted to show the influence of a pressure continuous or discontinuous interface. In this test, a rectangular cube model with dimensions of $2 \times 1 \times 1$ was considered. Figure 3.6A displays the geometry and additional embedded fibre vector field. In this study, the domain was divided

into two halves, where the right half experienced either isotropic or anisotropic growth while the left half of the beam did not experience G&R. We solved the problem both on a coarse and a fine grid using 16 and 1024 $\mathbb{Q}^2 - \mathbb{Q}^1$ elements, respectively, enabling us to verify solution convergence. In this test, the `maho` material law (Equation 3.11) was utilised. Isotropic growth was implemented by utilising $\boldsymbol{F}_g = \text{diag}(4.0, 4.0, 4.0)$. Whereas, anisotropic growth was defined by $\boldsymbol{F}_g = \text{diag}(4.0, 1.0, 1.0)$.

Idealised Artery test: This test case was defined to increase the complexity of the geometry, in this idealised artery test the analytical solution for simple G&R problems (radial, circumferential or longitudinal) could still be calculated. This idealised artery geometry was utilised as a preliminary stage for G&R in cardiac applications.

The fibre field used is illustrated in Figure 3.6B. We also considered three types of anisotropic growth, namely axial, circumferential (similar to eccentric growth patterns seen in biological tissue) and radial (similar to concentric growth).

Especially, circumferential growth can also be seen in biological tissues and reminds strongly of concentric growth in the heart. These types of G&R are achieved by applying either $\boldsymbol{F}_{g_{\text{axi}}} = \text{diag}(1.0, 1.0, 4.0)$, $\boldsymbol{F}_{g_{\text{circ}}} = \text{diag}(1.0, 4.0, 1.0)$ or $\boldsymbol{F}_{g_{\text{rad}}} = \text{diag}(4.0, 1.0, 1.0)$ to the geometry. The geometry ($r_o = 3$, $r_i = 2$ and $h = 10$, units are in m) was discretised with 200 hexahedral elements ($\mathbb{Q}^2 - \mathbb{Q}^1$) with 2 elements in the radial direction, 10 elements in the circumferential direction, and 10 in the axial direction.

An additional test was utilised in which we intentionally applied a kinematic growth tensor that did not hold the compatibility constraint introduced in Equation 3.18. Specifically, we used a global growth tensor in the form of:

$$\boldsymbol{F}_g = \begin{bmatrix} \lambda_g & 0.0 & 0.0 \\ 0.0 & \lambda_g & 0.0 \\ 0.0 & 0.0 & \lambda_g \end{bmatrix}, \text{ with } \lambda_g = \alpha t, \tag{3.31}$$

where

$$\alpha = \gamma \left(\left| \cos\left(\frac{2\pi}{d_o} x + \frac{\pi}{2} \right) \right| + \left| \sin\left(\frac{2\pi}{h} z \right) \right| \right) + 1; \tag{3.32}$$

γ in this formulation was associated with the amount of growth. The amount of growth introduced ($\gamma = 4$) into the body is not reflective of the amount of growth within the heart. In this particular case, we are applying a heterogeneous growth tensor to the geometry that is incapable of satisfying the compatibility requirement

$$(\nabla \boldsymbol{u} + \boldsymbol{I}) \boldsymbol{F}_g^{-1} = \boldsymbol{I}, \tag{3.33}$$

due to the dependency of the growth factors at all times on the x and z-direction, consequently resulting in a gradient of the displacement field ($\nabla \boldsymbol{u}$) diverting of the

prescribed kinematic growth tensor $\boldsymbol{F}_g$.

Idealised left ventricle heart test: The purpose of this test was to analyse the impact of cardiac growth modes on an idealised left ventricle. In this test case, an ellipsoid represented an idealised left ventricle (LV). The embedded fibre vector field angle varied between -60 degrees to 60 degrees from the epicardium to the endocardium with respect to the local circumferential direction, as shown in Figure 3.6C. The particular growth modes we investigated were defined with respect to the local microstructure and included growth along the fibre (Equation 3.17), radial fibre (Equation 3.16), sheet, and sheet-normal direction. The growth amount for this test case was set to incrementally increase from $\vartheta_i = 1$ with $i = \boldsymbol{f}, \boldsymbol{s}, \boldsymbol{n}$ to 4. This growth amount does not reflect physiological or pathological levels of cardiac hypertrophy. This problem was solved at two different refinement levels of hexahedral meshes: a coarse mesh with 56 $\mathbb{Q}^2 - \mathbb{Q}^1$ elements and a refined mesh consisting of 448 $\mathbb{Q}^2 - \mathbb{Q}^1$ elements.

Personalised biventricular heart test: This test case represents the most complex application in this study. Here we are interested in the identification of incompatibilities introduced by growth and the impact on the grown state. The applied G&R types, are concentric (Equation 3.16), eccentric (Equation 3.17), sheet or sheet-normal hypertrophy. Subsequently, we compared the output of the different growth simulations in a patient-specific geometry. The geometry of the heart was extracted from MRI imaging data. For the generation of a local fibre direction, a rule-based fibre field was constructed by utilising the Laplace-Dirichlet method proposed by Doste et al. [55] and Bayer et al. [26]. The resulting fibre angles vary between -60° and 60° in the epicardium and from -25° to 90° in the endocardium in the LV and RV, respectively. The fibre angles of the valve annuli are determined by the use of ex-vivo DTI measurements in porcine hearts. In the septal region, the fibres transition from 60deg in the LV endocardium to 90deg in the RV endocardium, while the midwall area exhibits angles around 0deg with respect to the local circumferential direction, see Figure 3.6(D). The variation of the fibre angle increases the complexity of the G&R problem, particularly in the junction area of the RV and LV. Another question that was investigated with this test case was the impact of growth on the valves and how the final grown domain varies between material laws. The problem was discretised using 408461 $\mathbb{P}^1 - \mathbb{P}^1$ Taylor hood elements.

Table 3.1 is a summary of the simulations performed to identify and analyse the impact of numerical choices on a growing domain, such as the complexity of the geometry, the properties of the kinematic growth tensor and the choice of constitutive law.

Table 3.1 A summary of the individual problems performed to identify the impact of individual problem choices on a growth problem.

	Block Test				Heterogeneous Growth test		Idealised Artery test				Idealised Left Ventricular Heart test				Personalised Bi-Ventricle test			
Challenge: Identification of underlying growth mechanisms...	... influenced of choice of material law, compressibility, fibre alignment and kinematic growth tensor				... focussing on the property of spatial heterogeneity of the kinematic growth tensor		... impacted by constraints of the kinematic growth tensor				... with the growth tensor defined by microstructure of the myocardium in a simplified heart				... with the growth tensor defined by microstructure in the heart			
Geometry	Block (1x1x1)				Rectangular cube (2x1x1)		Cylinder (r_o=3, r_i=2,h=10)				Idealised Left Ventricular Heart (ellipsoidal shape)				Personalised Bi-Ventricle			
Elements	8 HEX ($\mathbb{Q}^2 - \mathbb{Q}^1$)				16 HEX ($\mathbb{Q}^2 - \mathbb{Q}^1$)	1024 HEX ($\mathbb{Q}^2 - \mathbb{Q}^1$)	200 HEX ($\mathbb{Q}^2 - \mathbb{Q}^1$)				56 HEX ($\mathbb{Q}^2 - \mathbb{Q}^1$1)	448 HEX ($\mathbb{Q}^2 - \mathbb{Q}^1$)			408461 TET ($\mathbb{P}^1 - \mathbb{P}^1$)			
Micro-structural alignment along to	global CS	45 deg rot. wrt. x-axis	45 deg rot. wrt. y-axis	45 deg rot. wrt. z-axis	x-axis of global CS		x-axis of global CS				local CS				local CS			
Growth tensor alignment along to	global CS	45 deg rot. wrt. x-axis	45 deg rot. wrt. y-axis	45 deg rot. wrt. z-axis	global CS (sinusoidal)		local AXI dir.	local CIRC dir.	local RAD dir.	global CS	F	S	SN	SN+S	F	S	SN	SN+N
Type of Growth	ISO		ANI		ISO	ANI	ANI				ANI				ANI			
Material law	`neo`, `hog`, `ho`, `maho`				`neo`, `maho`		`neo`, `hog`, `ho`, `maho`				`neo`, `ho`				`neo`, `ho`			

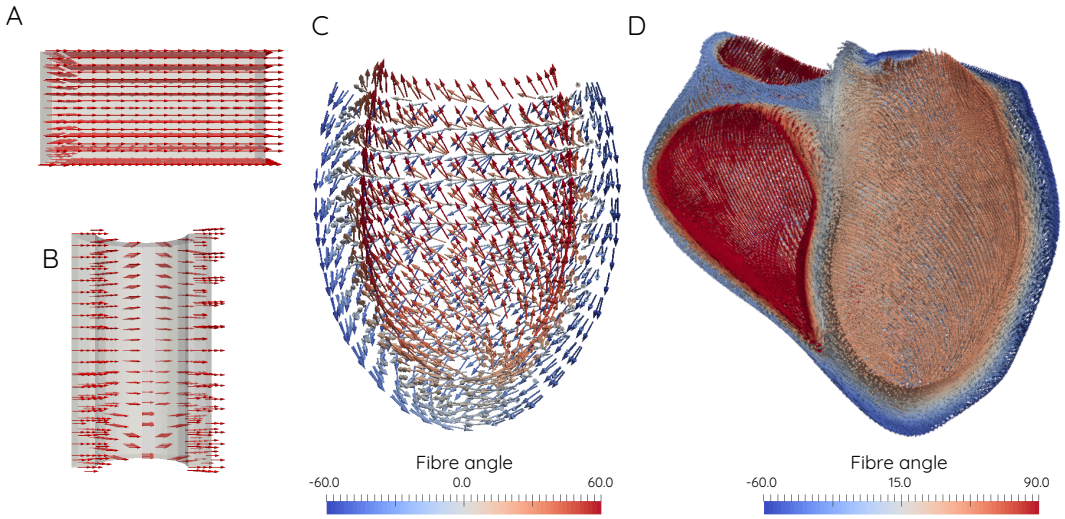

Figure 3.6 Fibre field of the individual discussed models. (A) visualises the fibre field in the beam model. The fibres are aligned along the x-axis. This information is of importance in the case of anisotropic growth. Since the anisotropic G&R test case is along the x-direction. In the cylindrical geometry (B) the fibre field is aligned to the x-axis. In the more complex case of the idealised LV model (D), the fibres vary from -60deg (epicardium) to 60deg (endocardium) concerning the local circumferential direction. (D) represents the fibre field and the related fibre angle with respect to the local circumferential direction of the biventricular (BiV) model.

3.3 Results

The following section contains the results of previously introduced tests. Here we investigated a geometrical comparison and further investigated the influence of G&R on the degree of incompatibility in Benchmark problems and cardiac applications.

3.3.1 Block test

Figure 3.7 displays the morphological changes resulting from the different growth tensor definitions which were applied to the cube model's.

The first level of the figure represents the reference cube model. The orange coordinate system (CS), specifies the orientation (x, y, z-direction) of the global CS with respect to the model's spatial orientation. In the second level, we observe the change of morphology by applying either an isotropic (left) versus anisotropic kinematic growth tensor (right). And in the final level, we have an overview of the alignment of the growth tensor perturbation. From left to right, we have the cases F_g aligned with (1) the CS (marked in blue) and the cube's edges, (2) aligned with the CS, but not the edges, (3) aligned with the fibres (green axes) and the edges, (4) aligned with the fibres but not the edges.

Solving a G&R problem in such a simplified geometry enables us to solely analyse the impact of growth and consequently on incompatibility related to the material law

and the kinematic growth tensor. The results of this particular test are attached to this work in the appendix, see Figure Appendix .1.1. After prescribing the different kinematic growth tensors $\boldsymbol{F}_g$, we observed the same displacements across all the test cases, see Table Appendix 1–20. The pressure norm difference resulted in pressures in machine precision, except for the `ho` solution, due to the isochoric material behaviour of the classical `ho` material law.

The results of these tests are all cases where $\boldsymbol{F}\boldsymbol{F}_g^{-1} = \boldsymbol{I}$ is satisfied and can further be satisfied by the applied displacement field $\boldsymbol{u}$. In this event, growth occurs, irrespective of Ψ as a consequence of $\boldsymbol{F}_e$ resulting in Ψ being minimal over the entire domain. These internal pressures are assumed due to the internal constraints of the fibres on the deformation. Comparing the individual levels of compatibility with the introduced metric (Equation 3.19), across the various perturbations of the growth problems resulted in $e_{inc} = 0$.

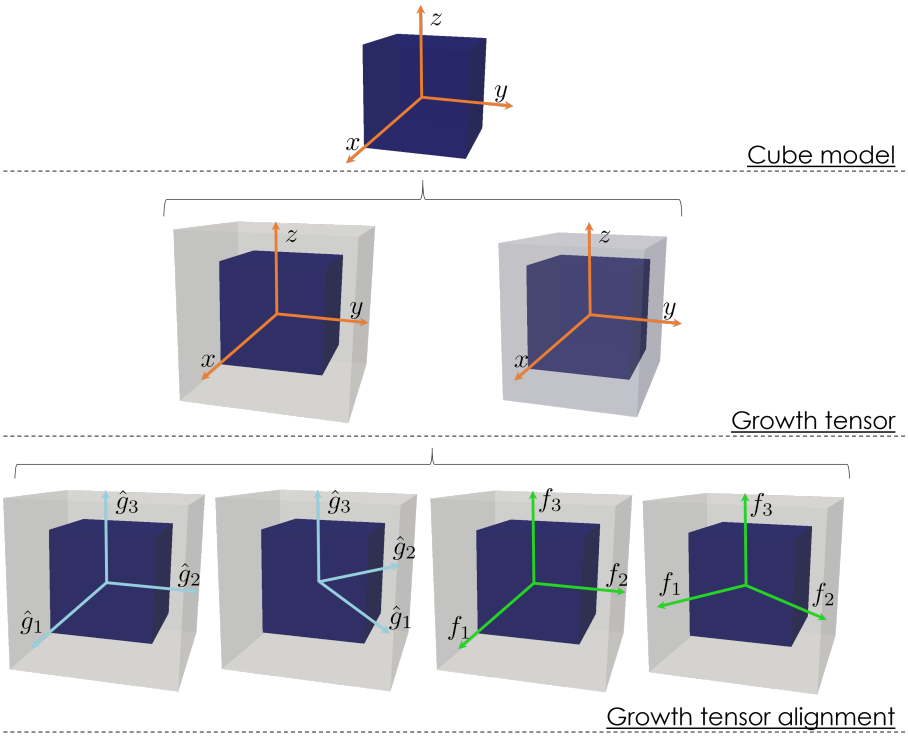

Figure 3.7 Perturbations for G&R problem in block test. For the growth tensor $\mathbf{F}_g$ we used either an isotropic (left) or an anisotropic (right) form. And subsequently, the growth tensor was either un-/aligned with the global coordinate system or the microstructure (here are only the results for isotropic case shown).

3.3.2 Heterogeneous G&R test

Figure 3.8 displays the geometrical changes and the linear regression between the `maho` and `neo` in a rectangular cuboid model. Here the applied kinematic growth tensor (left: isotropic, right: anisotropic) was only affecting the right half of the model while no G&R was applied to the left half of the model. Comparing the results obtained using a continuous (A3) versus a discontinuous (A4) pressure field representation, we observe

slight variations between the final grown states. While for the former, the right end of the domain appears to remain a plane surface, in the latter, the same surface appears to be warped. In contrast, applying an isotropic growth tensor resulted in growth being limited to the axial direction, the results being virtually indistinguishable between the different cases (continuous/discontinuous pressure, coarse/fine grid).

The correlation plots focus on the relation of the deformation gradient between the `neo` and the reduced `ho` material law. Subsequently, a narrow band along the correlation line means that the entries of the deformation gradient at each spatial node are similar. The linear regression plots of Figure 3.8 illustrate the correlation between the deformation gradients obtained with the `ho` and `neo` material laws. Applying an isotropic growth tensor (A1–A4) resulted in differences in the deformation gradient entries, with the highest values in the refined mesh with a discontinuous pressure field. Here the markers are widely spread over the plot. Compared to the isotropic case, applying an anisotropic growth tensor (B1–B4) resulted in markers only aligned along the compatibility line.

Table 3.2 contains the node-wise incompatibility metric e_{inc} in the heterogeneous G&R model test following growth was applied either isotropic or anisotropic on the right half. Further distinctions of the test include the simulation of a pressure continuous or discontinuous field with a neo-Hookean or modified Holzapfel-Ogden material law. These results show that after applying a spatially varying, anisotropic kinematic growth tensor, G&R processes do not necessarily introduce incompatibility in a body if a displacement field can be generated that satisfies Equation 3.33. In contrast, applying a discontinuous, isotropic growth tensor introduces incompatibility, especially in the transition region, between growth and no growth. Furthermore, we did not observe a decrease in incompatibility in a refined mesh with the same kinematic growth tensor applied.

Table 3.2 Mean and standard deviation (in brackets) of the node-wise incompatibility metric e_{inc} in the heterogeneous G&R test with an isotropic or anisotropic kinematic growth tensor applied to the right half of the coarse or refined domain, with a pressure continuous (Cont) or discontinuous (Disc) field.

	Isotropic			
	16 Elements		1024 Elements	
	Cont	Disc	Cont	Disc
`neo`	0.08(0.07)	0.10(0.08)	0.06(0.08)	0.06(0.08)
`maho`	0.08(0.07)	0.13(0.08)	0.08(0.08)	0.12(0.10)

	Anisotropic			
	16 Elements		1024 Elements	
	Cont	Disc	Cont	Disc
`neo`	0.0(0.0)	0.0(0.0)	0.0(0.0)	0.0 (0.0)
`maho`	0.0(0.0)	0.0(0.0)	0.0(0.0)	0.0(0.0)

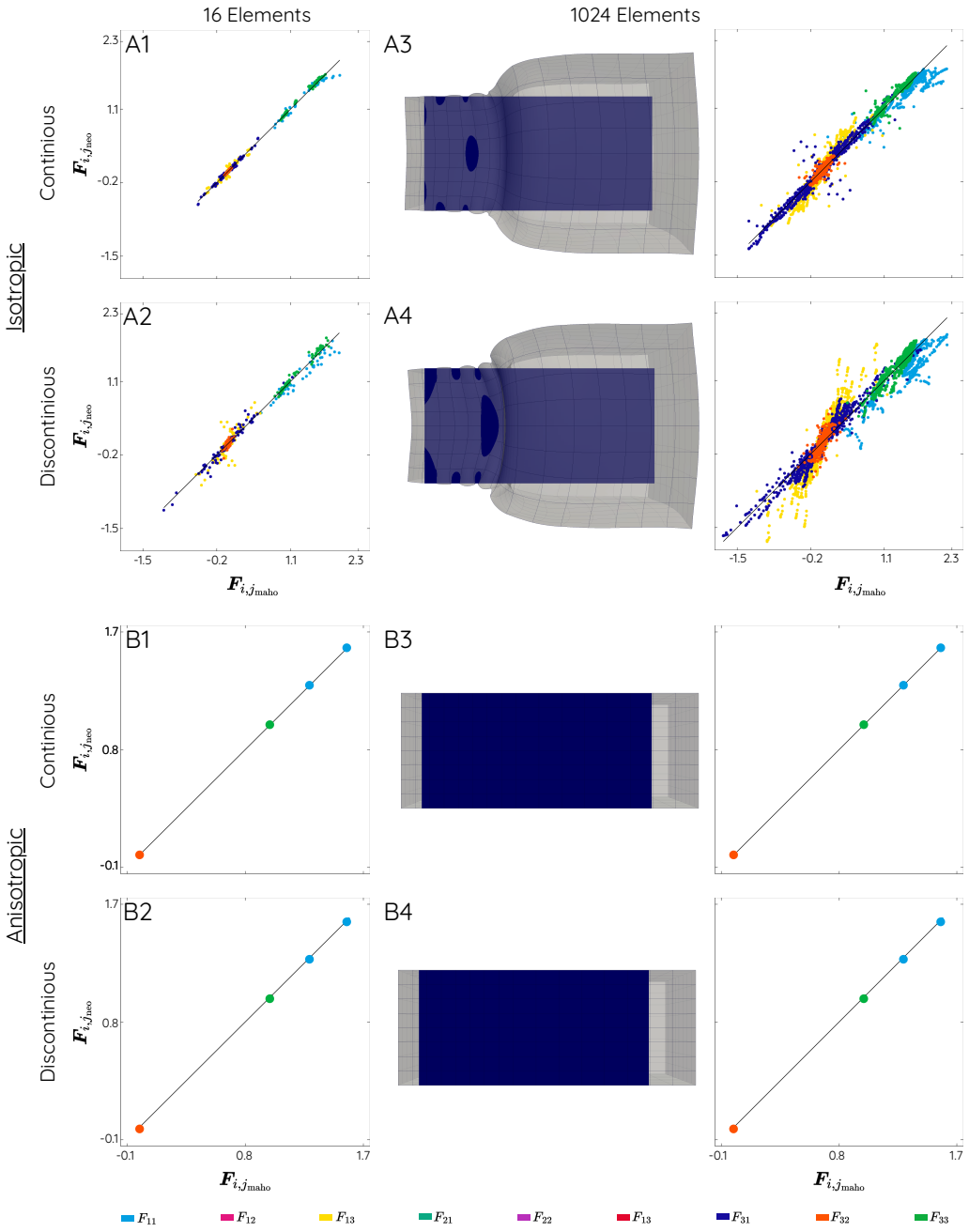

Figure 3.8 (A3–A4): Show the morphological changes in the fine grid, with the reference domain (blue) and the grown state after the final loading step. The plotted results are with a `neo` material law and with either a continuous (A1, A3) or discontinuous (A2, A4) pressure field at the interface area. Furthermore, it displays the linear regression plots for the coarse mesh (A1,A2) and the fine grid (A3,A4). In contrast, (B1–B4) illustrate the anisotropic G&R case. (B1, B2): Correlation plots for coarse grid with anisotropic growth on the right hemisphere and a continuous (B1) or discontinuous (B2) pressure field. (B3,B4): Geometrical changes and linear regression plots on a finer grid with pressure continuous (B3) and discontinuous (B4) field.

3.3.3 Idealised Artery test

Figure 3.9 shows the results from the G&R problem including all the combinations of growth tensor options. The left-hand side of this figure visualises the morphological changes and linear regression plots of different kinematic growth tensors applications such as axial (A), circumferential (B) and radial (C) spatial constant growth patterns. We can observe that axial (A), circumferential (B) and radial (C) G&R resulted into a marker alignment along the compatibility line in the linear regression plots.

The right column of Figure 3.9 illustrates the variation of a problem with a sinusoidal growth tensor varying along the axial and lateral direction (Equation 3.32) and different cardiac constitutive laws (D1) `hog`, (D2) `ho` and (D3) `maho`. Fig. (D1) and (D2) depict the relation of the `hog` or `ho` to the `neo` material, respectively. These two plots demonstrate a broad divergence of markers from the compatibility line over the whole spectrum of deformation gradient entries $\boldsymbol{F}_{ij}$. In contrast, we can see that the `maho` form in (D3) indicates a clustering of data points close to the compatibility line.

Analysing the node-wise incompatibility metric e_{inc}, see Table 3.3, of the different tests for the idealised artery tests, suggested that in the cases with a homogeneous kinematic growth tensor applied to the model, no incompatibility or residual stresses were introduced following growth. However, applying a more complex kinematic growth tensor to an idealised artery, it was not possible to satisfy Equation 3.33, which resulted in an increase of net incompatibility across the domain.

Table 3.3 Mean and standard deviation (in brackets) of the node-wise incompressibility metric e_{inc} of the idealised artery tests with an applied axial, circumferential, radial or heterogeneous (sinusoidal) kinematic growth tensor.

	`neo`	`hog`	`ho`	maho
Axial	0.0(0.0)	0.0(0.0)	0.0(0.0)	0.0(0.0)
Circumferential	0.0 (0.0)	0.0(0.0)	0.0(0.0)	0.0(0.0)
Radial	0.0(0.0)	0.0 (0.0)	0.0(0.0)	0.0(0.0)
Heterogeneous (sinusoidal)	0.13(0.04)	0.04(0.04)	0.14(0.05)	0.13(0.04)

3.3.4 Idealised Left Ventricular Heart test

Figure 3.10 displays the geometrical comparison and linear regression of different perturbations of the kinematic growth tensor with the same amount of growth along the fibre, sheet, normal or sheet-normal direction. Figure (A) shows eccentric G&R in an idealised left ventricular heart model. The figure shows that the wall thickness remained (quasi)-constant to the thickness of the reference model and so did the length of the ventricle. We could further observe that the cavity of the LV started to increase with the magnitude of growth. Figure (B,D) displays the morphological changes resulting from the use of the growth tensor defined in Equation 3.16, which corresponds to a concentric growth pattern.

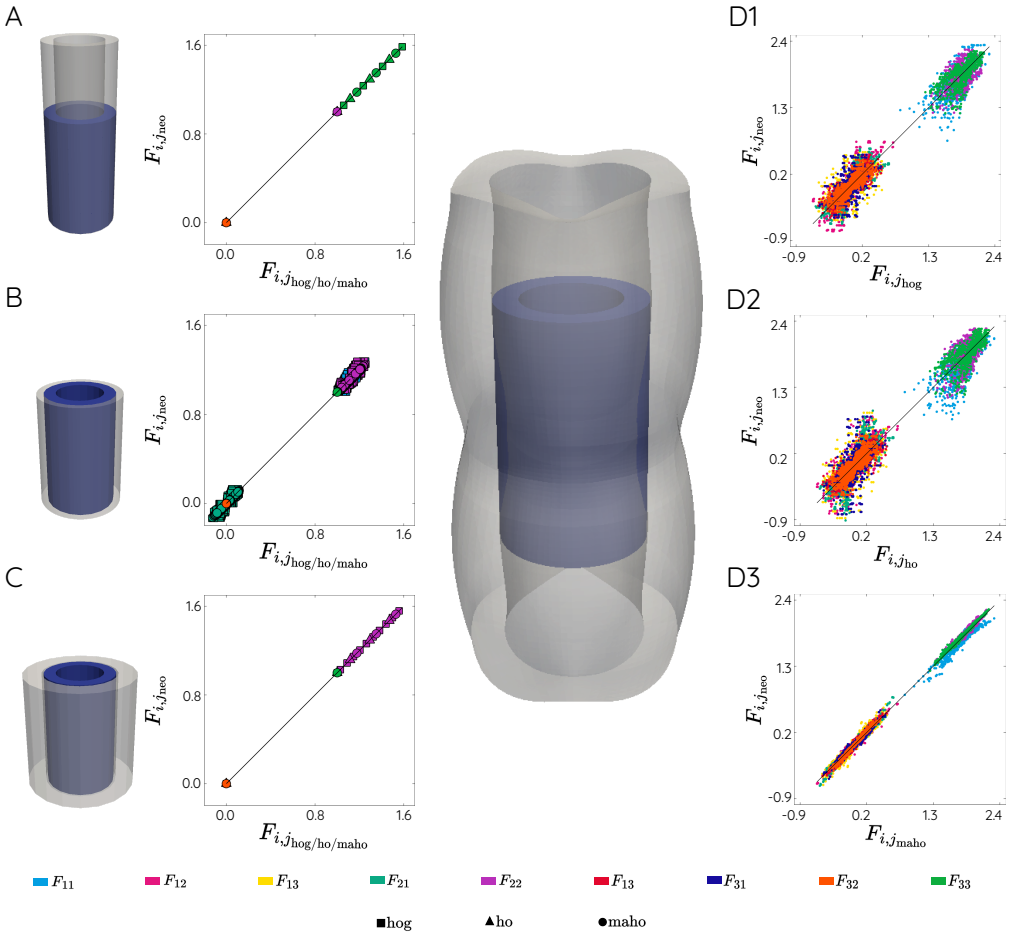

Figure 3.9 Left column: Morphological change and linear regression plots of the different G&R modes (A) axial B) circumferential and C) radial growth with varying material laws (`neo`, `hog`, `ho` and `maho`). The geometrical changes are compared between the reference model (blue) and the final grown state (translucent grey), here we only plotted the results of the `neo` constitutive law. Right column: Morphological changes and linear regression plot for the case of sinusoidal growth (Equation 3.32) applied. With a (D1) a `hog`, (D2) a `ho` and (D3) a `maho` material law utilised.

Restricting G&R to the sheet direction only (B) resulted in a slight increase in wall thickness and a marginal decrease in cavity volume. While the length of the ventricle remained the same.

In contrast, having a concentric growth tensor restricted to the normal direction, see Figure (C) the grown LV resulted in an elongated heart and led to an increase in cavity volume. Combining both sheet and normal G&R (D) resulted in: wall thickness change, LV elongation and reduction in cavity volume.

All of the linear regression plots, visualised in Figure (A–D) show a deviation from the compatibility line. Here, the markers in the eccentric growth case (A) showed the lowest deviation while the cases including sheet influences caused the markers to align in a broad band along the black line. Conversely, in the case of concentric growth,

we observed a more heterogeneous result, with some of the nodes clustering near the correlation line, while others diverged.

Table Appendix 21 and 22 contain the numerical results for the performed growth problems within a `neo` and `ho` material. The results include the norm difference of the solution of $\boldsymbol{u}$, p, the deformation gradient $\boldsymbol{F}$ along the growth directions $(\boldsymbol{g}_1, \boldsymbol{g}_2, \boldsymbol{g}_3)$ and the difference between the geometrical differences $\Delta\boldsymbol{u}$ with respect to the geometrical changes in a `neo` material following growth in %.

Across the different problems, it was possible to identify growth modes within the heart that lead to higher differences in geometrical changes in the final grown domain for a course and a refined mesh. In the coarse mesh, the highest discrepancy between the geometrical solution of the `neo` and the solution with a `ho` was observed after applying growth along the normal direction. However, fibre growth (eccentric growth) introduced the lowest amount of differences between the two different material models, see Table Appendix 21a.

Studying the same modes of growth in a more refined model leads to minor changes in the discrepancy between the materials for the case of fibre $\boldsymbol{f}$, sheet $\boldsymbol{s}$ and the combination of sheet and normal $\boldsymbol{sn}$ (concentric growth), see Table Appendix 22b. However the difference between the solutions in the case of normal $\boldsymbol{n}$ growth was significantly reduced to refinement, see Table Appendix 22a.

Table 3.4 contains the node-wise incompatibility metric e_{inc} in an idealised LV model following growth along the fibre $\boldsymbol{f}$ (eccentric), normal $\boldsymbol{n}$, sheet $\boldsymbol{s}$ or sheet and normal $\boldsymbol{sn}$ (concentric) direction, a visual representation of this metric is seen in Figure 3.11.

Table 3.4 Mean and standard deviation (in brackets) of the node-wise incompatibility metric e_{inc} in the idealised LV tests with an applied kinematic growth tensor along the fibre (eccentric), normal, sheet or sheet and normal (concentric) direction.

	Fibre $\boldsymbol{f}$	Normal $\boldsymbol{n}$	Sheet $\boldsymbol{s}$	Sheet and Normal $\boldsymbol{sn}$
`neo`	0.36(std=0.030)	0.36(std=0.028)	0.45(std=0.049)	0.58(std=0.02)
`ho`	0.35(std=0.024)	0.32(std=0.035)	0.45(std=0.051)	0.61(std=0.025)

3.3.5 Personalised Biventricular Heart test

Figure 3.12A–D display the geometrical changes and the linear regression plots of different growth patterns applied to the biventricular (BiV) heart model.

The different applied growth patterns represent G&R in either the fibre (A), sheet (B), or normal directions (C). Furthermore, Figure (D) shows the combination of growth directed in the sheet and the normal direction. What can be observed is that the wall thickness remains constant over time while a length change of the cavity chamber can

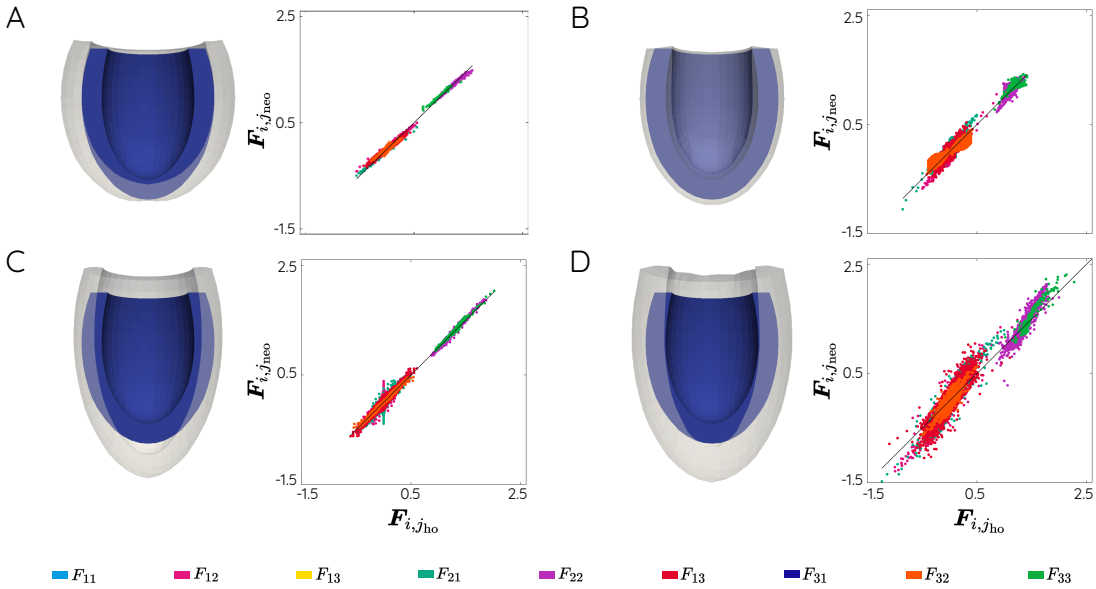

Figure 3.10 Reference model (blue) compared to the grown state of the model (translucent grey) after applying different G&R modes (A) fibre, (B) sheet, (C) normal and (D) mixed sheet and normal growth to an idealised LV model. The model itself utilises an isotropic Neo-Hookean material law. Correlation plot for the deformation gradient $\boldsymbol{F}_{ij}$ between Neo-Hookean and HO material law in the same order of the growth described on the left. The colour of the marker represents the individual entry of the deformation gradient from the global node of the model mesh.

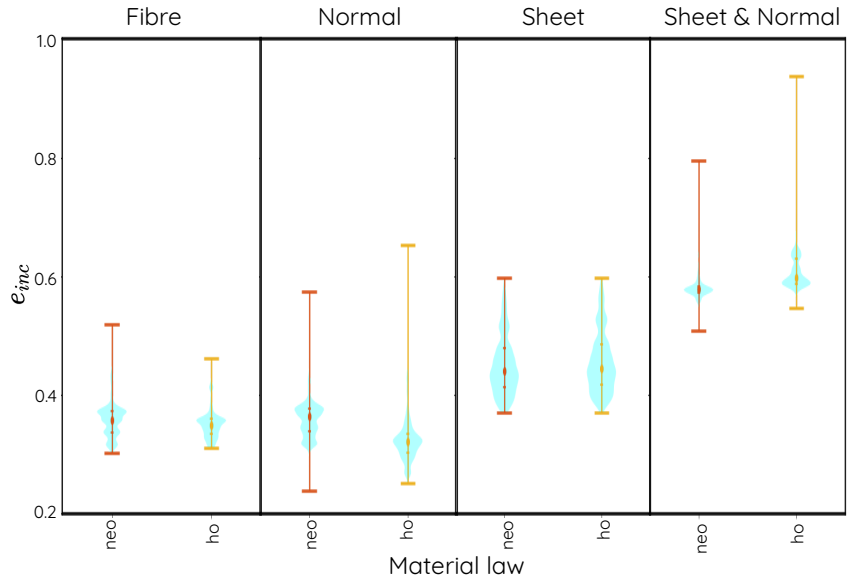

Figure 3.11 Incompatibility metric e_{inc} (Equation 3.19) in the idealised LV model utilizing a Neo-Hookean and a HO material law, defined with the Frobenius norm of $\boldsymbol{F}_e\boldsymbol{F}_g$. With $e_{inc} = 0$, indicating a compatible state following growth.

be observed after applying eccentric growth to a BiV model, see Figure 3.12A. Growth along the normal direction introduced a slight increase in wall thickness, where at the same time, the length of the ventricle remains relatively constant, see Figure 3.12C. In comparison Figure 3.12B illustrates G&R along the sheet direction. Instead of increasing the thickness, both ventricles display a change in cavity volume. The mixed G&R mode, illustrated in Figure 3.12D, indicates an increase in the cavity volume and wall thickness. Noteworthy to mention in this test case is the distinctive deformation in the valve area.

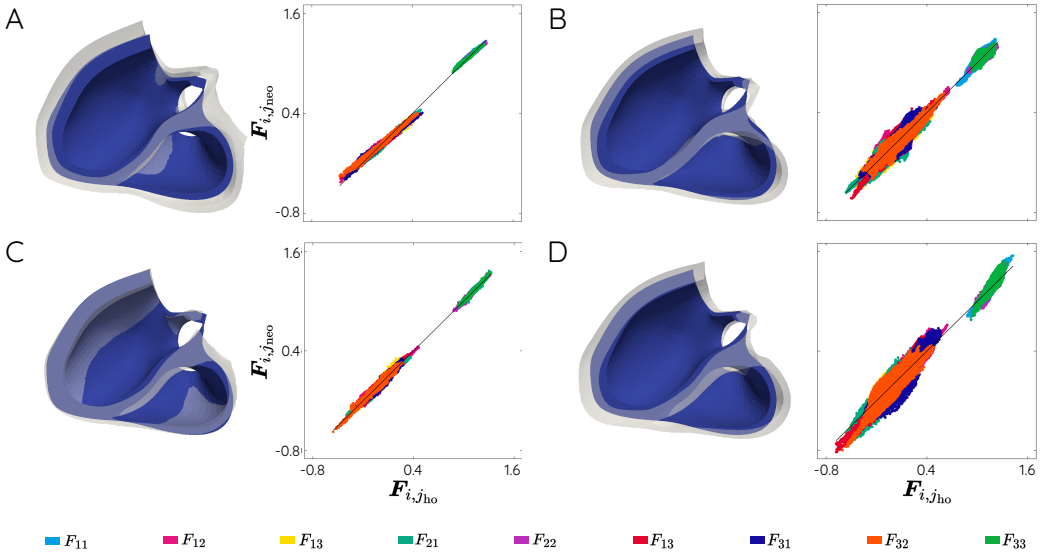

Figure 3.12 Comparison of the reference model (blue) to the grown state (translucent grey) of a BiV model after applying (A) fibre, (B) sheet, (C) normal and (D) mixed sheet and normal G&R modes to the geometry. $\boldsymbol{F}_{ij}$ correlation plot between `neo` and a reduced form of the `ho` material after applying (A) fibre, (B) sheet, (C) normal and (D) sheet and normal growth to the model. The marker colour indicates the individual entries of the deformation gradient at the global node.

In the plot of the fibre mode (Figure 3.12A), the entries are distributed along the black line in a thin band which indicates the solution may only show a minor difference between the material laws. The same distribution behaviour can be seen in the test with a normal growth pattern (Figure 3.12C). In contrast to the tightly aligned markers in the fibre and normal case, the tests involving growth in the sheet direction show higher variation in the correlation plots. At the same time, G&R restricted to the sheet direction (Figure 3.12B) showed a slight variation, especially in the range of lower values of the deformation gradient. Finally, there was a low correlation observed between the `neo` and the reduced `ho` in the mixed case of sheet and normal growth in the BiV model, visualised in Figure 3.12D.

Table Appendix 23 and 24 contain the numerical results for the performed growth problems within a `neo` and `ho` material, such as the norm difference of the solution of $\boldsymbol{u}$,

p, the deformation gradient $\boldsymbol{F}$ along the growth directions $(\boldsymbol{g}_1, \boldsymbol{g}_2, \boldsymbol{g}_3)$ and the difference between the geometrical differences $\Delta\boldsymbol{u}$ with respect to the geometrical changes in a `neo` material following growth in %.

Across the different problems, it was possible to identify growth modes within the heart that lead to higher differences in geometrical changes in the final grown domain. The highest discrepancy between the geometrical solution of the `neo` and the solution with a `ho` was observed after applying growth along the sheet $\boldsymbol{s}$ direction, see Table Appendix 23b.

On the other hand, fibre growth (eccentric) introduced the lowest amount of differences between the two different material models, see Table Appendix 23a. However, the combined case of growth along the sheet and normal $\boldsymbol{sn}$ direction (concentric growth) applied to a BiV model did not further increase the discrepancy between the solutions, see Table Appendix 24b.

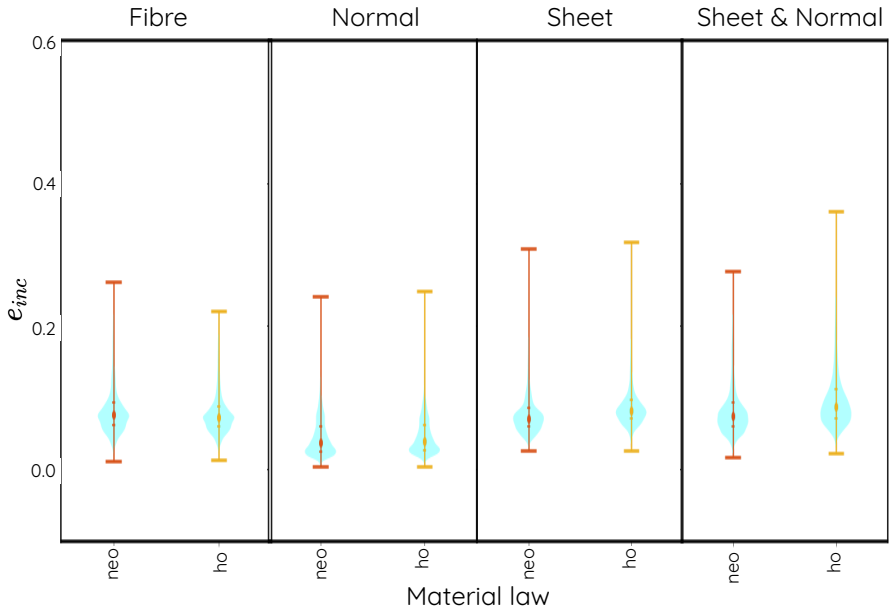

Figure 3.13 Incompatibility metric e_{inc} (Equation 3.19) in the personalised BiV model utilising a Neo-Hookean and a HO material law, defined with the Frobenius norm of $\boldsymbol{F}_e\boldsymbol{F}_g$. With $e_{inc} = 0$, indicating a compatible state following growth.

Figure 3.13, illustrates the states of incompatibility for the individual utilised test cases and material laws, and Table 3.5 gives the mean values for the illustrated e_{inc} metric. In the case of $e_{inc} = 0$, the grown state is assumed to be a compatible state without incompatibilities and residual stresses introduced.

Table 3.5 Mean and standard deviation (in brackets) of the node-wise incompatibility metric e_{inc} of the personalised heart tests with applied kinematic growth tensor along the fibre $\boldsymbol{f}$ (eccentric), normal $\boldsymbol{n}$, sheet $\boldsymbol{s}$ or sheet and normal $\boldsymbol{sn}$ (concentric) direction.

	Fibre $\boldsymbol{f}$	Normal $\boldsymbol{n}$	Sheet $\boldsymbol{s}$	Sheet and Normal $\boldsymbol{sn}$
`neo`	0.08(std=0.036)	0.04(std=0.026)	0.08(std=0.034)	0.08 (std=0.037)
`ho`	0.08(std=0.030)	0.05(std=0.025)	0.09(std=0.035)	0.1 (std=0.041)

3.4 Discussion

The following section is subdivided into individual key findings of the different tests we performed to understand the impact of numerical choices for modelling G&R processes in cardiac applications on the incompatibility state of the grown geometry.

3.4.1 Kinematic Growth and Material Laws

This problem setup was designed to investigate the numerical impact of the material law, properties of the kinematic growth tensor, and the influence of fibres in a highly simplified kinematic G&R problem description. Across all the different problem perturbations, such as growth mode, the orientation of growth, and the alignment to the microstructure, it could be observed that without any restriction on the growth and in a simplified geometry, the choice of material law became irrelevant. This behaviour was noted in cases with an applied isotropic or anisotropic material law. Even in tests with more complex kinematic growth tensors, such as anisotropy or alignment of the growth tensor, the separate material laws indicated comparable solutions in the block test, see correlation Figure Appendix 1. The same behaviour could be observed in the case of the idealised artery test with the kinematic G&R being either applied in the longitudinal, radial or circumferential direction. The outcome of these tests indicates that as long there are no external constraints, e.g. BC, the geometry can freely deform and satisfy the applied displacement field $\boldsymbol{u}$. In tests where incompatibility was observed, the solution of the different applied material laws was diverging. In these cases, incompatibility was introduced either via BC or more complex growth behaviour which did not allow the geometry to satisfy the applied displacement field.

3.4.2 Homogeneous versus Heterogeneous Growth

Tests where we noticed incompatibility were in the case of heterogeneous G&R, with isotropic growth applied to a beam geometry and sinusoidal growth within the idealised artery test. Both cases introduced incompatibility driven by the applied kinematic growth tensor.

In the case of heterogeneous G&R, a distinct regional jump in growth was applied. Here a separation of the solution is noticed and introduced by the strain energy function to satisfy the linear balance equation (Equation 3.27). Additionally, we analysed the

impact of a continuous versus a discontinuous pressure field within the growth geometry on the state of incompatibility. In the case of heterogeneous G&R with an underlying discontinuous pressure field, the discrepancy between the material laws was significantly higher than assuming an underlying continuous pressure field.

In regards to the idealised artery test with a sinusoidal growth pattern applied, results indicated different solutions for the compared material laws. This behaviour was a result of Equation 3.33 not being satisfied, where no displacement field could be defined to mimic the prescribed kinematic growth tensor point for point, resulting in incompatibilities in the final grown state that might be further linked to an increase of residual stresses in the body.

This behaviour was further observed in the correlation plot of the deformation gradients for the sinusoidal case, in which the solution for the material laws separated from each other. However, analysing the overall morphological changes due to growth resulted fairly in the same grown geometry across material laws.

This test indicates that even in similar-looking grown geometries the kinematics of materials may differ from each other and potentially introduce different levels of residual stresses in the grown domain. Subsequently, we assume that internal stresses may be inherited and might not have a big impact on the observed growth pattern despite not applying the prescribed growth deformation.

3.4.3 Application to the Heart

Comparing the two analysed material laws, the differences between the final grown states were minimal. This result suggests that this type of growth may only introduce a minimal deviation in a compatible deformation state. Evidence for this is that the anisotropic (i.e. fibre, normal, sheet) growth tensors led to a higher discrepancy between the models than the combined (sheet + normal). In the concentric case, it is possible to assume that G&R introduces high residual stress values and may also be the main contributor to these stresses in the heart during embryonic development. Concluding from the summary tables in the Appendix (Table 21–22), in which the displacement errors are reported, it can be said that dependent on the type of G&R applied to this kind of geometry, the characteristic of the individual material law is more pronounced, resulting in significant differences between results computed with the cardiac material laws and `neo`. Conversely, applying growth in the sheet direction only introduces 50% differences. These results were largely independent of mesh refinement, with a similar degree of differences between results. The exception to this was the case of growth in the normal direction, where we saw significant changes. In contrast, the other G&R modes remained around the same level of arithmetic difference.

The right-hand side of Figure 3.12B and D indicates that types involving growth in the

sheet direction resulted in a higher level of divergence around the black compatibility line. Figures (A,C) suggest that G&R in fibre or normal direction resulted in a narrow band of values aligned along the compatibility line of the deformation gradient entries. This behaviour implies in the case of a G&R problem in a BiV model, eccentric growth in the fibre direction introduces the least amount of residual stresses into the model. In contrast, the concentric growth with an active G&R component in the sheet and normal direction caused high stresses in the final grown configuration. The main takeaway from Figure 3.13, is that across all the distinct tests, a significant degree of incompatibility is introduced through G&R. Defining G&R along the fibre, normal or sheet direction leads to approximately the same degree of incompatibility with either a `neo` or a `ho` material. In contrast, the coupled case with growth along the sheet and normal direction induced higher levels of incompatibility in the final state. This behaviour can be explained by the fact that in the case of concentric growth, the tissue needs to push and pull the material around as it adapts[190]. A consequence of this process could be a potential increase of residual stresses in the myocardium that further have a harmful impact on the cells within the tissue and could lead to an early onset of HF a common adverse effect of cardiac G&R[242].

3.5 Conclusion

This study focused on the main challenges of modelling G&R in cardiac applications, by investigating different numerical assumptions and identifying the impact on the incompatibility states on the grown body. To address the effect of different growth problem perturbations, we introduced various benchmark tests designed to assess incompatibility and residual stresses in G&R modelling, which could be introduced by material law, properties of the kinematic growth tensor or boundary condition.

One key takeaway that we observed was that in the case in which growth was applied to a highly simplified geometries, the choice of material law becomes irrelevant, even in cases with complex kinematic growth tensors. These results indicated that in the absence of constrictions on G&R, the geometry can deform without introducing incompatibility or residual stress into the body.

However, another key finding was that the differences between the solution of growth problems conducted with different material laws became apparent in tests where the geometry could not generate a displacement field to match the applied growth deformation. An example of this is evident when the kinematic growth tensor is heterogeneous over the geometry and consequently unable to satisfy the compatibility constraint $\boldsymbol{F}\boldsymbol{F}_g^{-1} = \boldsymbol{I}$ point for point.

In the case of the idealised artery, we noticed that even if the geometries appear similar with different material laws, residual stresses are inherited. This particular test

demonstrates that spatial variation of growth in cardiac applications introduces incompatibilities that should be analysed by using a cardiac material law instead of utilising an isotropic `neo` material law to study these phenomena.

In the last tests, we performed assessments of incompatibilities associated with cardiac applications by applying various G&R modes associated with the microstructure of the myocardium, e.g. growth along the fibre, sheet, sheet-normal or a combination of sheet and sheet normal (assumed to mimic concentric growth) to an idealised LV and personalised heart. Notably, we observed that G&R associated with the sheet direction introduces the highest amount of incompatibilities and residual stresses. This particular results demonstrated that dependent on the type of growth higher amounts of incompatibility and further inherent residual stresses that potentially could be more harmful to the cells and introduce earlier onset of HF.

4 Exploratory Assessment of Focused Septal Growth in Hypertrophic Cardiomyopathy

Various studies in the literature are utilising the kinematic growth approach to assess and predict G&R patterns for cardiac pathologies, such as heart failure (HF), desynchonisation therapy, etc. However, as yet the application of the kinematic growth theory was not applied to model hypertrophic cardiomyopathy (HCM). The phenotypical growth pattern in HCM is highly heterogeneous in patients, even in familial lines the patterns vary. Consequently, we were interested in the underlying reasons for the dominant growth pattern of left ventricular outflow obstruction (LVOTO) which affects regions in the septum to grow independent of the mechanical loading. Section 4.2, establishes three test cases for spatial varying G&R in a cardiac application that were compared to observed cases of LVOTO in patients with HCM.

This chapter has been published as a standalone article: Sandra P. Hager, Will Zhang, Renee M. Miller, Jack Lee, David A. Nordsletten. "An Exploratory Assessment of Focused Septal Growth in Hypertrophic Cardiomyopathy". *In Functional Imaging and Modeling of the Heart: 11th International Conference* (Published, 2021)[101].

Abstract

Growth and Remodelling (G&R) processes are typical responses to changes in the heart's loading conditions. The most frequent types of G&R in the heart are thought to involve growth parallel to (eccentric) or perpendicular to (concentric) the fibre direction. However, hypertrophic cardiomyopathy (HCM), a genetic mutation of the sarcomeric proteins, exhibits heterogeneous patterns of growth and fibre disarray despite the absence of clear changes in loading conditions. Previous studies have predicted cardiac G&R due to increased overload in the heart[98,121,194] as well as modelled inverse G&R post-treatment[145,16]. Since observed growth patterns in HCM are more complex than standard models of hypertrophy in the heart, fewer studies focus on the geometric changes in this pathological case. By adapting established kinematic growth tensors for

the standard types of hypertrophy in an isotropic and orthotropic material model, the paper aims to identify different factors which contribute to the heterogeneous growth patterns observed in HCM. Consequently, it was possible to distinguish that fibre disarray alone does not appear to induce the typical phenotypes of HCM. Instead, it appears that an underlying trigger for G&R in HCM might be a consequence of factors stimulating isotropic growth (e.g. inflammation). Additionally, morphological changes in the septal region resulted in higher amounts of incompatibility, evidenced by increased residual stresses in the grown region.

4.1 Introduction

Nearly 1 in 200 people are affected by hypertrophic cardiomyopathy (HCM)[211], a genetic disease impacting the key sarcomeric proteins in cardiomyocytes. The histological phenotype of HCM includes hypertrophy, reorientation of the myocytes[161] and interstitial fibrosis (Figure 4.1). Inflammation, as a response to fibrosis, is an accepted indicator of the severity in HCM cases[62]. The rationale for the disorganization of cardiac muscle cells in the ventricular septum is still not fully understood. However, septal disarray can be seen in 94% of patients with HCM[161].

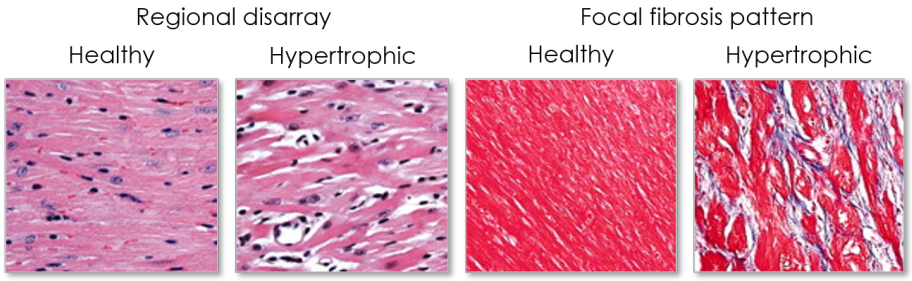

Figure 4.1 Histological images of healthy and hypertrophic myocardial tissue (adapted with permission from Wolf et al.[243], Copyright (2005) National Academy of Sciences, U.S.A.) visualizing the regional disarray (left) with H&E staining. blue: nucleus, red: cytoplasm, varying red: collagen fibres and ECM. The right describes changes due to focal fibrosis with Masson's trichrome staining. blue: cytoplasm in necrotic myocardium, red: cytoplasm in viable myocardium.

On the whole-organ level, regional growth is observed despite no noticeable change in loading conditions[158,159,126,150,49]. Growth patterns in HCM are heterogeneous amongst patients, but around a third of patients have hypertrophy in the basal interventricular septal region[157] and in later stages develop an LV outflow obstruction (LVOTO) accompanied by systolic anterior motion of the mitral valve leaflet. A commonly observed HCM growth pattern involves hypertrophy in the antero-septal region of the left ventricular wall[222,49] which is quantified with a thickness of 13–15 mm in mild versions of the disease and $\geq$30 mm in severe cases[158]. Besides the noticeable changes in geometry, HCM patients are at higher risk of cardiac arrhythmias, sudden cardiac death (SCD) and heart failure (HF)[158].

Recent papers support utilizing the kinematic growth approaches to computationally model and predict hypertrophy due to deviation from the heart's homeostatic state. For a general overview of the phenomenological growth laws, the interested reader is referred to Witzenburg and Holmes [242]. The challenge of most growth laws rests in the definition of the growth trigger that varies between mimicking sarcomergenesis inside the cells [98] to electromechanical changes in behaviour due to concentric hypertrophy [50].

This paper aims to investigate growth in HCM by examining drivers of septal thickening using computational modelling. Test cases are generated in order to evaluate possible mechanisms in an isotropic and orthotropic material model which lead to pathophysiological changes, such as remodelling of the fibre orientation, inflammation and different growth responses in a predefined septal region. Across the test cases, asymmetric septal growth might be triggered by an underlying isotropic growth stimulus that also results in enhanced residual stress in the septal area.

4.2 Methods

4.2.1 General Kinematic Framework for Finite Growth

The problem setup is based on a mechanical problem, accounting for the linear momentum balance and mass conservation equation, such that $(\boldsymbol{u}, p) \in \mathcal{U} \setminus \mathcal{Q}$ and $p \in \mathcal{P}$,

$$\int_{\Omega_X} \boldsymbol{P}(\boldsymbol{F}, p) : \nabla_X \boldsymbol{w} + q(J-1)\mathrm{d}X = 0, \ \forall \ \boldsymbol{w} \in \mathcal{U} \setminus \mathcal{Q} \text{ and } q \in \mathcal{P}, \tag{4.1}$$

where $\mathcal{U}, \mathcal{P}$ denote appropriate function spaces for the test functions $\boldsymbol{w}$ (displacement $\boldsymbol{u}$) and q (pressure p) and $\mathcal{Q}$ denotes the space of orthonormal rotations and translations. The problem is set up to solve for the physical displacement $\boldsymbol{u}$ and the hydrostatic pressure p. The system is defined over the initially ungrown reference domain Ω_X. $\boldsymbol{P}$ represents the first Piola-Kirchhoff stress tensor and is dependent on the deformation gradient $\boldsymbol{F}$ and the pressure in the continuum body. Subscript $\mathbf{X}$ of ∇ denotes that derivatives of the gradient are defined with respect to the material coordinates. J denotes the determinant of the deformation gradient $\boldsymbol{F}$ and provides information on the volume change due to growth and the subsequent elastic deformation from a continuity constraint.

4.2.2 Kinematic Equations for Growth

The kinematic growth approach represents one of the two traditional theories for computational modelling of growth, the other being the constrained mixture theory [201,114]. This postulate provides an easy parameterisation of the material and the usage of phenomenological rate equations to interpret the growth process. An accepted belief is the existence of a stress-free intermediate grown reference configuration, which was

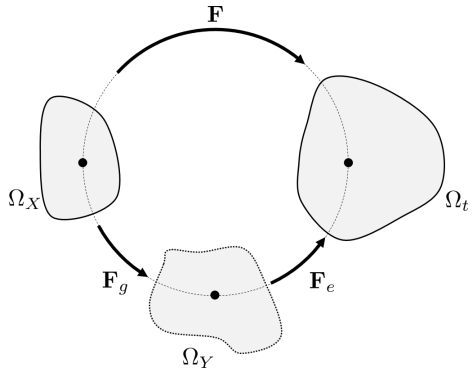

Figure 4.2 Schematics of multiplicative decomposition of $\boldsymbol{F}$ into an elastic ($\boldsymbol{F}_e$) and inelastic deformation gradient ($\boldsymbol{F}_g$).

mathematically confirmed by Goodbrake et al.[87].

Based on this assumption, a multiplicative decomposition of the deformation gradient $\boldsymbol{F}$ into its elastic and inelastic parts (Figure 4.2) leads to

$$\boldsymbol{F} = \boldsymbol{F}_e \cdot \boldsymbol{F}_g. \tag{4.2}$$

Here, $\boldsymbol{F}_g$ denotes the growth from an initial traction-free configuration ($\Omega_{\mathbf{X}} \subset \mathbb{R}^3$) to an intermediate local stress-free state ($\Omega_Y \subset \mathbb{R}^3$). The elastic part ($\boldsymbol{F}_e$) of the deformation gradient maps the intermediate state to the physical configuration and ensures the continuity of the body. By enforcing a continuity constraint on the body, residual stress may be introduced. This stress links with another important G&R parameter which is the degree of incompatibility, quantifying incompatibility following a growth process, where the measured geometric G&R process fails to reflect the kinematic growth tensors applied G&R field, provides an opportunity to understand growth-induced residual stress in the heart. From a mathematical perspective a compatible kinematic growth tensor can be rewritten as the gradient of the inelastic mapping, while, in the incompatible case, a direct mapping through a tensor gets lost. The proposed definition for compatibility is only true in the grown unloaded state and is based on the assumption that a compatible growth deformation holds

$$\boldsymbol{F}_e = \boldsymbol{F} \cdot \boldsymbol{F}_g^{-1} = \boldsymbol{I}. \tag{4.3}$$

Deviations from the introduced compatibility (Equation 4.3) are defined by the degree of incompatibility in the region of interest, such that The following metric was utilised to determine if a grown body is compatible or incompatible,

$$e_{inc} = \frac{||\boldsymbol{F}\boldsymbol{F}_g^{-1} - \boldsymbol{I}||}{||\boldsymbol{F}|| \cdot ||\boldsymbol{F}_g^{-1}|| + \sqrt{\mathrm{tr}\boldsymbol{I}}}, \tag{4.4}$$

where $e_{inc} \geq 0$ is associated with the degree of incompatibility following growth. In the

case $e_{inc} = 0$, the system is compatible, which means the kinematic growth tensor is the same as the deformation gradient $\boldsymbol{F}$. Whereas the upper bound for incompatibility is represented by $e_{inc} \leq 1$. Since the elastic deformation is the sole contributor to the mechanical problem, Equation 4.1 can be mapped from the reference domain to the intermediate state. Additionally, the deformation gradient is substituted with its multiplicatively-decomposed parts.

In the heart, two G&R modes can be identified, concentric and eccentric hypertrophy. Concentric growth behaviour is often seen as a typical response to an elevated afterload in the heart, whereas eccentric hypertrophy aims to compensate for a volume overload inside the ventricle. These G&R modes can be generally regarded as

$$\boldsymbol{F}_g = \boldsymbol{F}_g = \vartheta_{\boldsymbol{f}} \mathbf{e}_{\boldsymbol{f}} \otimes \mathbf{e}_{\boldsymbol{f}} + \vartheta_{\boldsymbol{s}} \mathbf{e}_{\boldsymbol{s}} \otimes \mathbf{e}_{\boldsymbol{s}} + \vartheta_{\boldsymbol{n}} \mathbf{e}_{\boldsymbol{n}} \otimes \mathbf{e}_{\boldsymbol{n}}, \tag{4.5}$$

where $\boldsymbol{f}$ defines the orientation of the myocyte and is defined using a rule-based method[55], Figure 4.3 left. The sheet vector $\boldsymbol{s}$ describes the alignment of the cell bundles, and $\boldsymbol{n}$ is the sheet plane normal direction; ϑ_i with $i = \boldsymbol{f}, \boldsymbol{s}, \boldsymbol{n}$ represents the growth factor in each individual direction. Concentric hypertrophy leads to an increase in wall thickness, which can be defined by setting the growth multiplier in the myocytes' radial direction $\vartheta_{\perp} > 1$ and keeping $\vartheta_{\boldsymbol{f}} = 1$. In contrast, eccentric G&R causes growth along the axial direction of the fibres with $\vartheta_{\boldsymbol{f}} > 1$ and the axial components remaining 1. The value for the individual growth multiplier can be defined using ordinary differential equations as G&R laws. However, for this study, they were set to be constant value fields and applied iteratively to converge.

4.2.3 Material Law, Boundary Conditions, and G&R Problem

Hypertrophy was analysed and investigated at the final grown state in a patient-specific biventricular (BiV) mesh. The geometry was created from neural network-generated segmentations of SSFP images from a patient with hypertrophic cardiomyopathy. From these segmentations, a BiV model template was fit to the segmented contours of the left and right ventricles as well as valve landmarks[163]. To generate local muscle fibre directions, a rule-based fibre field was created using the Laplace-Dirichlet method, proposed by both Doste et al.[55] and Bayer et al.[26]. Fibre angles varied from -60 deg to 60 deg and -25 deg to 90 deg from the epicardium to endocardium in the LV and RV, respectively. Fibre angles at the valve annuli were determined based on high-resolution DTI measurements from ex-vivo porcine hearts. Across the septum, fibres transitioned between 60° at the LV endocardium to 0° at the midwall to 90° at the right ventricle (RV) endocardium.

The presented simulations compare a Neo-Hookean material model (with a bulk modulus $\mu = 30$[kPa]) with the Holzapfel-Ogden cardiac model[110] (with $a = 2, b = 5, a_{\boldsymbol{f}} = 10, b_{\boldsymbol{f}} = 7.5, a_{\boldsymbol{s}} = 0, b_{\boldsymbol{s}} = 0, a_{\boldsymbol{fs}} = 0, b_{\boldsymbol{fs}} = 0$). Parameters a are stress-like parameters

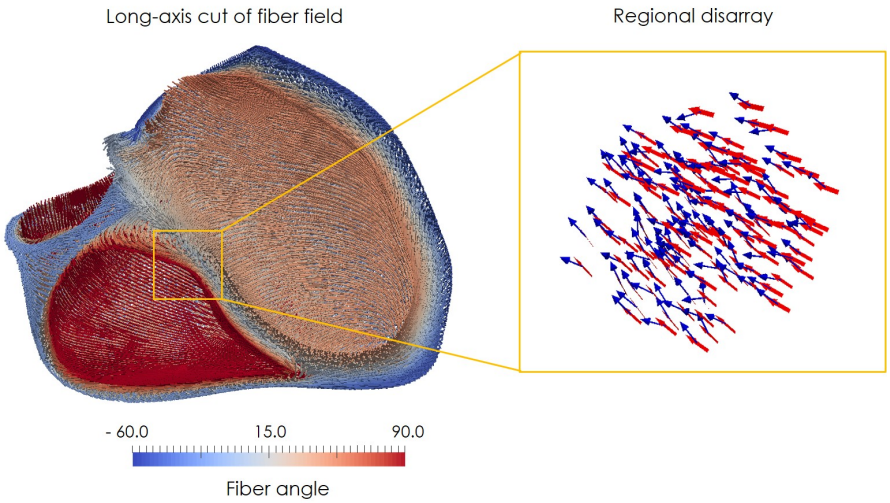

Figure 4.3 Left: Fibre angle of the field with respect to the local circumferential direction. Right: Regional disarray of the myocytes in the septal region. red arrows: fibres are aligned in the septum; blue arrows: disarray of the fibres.

in [kPa] while b are unitless scalar values. The utilised cardiac law takes into consideration the increased stiffness along the fibre direction ($a_{\boldsymbol{f}}, b_{\boldsymbol{f}} > 0$) and assumes no enhanced stiffness rates along the radial direction of the myocytes ($a_{\boldsymbol{s}}, b_{\boldsymbol{s}}, a_{\boldsymbol{fs}}, b_{\boldsymbol{fs}} = 0$). Both of the material laws are assumed to be nearly incompressible. The following test cases modify the global growth tensors of concentric and eccentric hypertrophy with the aim of recreating growth patterns observed in HCM. We note that the G&R simulated is driven by $\vartheta_{\boldsymbol{f}}$ and $\vartheta_{\perp}$ in these test cases and are not optimised to simulate patient data. Instead, these parameters are chosen and pushed to examine the influence of these mechanisms to meet the current objective of recreating an asymmetrical growth pattern in the septal area of a BiV geometry.

Simulations of the test cases were run both with and without regional disarray introduced in the interventricular septum. The remodelling of the fibre orientation was achieved by adding stochasticity to the mean fibre $\boldsymbol{f}_0$ and sheet direction $\boldsymbol{s}_0$, which leads to a modification of the growth tensor in the defined septal region (Figure 4.3). In this region, a new mean fibre, $\boldsymbol{f}_0'$ was defined whereby

$$\boldsymbol{f}_0'(\mathbf{X}) = \boldsymbol{f}_0(\mathbf{X}) + aw(\mathbf{X})\boldsymbol{b}(\mathbf{X}). \tag{4.6}$$

Here $w : \Omega_X \to \mathbb{R}$ is a weighting function $w(\mathbf{X}) \in [0, 1]$ defining the region of disarray, $a \in [0, 1]$ defining the degree of disarray, and $\boldsymbol{b} : \Omega_X \to \mathbb{R}^3$ is a vector where $\boldsymbol{b}(\mathbf{X})$ is a random vector on the unit sphere. Equation 4.6 provides a general formulation for adding stochasticity to the fibre field in the septal region (and similarly for the sheet vector, with the normal vector generated as the cross product of the two). Note that the vectors from Equation 4.6 are subsequently normalised so that unit vectors are utilised in the G&R and constitutive models.

To examine different potential explanations for the localised growth observed in HCM, three test cases are considered. **Test case 1** concentrates on the influence of disarray in the septal area to recreate a septal G&R pattern seen in HCM. For this, a homogeneous global growth tensor (eccentric or concentric) is applied to the BiV geometry. **Test case 2** explores the impact of spatially heterogeneous growth tensors with a variation of the growth multipliers in the LV septal region. The theory behind this test case is that the septum's diseased area reacts with higher amounts of growth than the remote area to global G&R drivers. For this study, the first test case was extended doubling the growth factor in the septal region only. Finally, **test case 3** investigates the influence of a spatially heterogeneous growth tensor, particularly with an isotropic regional growth tensor in the septum. The theory is that a consequence of factors in the tissue may drive G&R in equal amounts in all microstructural directions (e.g. inflammation). Computationally this behaviour is imitated by an adaptation of Equation 4.5, where ϑ^i with $i = \boldsymbol{f}, \boldsymbol{s}, \boldsymbol{n}$ is defined in all directions equally in the septal region and using an eccentric or concentric growth stimulus outside of the septal area.

4.3 Results and Discussion

Figure 4.4 illustrates some of the permutations of G&R applied in a BiV geometry with a Neo-Hookean material. Each test contains data from eccentric and concentric growth modes and further compares the simulations' displacement magnitudes. Table 4.1 includes the values for the wall thickness in the septal region after growth was applied and the percentage change relative to the initial wall thickness (7.74[mm]) for the isotropic Neo-Hookean and the orthotropic Holzapfel-Ogden material law. The reference values refer to continuous G&R modes applied to the geometry and are used to identify the difference between HCM-triggered growth with disarray and growth due to increased loading.

Table 4.1 Septal wall thickness t (mm) after growth and change as a percentage t% of the original thickness for the reference simulations and the defined test cases with disarray and isotropic and cardiac material law, where SN and F represent concentric and eccentric growth respectively.

Neo-Hookean

	Reference		Test case 1		Test case 2		Test case 3	
	SN	F	SN	F	SN	F	SN	F
t	9.59	8.61	9.66	8.50	11.19	9.00	12.56	11.65
t%	123.86	111.17	124.68	109.73	144.45	116.22	162.19	150.39

Holzapfel-Ogden

	Reference		Test case 1		Test case 2		Test case 3	
	SN	F	SN	F	SN	F	SN	F
t	9.78	8.57	9.79	8.46	11.25	8.97	12.34	10.67
t%	126.25	110.68	126.44	109.26	145.27	115.83	159.39	137.97

The left column in Figure 4.4 visualises the first test case, with a spatially homogeneous growth tensor (concentric or eccentric) applied over the entire geometry. The significant aspect of this simulation is the introduced disarray in the predefined septal region.

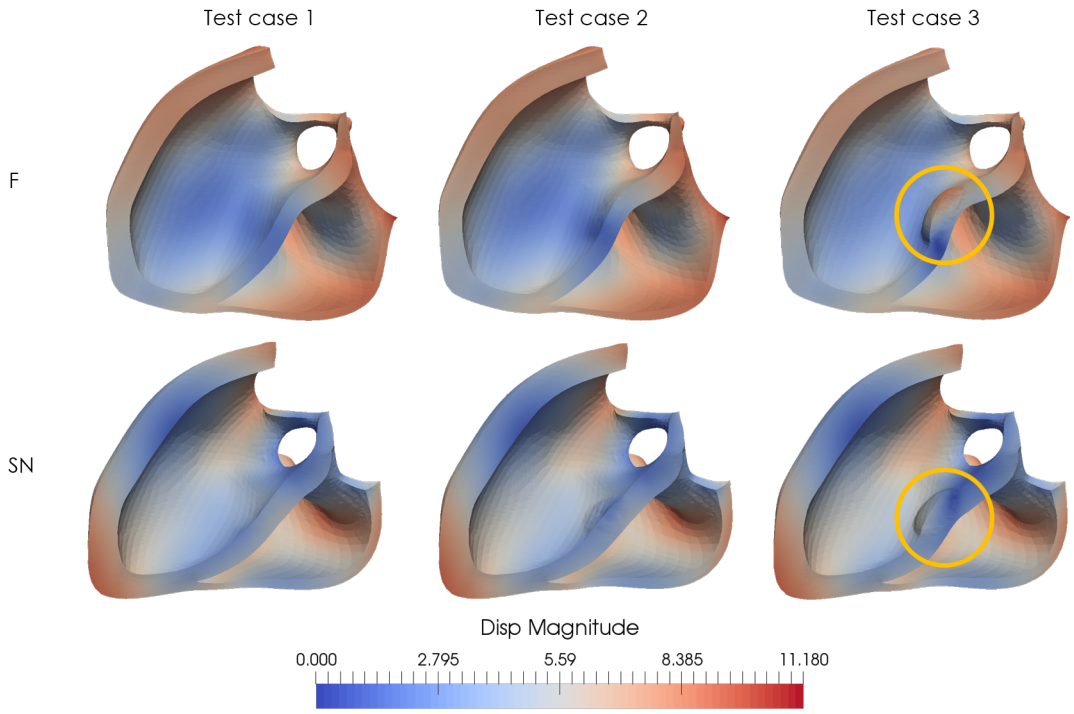

Figure 4.4 Comparison of the displacement magnitude (mm) between three separate test cases and the applied G&R types utilising a Neo-Hookean material law. Yellow circles highlight a septal growth pattern in the LV.

Neither the eccentric nor the concentric growth type showed clear manifestation of septal growth pattern. Table 4.1 additionally reveals that eccentric G&R (F) in this test results in dilation of the septal wall compared to the reference simulation. Our results in this case do not support the theory that regional hypertrophy in HCM is caused by regional disarray alone.

Simulations with disarray and a spatially heterogeneous growth tensor with higher amounts of growth in the septal region (middle column Figure 4.4) failed to reproduce a septal growth pattern. However, looking at this test case in Table 4.1, the value for the wall thickness in the SN growth case shows a difference of around 1mm compared to the reference G&R case.

In comparison to the first two test cases, the right panel in Figure 4.4 displays the application of a heterogeneous growth tensor with isotropic growth in the septal area. With concentric and eccentric G&R, the geometry exhibited growth patterns typical to the ones seen in septal HCM. Across the different test cases the difference between the two laws showed minimal deviation of the septal thickness except in test case 3, eccentric growth with disarray exhibited a difference of around 1[mm] (Table 4.1). Figure 4.5 illustrates the difference of displacement between the isotropic Neo-Hookean and the orthotropic Holzapfel-Ogden material law in the G&R simulation test case 3, eccentric G&R. The left image visualises the Neo-Hookean's (dark red) and Holzapfel-Ogden (grey-semitransparent) grown states compared to each other. The figure shows that

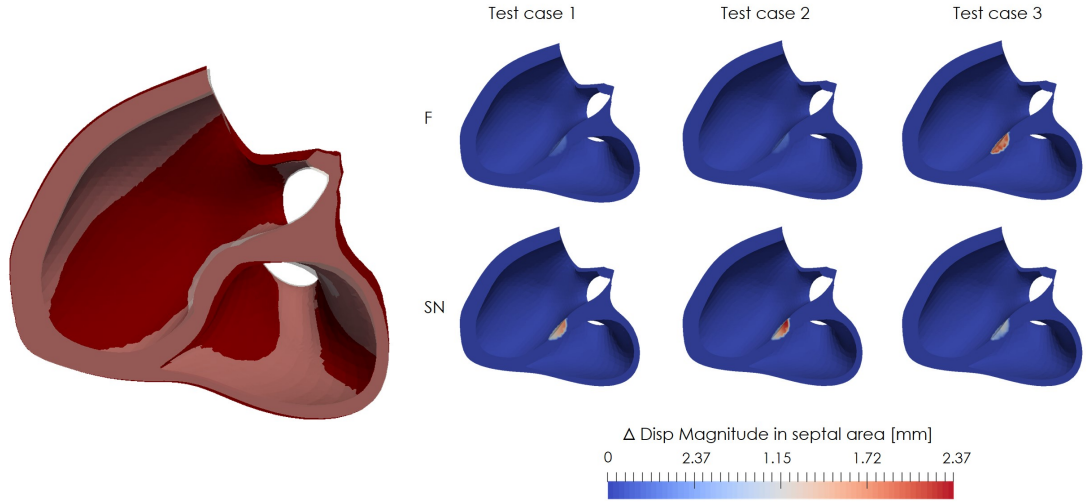

Figure 4.5 Left: Long axis cut of eccentric growth in test case 3 to compare Neo-Hookean and Holzapfel-Ogden material law. dark red: Neo-Hookean geometry, grey-semitransparent: Holzapfel-Ogden body. Right: Illustrates the difference in the displacement magnitude between the two constitutive laws in the septal region.

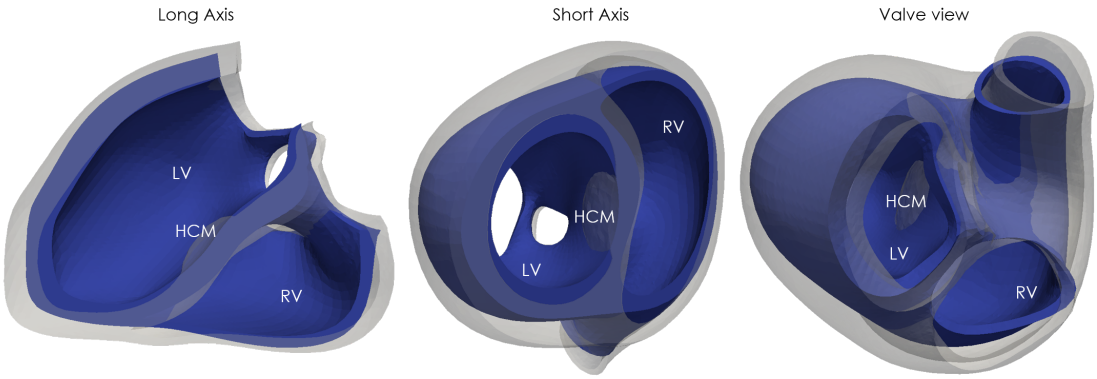

Figure 4.6 Concentric growth tensor with isotropic growth in the septal region of the LV, viewed from different orientations. blue: reference geometry, grey-semi-transparent: grown body.

both material laws are somewhat prone to buckle into the LV instead of solely increasing the mass in the septal region. Yet, it appears that the cardiac material tends to buckle more to hold Equation 4.1. The right-hand side illustrates the difference in displacement magnitude between material laws for the individual test cases and G&R modes focusing on the septal region. In the eccentric case of test case 3, a continuous difference of the displacement magnitude over the septal area can be observed. In contrast, across the test cases, the concentric growth modes seem to exhibit higher differences towards the base. Figure 4.6 illustrates a concentric growth tensor with isotropic growth in the septal region, equivalent to the test case in the bottom right corner in Figure 4.4. This image indicates that with higher amounts of growth in the septal area, the septum's hypertrophic tissue starts to develop an LVOTO.

Figure 4.7 summarises the incompatibility metric e_{inc} in the septal region of the heart

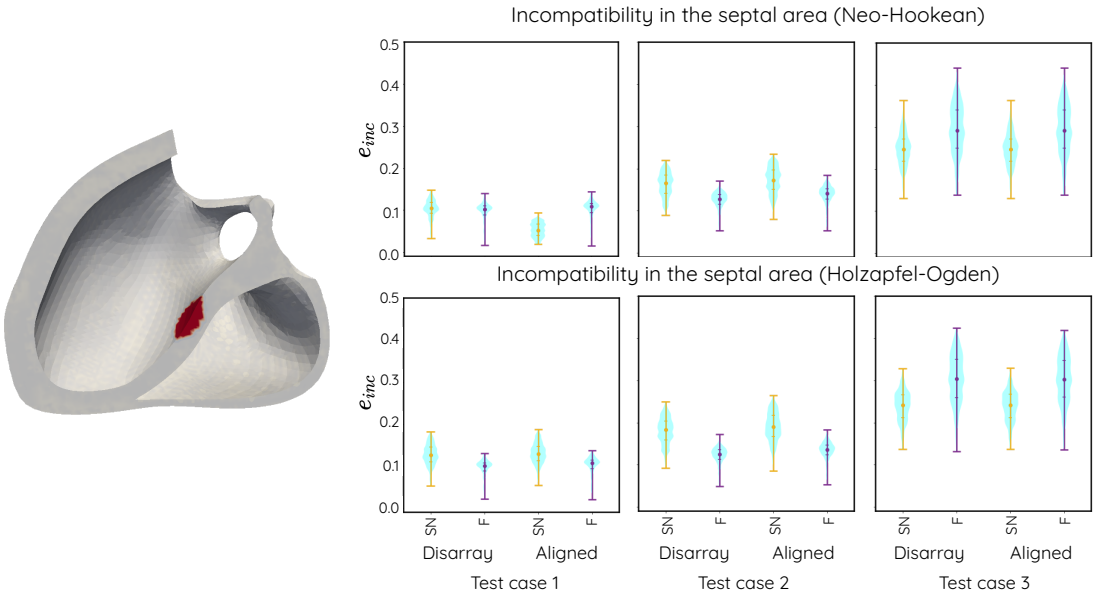

Figure 4.7 Incompatibility in the septal region (red area in the left image) over all test cases utilising Neo-Hookean and Holzapfel-Ogden material law, defined with the incompatibility metric e_{inc} defined in Equation 4.4.

in the various test cases with and without regional disarray and enables an objective way to compare the generated residual stresses across simulations and material laws. Noticeable is that disarray in the heart's septal region has little impact on the degree of incompatibility. Given these simulation results, incompatibility is dependent on the type of growth tensor applied to the geometry. The highest incompatibility was seen in the third test case, indicating a high level of residual stress generated in the septal region by growth.

One of the limitations of this study is due to the simplification of the G&R law. Utilising a constant G&R law to model G&R in HCM disregards growth drivers such as pressure or strain in the tissue that might also introduce hypertrophic patterns. Physiological G&R laws will be implemented in subsequent studies.

4.4 Conclusion

With homogeneous growth, disarray alone within the septal region did in neither of the material laws result in septal growth patterns observed in HCM patients. In contrast, regional isotropic growth in the septal area did result in regional hypertrophy. This observation supports the idea that hypertrophy in the septum may not be driven by the fibre structures disruption but rather by focal fibrosis and inflammation.

5 Computational Study of Growth and Remodelling following AVR

Growth and remodelling (G&R) commonly occur in response to changes in hemodynamic loading conditions. Pathological hypertrophy can result from various underlying reasons, including aortic stenosis (AS) which occurs when the aortic valve (AV) calcifies over time leading to a high pressure gradient between the left ventricle (LV) and the aorta. The resulting increase in systolic LV pressure and stroke work triggers the myocardial tissue to adapt its structure and function to maintain cardiac output. If left untreated, AS can ultimately lead to heart failure (HF). Aortic valve replacement (AVR) is a common treatment for this condition where the heart reacts with an immediate drop of pressure in the LV cavity and over time with G&R. While the wall thickness decreases during cases of reverse growth, our understanding of underlying G&R modes that resemble the observed reverse growth during this process remains incomplete. Utilising the kinematic growth theory provides a powerful way to understand reverse growth following AVR. Within this study, we introduce a computational modelling pipeline for patient-specific data to examine, unloading and regional reverse growth within the heart. Furthermore, we compare different metrics of the pre-surgery and post-surgery imaging data with the modelled post-surgery results to identify potential G&R modes reflecting changes seen from imaging. The results of this study indicated that concentric G&R may be a common growth pattern in patients following AVR. In contrast, no specific growth pattern could be associated with adverse growth.

This chapter is an article which is in submission:
Sandra P. Hager, Will Zhang, Marc Hirschvogel, Javiera Jilberto Vallejos, Jack Lee, David A. Nordsletten. "Computational Study of Growth and Remodelling following AVR".

5.1 Introduction

Aortic stenosis (AS) is the most prevalent valvular heart disease in Europe and North America, with a rapidly rising prevalence due to ageing[230,226]. AS progresses with

initial plaque formation in the valve area and transitions into calcification over time[71]. As calcification limits normal valvular dynamics, the pressure gradient between the aorta and the left ventricle (LV) increases, and the ejection fraction (EF) decreases. In response, the heart reacts by undergoing growth and remodelling (G&R) processes in the ventricles[198]. Early stages of AS result in increased wall thickness (concentric hypertrophy) in the LV. Eventually, the LV starts to dilate (i.e. eccentric growth) to compensate for the change in loading conditions in the heart. Treatment methods aim to restore normal valve function and facilitate ventricular reverse remodelling[151]. In this study, we focus on the ventricular reverse remodelling processes triggered by transcatheter aortic valve replacement TAVR and surgical aortic valve replacement (SAVR).

Computational methods represent powerful tools to close the gap between observed G&R phenomena and the underlying mechanisms for this behaviour. Common theories to model G&R are the kinematic[201] and the constrained mixture[114] approach and combinations of both methods (homogenized constrained mixture[46]). The generalised approach of the constraint mixture theory accounts for different turnover rates (dynamics of death and regeneration) of the individual constituents in the tissue. Still, the amount of information necessary to utilise this method for ventricular hypertrophy can not be extracted from medical images alone, making their application challenging. An alternative is the phenomenological approximation of G&R via the kinematic approach, which models volumetric growth in the tissue through a multiplicative split of the deformation gradient into elastic and inelastic components.

The benefits of this method are the model simplicity and the relative availability of data necessary to build these models. In literature, numerical studies indicate a good agreement between patient-specific G&R and computational prediction. Applications which modelled maladaptive cardiac G&R were made by Göktepe et al.[98] and Göktepe et al.[97] based on sarcomerogenesis and adaptation to elevated pressure or strain values in the tissue. By coupling a strain-based growth law with a closed-loop reduced-order model (hemodynamics), Kerckhoffs et al.[121] was able to model eccentric and concentric hypertrophy based on a single parameter. It is further possible to utilise the same framework to make predictions concerning a reduction of mass in the heart after a surgical or pharmaceutical intervention[145].

Even after identifying the mass changes in the heart, we do not have a clear understanding of regional changes in the tissue. The implementation of a kinematic growth tensor, for cardiac tissue, is defined by growth along the microstructure. However, we do not know if the observed growth pattern can be really simulated by applying G&R in these directions. In addition to not having a clear idea of the regional growth tensor definition, utilising the kinematic growth theory to simulate G&R in the heart may introduce kinematic incompatibilities and residual stresses. Research on this type of

introduced incompatibilities following growth is still limited.

In this study, we are trying to understand underlying G&R processes in the heart following surgical treatment. To accomplish this, we are utilising pre-operative data and applying different modes of growth and comparing them to the post-operative data. This workflow accounts for the different loading states between the pre-and post-operative and focuses on adverse growth within three separate myocardial compartments, left ventricular free wall (LVFW), right ventricular free wall (RVFW) and septum with also accounting for changes of the loading following AVR. Furthermore, we analysed the incompatibility state of the differently modelled post-AVR states to assess regional changes in stress and strain within the body.

Section 5.2 introduces necessary kinematics and kinetics of cardiac growth and the application towards patient-specific modelling. In Section 5.3, we summarise and visualise the outcome of the mass, cavity volume and morphological changes computed by the presented pipeline. In the discussion section (Section 5.4), we statistically analyse the key outcomes of ventricular reverse growth following AVR and what we can conclude from the result section, focussing on identifying the mode of RR following AVR. The limitations of this study are listed in Section 5.5.

5.2 Materials and Methods

In this section, we will focus on the concepts of cardiac biomechanics, G&R and propose a workflow to model morphological changes post-AVR. For this purpose, we will first state the relationship between cardiac biomechanics and growth and further adapt this concept in the different substeps of the pipeline. The pipeline focused on two essential goals: the generation of a personalised biomechanical pre-AVR model and the prediction of a modelled post-AVR state. The objective of the personalised biomechanical pre-AVR was to establish a comparative loaded state of the heart before surgery and identify the passive myocardial parameters. The personalised reverse growth component attempts to mimic reverse growth following AVR to generate a compatible post-AVR configuration comparable to that of the post-AVR structure extracted from the CT images.

5.2.1 Cardiac Biomechanics and Growth

5.2.1.1 Kinematics

This subsection reviews the classical kinematics and establishes the notation for the following sections for deformation in nonlinear mechanics[31,186,108]. Classical kinematics relates deformations in the heart related to the motion of material points from the reference configuration $\Omega_0 \subset \mathbb{R}^3$ to that of their physical configuration at time t, $\Omega_t \subset \mathbb{R}^3 \ \forall t \in [0, T]$. Thus, we use $\mathbf{X} \in \Omega_0$ to describe Lagrangian coordinates and similarly,

and $\boldsymbol{x} \in \Omega_t$ to denote material coordinates. Furthermore, these two fields are linked through a displacement field $\boldsymbol{u} \in \Omega_0 \times [0, T]$ such that $\boldsymbol{x}(\mathbf{X}, t) = \boldsymbol{u}(\mathbf{X}, t) + \mathbf{X}$. We also introduce the tensor $\boldsymbol{F}$ which denotes the deformation gradient and is defined as $\boldsymbol{F} = \partial(\boldsymbol{x})/\partial\mathbf{X} = \nabla_{\mathbf{X}}\boldsymbol{u} + \boldsymbol{I}$. $J = \det \boldsymbol{F} > 0$ indicates the volume change of a body. As it is common in literature, we assume our materials to be isochoric, although it should be noted that this has been called into question, see Avazmohammadi et al. [20]. To describe the internal strain, we use the Green-Lagrange strain tensor $\boldsymbol{E} = \frac{1}{2}(\boldsymbol{C} - \boldsymbol{I})$ with the right Cauchy-Green tensor $\boldsymbol{C} = \boldsymbol{F}^T\boldsymbol{F}$. To eliminate any coordinate system dependence, we can define a set of invariants of the Green-Cauchy stress tensor [108,40]

$$I_1(\boldsymbol{C}) = \mathrm{tr}\boldsymbol{C}, \tag{5.1}$$

$$I_2(\boldsymbol{C}) = \boldsymbol{C} : \boldsymbol{C}, \tag{5.2}$$

$$\text{and} \quad I_3(\boldsymbol{C}) = \det(\boldsymbol{C}). \tag{5.3}$$

Contrary to isochoric deformations, compressible hyperelasticity incorporates a multiplicative decomposition of $\boldsymbol{F}$ and $\boldsymbol{C}$ into a volume-changing and volume-preserving components, resulting in

$$\bar{\boldsymbol{F}} = J^{-1/3}\boldsymbol{F}, \quad \bar{\boldsymbol{C}} = J^{-2/3}\boldsymbol{C}. \tag{5.4}$$

The internal architecture in the myocardium resembles a sheet-like structure defined by an orthonormal basis $\{\boldsymbol{e}_\mathrm{f}, \boldsymbol{e}_\mathrm{s}, \boldsymbol{e}_\mathrm{n}\}$, with (f), (s) and (n) denoting cardiomyocytes, sheet and sheet-normal orientation, respectively [148]. To account for material anisotropy , e.g. cardiomyocytes, collagen, elastin, glycoproteins, and proteoglycans [71], we expand our set of invariants with additional terms which take into account the tissue architecture: such that

$$I_{ab} = \boldsymbol{C} : \mathrm{sym}(\mathbf{e}_a \otimes \mathbf{e}_b), \quad a, b \in \{\boldsymbol{f}, \boldsymbol{s}, \boldsymbol{n}\}. \tag{5.5}$$

When $\boldsymbol{a} = \boldsymbol{b}$, these terms gain the physical meaning of stretch along the $\boldsymbol{f}$, $\boldsymbol{s}$, $\boldsymbol{n}$, and, using the common literature notation, we refer these simply as

$$I_a = \mathbf{e}_a \cdot \boldsymbol{C}\mathbf{e}_a \quad a \in \{\boldsymbol{f}, \boldsymbol{s}, \boldsymbol{n}\}. \tag{5.6}$$

5.2.1.2 Cardiac Structure and Growth

In this subsection, we describe in detail the microstructure of the myocardium and show the relationship to well-established growth laws for cardiac tissue. Heart tissue exhibits a hierarchical architecture of fibres and sheets. Traversing the heart wall, from near the endocardium to epicardium, the fibre orientation ($\boldsymbol{f}$) in these regions undergoes a rotation in the transmural direction from $-60°$ to $+60°$, with respect to the local circumferential direction of the left ventricle [110]. The myocytes are further organised in a layered structure with endomysial collagen surrounding the fibre bundles, resulting

in a sheet-like architecture inside the tissue ($\boldsymbol{s}$). Orthogonal to the fibre and sheet direction is the sheet-normal axis ($\boldsymbol{n}$).

The kinematic G&R theory of Rodriguez et al.[201], based on the earlier work of Lee[142], factorises the elasto-plastic finite strains into elastic and plastic components $\boldsymbol{F} = \boldsymbol{F}_e\boldsymbol{F}_{plast}$. In the context of G&R, a similar form has been adopted (see Figure 5.1), where

$$\boldsymbol{F} = \boldsymbol{F}_e\boldsymbol{F}_g. \tag{5.7}$$

Here, the deformation gradient $\boldsymbol{F}$ denotes the mapping of a material point in the reference configuration $\mathbf{X} \in \Omega_0 \subset \mathbb{R}^3$ to a point in the grown unloaded physical configuration $\boldsymbol{x} \in \Omega_t \subset \mathbb{R}^3$, see Figure 5.1. $\boldsymbol{F}_g$ defines the kinematic growth tensor denoting and describes a mapping between a material point in the reference configuration to a point in the fictitious grown configuration following point-wise deformation (e.g. growth or atrophy), with a coordinate system defined as $\mathbf{X}_g \in \Omega_g \subset \mathbb{R}^3$. Noteworthy, $\boldsymbol{F}_g$ can be both anisotropic and spatially heterogeneous. In Chapter 3, the latter property was identified as being the potential cause of incompatibilities and residual stresses in the body. $\boldsymbol{F}_e$ denotes the elastic components of the deformation which are the sole contributor to the strain-energy function, describing the mapping between a point in the fictitious grown configuration to the physical configuration $\boldsymbol{x} \in \Omega_t \subset \mathbb{R}^3$.

Supposed that $\boldsymbol{F}_g$ introduces a compatible grown state in a body without any external load, then no additional residual stress is considered to be introduced in the body and the elastic deformation $\boldsymbol{F}_e = \boldsymbol{I}$ and associated with

$$\boldsymbol{F}_e = \boldsymbol{F} \cdot \boldsymbol{F}_g^{-1} = \boldsymbol{I}. \tag{5.8}$$

The following metric was utilised to determine if a grown body is compatible or incompatible,

$$e_{inc} = \frac{||\boldsymbol{F}\boldsymbol{F}_g^{-1} - \boldsymbol{I}||}{||\boldsymbol{F}|| \cdot ||\boldsymbol{F}_g^{-1}|| + \sqrt{\mathrm{tr}\boldsymbol{I}}}. \tag{5.9}$$

Where $e_{inc} \geq 0$ is associated with the degree of incompatibility following growth. In the case $e_{inc} = 0$, the system is compatible, which means the kinematic growth tensor is the same as the deformation gradient $\boldsymbol{F}$. Whereas the upper bound for incompatibility is represented by $e_{inc} \leq 1$.

Cardiac hypertrophy can have different causes, from genetic drivers such as hypertrophic cardiomyopathy to chronically overloaded states[180]. Pathological growth is commonly[81,98,121] modelled using one of three distinct modes: concentric, eccentric or isotropic. Concentric hypertrophy describes the process in which free sarcomeres start aligning parallel to the organised sarcomeres, resulting in an increase in thickness for the myocytes and an increase in the ventricular wall thickness. A serial addition of free sarcomeres in the meantime leads to an elongation of the myocyte fibres and, conse-

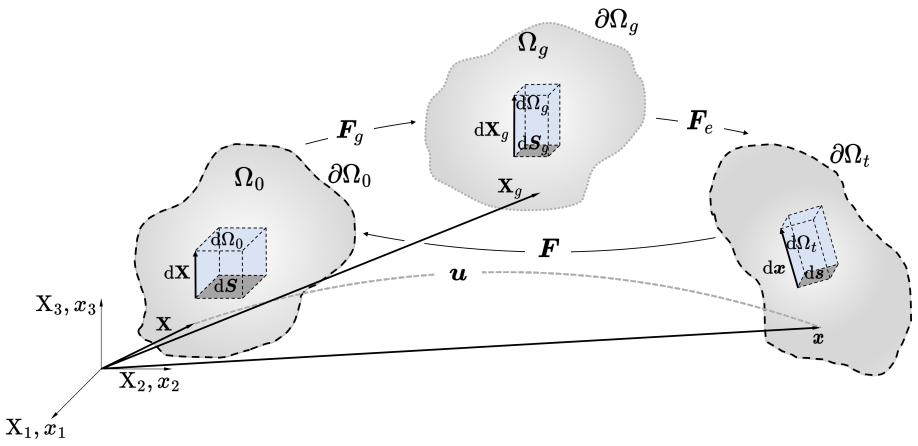

Figure 5.1 Kinematics within deformed bodies, with the reference domain Ω_0, bounded by $\partial\Omega_0$, the physical domain Ω_t, bounded by $\partial\Omega_t$ and the virtual growth domain Ω_g, bounded by $\partial\Omega_g$ that are linked via the deformation gradient $\boldsymbol{F}$, the growth deformation gradient $\boldsymbol{F}_g$ and the elastic deformation gradient $\boldsymbol{F}_e$.

quently, a lengthening of the ventricle, referred to as eccentric growth[71]. In contrast to concentric and eccentric growth, where hypertrophy is directly related to changes in the fibres' radial or axial direction, isotropic hypertrophy is not associated with a clear defined growth direction. This type of growth could occur due to swelling, fibrosis and other underlying processes in the myocardium.

A generic growth tensor for cardiac tissue links changes of the macroscale to adaptions in the microscale, and can be described as

$$\boldsymbol{F}_g = \vartheta_{\boldsymbol{f}}\mathbf{e}_{\boldsymbol{f}} \otimes \mathbf{e}_{\boldsymbol{f}} + \vartheta_{\boldsymbol{s}}\mathbf{e}_{\boldsymbol{s}} \otimes \mathbf{e}_{\boldsymbol{s}} + \vartheta_{\boldsymbol{n}}\mathbf{e}_{\boldsymbol{n}} \otimes \mathbf{e}_{\boldsymbol{n}}. \tag{5.10}$$

Here the ϑ_i, with $i = \boldsymbol{f}, \boldsymbol{s}, \boldsymbol{n}$, measures growth along the local myocyte direction $\{\mathbf{e}_{\boldsymbol{f}}, \mathbf{e}_{\boldsymbol{s}}, \mathbf{e}_{\boldsymbol{n}}\}$. This general definition can be further adapted to describe specific modes of G&R. Thus, to simulate the changes referring to sarcomeres adding parallel inside the fibres (concentric) we adapt $\boldsymbol{F}_g$ to the more specific definition

$$\mathbf{F}_{g,\mathrm{con}} = \mathbf{e}_{\boldsymbol{f}} \otimes \mathbf{e}_{\boldsymbol{f}} + \vartheta_{\perp}(\mathbf{e}_{\boldsymbol{s}} \otimes \mathbf{e}_{\boldsymbol{s}} + \mathbf{e}_{\boldsymbol{n}} \otimes \mathbf{e}_{\boldsymbol{n}}). \tag{5.11}$$

Where $\vartheta_{\perp}$ represents a combined factor or radial growth in the directions $\{\mathbf{e}_{\boldsymbol{s}}\mathbf{e}_{\boldsymbol{n}}\}$. The first term $\{\mathbf{e}_{\boldsymbol{f}} \otimes \mathbf{e}_{\boldsymbol{f}}\}$, has a unit scaling to indicate the absence of growth in the direction. Mimicking elongation (eccentric growth) of the heart is assumed to solely affect the defined fibre field[55] along the fibre axis $\{\mathbf{e}_{\boldsymbol{f}}\}$, resulting in

$$\boldsymbol{F}_{g,\mathrm{ecc}} = \vartheta_{\boldsymbol{f}}\mathbf{e}_{\boldsymbol{f}} \otimes \mathbf{e}_{\boldsymbol{f}} + \mathbf{e}_{\boldsymbol{s}} \otimes \mathbf{e}_{\boldsymbol{s}} + \mathbf{e}_{\boldsymbol{n}} \otimes \mathbf{e}_{\boldsymbol{n}}, \tag{5.12}$$

with $\vartheta_{\boldsymbol{f}}$ being a measure of G&R in the fibre direction. During isotropic growth (e.g. during swelling), we assume that the tissue starts extending in all spacial directions

with the same growth factor $\vartheta_{\text{iso}} > 1$, such that

$$\mathbf{F}_{g,\text{iso}} = \vartheta_{\text{iso}}(\mathbf{e}_{\boldsymbol{f}} \otimes \mathbf{e}_{\boldsymbol{f}} + \mathbf{e}_{\boldsymbol{s}} \otimes \mathbf{e}_{\boldsymbol{s}} + \mathbf{e}_{\boldsymbol{n}} \otimes \mathbf{e}_{\boldsymbol{n}}). \tag{5.13}$$

In the case of growth, the G&R related parameter $\vartheta_i > 1$ along the $\mathbf{e}_i$ direction. More generally, the parameter can also be used to indicate the absence of growth, $\vartheta_i = 1$, or reverse growth, $\vartheta_i < 1$

5.2.1.3 Cardiac Kinetics

In the case of incompatible growth, stresses are introduced to the body with respect to the intermediate grown Ω_g to the physical domain Ω_t. Commonly, a mechanical problem can be described via the kinematic and kinetic tensors of the deformation, e.g.

$$\boldsymbol{F} = \frac{\partial \boldsymbol{x}}{\partial \mathbf{X}}, \quad \boldsymbol{C} = \boldsymbol{F}^T\boldsymbol{F}, \quad \boldsymbol{P} = \frac{\partial \Psi(\boldsymbol{F})}{\partial \boldsymbol{F}}. \tag{5.14}$$

By additionally introducing growth, these tensors can be reformulated with respect to the intermediate grown domain, leading to

$$\boldsymbol{F}_e = \frac{\partial \boldsymbol{x}}{\partial \mathbf{X}_g}, \quad \boldsymbol{C}_e = \boldsymbol{F}_e^T\boldsymbol{F}_e, \quad \boldsymbol{P}_e = \frac{\partial \Psi(\boldsymbol{F}_e)}{\partial \boldsymbol{F}_e}. \tag{5.15}$$

With the deformation gradient $\boldsymbol{F}_e = \boldsymbol{F}\boldsymbol{F}_g^{-1}$ and the Jacobian of the deformation gradient $J_e = J/J_g$. The balance laws of mass and momentum of the grown domain, in an incompressible body following growth, lead to

$$\nabla_{\mathbf{X}_g} \cdot \boldsymbol{P}_e + \boldsymbol{b}_e - \frac{\partial(\rho \boldsymbol{v}_e J_e)}{\partial t} = \mathbf{0} \quad \text{on } \Omega_g \tag{5.16}$$

$$J_e - 1 = 0. \quad \text{on } \Omega_g \tag{5.17}$$

Where $\nabla_{\mathbf{X}_g}$ is the gradient operator with respect to $\mathbf{X}_g$, and $\boldsymbol{b}_e = J_e\boldsymbol{b}$ is the jacobian-weighted body force.

Similarly, we can describe the first Piola-Kirchhoff stress tensor, $\boldsymbol{P}_e$ computed with respect to deformation quantities defined in the original reference domain, e.g.

$$\tilde{\boldsymbol{P}} = \left.\frac{\partial \Psi(\boldsymbol{F}_e)}{\partial \boldsymbol{F}_e}\right|_{\boldsymbol{F}_e = \boldsymbol{F}\boldsymbol{F}_g^{-1}}. \tag{5.18}$$

Utilising Nanson's formula combined with the Divergence theorem, we can state that

$$\nabla_{\mathbf{X}_g} \cdot \boldsymbol{P}_e = \nabla_{\mathbf{X}} \cdot (J_g \tilde{\boldsymbol{P}} \boldsymbol{F}_g^{-T}). \tag{5.19}$$

Combining the established relations with Equation 5.16 and 5.17, it is possible to define

the strong form of the balance laws of mass and momentum, e.g.

$$J_g \nabla_{\mathbf{X}} \cdot \left(J_g \tilde{\boldsymbol{P}} \boldsymbol{F}_g^{-T} \right) + J\boldsymbol{b} - \frac{\partial(\rho \boldsymbol{v} J)}{\partial t} = \mathbf{0} \quad \text{on } \Omega_0 \tag{5.20}$$

$$J - J_g = 0. \quad \text{on } \Omega_0 \tag{5.21}$$

The equation is now set up to run on the reference domain which means no explicit formation of Ω_g is needed to solve kinetics in the grown state.

In this study, we utilise a reduced Holzapfel-Ogden material law[100] to describe the passive behaviour of the myocardium in the nearly-incompressible formulation, such that

$$\begin{aligned} \Psi_{\mathtt{ho}} = \frac{k_1}{2k_2} \left[\exp^{k_2(I_1-3)} - 1 \right] + \sum_{i \in \{\boldsymbol{f},\boldsymbol{s}\}} \frac{k_{1_i}}{2k_{2_i}} \left[\exp^{k_{2_i}(I_i-1)^2} - 1 \right] \\ + \frac{k_{1_{\boldsymbol{fs}}}}{2k_{2_{\boldsymbol{fs}}}} \left[\exp^{k_{2_{\boldsymbol{fs}}} I_{\boldsymbol{fs}}^2} - 1 \right] - p(J-1). \end{aligned} \tag{5.22}$$

Here, k_{1_i}[kPa] and k_{2_i}[-] are material parameters associated to the fibre $\boldsymbol{f}$ or sheet $\boldsymbol{s}$ direction of the myocardium. While, p denotes the hydrostatic pressure, which also acts as a Lagrange multiplier to enforce incompressibility.

To solve the mechanics of the heart, a saddle point problem approach for a quasi-static system in the way Asner et al.[17] performed it was utilised. Where the displacement and pressure state variables have to satisfy the saddle point condition[31], such that $(\boldsymbol{u}, p) \in \mathcal{U} \setminus \mathcal{Q}$ and $p \in \mathcal{P}$,

$$\Pi_t(\boldsymbol{u}, p) = \inf\{\sup\{\Pi_t(\boldsymbol{w}, q), q \in \mathcal{P}\}, \boldsymbol{w} \in \mathcal{U}\}. \tag{5.23}$$

Here $\mathcal{U}, \mathcal{P}$ represent the function spaces of the displacement $\mathcal{U}$ and q (pressure p) and $\mathcal{Q}$ is the space of orthonormal rotations and translations. The total potential energy function $\Pi_t = \Pi_t^{\text{int}} + \Pi_t^{\text{ext}}$ is a combination of the internal (int) and external (ext) potential energy. Incorporating in the internal potential energy are the modified above mentioned kinematics the internal energy. Assuming a nearly incompressible material for the cardiac tissue and the sole mechanical contribution from the elastic part of the deformation gradient, with $\boldsymbol{F}_e = \boldsymbol{F}\boldsymbol{F}_g^{-1}$ and $J_e = JJ_g^{-1}$, such that

$$\Pi_t^{\text{int}}(\boldsymbol{u}, p) = \int_{\Omega_0} \Psi + p(JJ_g^{-1} - 1) \mathrm{d}\mathbf{X}. \tag{5.24}$$

Where, $\int_{\Omega_X}$ shows that the system is defined over the initially ungrown reference domain.

The external term in Equation 5.23 refers to boundary constraints of the mechanical

problem, leading to

$$\Pi_t^{\text{ext}}(\boldsymbol{w}, \boldsymbol{\mu}) = \sum_{k \in i} \Pi_t^{\text{k}}(\boldsymbol{w}, \boldsymbol{\mu}_k), \tag{5.25}$$

where $\boldsymbol{\mu}$ denotes the traction or pressure on the individual boundary domains Γ^i. Generally, in cardiac mechanic models, we assume a constant pressure inside the LV and the RV. In our study, we retrieve these pressures (P_{LV} and P_{RV}) from patient data and apply them as an endocardial traction force inside the cavities. In patient cases where no pressure values could be acquired, pressure changes were estimated by utilising cases with the equivalent amount of mass changes in the entire heart.

An additional boundary constraint, Neumann boundary condition, is applied to the valve surfaces. During parameter identification via Klotz-curve [125] and the loading of the LV and RV pre-AVR to the post-AVR pressures, the valves surfaces and midpoints are constrained against rotation and translation, in the way Kuchta et al. [130] introduced in their paper, such that

$$\int_{\partial\Omega_{\text{valve}}} f \mathrm{d}\boldsymbol{x} + \int_{\partial\Omega} h \mathrm{d}s = 0, \tag{5.26}$$

$$\int_{\partial\Omega_{\text{valve}}} f \times \boldsymbol{x} \mathrm{d}\boldsymbol{x} + \int_{\partial\Omega} h\boldsymbol{x} \mathrm{d}s = 0. \tag{5.27}$$

Here the f and h are the net force and the net torque, respectively, acting on $\partial\Omega_{\text{valve}}$ and giving a unique solution if and only if $f = 0$ and $h = 0$. The constraint was enforced by using a Lagrange multiplier and is in parallel solved during the parameter estimation and the pressure adaption problems. During the G&R part of the pipeline, a Dirichlet boundary condition with a penalty term is applied to the valve surfaces instead of the centre of mass Neumann boundary conditions in Equation 5.26 and 5.27. The displacement field for the boundary condition (BC) was extracted by running a surface registration algorithm with the group of all four valves of the Pre-AVR model valves registered to the Post-AVR valves via Amberg et al. [7].

5.2.2 Personalised biomechanical Pre-AVR model

This section's focus is creating a pipeline to model a personalised biomechanical Pre-AVR state, see Figure 5.2. Fast-evolving medical imaging techniques in computer tomography (CT) enable more detailed anatomical feature extraction for patient-specific models. However, the generation of geometrical models is only one of component for patient-specific simulations. Gaining insight into the loading conditions of the heart can be a challenging task. This can be achieved through invasive methods such as catheterisation or non-invasive methods such as echocardiography, both of which provide valuable information about the function of the heart. Pressure data and EF parameters can be accessed from patient sheets, allowing researchers to study the hemodynamic status of the heart in various conditions. The first part of the presented pipeline (see

Figure 5.2) in this paper targets to solve the challenge of identifying an unloaded reference configuration and establishing a parameter set for the cardiac material, resulting in a personalised biomechanical model for the pre-surgery state.

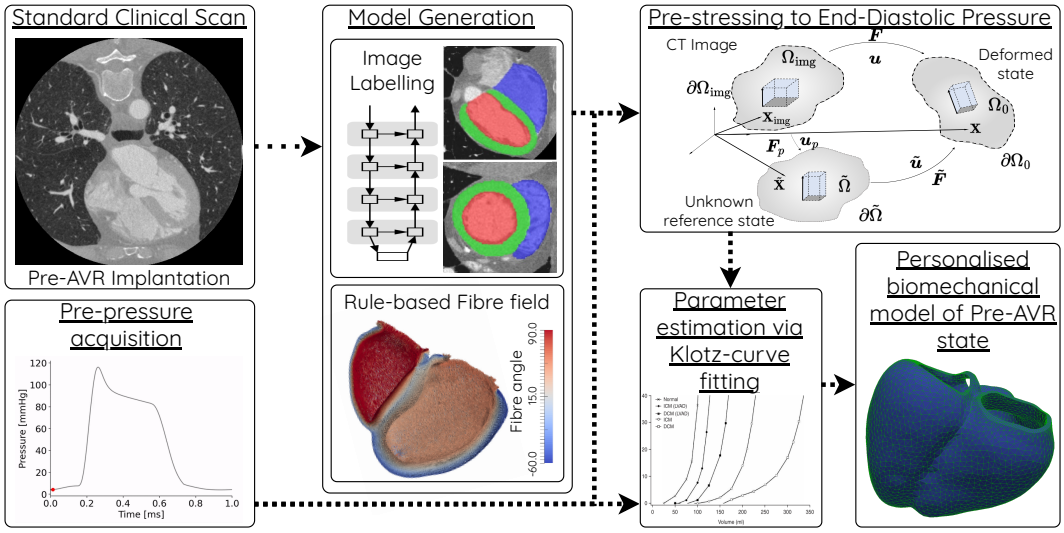

Figure 5.2 Personalised biomechanical model of the Pre-AVR state, enables the mimicking of the heart's behaviour during loading. This part of the workflow incorporates the residual stressing of the cardiac muscle and enables an estimation of the myocardial material parameters (a and a_f). The first stage of the pipeline incorporates the model generation, in which a U-Net neural network[245] was utilised to extract the labels for the various components of the heart. A fibre field was generated via a rule-based laplace problem[171]. The next step focuses on incorporating the residual stresses in the tissue via a Modified Updated Lagrangian Formulation (MULF) within an inverse mechanics problem[78]. Furthermore, the passive myocardium parameters were estimated via deflation along the Klotz-curve[125]. Combining the outcomes of MULF, Klotz-curve fitting and the pre-pressure acquisition, a personalised biomechanical model of the Pre-AVR state was developed.

5.2.2.1 Patient Cohort and Data Processing

This study consists of eight patients who underwent AVR surgery, for this, we collected CT and catheterisation data before and after intervention at end-diastole. The patient cohort was separated into the type of intervention the patient underwent (SAVR or TAVR) and further divided into a reverse and an adverse remodelling cohort. Patients who indicated a positive response, with a net reduction of mass are assigned to the reverse remodelling cohort. Whereas patients with a net increase of mass following AVR are classified as an adverse remodelling cohort. Clinical reasons for reverse remodelling or rehospitalization after 1-year post-Aortic Valve Replacement (AVR) due to heart failure (HF) occur at a rate of 6.7%, with 9.7% attributed to composite HF, valve-related, or procedure-related causes[113]. Table 5.1, includes the patient-specific metrics for a case with reverse growth (SAVR 1) and a case with adverse growth (SAVR 2). In some of the patients, the EDP for the LV or RV was not acquired during surgery (marked in brackets). In cases where the LV and RV pressures were not recorded, a pressure estimation was done by utilising patient data which indicated the same change

in EF or mass change of the heart.

Table 5.1 Patient characteristics from echocardiographic and catheterization data Pre- and Post-SAVR

(a) Patient characteristics from echocardiographic and catheterization data Pre-SAVR

	SAVR 1	SAVR 2
EF [%]	55	65
LV EDP [mmHg]	(30)	(21)
RV EDP [mmHg]	(11)	(17)
State of AV (stenosis)	severe	yes
State of MV (regurgitation)	mild	minimal
State of PV (regurgitation)	none	minimal
State of TV (regurgitation)	minimal	minimal
State of LV (size & function)	normal concentric hypertrophy	normal
State of RV (size & function)	normal	normal

(b) Patient characteristics from echocardiographic and catheterization data Post-SAVR

	SAVR 1	SAVR 2
EF [%]	-	65
LV EDP [mmHg]	(23)	(20)
RV EDP [mmHg]	(16)	(9)
State of AV (regurgitation)	-	none
State of MV (regurgitation)	-	moderate
State of PV (regurgitation)	-	none
State of TV (regurgitation)	-	mild
State of LV (function & size)	-	normal
State of RV (function & size)	-	normal
Days after surgery	133	70
Aortic root enlargement	yes	yes

A summary of the patient data acquired from catheterisation, echocardiography and computed tomography for all pre- and post-SAVR and TAVR patients can be found in the appendix, see Table 25 and 27 for the pre-AVR data and Table 26 and 28.

In the postoperative data set, static Computer tomography (CT) images were acquired during the end-diastolic time frame. These images were either taken by a GE Medical systems-Revolution CT (pre-AVR) or a GE Medical systems-Light speed VCT (post-AVR) scanner. For a direct comparison of the pre- and post-AVR data, we chose the end-diastolic frame from the dynamic CT pre-data set. The spatial resolution of the CT scanner for the pre- and post-data in the z-axis is approximately (0.625mm/0.625mm) and about 0.625mm/1.25mm in the x- and y-axes. The temporal resolution of the pre-AVR CT is 280ms and gated (cine mode) for the pre-data set and 400ms for the non-gated CT scan after a minimal 70 days post-surgery. The pressure data for before (up to 1 year prior) and during/after (up to 2 years) surgery are acquired via catheterization and further measurements such as EF via echocardiogram. The pressure measurements

utilised in the presented paper focus on the end-diastolic pressures.

The geometric models utilised in this study are based on the segmentation output of a U-Net framework algorithm of Xu et al.[245]. The algorithm is split up into five intermediate steps, starting with an initial segmentation (U-Net 1), pulmonary valve identification (U-Net 1 no pulmonary artery (PA)), PA extrapolation (U-Net 2), parcellation of the left atrium (U-Net 3) and label map fusion with coronary computed tomography angiography (CCTA) images. The final output contains ten labels of segmentations for the heart, including the LV myocardium and the blood pool of the LV, RV, aorta, pulmonary artery, and left and right atrium, besides other labels not considered in our paper.

Afterwards, we loaded the automated segmentation into 3DSlicer (http://www.slicer.org[63]). Considering that the NN exclusively segments the RV blood pool and disregards the RV myocardium, a 3 [mm][196] layer surrounding the RV blood pool segmentation was added. Subsequently, the LV and RV valve planes were assessed and corrected to match the imaging data. By utilising the software ITK-SNAP (www.itksnap.org[250]) a surface discretised model of the BiV was generated and further utilised for the mesh generation part of the pipeline.

Lastly, this data was loaded into SimModeler (Simmetrix-http://www.simmetrix.com/), and a biventricular (BiV) model based on tetrahedral elements was developed. A rule-based method from Doste et al.[55] and Bayer et al.[26] was adapted to generate a fibre field for the BiV model. The fibre angles transitioned transmurally (epicardium towards endocardium) between -60 to 60° and -25 to 90° concerning the local circumferential direction in the LV and RV, respectively. The fibre field at the valve annuli was defined according to high-resolution DTI measurements on ex-vivo porcine hearts with different angles for the specific valves. The metrics of the linear tetrahedral $\mathbb{P}^1$ elements for the pre-SAVR and pre-TAVR meshes are listed in Table 29 and 30 in the appendix.

5.2.2.2 Inverse Mechanics using MULF Method

Biomechanical problems usually involve dealing with patient-specific geometries imaged and extracted at a loaded state, whereas stress-strain curves of tissue samples used for parameter identification naturally are recorded at an unloaded state. To bridge the gap from the loaded imaged state to the unloaded stress-free configuration, inverse mechanics approaches have been proposed[210] and adopted for finite hyperelasticity[90]. Biomechanical applications of the inverse problem have been shown in[153,79] for abdominal aortic aneurysms (AAA) and myocardium[19,73]. Nevertheless, solution uniqueness is not guaranteed within classical inverse finite elasticity problems, meaning that multiple undeformed configurations may produce the same deformed state for a prescribed set of BCs[90]. Therefore, approximate solutions to the inverse problem have been proposed,

applied for AAAs[199] or using iterative fixed-point solutions[30].

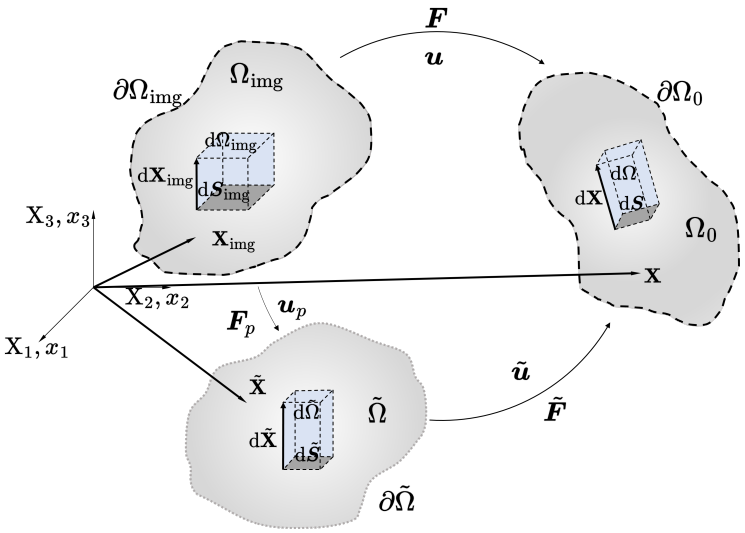

Figure 5.3 Schematics of the Modified Updated Lagrangian Formulation (MULF)

Furthermore, methods of incorporating the prestressed stage of the imaged configuration has been proposed, e.g. the so-called Modified Updated Lagrangian Formulation (MULF)[78,79], which we adopt here in order to estimate a zero-stress reference state. An overview of inverse mechanics problems applied in the biomechanical context can be found in Bracamonte et al.[34].

The MULF method starts with the so-called "prestressing phase", where a history-dependent deformation gradient $\boldsymbol{F}_p$ is sought such that a forward problem formulated with respect to the imaged configuration Ω_{img} is in equilibrium with the acting boundary conditions in the introduced zero-load reference configuration Ω_0, see Figure 5.3. In the "poststressing" phase, a displacement field $\boldsymbol{u}$ is computed, while the total deformation gradient is defined as

$$\boldsymbol{F} = \left(\boldsymbol{I} + \frac{\partial \boldsymbol{u}}{\partial \tilde{\boldsymbol{X}}}\right) \boldsymbol{F}_p. \tag{5.28}$$

Here $\tilde{\boldsymbol{X}} = \mathbf{X}_{\text{img}} + \boldsymbol{u}_p$ is the "virtual" configuration that is obtained by imposing an accumulated displacement field $\boldsymbol{u}_p$ from the prestressing phase.

A recent transformation of variables for MULF has been proposed by Schein and Gee[209], circumventing the need for incremental determination of $\boldsymbol{F}_p$ by directly incorporating the prestress displacement field $\boldsymbol{u}_p$. Considering $\boldsymbol{F}_p = \frac{\partial \tilde{\boldsymbol{X}}}{\partial \mathbf{X}_{\text{img}}} = \boldsymbol{I} + \frac{\partial \boldsymbol{u}_p}{\partial \mathbf{X}_{\text{img}}}$, we reformulate Equation 5.28 such that

$$\begin{aligned} \boldsymbol{F} &= \frac{\partial(\tilde{\boldsymbol{X}} + \boldsymbol{u})}{\partial \tilde{\boldsymbol{X}}} \frac{\partial \tilde{\boldsymbol{X}}}{\partial \mathbf{X}_{\text{img}}} = \frac{\partial(\tilde{\boldsymbol{X}} + \boldsymbol{u})}{\partial \mathbf{X}_{\text{img}}} \\ &= \frac{\partial(\mathbf{X}_{\text{img}} + \boldsymbol{u}_p + \boldsymbol{u})}{\partial \mathbf{X}_{\text{img}}} = \boldsymbol{I} + \frac{\partial(\boldsymbol{u} + \boldsymbol{u}_p)}{\partial \mathbf{X}_{\text{img}}}. \end{aligned} \tag{5.29}$$

Equation 5.29, denotes a formulation of the displacement gradient $\boldsymbol{F}$ from the imaging data to the zero-stress configuration Ω_0. These two initial steps, the "prestressing" and "poststressing" are steps to introduce residual stresses into the reference configuration. During the "prestressing" phase, the is solved for a displacement ($\boldsymbol{u}_p$) and hydrostatic pressure (p) field, such that

$$\Pi_t^{\text{int}}(\boldsymbol{u}_p, p) - \Pi_t^{\text{ext}}(\boldsymbol{0}) \rightarrow \min . \tag{5.30}$$

In this static system, the outside potential Π_t^{ext} are assumed to become zero as a result of the deflation process. While the "poststressing" potential energy, seeks the displacement and hydrostatic pressure $\boldsymbol{u}$ and p such that

$$\Pi_t^{\text{int}}(\boldsymbol{u} + \boldsymbol{u}_p, p) \rightarrow \min, \tag{5.31}$$

imposing zero external traction loads, revealing a stress-free unloaded configuration.

Subsequently, we load this stress-free unloaded configuration to the post-AVR pressures which introduce residual stresses into the system and utilise the configuration as a reference configuration for the G&R process.

5.2.2.3 Passive Parameter Estimation and Klotz-Curve

The combination of imaging and pressure data provides information about the loaded configuration. However, identifying the material parameters of the myocardium from this data alone is unfeasible due to uncertainty in the imaged loading state of the heart. The introduced MULF method can offer compatible conditions for the loaded configuration. Still, for utilising and specifying a loaded condition, see Section 5.2.2.2, an estimation for the parameter set of the reduced Holzapfel-Ogden material law (a, a_f, b, b_f) is needed.

Klotz et al.[125] proposed a single-beat approach to estimate the complete end-diastolic pressure-volume relationship (EDPVR) from solely one measurement point. The study was based on EDPVR from 80 human hearts of different etiologies, e.g. healthy, congestive HF, and left ventricular assistive device support. Unrelated to the physiological state of the heart, EDPVR normalised by the scaling of the LV volumes showed only marginal differences within the entire data set and exhibited a common shape over different etiologies and species. The proposed relation

$$V_{0,\text{Klotz}} = V_m(0.6 - 0.006 \cdot P_m) \tag{5.32}$$

describes the link between the measured point and the predicted volume at the pressure of ~ 0 mmHg (V_0) on the EDPVR curve. End-diastolic volume (EDV) was measured from the ED configuration of the BiV mesh and the end-diastolic pressure (EDP) was

acquired from invasive catheterisation. A forward passive inflation model was executed as a deflation process, starting from the EDV/EDP measurement point and reducing the pressure inside the LV and RV cavity lumen to $\sim$ 0mmHg. As BC, we constricted the valve surfaces against translation and rotation. During the deflation process, a forward passive inflation model was carried out within the LV and RV cavities. To restrict the passive parameter space to only one unknown, we assume that a and a_f are linked together via the parameter ratio $\gamma = a/a_f$ [99,18,171] and fix the other parameters such that $\gamma = 0.4234$ and $b = b_f = 3.0$.

In order to identify a unique value for a, we minimised the error between the Klotz-curve estimate V_0^{klotz} and the numerical version (V_0^{num}). We measure this error using the objective function:

$$\mathcal{J} = |V_0^{\text{klotz}} - V_0^{\text{num}}|. \tag{5.33}$$

Here, V_0^{num} is the calculated volume of the deflated pre-stressed model following MULF to pressures of 0mmHg within both cavities.

Table 5.2 contains the material parameters for SAVR 1 and SAVR 2 that are utilised for the forward computation of the grown states.

Table 5.2 Personalised estimates for the biomechanical parameters of the passive myocardium within a reduced Holzapfel-Ogden material law

	a	b	a_f	b_f	a_s	b_s	a_n	b_n
SAVR 1	2.08	3.0	4.913	3.0	-	-	-	-
SAVR 2	0.95	3.0	2.008	3.0	-	-	-	-

A summary of the material parameters for the reduced Holzapfel-Ogden material for the remaining SAVR and TAVR cases are attached in the appendix, see Table 31.

5.2.3 Personalised Post-AVR modelled state

In this section, the key aim is to apply reverse growth to the pre-AVR model and predict the post-AVR morphology of the heart via the introduced pipeline, as shown in Figure 5.4. The workflow begins with the first stage, which involves pressure unloading the pre-AVR model to the post-AVR pressures. This response of the heart can be immediately observed in the heart following AVR.

Contrasting with this, G&R processes are characterised by taking place over a longer time interval, with changes in myocardium volume typically noticed six months or more after the intervention. This makes it possible to apply a quasi-static elastic problem. To determine the amount of adverse growth or reverse growth, we compared the regional change of myocardium volume in the pre- and post-AVR within the LV, RV, and septum.

Next, growth stretches were applied via the Jacobian and the stretch ratio (ϑ^i with $i = f, s, n$) along the cardiomyocyte coordinates. Once the post-AVR models were simulated, they were compared with the post-AVR data, utilising different metrics in an attempt to identify a G&R mode most similar to the post-AVR imaging data. These metrics included mass, cavity volume, long-axis and short-axis distance, sphericity, wall thickness, and morphology.

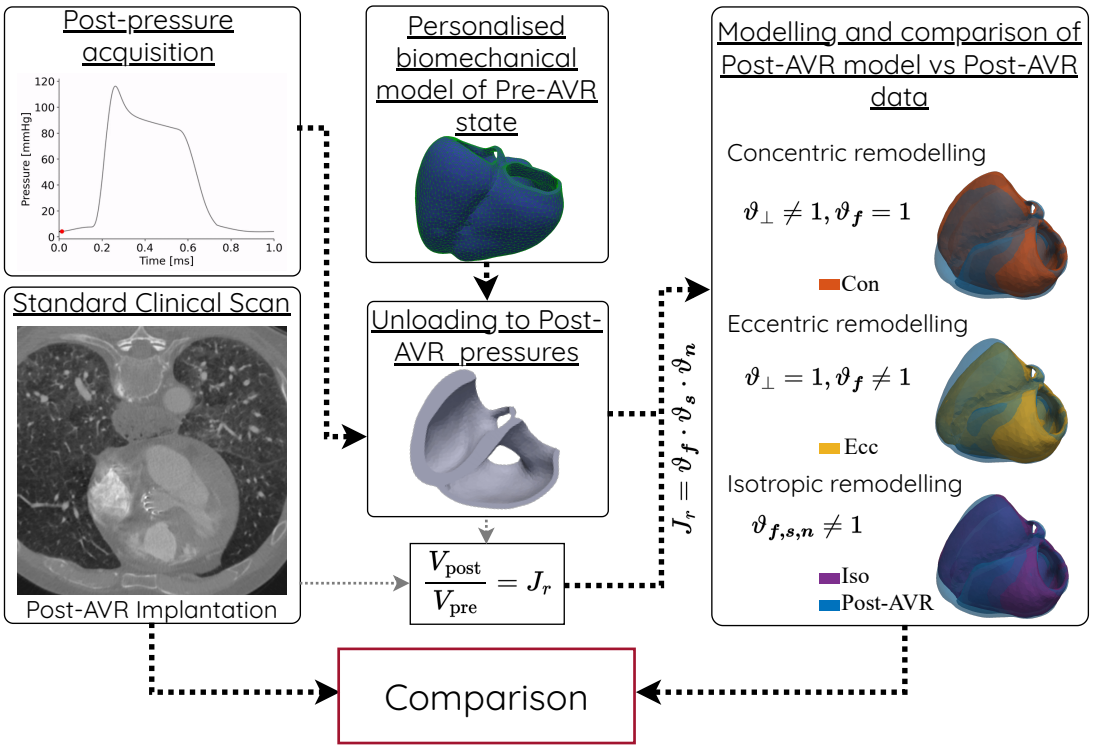

Figure 5.4 Personalised workflow for reverse growth following AVR to obtain a contemporary mechanically balanced state, referred to as Post-AVR state. As a first step in this pipeline, a pressure adaption to the post-AVR pressures is performed within the LV and RV. Following this, a model of the post-AVR state is generated and a regional comparison of the volume of the LV, RV and septum volume change is computed and further utilised as an input for the G&R problem as a heterogeneous growth tensor across the heart and within the LV, RV or septum homogeneous. The final step of the pipeline is centred around comparing the modelled post-AVR state with the post-AVR data.

5.2.3.1 Characterisation of Post-AVR Growth and Remodelling

To characterise the changes between pre- and post-op surgery, we start by creating a geometric model of the post-AVR state. For this reason, we repeated the steps previously applied to the pre-AVR CT images to generate a BiV model, see Section 5.2.2.1. The metrics of the linear $\mathbb{P}^1$ tetrahedral elements for the post-SAVR and post-TAVR meshes are listed in Table 29 and 30.

In an attempt to identify the type of reverse growth which occurs between the pre- and post-op heart, we specified three distinctive heart regions (LV-, RV- and septal myocardium). This separation permits the identification of growth regions and accounts

for some potential spatial heterogeneity in F_g. The LV, RV and septal regions were predefined via a Matlab script[162]. Further, we calculated the volume of the mesh elements in the LV, RV or septal region of the pre- (V^i_{pre} with $i = \text{lv}, \text{rv}, \text{sep}$) and post-op heart ($V^i_{\text{post}}$ with $i = \text{lv}, \text{rv}, \text{sep}$).

Based on the relationship, $V^i_{\text{post}} = J^i_g \cdot V^i_{\text{pre}}$ we can compute the volume change (J^i_g) by comparing the unloaded pre- and the follow-up scan model

$$J^i_g = \frac{V^i_{\text{post}}}{V^i_{\text{pre}}}, \tag{5.34}$$

J^i_g defined the overall volume change in the LV, RV or septum and was used to define reverse growth factors ($\boldsymbol{\vartheta}^i_{\text{g}} = \{\vartheta_{\text{f}}, \vartheta_{\text{s}}, \vartheta_{\text{n}}\}$) for the different reverse remodelling modes

$$\boldsymbol{\vartheta}^i_{\perp} = \begin{pmatrix} 1.0 \\ \sqrt{J^i_g} \\ \sqrt{J^i_g} \end{pmatrix}, \; \boldsymbol{\vartheta}^i_{f} = \begin{pmatrix} J^i_g \\ 1.0 \\ 1.0 \end{pmatrix}, \; \boldsymbol{\vartheta}^i_{iso} = \begin{pmatrix} \sqrt[3]{J^i_g} \\ \sqrt[3]{J^i_g} \\ \sqrt[3]{J^i_g} \end{pmatrix}. \tag{5.35}$$

Where $\boldsymbol{\vartheta}^i_{\perp}$ relates to concentric growth, $\boldsymbol{\vartheta}^i_{f}$ denotes eccentric growth and $\boldsymbol{\vartheta}^i_{iso}$ describes isotropic growth and is integrated into the general kinematic growth tensor formulation, see Equation 5.10 and adapted to represent the individual G&R mode.

5.2.3.2 Modelling Growth Response

Simulating reverse growth in the heart after intervention requires addressing short- and long-term changes. Right after AVR, alterations in the loading configuration (post-AVR) are observed which cause a significant change in the luminal pressure inside the LV. The drop of the pressure gradient between the aorta and the LV triggers further long-term anatomical changes in the post-AVR loaded state. Following the pressure adaption, we simulated the myocardium's reverse growth in the different regions of the heart.

For a direct comparison of the post-AVR modelled heart and the post-AVR data, we have to address the immediate response of the pre-AVR loading state to the pressure values of the Post-AVR. The pressure data were acquired during AVR via catheterisation for the LV/RV (P_{lv}/P_{rv}). The decrease from the recorded pre- to post-surgery pressure value was applied in increments.

After unloading the intraventricular pressure inside the modelled Post-AVR model reverse growth was introduced to account for changes on the long-time scale. The challenge here is that the regional mass change (J^i_g) estimated from Equation 5.34 does not give any information about the type of reverse growth inside the myocardium. To identify the correlating growth mode with the imaging data, we applied common G&R modes observed in the heart and compared the computational output with the post-

AVR imaging data. Applying different modes of reverse growth (concentric/eccentric or isotropic) enables a fundamental understanding of the myocyte response to AVR and changes in anatomy. Reverse growth was done by incrementally decreasing the initial $\vartheta^i = 1$ to the calculated ϑ^i_j and inserting the growth factor into F_g of our problem.

5.2.3.3 Modelled Post-AVR vs Post-AVR imaging data state

As a means of verifying the accuracy and reliability of the results obtained, a validation of our G&R problem was conducted. Where we compared the mass of our predicted post-AVR model with the mass of the post-AVR imaging data model. Since G&R was informed by a mass change in Equation 5.24, the mass of the grown model and the post data should match. Therefore, we computed the regional volume V^i_j with $i = \{lv, rv, sep\}$ for the pre-AVR and the post-surgery heart and then multiplied it with the myocardial tissue density $\rho = 1.055 g/ml$ [84]. Concurrent with the mass change during G&R, is also the alteration of the intraventricular lumen. This modification is not directly driven by the reverse growth and can give further insight into the anatomical changes caused by the different reverse growth modes following AVR. The intraventricular cavity volume was calculated from the reverse grown model (concentric, eccentric or isotropic) in Matlab [162].

Following growth, the changes of mass were verified with the applied volume change through J. Additionally, the cavity volume change was verified and compared with the post-AVR imaging data. However, these values don't give insight into the morphological changes following G&R. Therefore, additional anatomical measurements were considered, such as long-axis (LA) length, short-axis (SA) diameter and sphericity of the heart [52,24,48,51]. In this work, we defined the heart's LA length by computing the distance between the mitral valve's midpoint (MV) and LV apex point. The SA diameter was estimated by identifying an orthogonal vector on the LA at the location (LA length)/2. The sphericity (SI) of the heart is derived by calculating utilising the LV EDV and the long-axis length of the LV [179]

$$SI = \frac{LVEDV}{\frac{4\pi}{3}\left(\frac{LA}{2}\right)^3}. \tag{5.36}$$

In a healthy heart the LV SI is 0.49 and 0.48 for men and women, respectively [176].

To measure the morphological changes triggered by the different reverse growth modes, a surface-to-surface registration [7] between the predicted grown model and the post-AVR data was utilised. More specifically, the LV and RV endocardial surfaces and the epicardial surface of the hearts were compared (see Figure 5.5). The mapping of the predicted grown model to the post-AVR model was based on a nearest-point search on the target. The individual nodes of the source mesh were iteratively deformed for the mapping to the closest point of the target mesh based on an active stiffness

calculation. A displacement field for the mapping between the predicted grown model and the target was the output. This point-wise displacement field provides insight into the shape changes caused by the different reverse growth modes and indicates regions with higher discrepancies. It enables the identification of the reverse growth mode that is most similar to the post-data.

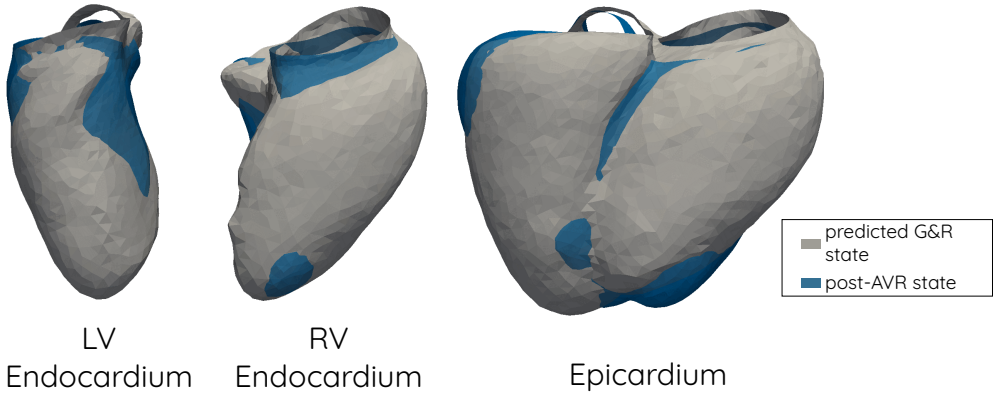

Figure 5.5 A morphological comparison between the modelled Post-AVR state (grey) and the image-based Post-AVR state (turquoise) via surface registration proposed by Amberg et al. [7] was conducted. Emphasising on the LV-, RV endocardium and epicardium.

All physics simulations were performed in ***CHeart*** [143] and any follow-up data post-processing is a result of both additional ***CHeart*** functionalities or was performed in MATLAB [162].

5.3 Results

In this section, we introduce the results obtained from cases SAVR 1 and SAVR 2. For a more comprehensive view of the entire cohort, covering both SAVR and TAVR cases, see Figure Appendix 4-9. For consistency, in this study, we use dark-red to refer to pre-AVR data and blue for post-AVR data. Similarly, orange, yellow and purple were used to distinguish between the simulation derived growth patterns, specifically, for concentric, eccentric and isotropic G&R, respectively.

Figure 5.6 and 5.7(A) illustrate the mass changes in the regions of the heart, such as heart, LV, RV or septal mass, which was computed by using Equation 5.35. G&R in this work is driven by the mass changes observed between the pre-AVR and post-AVR data and is highly heterogeneous across the different regions in the heart. This mass change is implemented via Equation 5.35 with respect to the LV, RV or septal volume of the mesh in the representative region. Due to the previously stated fact that we constrained the mass change in each model, the comparison between predicted and recorded values serves as a validation criterion for the presented pipeline in general. Throughout the different patients, the introduced pipeline performed as predicted, with the predicted post-AVR values matching those of the post-AVR data, see Table 5.3a–

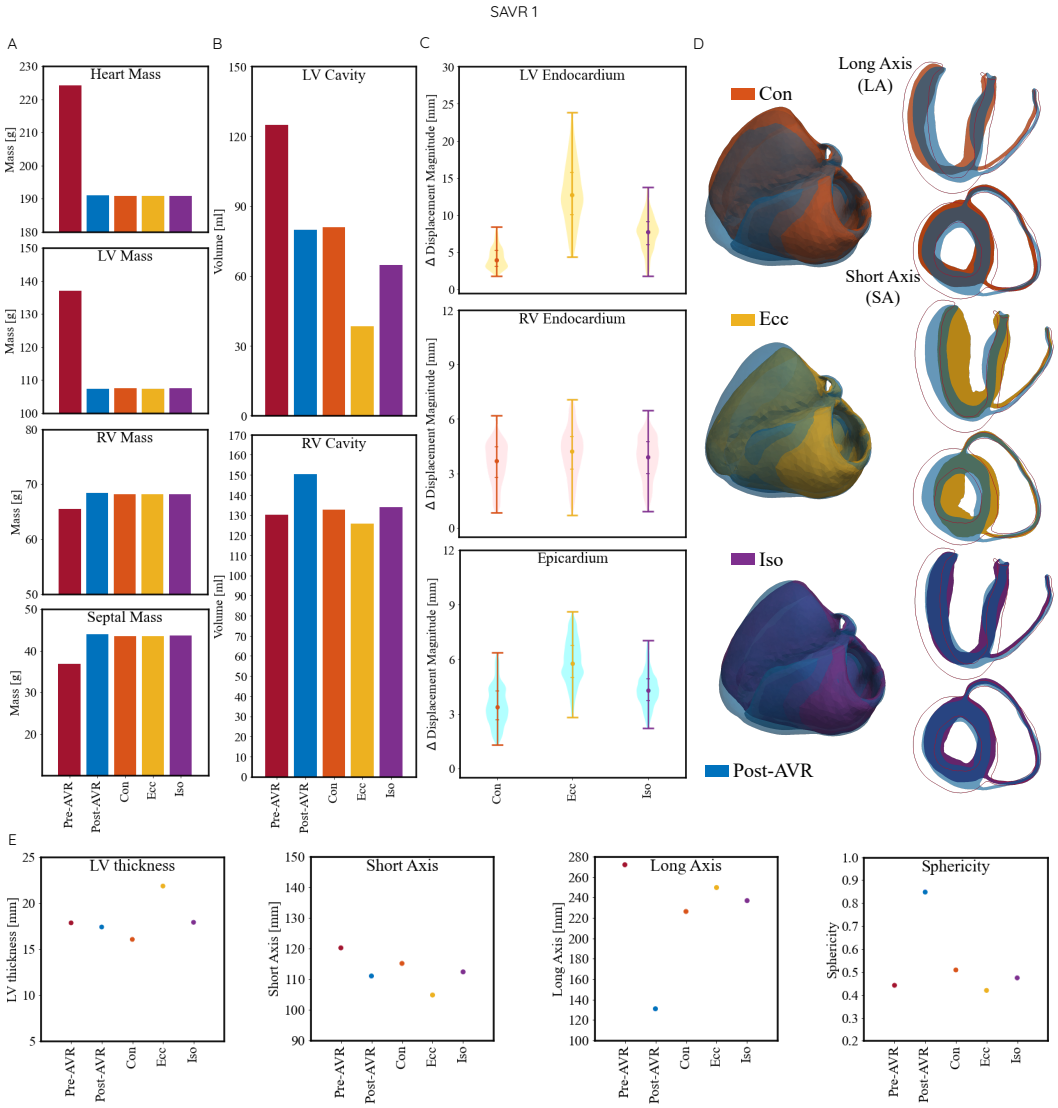

Figure 5.6 Comparison between the Pre-, the concentric, eccentric, or isotropic reverse grown Post-AVR, and Post-AVR data following AVR. (A) Illustrates the mass [g] alteration of the heart (top) and within the LV (second plot from the top), the RV (third plot from the top) and the septum (bottom) related to the different models. (B) Displays the changes of the LV (top) and RV (bottom) cavity volume with respect to the model. (C) Statistical comparison of a surface registration algorithm of the LV-, RV-endocardium and the epicardium between the imaging data and the reverse growth simulations. (D) Shows the comparison of the Post-AVR data and the different models after applying one of the reverse G&R modes. On the right, the long axis (LA) cuts and short axis (SA) are visualised (red outline) as a reference for the Pre-AVR state. (D) visualises the changes of certain cardiac metrics, such as long axis length (LA), short axis (SA) diameter and LV wall thickness in [mm] and additionally the sphericity index (SI). The different colours represent the individual models, dark red: Pre-AVR model, blue: Post-AVR model, and the modelled Post-AVR concentric, eccentric and isotropic state with orange, yellow and purple, respectively.

5.4b. A summary of the entire mass changes across the patient cohort, SAVR and TAVR can be found in the appendix, see Table 34–37.

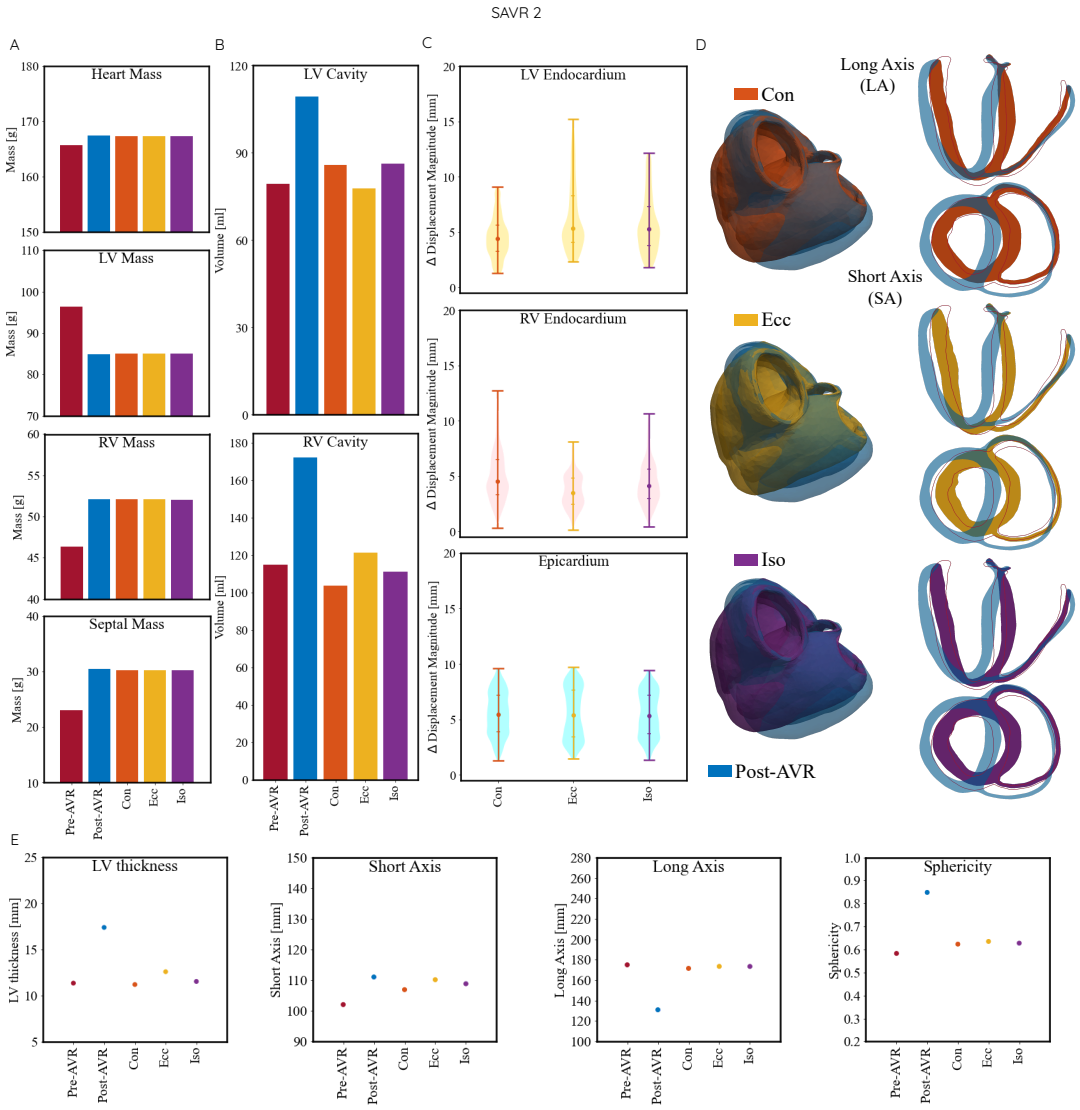

Figure 5.7 Comparison between the Pre-, the concentric, eccentric, or isotropic adverse grown Post-AVR, and Post-AVR data following AVR. (A) Illustrates the mass [g] alteration of the heart (top) and within the LV (second plot from the top), the RV (third plot from the top) and the septum (bottom) related to the different models. (B) Displays the changes of the LV (top) and RV (bottom) cavity volume with respect to the model. (C) Statistical comparison of a surface registration algorithm of the LV-, RV-endocardium and the epicardium between the imaging data and the adverse growth simulation. (D) Shows the comparison of the Post-AVR data and the different models after applying one of the adverse G&R modes. On the right, the long axis (LA) cuts and short axis (SA) are visualised (red outline) as a reference for the Pre-AVR state. (D) visualises the changes of certain cardiac metrics, such as long axis length (LA), short axis (SA) diameter and LV wall thickness in [mm] and additionally the sphericity index (SI). The different colours represent the individual models, dark red: Pre-AVR model, blue: Post-AVR model, and the modelled Post-AVR concentric, eccentric and isotropic state with orange, yellow and purple, respectively.

Figure 5.6 and 5.7(B) illustrate the LV and RV cavity volume changes of the modelled post-AVR state to the pre- and post-AVR data, numerical changes are reported in

Table 5.3 Mass change following G&R in the case of reverse growth (SAVR 1) and adverse growth (SAVR 2) of the heart and the LV. With post-AVR data, and simulated G&R results (concentric, eccentric or isotropic growth) compared to the pre-AVR state in %.

(a) Heart mass change following G&R in [%].

	SAVR 1	SAVR 2
Post	-20.5	+1.0
Con	-20.6	+1.0
Ecc	-20.7	+1.0
Iso	-20.6	+1.0

(b) LV mass change following G&R in [%].

	SAVR 1	SAVR 2
Post	-35.9	-11.8
Con	-35.7	-11.7
Ecc	-35.8	-11.7
Iso	-35.7	-11.7

Table 5.4 Mass change following G&R in the case of reverse growth (SAVR 1) and adverse growth (SAVR 2) within RV and septum. With post-AVR data, and simulated G&R results (concentric, eccentric or isotropic growth) compared to the pre-AVR state in %.

(a) RV mass change following G&R in [%].

	SAVR 1	SAVR 2
Post	+4.4	+12.3
Con	+4.0	+12.3
Ecc	+4.1	+12.3
Iso	+4.1	+12.3

(b) Mass changes in the septum following G&R in [%].

	SAVR 1	SAVR 2
Post	+19.5	+32.1
Con	+18.2	+31.1
Ecc	+18.2	+31.4
Iso	+18.3	+31.3

Table 5.5. In the case of reverse growth in SAVR 1, we observed a reduction of the LV cavity volume ranging from -35.2% to -69.3% between the pre-AVR state and the modelled post-AVR states. With concentric growth being in good agreement with 1% difference in reduction to the post-AVR data. We observed that the real volume in the case of eccentric and isotropic growth patterns is underestimated by at least 12%, in the case of isotropic growth and up to 33% for eccentric growth. In contrast in SAVR 2, the predicted volumes are much closer to the pre-AVR state, -2.1% to 37.8%, and generally underestimate the real post-AVR volume by at least 29% following isotropic G&R. Similar patterns can be seen for the RV, where in SAVR 1 we generally underestimate the post-AVR volume by 12% to 18%, and in the case of SAVR 2, by 40% to 53%. A summary of the entire LV and RV cavity changes across the patient cohort, SAVR and TAVR can be found in the appendix, see Table 38–39.

Table 5.5 LV and RV cavity volume change following G&R in the case of reverse remodelling (SAVR 1) and adverse growth (SAVR 2) of the heart. With post-AVR data, and simulated G&R results (concentric, eccentric or isotropic growth) compared to the pre-AVR state in [%].

(a) LV cavity volume change following G&R in [%].

	SAVR 1	SAVR 2
Post	-36.1	+37.8
Con	-35.2	+8.3
Ecc	-69.3	-2.1
Iso	-48.2	+8.9

(b) RV cavity volume change following G&R in [%].

	SAVR 1	SAVR 2
Post	+15.5	+50.0
Con	+2.0	-9.7
Ecc	-3.5	+5.7
Iso	+2.9	-3.3

In Figure 5.6 and 5.7(C), the LV and RV endocardial surfaces and the epicardial surface of the hearts were compared to the post-AVR data to address morphological changes in the heart. Table 5.6a–5.6c show the numerical mean and standard variation of the registration displacement field illustrated values in Figure 5.6 and 5.7(C) in [mm]. In the case of reverse growth in SAVR 1, we observe that the mean and standard deviation of the displacement field applied to the predicted post-AVR surfaces to register with the post-AVR data surfaces ranges between 1.3(0.6)[mm] to 5.4[mm]. Where the RV endocardium appears to have the highest agreement overall in the G&R cases. A high dissimilarity between the surfaces of the heart could be observed in the case of eccentric reverse growth with a focus on the LV endocardium with a mean displacement of 5.4[mm] and a standard deviation of 2.1[mm]. In contrast in SAVR 2, the mean displacement showed an overall high discrepancy of all surfaces of the modelled post-AVR states compared to the post-AVR data ranging between 3.6[mm] of the RV endocardium with eccentric adverse growth up to 6.4[mm] for eccentric adverse growth in the LV endocardium. A summary of the entire surface registration metrics across the patient cohort, SAVR and TAVR can be found in the appendix, see Table 40–42.

Table 5.6 Mean and standard deviation of registration displacement field between LV and RV endocardial and endocardial surfaces in [mm]. Amberg et al.[7] surface registration algorithm was utilised to compute the displacement field between the predicted grown state surface and the post-AVR data surface.

(a) Mean and standard deviation of LV endocardium registration displacement field in [mm].

	SAVR 1	SAVR 2
Con	1.3 (0.6)	4.6 (1.9)
Ecc	5.4 (2.1)	6.4 (3.1)
Iso	1.2 (0.4)	5.7 (2.6)

(b) Mean and standard deviation of RV endocardium registration displacement field in [mm].

	SAVR 1	SAVR 2
Con	2.1 (0.8)	5.1 (2.4)
Ecc	1.9 (0.9)	3.6 (1.5)
Iso	1.9 (0.7)	4.4 (2.0)

(c) Mean and standard deviation of epicardium registration displacement field in [mm].

	SAVR 1	SAVR 2
Con	2.4 (0.9)	5.5 (2.0)
Ecc	3.1 (1.3)	5.5 (2.3)
Iso	1.6 (0.6)	5.4 (2.0)

Figure 5.6 and 5.7(D) illustrate the different morphologies of the predicted G&R hearts including the 3D geometries, as well as the long- and short-axis cuts. As mentioned in regard to the endocardial surface registration, in cases with significant mass changes, especially in the LV region. In the case of eccentric reverse growth, we observe a thickness increase in the septal area. Besides growth, we also observed in both cases, reverse growth and adverse growth an outwards twist of the apex region. In contrast in SAVR 2, we notice that within all predicted adverse G&R cases the septal area collapsed into the RV cavity towards the RV free wall.

Figure 5.6 and 5.7(E), illustrate additional cardiac metrics, such as the LV thickness, short axis diameter, long axis length, and the sphericity index of the hearts, numerical results are listed in Table 5.7 and 5.8. In the case of reverse growth in SAVR 1 a

change of the LV thickness was observed ranging between -10.1 % to +22 % related to the pre-AVR state, with the isotropic G&R state (+0.3%) in high agreement with the post-AVR data (-2.5%) compared to the pre-AVR state. Related to changes of the short axis diameter, concentric (-4.2%) and isotropic (-6.5%) remodelling behaved in a similar way than the post-AVR data indicate (-7.6%). Studying the changes along the long axis of the heart, we observe a overall reduction between -8.2% up to -51.9%, with the highest reduction seen in the post-AVR data. Changes of the sphericity index compared with the pre-AVR data were ranging from -5% in the case of eccentric remodelling up to +91% in the post-AVR data. Overall, the long axis and sphericity index are highly underestimated in all of the reverse remodelled states in SAVR 1. In contrast in SAVR 2, we observed an overall high discrepancy in the LV thickness, short-axis diameter, long-axis length and sphericity index change of the adverse grown states compared to the post-AVR data changes following adverse growth. A summary of the entire mass changes across the patient cohort, SAVR and TAVR can be found in the appendix, see Table 43–46.

Table 5.7 Change of LV thickness and short-axis diameter following G&R in the case of reverse growth (SAVR 1) and adverse growth (SAVR 2) of the heart. With post-AVR data, and simulated G&R results (concentric, eccentric or isotropic growth) compared to the pre-AVR state in %.

(a) LV thickness change following G&R in [%].

	SAVR 1	SAVR 2
Post	-2.5	-19.7
Con	-10.1	-1.3
Ecc	+22.4	+10.9
Iso	+0.3	+1.6

(b) Short axis diameter change following G&R in [%].

	SAVR 1	SAVR 2
Post	-7.6	-3.1
Con	-4.2	+4.8
Ecc	-12.8	+8.0
Iso	-6.5	+6.7

Table 5.8 Change of long-axis length and sphericity index following G&R in the case of reverse growth (SAVR 1) and adverse growth (SAVR 2) of the heart. With post-AVR data, and simulated G&R results (concentric, eccentric or isotropic growth) compared to the pre-AVR state in %.

(a) Long axis length change following G&R in [%].

	SAVR 1	SAVR 2
Post	-51.9	-31.8
Con	-16.8	-2.0
Ecc	-8.2	-0.9
Iso	-12.9	-0.9

(b) Sphericity index change following G&R in [%].

	SAVR 1	SAVR 2
Post	+91.9	+42.1
Con	+15.2	+6.9
Ecc	-5.0	+8.9
Iso	+7.3	+7.7

Besides the geometrical changes, we also analysed the incompatibility states following growth. Therefore, we utilised the incompatibility metric e_{inc}, defined in Equation 5.8. Figure 5.8 illustrates the incompatibility metric e_{inc} in the case of SAVR 1 and SAVR 2 for concentric, eccentric and isotropic G&R, the numerical results are recorded in Table 5.9. In the event of compatibility of the G&R process, $e_{inc} = 0$, where growth

Table 5.9 The mean of the incompatibility metric e_{inc} within the predicted post-AVR states (concentric, eccentric or isotropic growth) following reverse growth (SAVR 1) or adverse growth (SAVR 2).

	SAVR 1	SAVR 2
Con	0.211(std=0.080)	0.197(std=0.070)
Ecc	0.251(std=0.077)	0.207(std=0.076)
Iso	0.200(std=0.093)	0.203(std=0.072)

does not introduce incompatibilities or residual stresses into the predicted post-AVR state. With the upper bound for incompatibility, $e_{inc} = 1$. A summary of results for the incompatibility metric e_{inc} for the modelled post-AVR states of SAVR and TAVR patients are attached in the appendix, see Figure 2–3 and Table 32–33.

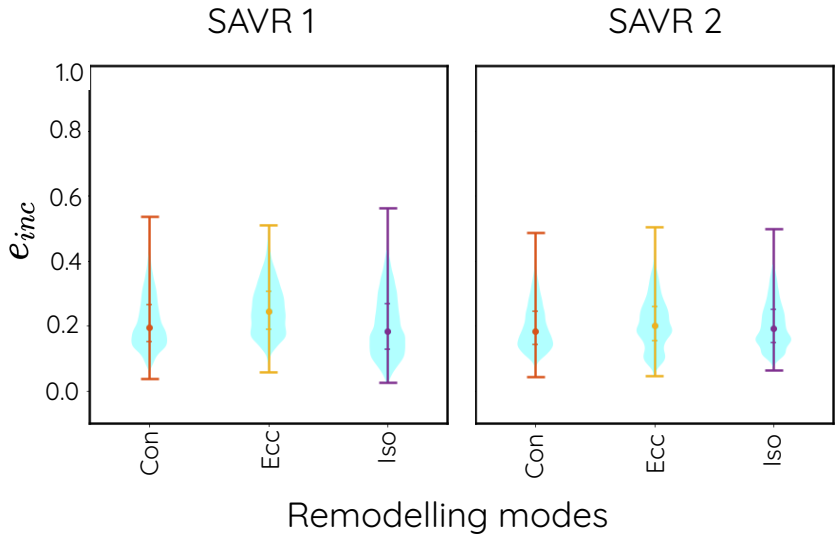

Figure 5.8 Incompatibility metric e_{inc} within the predicted post-AVR states, concentric (Con), eccentric (Ecc) or isotropic (Iso) growth following reverse growth (SAVR 1) or adverse growth (SAVR 2).

The complete set of results, expanded to the entire cohort and covering the SAVR and TAVR cases can be seen in Figure 4–8.

5.4 Discussion

In this section, we discuss the results obtained from cases SAVR 1 and SAVR 2 and further attempt to identify a growth pattern that best matches the post-AVR data following AVR.

5.4.1 Comparison of Modelled Post-AVR and Post-AVR Data

To identify a G&R mode which agrees best with the post-AVR data, we analysed cavity volume changes, morphology properties and changes in long-axis length, short-

axis diameter, sphericity index and LV wall thickness of the predicted post-AVR states and compared it with the post-AVR data.

In cases of reverse growth in SAVR 1, it could be identified that modes with atrophy in the sheet direction, including reverse growth in the sheet-normal direction resulted in modelled Post-AVR states close to the model extracted from the data. This hypothesis is reflected by the entirety of the computed and collected post-AVR data. Within the cavity volume examination (Figure 5.6B), it was observed that reverse growth triggered a large decrease in the LV cavity volume. Additionally, this specific case indicated a further increase in the RV cavity volume following AVR, this change was not captured by any of the modelled Post-AVR geometries. Figure 5.6C, further demonstrates that the mean and standard deviation of the error between the data and model configuration is in concentric and isotropic reverse growth lower than during eccentric reverse growth. This behaviour might also be a strong indication of the spatial variation within the individual regions of the heart. Inspecting the dissimilarities of the pre-AVR (dark red line) in Figure 5.6D, modelled post-AVR and the post-AVR morphology, revealed that eccentric growth induces significant shortening of the LV long axis. A potential reason for the observed thickening during eccentric reverse growth might result from the definition of the kinematic growth tensor along the fibre orientation in the septum. Within the septum the orientation of the fibres transition from 60° to 90° from the LV endocardium to the RV endocardium with 0° in the septal midwall which could be the underlying reason for what we observed in G&R cases with a high reduction in mass during eccentric reverse growth.

In all G&R modes, both a shift and twist of the LV apex area were noticed. This may be caused by the type of BC considered with only restricting the movement of the valve plane area. Evaluating the short-axis, long-axis, sphericity index and LV thickness, seen in Figure 5.6(E), showed that reverse growth in the radial direction produced a more accurate representation of the post-AVR state compared to the concentric mode, confirming our previous observation made with the other metrics. In conclusion, in the event of reverse growth, we can state that in a successful AVR procedure resulting in an unloading of the heart, the myocardium initiates reverse growth in the sheet and sheet-normal direction. This behaviour appears to be similar but opposite to what is observed in the early stage of AS where the fibres also undergo high amounts of alterations in the sheet and sheet-normal direction.

However, growth may also occur as a result of the intervention itself, where additional complications may occur, such as valve regurgitation and leaking due to incorrect positioning, which themselves might trigger additional maladaptive adverse growth. In the event of adverse growth, we were not able to identify a clear type of G&R mode. None of the classical hypertrophy modes was able to successfully prescribe the changes of LV cavity volume following AVR with a net increase of the heart mass, see Figure 5.7B.

Each of the growth modes underestimated the ventricle cavity volume compared to the imaged post-AVR cavity volumes. Additionally, we observed high levels of morphological differences between the modelled LV, RV endocardium and epicardium (Figure 5.7C), with a higher difference of the surfaces in the LV for eccentric remodelling. Whereas concentric and isotropic remodelling lead to a higher discrepancy in the RV endocardium. All G&R incidents indicated high differences in the epicardial surfaces between the modelled and the imaged post-AVR state. Figure 5.7D further indicates that in all modelled post-AVR models the septum progresses towards the RV-free wall, causing some of the geometries to experience a decrease of the RV cavity despite the observing growth of the RV myocardial tissue.

There are several hypotheses which could explain the observed twisting of the apex. A cause could be the specific BC type used in the modelling of G&R. This BC enforces the alignment of the valve in the predicted G&R state and the post-AVR data. As discussed in Chapter 3, applying BCs to a growing geometry may introduce incompatibilities and residual stresses in the heart as a result of heterogeneity or not satisfying the condition $(\nabla u + I)\boldsymbol{F}_g^{-1} = \boldsymbol{I}$. Due to this, we decided to apply a BC which would allow growth without enforcing strong constraints on the process and, as a result, the apex was not directly constrained. Specifically, the twisting may be caused by the heterogeneous fibre network, with fibres being arranged helically at the apex and transitioning between -60 to +60 deg transmurally as we move towards the base.

5.5 Limitations

Whereas classic inverse design methods seek an unloaded stress-free reference state, using MULF only provides an approximate unloaded state.

As a result of the multiplicative split of the deformation gradient $\boldsymbol{F}$ into its elastic and growth component, we can not guarantee the uniqueness of the product of Equation 5.7. This indicates that there can be different combinations of $\boldsymbol{F}_e$ and $\boldsymbol{F}_g$ lead to the same $\boldsymbol{F}$. In this study, we assumed that reverse growth follows a homogeneous pattern within each region (LV, RV or septum). This simplification leads to insufficient knowledge about the spatial distribution of the volume change J_g^i with $i \in \{lv, rv, sept\}$. However, in reality, reverse growth following TAVR is a challenging process incorporating alterations in fibre alignment, material properties and volume, in contrast, this study solely introduced volume changes into the problem setup.

An additional limitation concerning the kinematic growth tensor is the definition of the growth stimulus. In this study, G&R was introduced by computing volume changes in the LV, RV and septal region of the post-AVR model compared to the pre-AVR model, which was then used to compute ϑ^i with $i \in \{lv, rv, sept\}$ in Equation 5.10. However, G&R is assumed to be an adaption process in the heart to achieve a new mechanical

equilibrium state with ϑ being dependent on either stress or strain in the heart.

Another limitation is that the surface registration algorithm treats each surface individually and does not account for the volumetric shape changes which occur within the heart.

Hence, other boundaries affecting the reverse growth of the heart, such as the influence of the chest cavity, were neglected and resulted in the case of the LV apex to higher differences between the modelled Post-AVR and the baseline Post-AVR data. Another limitation is our inability to address the unphysiological apex twisting which can not be explained yet.

5.6 Conclusion

Within this study, we successfully introduced a workflow for modelling the G&R processes following an AVR procedure and identified concentric or isotropic reverse growth as possible G&R modes in patients following a successful AVR considering the cavity changes. In contrast, eccentric reverse growth resulted in a high discrepancy between the modelled post-AVR state and the post-AVR data and further induced wall thickening in the septal area. However, in the case of adverse growth following AVR, none of the predicted G&R modes was in agreement with the post-AVR data. The key takeaway of this study was that G&R following AVR is highly heterogeneous, across all the studied regions of the heart and even within the LV, RV and septum we assume high spatial variation of remodelling following intervention.

6 Identification of Reverse Remodelling via Clinical Data

This chapter covers an alternative method to the previously utilised forward problem approach to model G&R processes by identifying reverse remodelling pattern via clinical data. When using a forward problem approach, the kinematic growth tensor is predefined and applied to the reference state. In contrast, an inverse treats the growth tensor as an unknown field. Hence, it uses a data-driven approach that utilises CT images of the reference and physical frames to compute the tissue deformation field from which the growth tensor can be reconstructed. Inverse problems are commonly applied in order to identify material parameters of soft tissue [21] and soft filaments [77]. A brief review of open forward and inverse problems used in modelling adaptations in bone tissue was conducted by Zadpoor [251] to highlight potential insight into the underlying mechanism of G&R by employing a data-driven approach. Employing fetal human brain MRI data combined with a modification morphoelastic growth approach assuming an evolving reference configuration, Wang et al. [236] tracked the development and local volume changes in the brain *in utero* between week 21 up to week 25.

This chapter intends to utilise clinical data sets of SAVR and TAVR patients with the aim to identify different characteristics of the kinematic growth tensor $\boldsymbol{F}_g$ by analysing properties of the right Cauchy–Green deformation tensor $\boldsymbol{C}_g = \boldsymbol{F}_g^T \boldsymbol{F}_g$, such as inherent heterogeneity within regions of the heart, alignment, anisotropy and directional relevance to the microstructure. This aims to enhance our understanding of regional variation and typical growth behaviour following the pressure unloading of the heart. To achieve this, we create a universal ventricular coordinate (UVC) [25] system which allows us to objectively compare the geometric models corresponding to pre- and post-AVR states.

6.1 Methods

6.1.1 Universal Ventricular Coordinates

In order to account for inter-patient variability in manual segmented and generated hearts or different time states of the heart in the CT images, for example, pre-AVR and post-AVR, it is necessary to create a common coordinate system to compare the models. In the case of LV models, Bayer et al.[25] developed a pipeline, based on the Laplace equations, for generating a four-component coordinate system, referred to as the universal ventricular coordinates (UVC).

The coordinates introduced by UVC are the long-axis (ζ), the transmural (ρ), the circumferential (ϕ), and chamber (ν). The long axis, ζ, is defined such that varies from 0, at the apex, to 1 at the valve planes. The transmural direction, ρ, is specified between 0, at the endocardium, and 1 at the epicardium. The circumferential rotation, ϕ, is restricted such that it varies from $-\pi$, at the septum, to $+\pi$ in the anteroseptal region. The chamber, ν, is determined such that -1, is associated with the LV, and 1 relates to coordinates in the RV.

In this work, we use a Python-based adaptation of the approach proposed by Bayer et al.[25], in to transform the original Cartesian space of the nodal coordinates into a corresponding UVC one. Figure 6.1 illustrates the application of this method and its use in calculating a displacement map between the pre- and post-AVR models. Thus, a first step is the introduction of additional boundary patches, e.g. the one used to identify the septal surface of corresponding to the RV. This was done using the internal Python class kd-tree and applying the nearest-neighbour method on the LV, RV and epicardial surfaces.

The next step required solving defined Laplace problems within the Bayer et al.[25] framework to obtain the UVC coordinates of the LV domain of the pre-AVR and post-AVR state, and was performed using our in-house multiphysics simulation software, ***CHeart*** .

Following the construction of the UVC for the two different growth states of the LV we computed the closest match between the nodal coordinates of the pre- and post-AVR meshes and identified, which allowed us to compute the displacement field in UVC coordinates. Subsequently, the displacement field was mapped back into the Cartesian coordinates.

By employing the UVC framework it was possible to perform a direct comparison between two individual meshes and analyse the changes introduced by growth on regional, element or nodal levels. This means, for example, that for each node in the pre-AVR space, we can find a corresponding coordinate in the post-AVR space. After obtaining the displacement field $\boldsymbol{u}$ we utilise the theory of kinematic growth to compute the

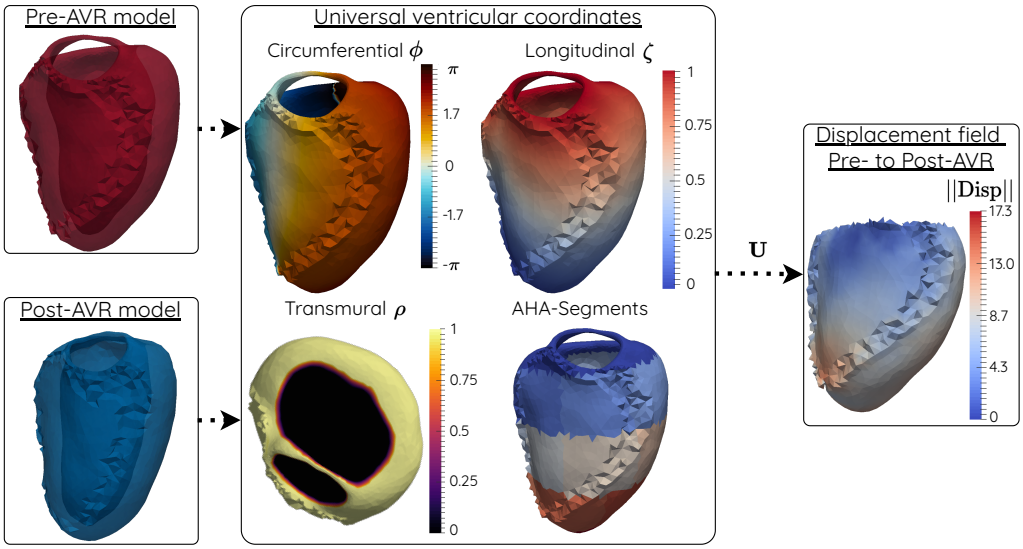

Figure 6.1 Personalised workflow for inverse modelling of G&R following AVR. After extracting the Pre-AVR (red) and Post-AVR (blue), the universal ventricular coordinates (UVC) for each model are generated. The circumferential coordinates ϕ of the model are defined in the range $+/-\phi$. The long-axis of the LV is defined with $0 \leq \zeta \leq 1$. The transmural direction is defined across the heart wall, from the endocardium to the epicardium with 0 to 1, respectively. For each model, the AHA-segments are further calculated. The final step calculates the displacement field $\mathbf{u}$ by interpolating the UVC coordinates of the Pre-AVR model to the Post-AVR model coordinates. The last frame visualises the Post-AVR model with the warped Pre-AVR model (yellow points).

deformation gradient $\boldsymbol{F}$ and subsequently derive the inelastic growth deformation gradient $\boldsymbol{F}_g$ and further the right Cauchy–Green deformation tensor $\boldsymbol{C}_g$ for each node. Subsequently, we performed an eigendecomposition on the individual nodes and then averaged the outputs within the AHA segments.

6.1.2 Kinematic Growth and the corresponding Geometrical Changes in the Heart following AVR

This section gives an overview of the well-established theory of kinematic growth based on the multiplicative decomposition of the deformation gradient $\boldsymbol{F}$ into an elastic and inelastic thermodynamic system[142], for a deeper discussion of the kinematics of the reader is directed to Chapter 2.4. Stating the reference position of material points in $\mathbf{X} \in \mathbb{R}^3$, the material follows a path that is defined via the displacement field $\boldsymbol{u} \in \mathbb{R}^3$ during deformation resulting in the current position in $\boldsymbol{x} \in \mathbb{R}^3$, illustrated in Figure 6.2. And can be defined by the deformation gradient $\boldsymbol{F}(\mathbf{X},t) = \partial \boldsymbol{u}/\partial \mathbf{X} + \boldsymbol{I}$ that describes local changes of stress, strain and deformation with respect to surrounding material points.

Within the kinematic G&R framework, this bijective deformation gradient is split into an inelastic (growth) $\boldsymbol{F}_g$ and an elastic component $\boldsymbol{F}_e$, resulting in a description of the

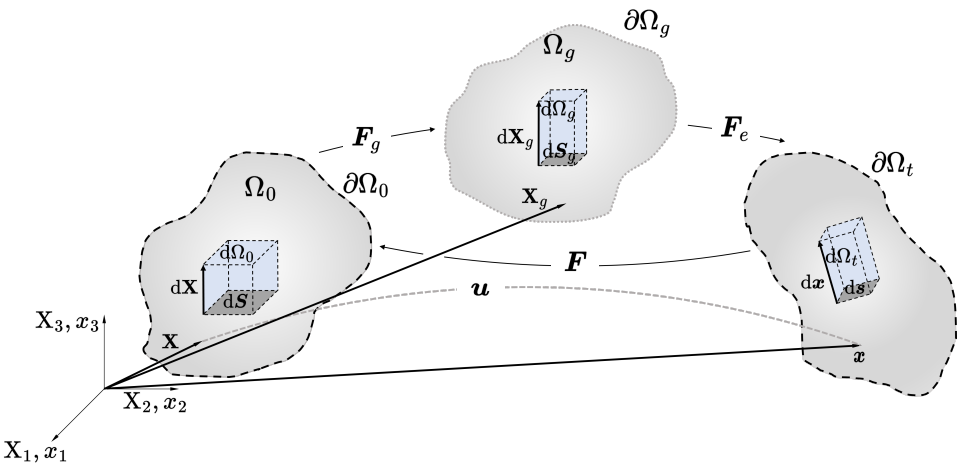

Figure 6.2 Kinematics of a growing body, with the reference domain Ω_0, and the physical domain Ω_t that are mapped via the deformation gradient $\boldsymbol{F}$, the growth deformation gradient $\boldsymbol{F}_g$ and the elastic deformation gradient $\boldsymbol{F}_e$.

deformation gradient as

$$\boldsymbol{F} = \boldsymbol{F}_e \boldsymbol{F}_g. \tag{6.1}$$

Incompatibility of G&R is assumed to result from the decomposition of the $\boldsymbol{F}_g$ term, which can not be captured by a gradient field in the way $\boldsymbol{F}$ arises from $\boldsymbol{u}$, and therefore does not satisfy classical kinematic compatibility conditions[236]. The scope of this chapter centres around analysing certain properties of the growth tensor, such as eigenvalues and eigenvectors, and identifying or establishing a relationship to the underlying microstructure of the myocardium. Consequently, we constrained the deformation gradient $\boldsymbol{F}$ to be solely dependent on $\boldsymbol{F}_g$ by setting $\boldsymbol{F}_e = \boldsymbol{I}$ resulting in relation

$$\boldsymbol{F} = \boldsymbol{I}\boldsymbol{F}_g, \tag{6.2}$$

where the body undergoes zero elastic deformation. The commonly agreed definition of the kinematic growth tensor goes back to the description of growth along the myocardial microstructure[98,97,80,200,168], resulting in

$$\boldsymbol{F}_g = \vartheta_{\boldsymbol{f}} \mathbf{e}_{\boldsymbol{f}} \otimes \mathbf{e}_{\boldsymbol{f}} + \vartheta_{\boldsymbol{s}} \mathbf{e}_{\boldsymbol{s}} \otimes \mathbf{e}_{\boldsymbol{s}} + \vartheta_{\boldsymbol{n}} \mathbf{e}_{\boldsymbol{n}} \otimes \mathbf{e}'_{\boldsymbol{n}} \tag{6.3}$$

where $\mathbf{e}_i$ with $i = \boldsymbol{f}, \boldsymbol{s}, \boldsymbol{n}$ is associated with a unit vector along fibre ($\boldsymbol{f}$), sheet ($\boldsymbol{s}$) and sheet-normal ($\boldsymbol{n}$) direction and ϑ_i are the growth stretches in the respective direction. In this study, we didn't make any assumptions regarding the main growth directions. Instead, we assessed the eigenvalues, eigenvectors and Frobenius norm of the computed right Cauchy-Green growth strain tensor $\boldsymbol{C}_g$ from the displacement field $\boldsymbol{u}$ within the standard American Heart Association[39] (AHA) regions of the LV and the RV junction. The AHA divides the LV into 17 anatomical segments by equal thirds perpendicular to the long axis of the heart, which generates three circular sections basal, mid-cavity and

apical from the valve area down to the apex, respectively, see Figure 6.3. The basal section is further divided into six identical sections along the circumferential direction: basal anterior (1), basal anteroseptal (2), basal inferorseptal (3), basal inferior (4), basal inferolateral (5) and basal anterolateral (6). The second ring with six elements indicates the mid-cavity section with the mid anterior (7), mid anteroseptal (8), mid inferorseptal (9), mid inferior (10), mid inferolateral (11) and mid anterolateral (12) sections of the LV. Segments surrounding the apex area are the apical anterior (13), apical septal (14), apical inferior (15) and apical lateral (16) elements. The inner circle represents the apex (17) segment of the LV. Utilising the AHA model gives also additional insight into the locations of the coronary arteries such as left anterior descending (LAD), right coronary artery (RCA) and left circumflex (LCX) with respect to the areas of the LV.

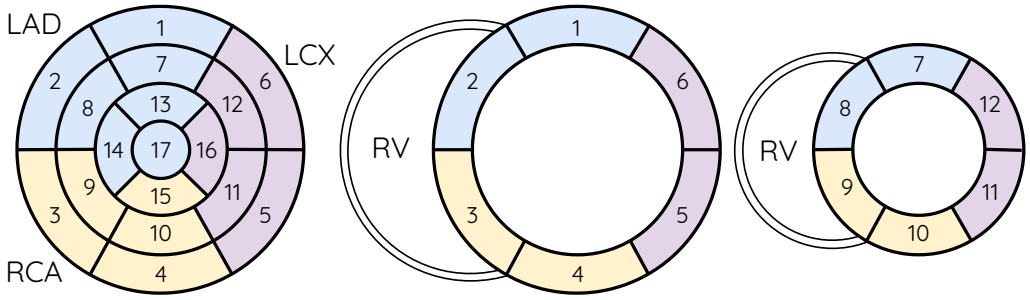

Figure 6.3 Regions of the LV defined by the standard American Heart Association 17-segment model (AHA) and the junction regions to the RV. The areas defined along the base plane (outer ring): 1. basal anterior, 2. basal anteroseptal, 3. basal inferorseptal, 4. basal inferior, 5. basal inferolateral and 6. basal anterolateral. Sections in the mid-cavity (second outermost ring) area are referenced as 7. mid anterior, 8. mid anteroseptal, 9. mid inferorseptal, 10. mid inferior, 11. mid inferolateral and 12. mid anterolateral. Surrounding the apex: 13. apical anterior, 14. apical septal, 15. apical inferior and 16. apical lateral. And with the apex represented by the element 17. The additional labels around the model are the regions related to the coronary arteries such as left anterior descending (LAD), right coronary artery (RCA) and left circumflex (LCX).

6.1.3 Patient Cohort

This study is comprised of eight AS cases in which the patients underwent either TAVR (n=4) or SAVR (n=7) treatments. Dynamic CT images and the LV and RV cavity pressure were acquired before surgery (up to 3 years in advance) over an entire cardiac cycle, cavity pressures for pre- and post-intervention are given in Tables 25–28. The data of the post-state incorporated static CT images and cavity pressures at the ED state up to 1 year post-surgery. For direct comparison, patient-specific models were generated at the ED state of the heart.

6.2 Results and Discussion

6.2.1 Patient-specific Comparison between Reverse Growth and Adverse Growth Outcome following SAVR

This section compromises preliminary results of two SAVR patient cases (SAVR 1 and SAVR 7) where the patients responded either with myocardial net-volume decrease, referred to as reverse growth or with adverse growth, a further net-volume increase of the myocardial volume. Additional results are included in the Section Appendix .3, Figure Appendix 10-18 This Section Appendix .3 contains a broader cohort with, for example, less successful deployments of AVR or mitral regurgitation, displaying persistent volume overload states.

Initially, the volume change between the Post-AVR and Pre-AVR states was compared to identify the apparent changes within the AHA regions. Here we quantified the change as $v/V0$, with values below one indicating reverse growth, those over one indicating growth, and those equal to 1 corresponding to no growth. In Figure 6.4 and 6.5(A), the volume ratio following SAVR in a case of reverse growth or adverse growth are visualised, respectively. The blue colour scheme represents areas of reverse growth as a response to the surgery, while red regions indicate additional growth and grey areas indicate no significant volume change between the states. In both cases, reverse growth and adverse growth, an average increase of the volume was observed in the basal anterior and basal anterolateral regions of the heart. In contrast, the basal inferoseptal region responded to pressure unloading with high amounts of reverse growth and even in the case of adverse growth the LV undergoes in comparison to the other AHA segments a lower quantity of growth in the LV free wall. Based on the volume comparison, no significant assumption about the growth tensor can be made due to the high heterogeneity of this quantity throughout the LV.

Subsequently, the Frobenius norm of the right Cauchy-Green growth tensor $\boldsymbol{C}_g$ was analysed to identify regions affected by G&R following a presumably successful or not successful SAVR procedure, visualised in Figure 6.4 and 6.5(B). In the case of no growth or changes due to inelastic deformation, the right Cauchy-Green growth tensor $\boldsymbol{C}_g$ equals the identity. Blue regions in the AHA indicate reverse growth, while red areas are subsequently linked to growth areas in the LV.

Similar to what we saw in volume ratio plots, the norm plots suggest that hearts which undergo reverse growth at the organ level can continue to display regions of adverse growth, in particular at the junction between the LV and RV. In both cases, reverse growth and adverse growth, we observe higher values for the norm of the right Cauchy-Green growth tensor in the LV free wall region, while the septal area indicates lower values for $||\boldsymbol{C}_g||$. In both cases, reverse growth and adverse growth we notice a heterogeneous pattern across the heart, see Figure 6.4 and 6.5 (B). Furthermore, higher

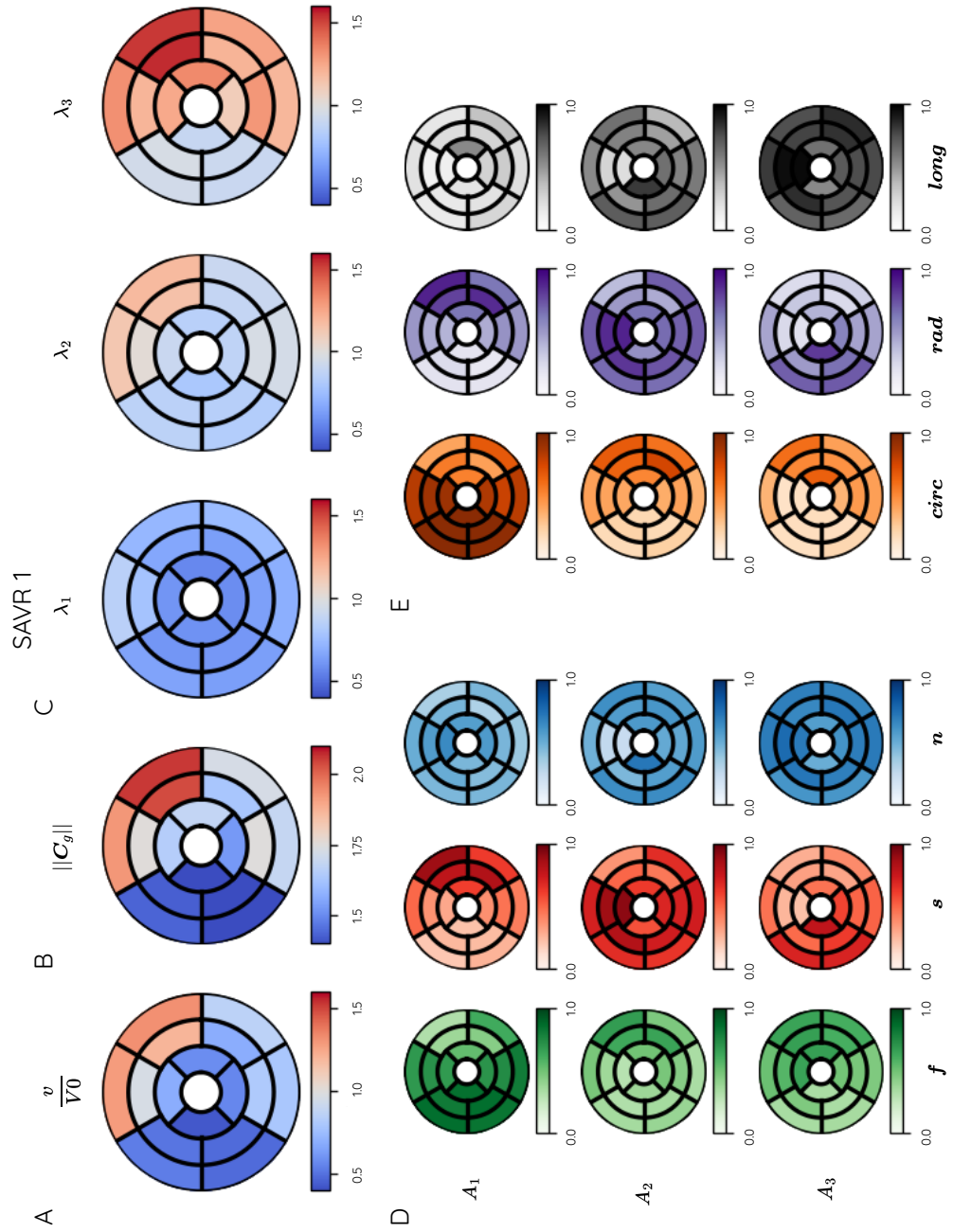

Figure 6.4 Reverse growth pattern analysis in SAVR 1. (A) displays the average volume ratio of the post-AVR state after adverse growth to the reference volume of the pre-AVR state across the LV. (B) illustrates the calculated mean Frobenius norm of the right Cauchy-Green growth tensor $\mathbf{C}_g$ within the 17 AHA segments. (C) presents the mean principal stretches λ_1, λ_2 and λ_3 in ascending order within the AHA regions of the LV. Previous colour codes refer to either high (red) or low (blue) values. (D) shows the associated eigenvectors to the principal stretches presented in (C), where a directional agreement with the fibres, sheet, or sheet-normal direction is indicated by green, red or blue, respectively. (E) shows the associated eigenvectors to the principal stretches presented in (C), where a directional agreement with the circumferential, radial, or longitudinal direction is indicated by grey, purple or orange, respectively.

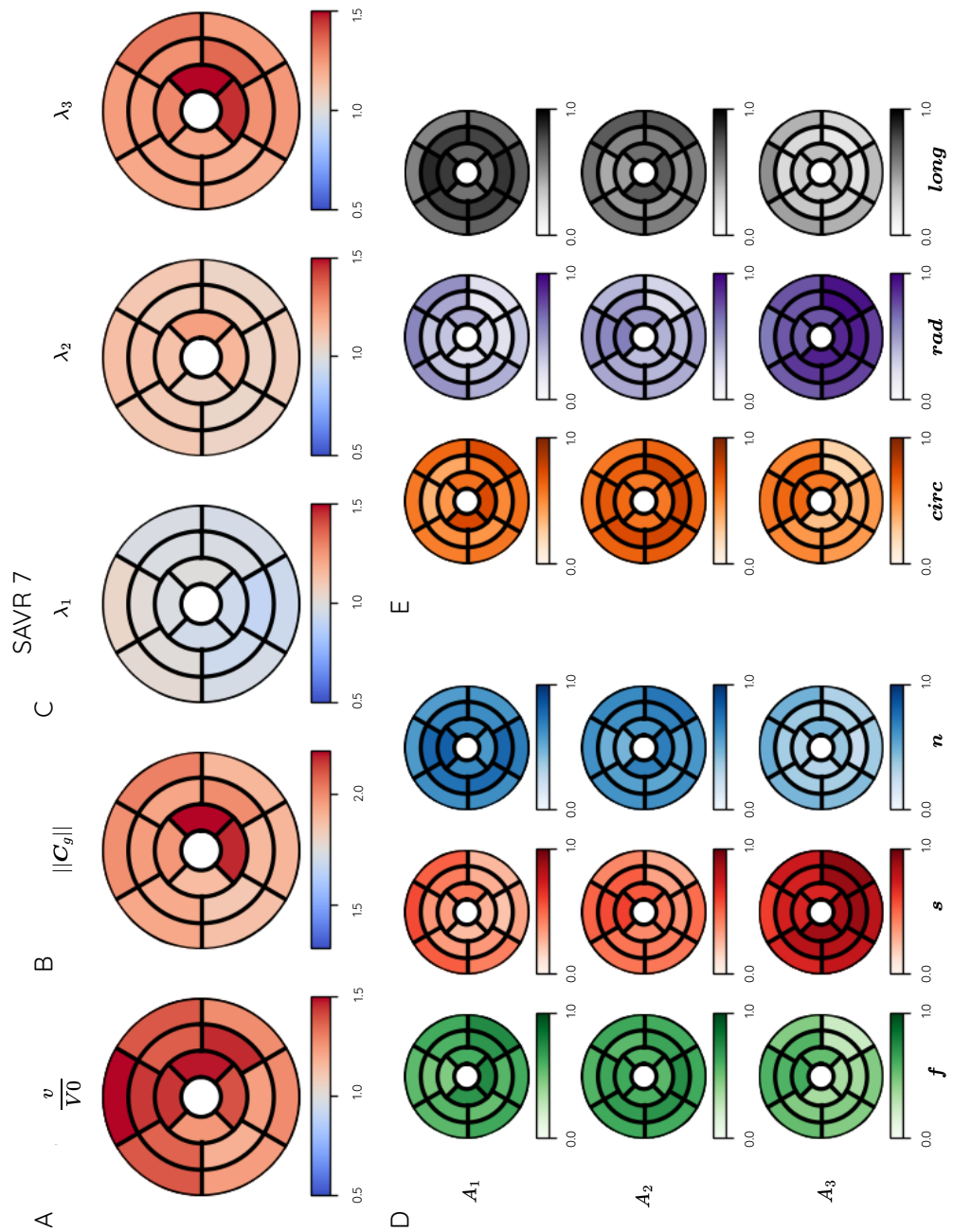

Figure 6.5 Adverse growth pattern analysis in SAVR 7. (A) displays the average volume ratio of the post-AVR state after adverse growth to the reference volume of the pre-AVR state across the LV. (B) illustrates the calculated mean Frobenius norm of the right Cauchy-Green growth tensor $\mathbf{C}_g$ within the 17 AHA segments. (C) presents the mean principal stretches λ_1, λ_2 and λ_3 in ascending order within the AHA regions of the LV. Previous colour codes refer to either high (red) or low (blue) values. (D) shows the associated eigenvectors to the principal stretches presented in (C), where a directional agreement with the fibres, sheet, or sheet-normal direction is indicated by green, red or blue, respectively. (E) shows the associated eigenvectors to the principal stretches presented in (C), where a directional agreement with the circumferential, radial, or longitudinal direction is indicated by grey, purple or orange, respectively.

levels of growth can be observed in the surrounding apical region of the heart in the case of adverse growth, see Figure 6.5(B).

Next, we analysed the spatial variation of the anisotropy and principal stretches of $\boldsymbol{C}_g$ (λ_1, λ_2 and λ_3). Spatial homogeneity may be indicated by comparable square roots of the eigenvalues of the right Cauchy-Green growth tensor $\mathbf{C}_g$ throughout the heart, with an isotropic growth pattern introducing equivalent growth along the eigenvectors. In contrast, an anisotropic growth pattern would be characterised by a heterogeneous distribution. The eigenvalues (λ_i with i=1,2,3) in Figure 6.4 and 6.5(C) are arranged in ascending order from left to right. With $\lambda < 1$ suggesting an average amount of reverse growth throughout the AHA segment and red ($\lambda > 1$) indicating adverse growth within the segment.

The first eigenvalue was associated with the lowest amount of change in the direction of the first eigenvector, see Figure 6.4C. In the case of reverse growth, the first eigenvalue suggests a heterogeneous reverse growth pattern indicated by all segments being blue throughout the heart. Higher amounts of reverse growth were observed in the septal and the apex surrounding areas. The second eigenvalue indicates a higher amount of heterogeneity is observed with values around the neutral area ($\lambda_2 = 1$), values around this value do not indicate any significant changes. The third eigenvalue included the highest eigenvalues along the third eigenvector and was linked to adverse growth in the different AHA regions. In this particular patient, a high amount of adverse growth in the LV free wall can be observed while the septal region remains to undergo reverse growth.

In contrast, adverse growth appeared more homogeneous across the second eigenvalue (λ_2), displayed in Figure 6.5C. The first eigenvalues of the AHA regions are aligned closely to $\lambda_1 = 1$. A homogeneous hypertrophy pattern can be observed in the third eigenvalue (λ_3) with lower values in the septal region and higher regions in the LV free wall and surrounding apical areas. The eigenvalue pattern in both of these cases, reverse and adverse growth, suggests a high spatial heterogeneity related to the first and third eigenvalues.

While the eigenvalues of $\boldsymbol{C}_g$ give an idea of the way G&R occurs (reverse growth or adverse growth) in the AHA segment, the corresponding eigenvector gives insight into the orientation of growth. Commonly utilised growth models are based on a kinematic growth tensor description via the underlying microstructure inside the myocardium, see Equation 6.3 or if growth appears to be aligned with the geometrical coordinates of the heart. Here we assess the eigenvectors of $\boldsymbol{C}_g$ and compare them with the alignment of the microstructure orientation to identify if this description of growth in cardiac tissue is a valid way to describe G&R or if the geometrical description gives further insight into the individual growth patterns.

In Figure 6.4 and 6.5(D) the mean basis vectors of the right Cauchy-Green growth tensor (A_1, A_2 and A_3), related to the AHA segments are illustrated with respect to the mean eigenvectors of the microstructure ($\boldsymbol{f}, \boldsymbol{s}$ and $\boldsymbol{n}$). Here, the individual colours represent the dominant orientation of the basis vector compared with the microstructure orientation. Where dark green indicates a strong alignment with the fibre ($\boldsymbol{f}$) orientation, dark red represents an alignment with the sheet ($\boldsymbol{s}$) orientation and dark blue depicts an alignment with the sheet-normal ($\boldsymbol{n}$) direction.

Figure 6.4D, suggests that in patients reacting with reverse growth following AVR the highest amount of reverse growth appears to be heterogeneous across the heart. The first eigenvector in the septal region aligned along the fibre direction and reverse growth aligned to the sheet direction within the LV free wall. The second eigenvector, suggests growth in the sheet direction across all AHA segments. In contrast, the third eigenvector appears predominately aligned with the sheet-normal direction of the myocardium.

However, Figure 6.5(D) shows a growth pattern in patients reacting with adverse growth following AVR. The entries of the first and second eigenvectors appear to be spatial heterogeneous with fibre and sheet-normal alignment. In comparison, the third eigenvector suggests hypertrophy predominantly in the sheet direction.

Apart from analysing hypertrophy concerning the microstructure of the myocardium we investigated the growth alignment with the geometrical structure of the heart, see Figure 6.4 and 6.5(E). To acquire this information, we examined the orientation of the eigenvectors of $\boldsymbol{C}_g$ (A_1, A_2 and A_3) related to the local geometrical coordinates (circumferential $\boldsymbol{circ}$, radial $\boldsymbol{rad}$ and longitudinal $\boldsymbol{long}$) further averaged the outcome within the AHA segments for a subsequent investigation.

Analysing the growth alignment concerning the geometrical directions following reverse growth suggested reverse growth primarily in the circumferential direction in the septal and junction area of the LV and RV, see Figure 6.4(E). Alternatively, A_3 was highly aligned in the longitudinal direction within the AHA segments.

Conversely, A_1 in the adverse growth patient suggested an alignment with the longitudinal direction, visualised in Figure 6.5E. A_2 indicated a high agreement of growth along the circumferential direction. Whereas the third eigenvector indicates mainly growth in the radial direction across the heart.

6.2.2 Cohort Comparison between Reverse Growth and Adverse Growth Outcome following SAVR

The previous results focused on growth patterns seen in individual patients (Section 6.2.1), this section focuses on identifying hypertrophy patterns across patients that underwent reverse growth (SAVR 1, SAVR 4, SAVR 5 and SAVR 6) or adverse growth

(SAVR 2, SAVR 3 and SAVR 7) following SAVR, as well as reverse growth following TAVR (TAVR 1, TAVR 2, TAVR 3 and TAVR 4). Latter cohort (TAVR RG) results are included in Figure Appendix 19. For a better understanding, we refer in this section to the reverse growth cohort following SAVR as RG cohort, and to the adverse cohort following SAVR as AG cohort. The cohort mean and standard deviations of the volume ratio, Frobenius norm of $\boldsymbol{C}_g$ and the principal stretches across the patients and the AHA segments for RG and AG cohorts are visualised in Figure 6.6 and 6.7, respectively. The upper bounds for the analysed value range within the different plots were adjusted to facilitate a direct pattern comparison between the RG and AG cohorts. This adjustment, especially in the AG cohort, resulted in segments exceeding the maximum values, which were indicated by an asterisk in the AHA region.

Figure 6.6 and 6.7(A) illustrate the average volume change in the RG and AG cohorts, respectively. We observed heterogeneous mean volume ratio changes in the RG group following SAVR, indicating a decrease in volume across the entire LV. Conversely, in the AG cohort, an increase in volume is primarily registered across the cohort. A common growth pattern in patients with adverse growth can be observed in the basal, mid, and apical inferior segments of the AG cohort, as shown in Figure 6.7A.

Figure 6.6 and 6.7(B) visualises the mean of the Frobenius norm of $\boldsymbol{C}_g$ across AHA regions of the LV in the event of reverse growth or adverse growth within the patient's hearts, respectively. In the RG cohort, we observed that the highest value of the average cohort Frobenius norm mean appears close to the values for the right Cauchy-Green tensor $\boldsymbol{C}_g = 1$. Furthermore, higher amounts of reverse growth are observed in the septal region (basal and mid anteroseptal regions) of the LV, while the free wall exhibits a mix of reverse growth and low amounts of adverse growth. In contrast, in the AG cohort, we see much higher values across the LV, particularly in the basal inferior, apical inferior and apical lateral regions. Both of the cohorts suggest heterogeneous behaviour responding to AVR.

Figure 6.6 and 6.7(C) illustrates the cohort averaged principal stretches (λ_1, λ_2 and λ_3) within the RG or AG cohort following SAVR, respectively. Examining the average first principal stretch in the RG, a homogeneous response of reverse growth in the LV was observed. In comparison, mean(λ_2) ranges around 1.0 and mean(λ_3) indicates high heterogeneity with adverse growth in the LV free wall and inferior LV and RV junction area. The eigenvalues in adverse growth appear across all principal stretches with higher heterogeneity than mean(λ_i) with $i = 1, 2, 3$ of the RG cohort. In the AG cohort, the first and second principal stretches appear to fluctuate around 1.0. The third eigenvalue suggests a homogeneous hypertrophy behaviour within the LV with higher values of growth in the inferior junction area of the LV and RV and the apical inferior and lateral segments.

Figure 6.6 and 6.7(D) visualises the standard deviation of the averaged volume changes

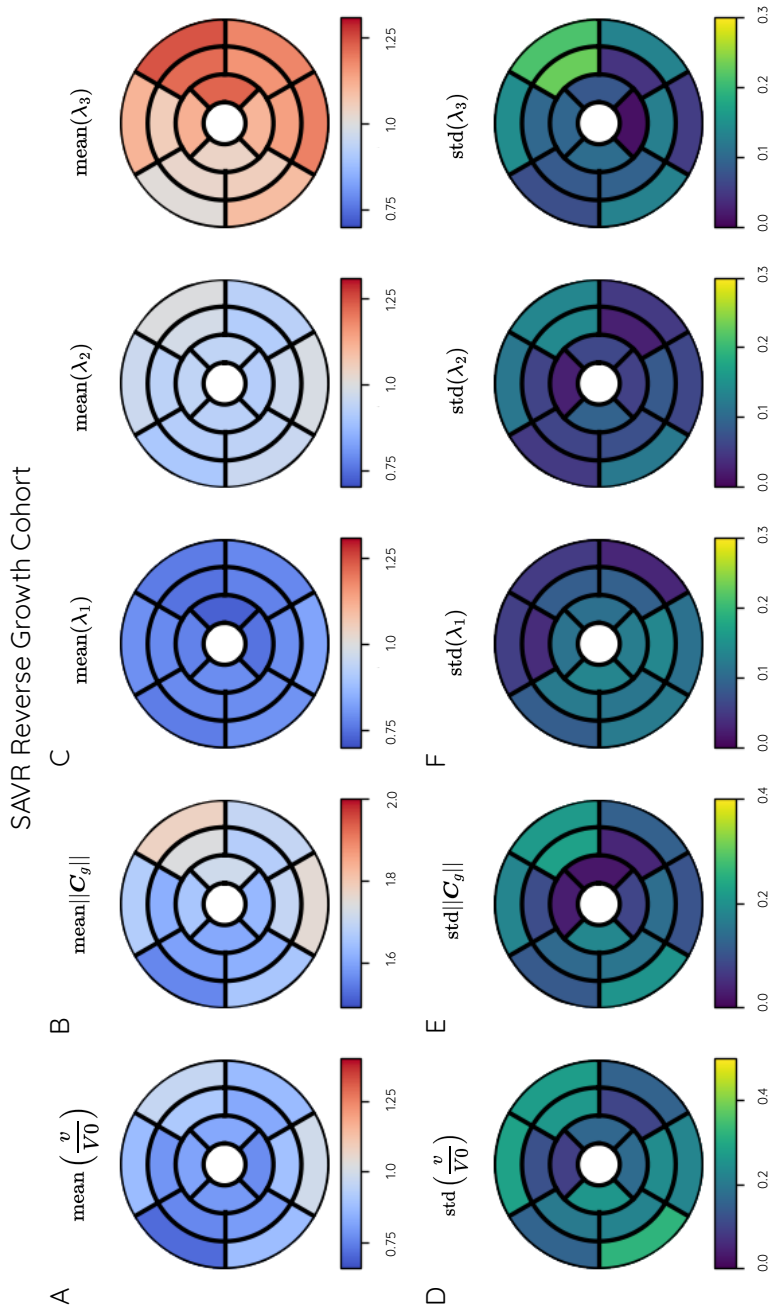

Figure 6.6 Reverse growth pattern analysis in SAVR patient cohort. (A) displays the mean volume ratio change of the post-AVR state after adverse growth to the reference volume of the pre-AVR state across the LV. (B) illustrates the calculated mean Frobenius norm of the right Cauchy-Green growth tensor $\mathbf{C}_g$ within the 17 AHA segments. (C) presents the mean square roots of the eigenvalues of $\mathbf{C}_g$ (λ_1, λ_2 and λ_3) in ascending order within the AHA regions of the LV. Previous colour codes refer to either high (red) or low (blue) values. (E) displays the standard deviation of the volume ratio of the post-AVR state after adverse growth to the reference volume of the pre-AVR state across the LV. (F) illustrates the calculated standard deviation of the Frobenius norm of the right Cauchy-Green growth tensor $\mathbf{C}_g$ within the 17 AHA segments. (G) presents the standard deviation of the eigenvalues of $\mathbf{C}_g$ in ascending order within the AHA regions of the LV. Previous colour codes refer to either high (yellow) or low (dark blue) values.

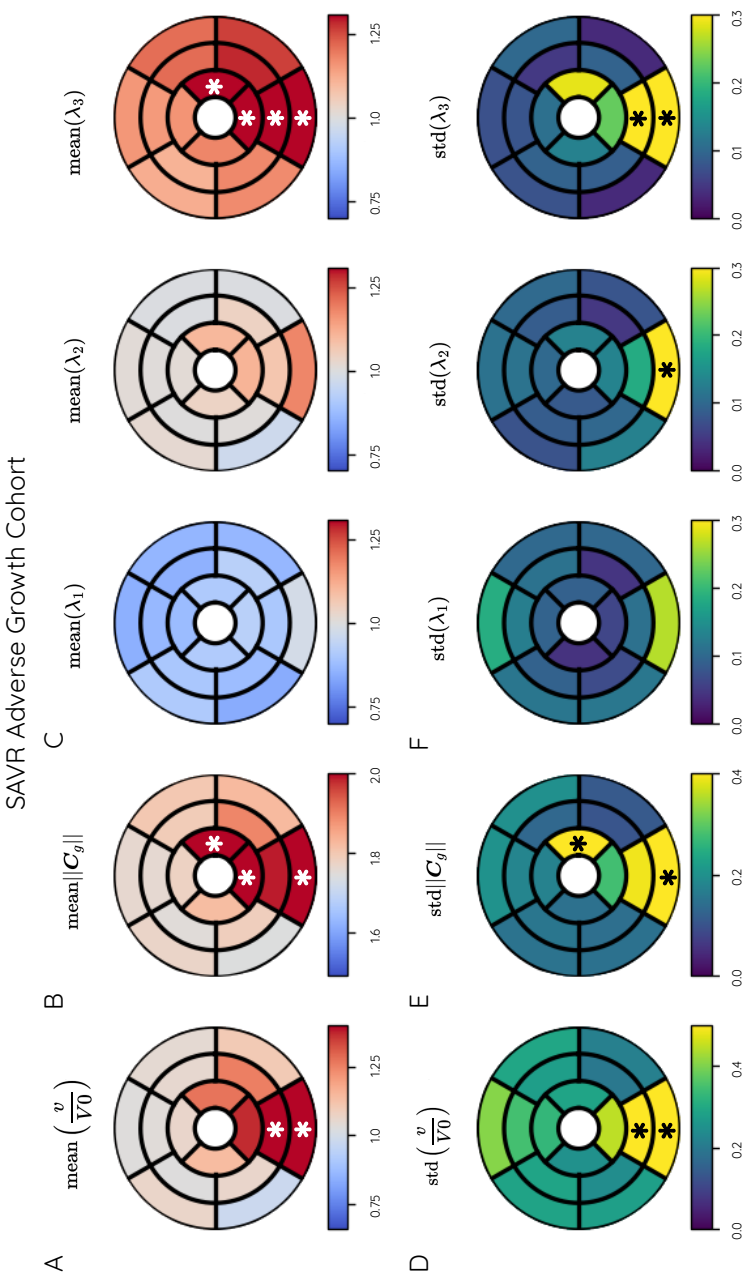

Figure 6.7 Adverse growth pattern analysis in SAVR patient cohort. (A) displays the mean volume ratio change of the post-AVR state after adverse growth to the reference volume of the pre-AVR state across the LV. (B) illustrates the calculated mean Frobenius norm of the right Cauchy-Green growth tensor $\mathbf{C}_g$ within the 17 AHA segments. (C) presents the mean square roots of the eigenvalues of $\mathbf{C}_g$ (λ_1, λ_2 and λ_3) in ascending order within the AHA regions of the LV. Previous colour codes refer to either high (red) or low (blue) values. (E) displays the standard deviation of the volume ratio of the post-AVR state after adverse growth to the reference volume of the pre-AVR state across the LV. (F) illustrates the calculated standard deviation of the Frobenius norm of the right Cauchy-Green growth tensor $\mathbf{C}_g$ within the 17 AHA segments. (G) presents the standard deviation of the eigenvalues of $\mathbf{C}_g$ in ascending order within the AHA regions of the LV. Previous colour codes refer to either high (yellow) or low (dark blue) values. An asterisk in the AHA segment indicates a value higher than the upper bound of the data range.

across the RG or AG patient cohort hearts, respectively. The small standard deviation of volume change in the RG group suggests minimal variation within the cohort as a response to the intervention. Conversely, in the AG cohort, we observe a higher variation of the adverse growth behaviour within the AHA segments following SAVR, with considerably greater variation than in the RG cohort, especially in the RV and LV junction segments. Notably, values in the basal and mid inferior regions exceed the upper bound for the volume ratio standard deviation.

However, analysing the mean standard deviation patterns of the Frobenius norm of the $\boldsymbol{C}_g$ indicated a lower variation between RG patients, see Figure 6.6E. In contrast, a higher variance of std$||\boldsymbol{C}_g||$ in the AG cohort was observed, particularly in the apical lateral, basal and mid inferior segments, displayed in Figure 6.7E.

Analysing the standard deviations across cohorts and comparing them, it becomes apparent that reverse growth has a low standard deviation of the principal stretches (λ_1, λ_2 and λ_3), with higher values of variation observed in the anterolateral regions in the post-intervention hearts, as shown in Figure 6.6F. However, reverse growth appears to progress similarly across patients following SAVR. At the same time, the AG cohort's post-interventional behaviour indicates a higher variability in the standard deviation across all principal stretches. The standard deviation of the first principal stretch indicates a higher variance within the basal RV and LV junction areas of the LV (basal anterior and basal inferior AHA segments). Additional, significant differences were observed in the third principal stretch of the AG cohort, particularly in the inferior segments and the apical inferior and lateral region, as seen in Figure 6.7F.

6.3 Limitations

A limitation of this study was the focus on the kinematic changes without addressing the changes of the pressure triggered by intervention. An immediate response of the heart to AVR is a decrease in the pressure gradient between the LV and aorta with the pathophysiological LV end-diastolic pressure (LVEDP) decreasing to a new pressure state following intervention. This study utilised the EDP geometries of the pre- and post-AVR states directly, yet the difference in loading between these two states was not considered. By incorporating the changes in the loading condition we potentially acquire further information on the kinematic changes of the heart due to G&R following AVR.

A further limitation of this study was that the kinematics of the RV were not considered and the study was restricted to the LV. This might give further insight into the spatial variation of the kinematic growth tensor within the joint area between LV and RV. As previously observed in Chapter 5, we could see a highly heterogeneous behaviour of the mass changes following AVR, which might be studied in detail by studying G&R in a

bi-ventricular model.

6.4 Conclusion

Within the scope of this study, we studied G&R patterns in the heart following AVR with an inverse problem approach. A special focus was on the identification of G&R patterns within different outcomes following AVR, such as reverse growth and adverse growth. Results across all patients individually suggested spatial heterogeneous and anisotropic G&R patterns following SAVR or TAVR.

Analysing G&R in patient cohorts including either reverse growth or adverse growth following SAVR, we noticed lower degrees of variability within the RG cohort, in particular in the first principal stretch λ_1. These results imply that in the event of reverse growth the heart adapts throughout this patient group in a similar way. On the other hand, adverse growth appears to exhibit higher variation between G&R patterns in the LV across a patient cohort especially in the basal basal inferior segments of the LV where the RV connects, where a particularly high variance was observed in the highest principal stretch λ_3 This could be caused by different reasons, for example, as a result of differing amounts of growth in the RV than in the LV. An alternative explanation for this could also be a higher degree of volume change in the valve area. Future studies may look into increasing the cohort size, in order to reduce the impact of outliers, and allow for a better understanding of G&R following AVR. Nevertheless, the results collected in this study exhibit that reverse growth (alignment of the first eigenvector) following SAVR occurs primarily in the sheet direction with combinations of fibre or sheet-normal growth in the myocardium. On the other, the third eigenvector suggests an orientation along the sheet-normal direction. Analysing the changes with respect to the geometrical coordinates of the LV indicated reverse growth in circumferential and radial directions. Whereas, the third eigenvector indicated an alignment in the longitudinal direction. In the case of adverse growth, further adverse growth after intervention appears to be aligned along the sheet and radial direction to adapt to the new loading condition of the LV. These findings are in strong agreement with the results computed in Chapter 5.

7 Conclusions and Future Directions

Growth and remodelling (G&R) phenomena are commonly observed in living structures to adapt to changes in the loading condition or other underlying mechanisms. G&R of the heart can either occur as an adverse response to a disease, such as HCM, AS, or MI, or in the case of reverse remodelling following drug therapy or surgical intervention.

With commonly available computational methods, the morphological changes caused by to remodelling can be tracked over time, however our understanding of the underlying mechanisms is still sparse. Utilising the kinematic growth theory that is based on a multiplicative split of the deformation gradient into its growth contribution and an elastic contribution permits the computational modelling of alterations due to G&R.

In Chapter 3, we analysed different properties of the kinematic growth tensor, specifically the potential introduction of incompatibility. We observed that within a highly simplified problem, i.e. where growth is not restricted, the choice of material law does not impact the outcome of growth. The individual cases suggested that perturbations of the kinematic growth tensor consistently resulted in a compatible grown state. In contrast, heterogeneous growth tensors or tensors which do not satisfy the condition $(\nabla \boldsymbol{u} + \boldsymbol{I})\boldsymbol{F}_g^{-1} = \boldsymbol{I}$, introduce incompatibilities or residual stresses. Conducting an in-depth investigation, we observed that incompatibilities lead to a distinct configurations in the grown states dependent on the constitutive laws.

Building on the previous results, we performed a growth pattern analysis of the phenotypical HCM growth pattern. We focused on this disease as it presents a high degree of heterogeneity. Within Chapter 4, we investigated three hypotheses (fibre disarray, heterogeneous growth or isotropic growth) in an attempt to model focused septal growth observed in phenomenological HCM hypertrophy patterns. We observed that throughout all tests, applying an isotropic growth tensor consistently led to the focal septal growth. This behaviour could be explained by an excess of fibrosis or inflammation in this area.

In the next step of this thesis, we moved forward on to cardiac applications involving AS patient-specific data (n=8; $n_{SAVR} = 6$, $n_{TAVR} = 2$) pre-AVR and post-AVR, see

Chapter 5. A modelling pipeline was introduced, which was split into a personalised biomechanical model generation of the pre-AVR state and a modelling of the post-AVR state. In the post-processing stage, we compared different metrics of the pre-AVR, post-AVR data with the modelled post-AVR states to determine the G&R patterns observed in the patients following AVR. G&R following AVR can take the form of either reverse growth or adverse growth, as such, in this study we analysed the individual growth patterns and additionally we investigated the potential existence of a coherent growth pattern within patient cohort. Thus in some cases, we were able to show a trend of concentric reverse growth in patients who have undergone SAVR. However, in others, no specific G&R mode could be linked to the changes following the intervention. These findings indicate a highly heterogeneous response to AVR.

In Chapter 6, we analysed G&R in an AS patient cohort (n=10; $n_{SAVR} = 7$, $n_{TAVR} = 4$), by employing an inverse modelling approach to identify G&R patterns. This method enables us to study G&R in living structures without the need for defining a kinematic growth tensor for the individual material points in the continuum body. One coherent pattern that we could identify in the reverse growth SAVR cohort was that the mean of the eigenvalues of the computed growth tensor $\boldsymbol{C}_g$ appears to be homogeneous across the heart. In contrast, within the adverse response group, we noticed a more heterogeneous pattern, especially, in the basal inferoseptal segment of the AHA LV. This may be caused by the heterogeneous growth behaviour of the LV and RV in this area or caused by the proximity to the valves, which also undergo G&R following AVR. Furthermore, we assessed the standard deviations of the reverse growth and adverse growth cohorts. Here the results indicated that in the event of reverse growth, the standard deviations appeared to be low, which indicates that the growth pattern within this cohort had a relatively low variation. On the other hand, for the adverse reaction patients, we instead observed a more significant variation.

7.1 Future directions

7.1.1 Heterogeneity

One way to make precise predictions of growth in cardiac applications would be the use of a patient cohort for which is the data is more consistently collected. In this work, specifically in Chapter 5 and 6, we had to impute some of the patient data, such as the pre- and post-AVR pressure, through estimations based on other patients which displayed the same amount of growth. An improvement of this study may thus require a more consistent protocol for acquiring the pressure traces as well as for the medical images. By doing this, it may be possible to minimise heterogeneity caused by data acquisition. Similarly, the study of Mehdipoor et al. [167], suggested the collection of LV G&R data within the range of 6-15 months post-TAVR.

An additional source of heterogeneity that is not related to the growth pattern may be caused by the relatively small sample size of patient-specific G&R cases. Hence, future work should consider an increase in the patient cohort size to identify reverse and adverse growth patterns in the heart following AVR. This would allow us to better detect outliers.

By removing these sources of heterogeneity we would be in a better position to assess other reasons for heterogeneity that are more physiologically relevant to G&R modelling. This further enables a study in which spatial coherent behaviour in G&R can be analysed across patients.

In Chapter 6, we utilised an inverse approach to assess local volume changes following AVR. The next step forward in this field would be to apply the knowledge gained from this study to a biventricular G&R problem. Through this process, we would be able to identify and verify the inverse remodelling approach for cardiac applications.

7.1.2 Growth drivers

Despite the fact that we were able to introduce heterogeneous G&R patterns in cardiac applications, such as a phenotypical HCM pattern or reverse growth following AVR, we did not include the influence of growth drivers in our studies, which may be of mechanical (stresses or strains within the tissue), genetic or hormonal origin. Existing biomechanical models for G&R utilise stress or strain measurements to introduce growth in the heart, by comparing them with baseline measurements. However, there is no consensus on which is the physiologically accurate approach.

Throughout this thesis we utilised ED pressures, see Chapter 5, as a driver for remodelling in quasi-static G&R problems. In Chapter 3, we identified that growth introduces incompatibilities and residual stresses in biventricular models. Combining these results with pressure adaptation over time in the G&R problem may be a way to identify and understand heterogeneous remodelling patterns in the heart.

7.1.3 Time-dependent changes in the heart caused by G&R

Alongside changes in volume caused by remodelling of the heart in the case of reverse or adverse remodelling, alternations of the fibre and stiffness are a common occurrence in G&R. For simplicity, the fibre alignment was preserved throughout the simulation with no changes relative to the reference state. However, this is not actually true as a change in fibre orientation has been previously observed[89]. It is believed that this process may assist with reducing the afterload of the LV. In general though, incorporating such a change within a model would incur high computational costs as a result of the need for continuous meshing intermediate model and as a result it is generally excluded from numerical studies, which instead focus on muscle volume changes. However, it may be that this assumption drastically alter the modelled G&R pattern.

Throughout this study, we applied consistent myocardial stiffness parameters during the modelling of the post-AVR state, see Chapter 5. Yet, an increase in myocardial stiffness in patients with LV hypertrophy has been previously noted and can significantly affect the outcome of AVR[105,42,9,247]. This alternation can be linked to an increase in myocardial hypertrophy, fibrosis and consequent LV stiffness in adverse remodelling. On the other hand, studies suggest that by removing the transverse aortic constriction, the myocardial stiffness decreases over time[181]. These facts raise the more general question of how transient myocardial stiffness may impact G&R patterns more generally.

A future longitudinal study may investigate time-dependent alterations of the heart and incorporate data over the progression of G&R, such as CT and pressure traces which would be acquired consistently over a time frame before and after AVR. This would enable us to provide a more accurate parameter estimation corresponding to the intermediate remodelled configurations and also permit updating the fibre field, or would assist with measuring the impact of these factors in the G&R of the heart.

Appendices

Appendix .1. Supplementary Chapter 3

Appendix .1.1. Correlation Plots for Block Test

Fig. 1 contains a summary of the computational results of the relationship between the assumed gold standard solution for the deformation gradient entries $\mathbf{F}_{ij}$ of the Neo-Hookean material compared to the deformation gradient entries of the tested material law. The left side of this figure studies incompressible material laws while the right-hand side focuses on compressible materials. All the different alterations for the perturbations of the problems show a high correlation between the Neo-Hookean and the different material laws. In the case of a direct correlation, all entries align on the black line.

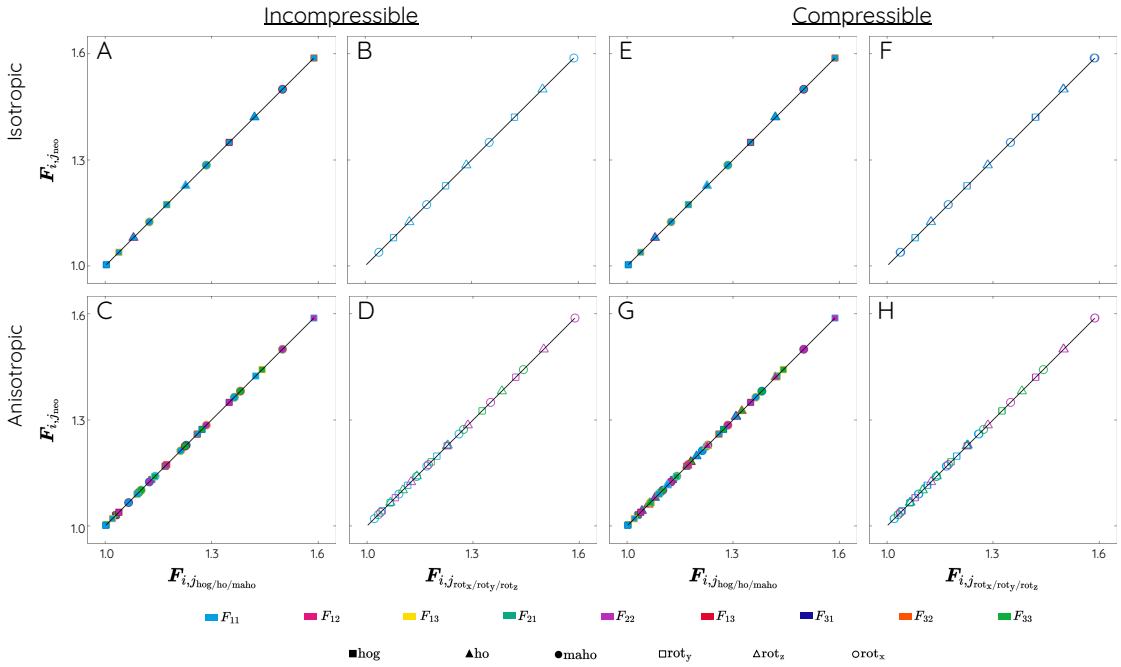

Figure 1 $\mathbf{F}_{ij}$ correlation plots in the cube model over time until the model reaches its final grown state (right top corner). (A–D) describes the individual tests in geometry for the related incompressible material laws, while (E–H) visualise in the corresponding ordering of the compressible material laws. The upper row shows the test cases in which an isotropic growth tensor was applied to the model. However, the bottom row displays the test cases with an anisotropic growth tensor in the same test. This way, it is only necessary to describe the difference between plots (A) and (B). (A) represents the progression of an isotropic growth tensor aligned or unaligned to the local coordinate system of the model with different material laws (filled marker shapes). (B) displays the trend of an aligned isotropic growth tensor with the model's coordinate system in an anisotropic material. In this specific plot, the impact of the microstructure is visualised by applying a rotation to the microstructure and making it unaligned to the coordinate system of the model itself (rot_X,rot_Y,rot_Z). This test was utilised with all of the fibre-reinforced models mentioned in the method section of this paper. For the correlation plot captioned with $\boldsymbol{F}_{ij}$ Rotation captures the behaviour of fibre-reinforced material laws with a 45° rotation in x, y or z-direction, represented by ∘, □ or △ respectively.

Fig. 1 in the appendix illustrates the correlation plots between the deformation gradient entries $\boldsymbol{F}_{ij}$ of the analysed material law and the gold standard solution (`neo`). In these figures, the various deformation gradient entries $\boldsymbol{F}_{ij}$ are visualised with a colour scheme for all the tests. Some figures combine the correlation plots of multiple material laws in one single plot. Here, the different shapes of the markers are related to the material law, e.g. ■, ▲ and • referring to the `hog`, `ho` and `maho` constitutive law, respectively. Furthermore, the black diagonal line throughout the figures indicates the case of compatibility between the deformation gradient entry of the investigated law to the entries of the `neo` material. This notation applies to all subsequent problems.

Appendix .1.2. Numerical Results for Block Test

This section contains numerical results of growth perturbations in a block domain with the kinematic growth tensor aligned or unaligned to the global coordinate system. Additional perturbations included analysing the impact of the compressible vs. the incompressible formulation of the material law. Further, we analysed the influence of the microstructural direction with respect to the kinematic growth tensor, A summary of perturbations is seen in Figure 3.5. The norm differences of the solution of $\boldsymbol{u}$, p, the deformation gradients $\boldsymbol{F}$ along the growth directions $(\boldsymbol{g}_1, \boldsymbol{g}_2, \boldsymbol{g}_3)$ and the difference between the geometrical differences $\Delta\boldsymbol{u}$ with respect to the geometrical changes in a `neo` material following growth in % was utilised to compare results.

Table 1 Isotropic growth aligned with respect to the global coordinate system of the block domain with an incompressible material law

	`neo`	`hog`	`ho`	`maho`
$\|\|(\boldsymbol{u}_{\text{neo}} - \boldsymbol{u}_*)\|\|_0$	-	1.54E-20	5.54E-21	1.29E-20
$\|\|(p_{\text{neo}} - p_*)\|\|_0$	-	1.11E-15	4.00	1.89E-20
$\|\|(\boldsymbol{F}_{\text{neo}} - \boldsymbol{F}_*)\hat{\boldsymbol{g}}_1\|\|$	-	1.61E-19	4.76E-20	5.02E-19
$\|\|(\boldsymbol{F}_{\text{neo}} - \boldsymbol{F}_*)\hat{\boldsymbol{g}}_2\|\|$	-	9.40E-21	1.02E-20	3.46E-21
$\|\|(\boldsymbol{F}_{\text{neo}} - \boldsymbol{F}_*)\hat{\boldsymbol{g}}_3\|\|$	-	3.05E-20	7.87E-21	3.22E-21
$\sqrt{\frac{\|\Delta\boldsymbol{u}\|^2}{\|\bar{\boldsymbol{u}}\|^2}} * 100$	-	8.16E-11%	4.89E-11%	7.44E-11%

Table 2 Isotropic growth unaligned with respect to the global coordinate system (45 degrees rotated around the z-axis) of the block domain with an incompressible material law

	`neo`	`hog`	`ho`	`maho`
$\|\|(\boldsymbol{u}_{\text{neo}} - \boldsymbol{u}_*)\|\|_0$	-	1.54E-20	5.54E-21	1.29E-20
$\|\|(p_{\text{neo}} - p_*)\|\|_0$	-	1.11E-15	4.00	1.89E-20
$\|\|(\boldsymbol{F}_{\text{neo}} - \boldsymbol{F}_*)\hat{\boldsymbol{g}}_1\|\|$	-	8.75E-20	3.34E-20	2.49E-19
$\|\|(\boldsymbol{F}_{\text{neo}} - \boldsymbol{F}_*)\hat{\boldsymbol{g}}_2\|\|$	-	8.33E-20	2.43E-20	2.56E-19
$\|\|(\boldsymbol{F}_{\text{neo}} - \boldsymbol{F}_*)\hat{\boldsymbol{g}}_3\|\|$	-	3.05E-20	7.87E-21	3.22E-21
$\sqrt{\frac{\|\Delta\boldsymbol{u}\|^2}{\|\bar{\boldsymbol{u}}\|^2}} * 100$	-	8.16E-11%	4.89E-11%	7.44E-11%

Table 3 Isotropic growth aligned with respect to the global coordinate system and rotated fibre field (45 degrees rotated around the x-/y- or z-axis) of the block domain with an incompressible `hog` material law

	`hog`	$\texttt{hog}_{\text{rot}_\text{x}}$	$\texttt{hog}_{\text{rot}_\text{y}}$	$\texttt{hog}_{\text{rot}_\text{z}}$
$\|\|(\boldsymbol{u}_{\text{neo}} - \boldsymbol{u}_*)\|\|_0$	-	1.49E-20	8.80E-20	1.30E-21
$\|\|(p_{\text{neo}} - p_*)\|\|_0$	-	9.09E-17	1.48E-15	3.81E-17
$\|\|(\boldsymbol{F}_{\text{neo}} - \boldsymbol{F}_*)\hat{\boldsymbol{g}}_1\|\|$	-	2.48E-19	6.07E-19	1.95E-20
$\|\|(\boldsymbol{F}_{\text{neo}} - \boldsymbol{F}_*)\hat{\boldsymbol{g}}_2\|\|$	-	3.65E-20	6.23E-22	2.05E-21
$\|\|(\boldsymbol{F}_{\text{neo}} - \boldsymbol{F}_*)\hat{\boldsymbol{g}}_3\|\|$	-	3.67E-20	1.48E-20	2.13E-22
$\sqrt{\frac{\|\Delta \boldsymbol{u}\|^2}{\|\bar{\boldsymbol{u}}\|^2}} * 100$	-	8.01E-11%	1.95E-10%	2.36E-11%

Table 4 Isotropic growth aligned with respect to the global coordinate system and rotated fibre field (45 degrees rotated around the x-/y- or z-axis) of the block domain with an incompressible `ho` material law

	`ho`	$\texttt{ho}_{\text{rot}_\text{x}}$	$\texttt{ho}_{\text{rot}_\text{y}}$	$\texttt{ho}_{\text{rot}_\text{z}}$
$\|\|(\boldsymbol{u}_{\text{neo}} - \boldsymbol{u}_*)\|\|_0$	-	0.00	5.57E-21	5.57E-21
$\|\|(p_{\text{neo}} - p_*)\|\|_0$	-	0.00	2.61E-19	2.61E-19
$\|\|(\boldsymbol{F}_{\text{neo}} - \boldsymbol{F}_*)\hat{\boldsymbol{g}}_1\|\|$	-	0.00	4.78E-20	4.78E-20
$\|\|(\boldsymbol{F}_{\text{neo}} - \boldsymbol{F}_*)\hat{\boldsymbol{g}}_2\|\|$	-	0.00	1.02E-20	1.02E-20
$\|\|(\boldsymbol{F}_{\text{neo}} - \boldsymbol{F}_*)\hat{\boldsymbol{g}}_3\|\|$	-	0.00	7.84E-21	7.86E-21
$\sqrt{\frac{\|\Delta \boldsymbol{u}\|^2}{\|\bar{\boldsymbol{u}}\|^2}} * 100$	-	0.00%	4.90E-11%	4.90E-11%

Table 5 Isotropic growth aligned with respect to the global coordinate system and rotated fibre field (45 degrees rotated around the x-/y- or z-axis) of the block domain with an incompressible `maho` material law

	`maho`	$\texttt{maho}_{\text{rot}_\text{x}}$	$\texttt{maho}_{\text{rot}_\text{y}}$	$\texttt{maho}_{\text{rot}_\text{z}}$
$\|\|(\boldsymbol{u}_{\text{neo}} - \boldsymbol{u}_*)\|\|_0$	-	0.00	5.92E-20	5.92E-20
$\|\|(p_{\text{neo}} - p_*)\|\|_0$	-	0.00	2.20E-20	2.20E-20
$\|\|(\boldsymbol{F}_{\text{neo}} - \boldsymbol{F}_*)\hat{\boldsymbol{g}}_1\|\|$	-	0.00	6.70E-19	8.73E-19
$\|\|(\boldsymbol{F}_{\text{neo}} - \boldsymbol{F}_*)\hat{\boldsymbol{g}}_2\|\|$	-	0.00	1.11E-20	5.58E-20
$\|\|(\boldsymbol{F}_{\text{neo}} - \boldsymbol{F}_*)\hat{\boldsymbol{g}}_3\|\|$	-	0.00	3.12E-20	1.35E-20
$\sqrt{\frac{\|\Delta \boldsymbol{u}\|^2}{\|\bar{\boldsymbol{u}}\|^2}} * 100$	-	0%	1.60E-10%	1.60E-10%

Table 6 Anisotropic growth aligned with respect to the global coordinate system of the block domain with an incompressible material law

	`neo`	`hog`	`ho`	`maho`
$\|\|(\boldsymbol{u}_{\text{neo}} - \boldsymbol{u}_*)\|\|_0$	-	1.24E-20	2.51E-22	1.67E-20
$\|\|(p_{\text{neo}} - p_*)\|\|_0$	-	1.39E-15	4.00	1.48E-020
$\|\|(\boldsymbol{F}_{\text{neo}} - \boldsymbol{F}_*)\hat{\boldsymbol{g}}_1\|\|$	-	1.33E-19	1.41E-21	5.27E-20
$\|\|(\boldsymbol{F}_{\text{neo}} - \boldsymbol{F}_*)\hat{\boldsymbol{g}}_2\|\|$	-	9.64E-21	9.57E-22	2.28E-19
$\|\|(\boldsymbol{F}_{\text{neo}} - \boldsymbol{F}_*)\hat{\boldsymbol{g}}_3\|\|$	-	2.72E-20	4.18E-22	1.07E-20
$\sqrt{\frac{\|\Delta \boldsymbol{u}\|^2}{\|\bar{\boldsymbol{u}}\|^2}} * 100$	-	7.32E-11%	1.04E-11%	8.47E-11%

Table 7 Anisotropic growth unaligned with respect to the global coordinate system (45 degrees rotated around the z-axis) of the block domain with an incompressible material law

	`neo`	`hog`	`ho`	`maho`
$\|\|(\boldsymbol{u}_{\text{neo}} - \boldsymbol{u}_*)\|\|_0$	-	1.39E-20	9.49E-20	4.12E-23
$\|\|(p_{\text{neo}} - p_*)\|\|_0$	-	1.22E-15	4.00	6.05E-20
$\|\|(\boldsymbol{F}_{\text{neo}} - \boldsymbol{F}_*)\hat{\boldsymbol{g}}_1\|\|$	-	8.96E-20	5.60E-20	3.40E-23
$\|\|(\boldsymbol{F}_{\text{neo}} - \boldsymbol{F}_*)\hat{\boldsymbol{g}}_2\|\|$	-	8.50E-20	1.65E-19	7.78E-23
$\|\|(\boldsymbol{F}_{\text{neo}} - \boldsymbol{F}_*)\hat{\boldsymbol{g}}_3\|\|$	-	2.75E-20	1.54E-20	3.56E-24
$\sqrt{\frac{\|\Delta \boldsymbol{u}\|^2}{\|\bar{\boldsymbol{u}}\|^2}} * 100$	-	7.74E-11%	2.02E-10%	4.21E-12%

Table 8 Anisotropic growth aligned with respect to the global coordinate system and rotated fibre field (45 degrees rotated around the x-/y- or z-axis) of the block domain with an incompressible `hog` material law

	`hog`	$\texttt{hog}_{\text{rot}_\text{x}}$	$\texttt{hog}_{\text{rot}_\text{y}}$	$\texttt{hog}_{\text{rot}_\text{z}}$
$\|\|(\boldsymbol{u}_{\text{neo}} - \boldsymbol{u}_*)\|\|_0$	-	1.46E-20	6.31E-20	1.30E-21
$\|\|(p_{\text{neo}} - p_*)\|\|_0$	-	1.41E-16	1.97E-15	6.18E-17
$\|\|(\boldsymbol{F}_{\text{neo}} - \boldsymbol{F}_*)\hat{\boldsymbol{g}}_1\|\|$	-	2.09E-19	4.35E-19	1.85E-20
$\|\|(\boldsymbol{F}_{\text{neo}} - \boldsymbol{F}_*)\hat{\boldsymbol{g}}_2\|\|$	-	2.56E-20	6.25E-22	2.80E-21
$\|\|(\boldsymbol{F}_{\text{neo}} - \boldsymbol{F}_*)\hat{\boldsymbol{g}}_3\|\|$	-	5.14E-20	1.43E-20	1.68E-22
$\sqrt{\frac{\|\Delta \boldsymbol{u}\|^2}{\|\bar{\boldsymbol{u}}\|^2}} * 100$	-	7.93E-11%	1.65E-10%	2.36E-11%

Table 9 Anisotropic growth aligned with respect to the global coordinate system and rotated fibre field (45 degrees rotated around the x-/y- or z-axis) of the block domain with an incompressible `ho` material law

	`ho`	$\texttt{ho}_{\text{rot}_\text{x}}$	$\texttt{ho}_{\text{rot}_\text{y}}$	$\texttt{ho}_{\text{rot}_\text{z}}$
$\|\|(\boldsymbol{u}_{\text{neo}} - \boldsymbol{u}_*)\|\|_0$	-	0.00	4.92E-21	6.42E-21
$\|\|(p_{\text{neo}} - p_*)\|\|_0$	-	0.00	1.60E-19	2.05E-19
$\|\|(\boldsymbol{F}_{\text{neo}} - \boldsymbol{F}_*)\hat{\boldsymbol{g}}_1\|\|$	-	0.00	1.58E-20	2.08E-20
$\|\|(\boldsymbol{F}_{\text{neo}} - \boldsymbol{F}_*)\hat{\boldsymbol{g}}_2\|\|$	-	0.00	4.28E-20	5.76E-20
$\|\|(\boldsymbol{F}_{\text{neo}} - \boldsymbol{F}_*)\hat{\boldsymbol{g}}_3\|\|$	-	0.00	2.60E-22	3.96E-22
$\sqrt{\frac{\|\Delta \boldsymbol{u}\|^2}{\|\bar{\boldsymbol{u}}\|^2}} * 100$	-	0.00%	4.61E-11%	5.26E-11%

Table 10 Anisotropic growth aligned with respect to the global coordinate system and rotated fibre field (45 degrees rotated around the x-/y- or z-axis) of the block domain with an incompressible `maho` material law

	`maho`	$\texttt{maho}_{\text{rot}_\text{x}}$	$\texttt{maho}_{\text{rot}_\text{y}}$	$\texttt{maho}_{\text{rot}_\text{z}}$
$\|\|(\boldsymbol{u}_{\text{neo}} - \boldsymbol{u}_*)\|\|_0$	-	0.00	9.26E-23	1.55E-21
$\|\|(p_{\text{neo}} - p_*)\|\|_0$	-	0.00	1.33E-22	2.36E-21
$\|\|(\boldsymbol{F}_{\text{neo}} - \boldsymbol{F}_*)\hat{\boldsymbol{g}}_1\|\|$	-	0.00	7.63E-22	6.35E-21
$\|\|(\boldsymbol{F}_{\text{neo}} - \boldsymbol{F}_*)\hat{\boldsymbol{g}}_2\|\|$	-	0.00	2.15E-21	2.85E-20
$\|\|(\boldsymbol{F}_{\text{neo}} - \boldsymbol{F}_*)\hat{\boldsymbol{g}}_3\|\|$	-	0.00	2.76E-22	3.85E-21
$\sqrt{\frac{\|\Delta \boldsymbol{u}\|^2}{\|\bar{\boldsymbol{u}}\|^2}} * 100$	-	0.00%	6.31E-12%	2.59E-11%

Table 11 Isotropic growth aligned with respect to the global coordinate system of the block domain with a compressible material law

	`neo`	`hog`	`ho`	`maho`
$\|\|(\boldsymbol{u}_{\text{neo}} - \boldsymbol{u}_*)\|\|_0$	-	1.53E-20	8.71E-07	1.29E-20
$\|\|(p_{\text{neo}} - p_*)\|\|_0$	-	1.00E-15	3.85	1.99E-20
$\|\|(\boldsymbol{F}_{\text{neo}} - \boldsymbol{F}_*)\hat{\boldsymbol{g}}_1\|\|$	-	1.53E-19	4.51E-06	5.02E-19
$\|\|(\boldsymbol{F}_{\text{neo}} - \boldsymbol{F}_*)\hat{\boldsymbol{g}}_2\|\|$	-	9.34E-21	5.27E-07	3.45E-21
$\|\|(\boldsymbol{F}_{\text{neo}} - \boldsymbol{F}_*)\hat{\boldsymbol{g}}_3\|\|$	-	3.08E-20	5.25E-07	3.22E-21
$\sqrt{\frac{\|\Delta \boldsymbol{u}\|^2}{\|\bar{\boldsymbol{u}}\|^2}} * 100$	-	8.11E-11%	6.13E-04%	7.46E-11%

Table 12 Isotropic growth unaligned with respect to the global coordinate system (45 degrees rotated around the z-axis) of the block domain with a compressible material law

	`neo`	`hog`	`ho`	`maho`
$\|\|(\boldsymbol{u}_{\text{neo}} - \boldsymbol{u}_*)\|\|_0$	-	1.53E-20	8.71E-07	1.29E-20
$\|\|(p_{\text{neo}} - p_*)\|\|_0$	-	1.00E-15	3.85	1.99E-20
$\|\|(\boldsymbol{F}_{\text{neo}} - \boldsymbol{F}_*)\hat{\boldsymbol{g}}_1\|\|$	-	8.31E-20	2.55E-06	2.49E-19
$\|\|(\boldsymbol{F}_{\text{neo}} - \boldsymbol{F}_*)\hat{\boldsymbol{g}}_2\|\|$	-	7.89E-20	2.49E-06	2.56E-19
$\|\|(\boldsymbol{F}_{\text{neo}} - \boldsymbol{F}_*)\hat{\boldsymbol{g}}_3\|\|$	-	3.08E-20	5.25E-07	3.22E-21
$\sqrt{\frac{\|\Delta \boldsymbol{u}\|^2}{\|\bar{\boldsymbol{u}}\|^2}} * 100$	-	8.11E-11%	6.13E-04%	7.46E-11%

Table 13 Isotropic growth aligned with respect to the global coordinate system and rotated fibre field (45 degrees rotated around the x-/y- or z-axis) of the block domain with a compressible `hog` material law

	`hog`	$\texttt{hog}_{\text{rot}_\text{x}}$	$\texttt{hog}_{\text{rot}_\text{y}}$	$\texttt{hog}_{\text{rot}_\text{z}}$
$\|\|(\boldsymbol{u}_{\text{neo}} - \boldsymbol{u}_*)\|\|_0$	-	1.46E-20	8.74E-20	1.30E-21
$\|\|(p_{\text{neo}} - p_*)\|\|_0$	-	7.55E-17	1.33E-15	3.33E-17
$\|\|(\boldsymbol{F}_{\text{neo}} - \boldsymbol{F}_*)\hat{\boldsymbol{g}}_1\|\|$	-	2.35E-19	5.96E-19	1.96E-20
$\|\|(\boldsymbol{F}_{\text{neo}} - \boldsymbol{F}_*)\hat{\boldsymbol{g}}_2\|\|$	-	3.67E-20	6.15E-22	2.01E-21
$\|\|(\boldsymbol{F}_{\text{neo}} - \boldsymbol{F}_*)\hat{\boldsymbol{g}}_3\|\|$	-	3.68E-20	1.51E-20	1.98E-22
$\sqrt{\frac{\|\Delta \boldsymbol{u}\|^2}{\|\bar{\boldsymbol{u}}\|^2}} * 100$	-	7.94E-11%	1.94E-10%	2.36E-11%

Table 14 Isotropic growth aligned with respect to the global coordinate system and rotated fibre field (45 degrees rotated around the x-/y- or z-axis) of the block domain with a compressible `ho` material law

	`ho`	$\texttt{ho}_{\text{rot}_\text{x}}$	$\texttt{ho}_{\text{rot}_\text{y}}$	$\texttt{ho}_{\text{rot}_\text{z}}$
$\|\|(\boldsymbol{u}_{\text{neo}} - \boldsymbol{u}_*)\|\|_0$	-	0.00	3.54E-31	3.53E-31
$\|\|(p_{\text{neo}} - p_*)\|\|_0$	-	0.00	6.04E-30	6.03E-30
$\|\|(\boldsymbol{F}_{\text{neo}} - \boldsymbol{F}_*)\hat{\boldsymbol{g}}_1\|\|$	-	0.00	5.63E-30	9.21E-30
$\|\|(\boldsymbol{F}_{\text{neo}} - \boldsymbol{F}_*)\hat{\boldsymbol{g}}_2\|\|$	-	0.00	5.37E-31	4.46E-31
$\|\|(\boldsymbol{F}_{\text{neo}} - \boldsymbol{F}_*)\hat{\boldsymbol{g}}_3\|\|$	-	0.00	3.72E-31	7.03E-31
$\sqrt{\frac{\|\Delta \boldsymbol{u}\|^2}{\|\bar{\boldsymbol{u}}\|^2}} * 100$	-	0.00%	3.91E-16%	3.90E-16%

Table 15 Isotropic growth aligned with respect to the global coordinate system and rotated fibre field (45 degrees rotated around the x-/y- or z-axis) of the block domain with a compressible `maho` material law

	`maho`	$\texttt{maho}_{\text{rot}_\text{x}}$	$\texttt{maho}_{\text{rot}_\text{y}}$	$\texttt{maho}_{\text{rot}_\text{z}}$
$\|\|(\boldsymbol{u}_{\text{neo}} - \boldsymbol{u}_*)\|\|_0$	-	0.00	5.92E-20	5.92E-20
$\|\|(p_{\text{neo}} - p_*)\|\|_0$	-	0.00	2.22E-20	2.22E-20
$\|\|(\boldsymbol{F}_{\text{neo}} - \boldsymbol{F}_*)\hat{\boldsymbol{g}}_1\|\|$	-	0.00	6.70E-19	8.73E-19
$\|\|(\boldsymbol{F}_{\text{neo}} - \boldsymbol{F}_*)\hat{\boldsymbol{g}}_2\|\|$	-	0.00	1.11E-20	5.59E-20
$\|\|(\boldsymbol{F}_{\text{neo}} - \boldsymbol{F}_*)\hat{\boldsymbol{g}}_3\|\|$	-	0.00	3.12E-20	1.35E-20
$\sqrt{\frac{\|\Delta \boldsymbol{u}\|^2}{\|\bar{\boldsymbol{u}}\|^2}} * 100$	-	0.00%	1.60E-10%	1.60E-10%

Table 16 Anisotropic growth aligned with respect to the global coordinate system of the block domain with a compressible material law

	`neo`	`hog`	`ho`	`maho`
$\|\|(\boldsymbol{u}_{\text{neo}} - \boldsymbol{u}_*)\|\|_0$	-	1.23E-20	6.15E-07	1.67E-20
$\|\|(p_{\text{neo}} - p_*)\|\|_0$	-	1.39E-15	3.85	1.48E-20
$\|\|(\boldsymbol{F}_{\text{neo}} - \boldsymbol{F}_*)\hat{\boldsymbol{g}}_1\|\|$	-	1.33E-19	3.08E-06	5.28E-20
$\|\|(\boldsymbol{F}_{\text{neo}} - \boldsymbol{F}_*)\hat{\boldsymbol{g}}_2\|\|$	-	9.64E-21	4.95E-07	2.29E-19
$\|\|(\boldsymbol{F}_{\text{neo}} - \boldsymbol{F}_*)\hat{\boldsymbol{g}}_3\|\|$	-	2.72E-20	4.29E-07	1.07E-20
$\sqrt{\frac{\|\Delta \boldsymbol{u}\|^2}{\|\bar{\boldsymbol{u}}\|^2}} * 100$	-	7.28E-11%	5.1508E-04%	8.48E-11%

Table 17 Anisotropic growth unaligned with respect to the global coordinate system (45 degrees rotated around the z-axis) of the block domain with a compressible material law

	`neo`	`hog`	`ho`	`maho`
$\|\|(\boldsymbol{u}_{\text{neo}} - \boldsymbol{u}_*)\|\|_0$	-	1.38E-20	6.92E-07	4.16E-23
$\|\|(p_{\text{neo}} - p_*)\|\|_0$	-	1.09E-15	3.85	6.05E-20
$\|\|(\boldsymbol{F}_{\text{neo}} - \boldsymbol{F}_*)\hat{\boldsymbol{g}}_1\|\|$	-	8.58E-20	1.90E-06	3.43E-23
$\|\|(\boldsymbol{F}_{\text{neo}} - \boldsymbol{F}_*)\hat{\boldsymbol{g}}_2\|\|$	-	8.12E-20	2.04E-06	7.87E-23
$\|\|(\boldsymbol{F}_{\text{neo}} - \boldsymbol{F}_*)\hat{\boldsymbol{g}}_3\|\|$	-	2.77E-20	4.29E-07	3.54E-24
$\sqrt{\frac{\|\Delta \boldsymbol{u}\|^2}{\|\bar{\boldsymbol{u}}\|^2}} * 100$	-	7.70E-11%	5.4640e-04%	4.24E-12%

Table 18 Anisotropic growth aligned with respect to the global coordinate system and rotated fibre field (45 degrees rotated around the x-/y- or z-axis) of the block domain with an incompressible `hog` material law

	`hog`	$\texttt{hog}_{\text{rot}_\text{x}}$	$\texttt{hog}_{\text{rot}_\text{y}}$	$\texttt{hog}_{\text{rot}_\text{z}}$
$\|\|(\boldsymbol{u}_{\text{neo}} - \boldsymbol{u}_*)\|\|_0$	-	1.44E-20	6.18E-020	1.30E-021
$\|\|(p_{\text{neo}} - p_*)\|\|_0$	-	1.13E-16	1.73E-015	5.37E-017
$\|\|(\boldsymbol{F}_{\text{neo}} - \boldsymbol{F}_*)\hat{\boldsymbol{g}}_1\|\|$	-	1.97E-19	4.24E-19	1.86E-20
$\|\|(\boldsymbol{F}_{\text{neo}} - \boldsymbol{F}_*)\hat{\boldsymbol{g}}_2\|\|$	-	2.56E-20	6.14E-22	2.75E-21
$\|\|(\boldsymbol{F}_{\text{neo}} - \boldsymbol{F}_*)\hat{\boldsymbol{g}}_3\|\|$	-	5.15E-20	1.45E-20	1.54E-22
$\sqrt{\frac{\|\Delta\boldsymbol{u}\|^2}{\|\bar{\boldsymbol{u}}\|^2}} * 100$	-	7.86E-11%	1.63E-10%	2.37E-11%

Table 19 Anisotropic growth aligned with respect to the global coordinate system and rotated fibre field (45 degrees rotated around the x-/y- or z-axis) of the block domain with a compressible `ho` material law

	`ho`	$\texttt{ho}_{\text{rot}_\text{x}}$	$\texttt{ho}_{\text{rot}_\text{y}}$	$\texttt{ho}_{\text{rot}_\text{z}}$
$\|\|(\boldsymbol{u}_{\text{neo}} - \boldsymbol{u}_*)\|\|_0$	-	0.00	2.22E-21	3.58E-21
$\|\|(p_{\text{neo}} - p_*)\|\|_0$	-	0.00	7.25E-20	1.05E-19
$\|\|(\boldsymbol{F}_{\text{neo}} - \boldsymbol{F}_*)\hat{\boldsymbol{g}}_1\|\|$	-	0.00	9.51E-21	2.32E-20
$\|\|(\boldsymbol{F}_{\text{neo}} - \boldsymbol{F}_*)\hat{\boldsymbol{g}}_2\|\|$	-	0.00	1.99E-20	3.46E-20
$\|\|(\boldsymbol{F}_{\text{neo}} - \boldsymbol{F}_*)\hat{\boldsymbol{g}}_3\|\|$	-	0.00	2.42E-22	1.11E-21
$\sqrt{\frac{\|\Delta\boldsymbol{u}\|^2}{\|\bar{\boldsymbol{u}}\|^2}} * 100$	-	0.00%	3.10E-11%	3.93E-11%

Table 20 Anisotropic growth aligned with respect to the global coordinate system and rotated fibre field (45 degrees rotated around the x-/y- or z-axis) of the block domain with an incompressible `maho` material law

	`maho`	$\texttt{maho}_{\text{rot}_\text{x}}$	$\texttt{maho}_{\text{rot}_\text{y}}$	$\texttt{maho}_{\text{rot}_\text{z}}$
$\|\|(\boldsymbol{u}_{\text{neo}} - \boldsymbol{u}_*)\|\|_0$	-	0.00	9.13E-23	1.55E-21
$\|\|(p_{\text{neo}} - p_*)\|\|_0$	-	0.00	1.30E-22	2.35E-21
$\|\|(\boldsymbol{F}_{\text{neo}} - \boldsymbol{F}_*)\hat{\boldsymbol{g}}_1\|\|$	-	0.00	7.52E-22	6.35E-21
$\|\|(\boldsymbol{F}_{\text{neo}} - \boldsymbol{F}_*)\hat{\boldsymbol{g}}_2\|\|$	-	0.00	2.13E-21	2.86E-20
$\|\|(\boldsymbol{F}_{\text{neo}} - \boldsymbol{F}_*)\hat{\boldsymbol{g}}_3\|\|$	-	0.00	2.74E-22	3.86E-21
$\sqrt{\frac{\|\Delta\boldsymbol{u}\|^2}{\|\bar{\boldsymbol{u}}\|^2}} * 100$	-	0.00%	6.27E-12%	2.59E-11%

Appendix .1.3. Numerical Results for Idealised LV Heart

Table 21 Numerical results of a growth problem with anisotropic growth modes applied along the fibre or sheet microstructural direction in a coarse (56 tetrahedral elements) or refined (448 tetrahedral elements) LV model. The norm differences of the solution of $\boldsymbol{u}$, p, the deformation gradients $\boldsymbol{F}$ along the growth directions $(\boldsymbol{g}_1, \boldsymbol{g}_2, \boldsymbol{g}_3)$ and the difference between the geometrical differences $\Delta\boldsymbol{u}$ with respect to the geometrical changes in a `neo` material following growth in %.

(a) Anisotropic growth along fibre direction in LV model

	`neo`	`ho`(56)	`ho`(448)
$\|\|(\boldsymbol{u}_{\text{neo}} - \boldsymbol{u}_*)\|\|_0$	-	1.69E-10	1.89E-10
$\|\|(p_{\text{neo}} - p_*)\|\|_0$	-	1.15E-02	1.26E-02
$\|\|(\boldsymbol{F}_{\text{neo}} - \boldsymbol{F}_*)\hat{\boldsymbol{g}}_1\|\|$	-	2.15E-07	2.33E-07
$\|\|(\boldsymbol{F}_{\text{neo}} - \boldsymbol{F}_*)\hat{\boldsymbol{g}}_2\|\|$	-	1.53E-07	1.67E-07
$\|\|(\boldsymbol{F}_{\text{neo}} - \boldsymbol{F}_*)\hat{\boldsymbol{g}}_3\|\|$	-	2.60E-07	2.83E-07
$\sqrt{\frac{\|\Delta\boldsymbol{u}\|^2}{\|\bar{\boldsymbol{u}}\|^2}} * 100$	-	14.44%	15.26%

(b) Anisotropic growth along sheet direction in LV model

	`neo`	`ho`(56)	`ho`(448)
$\|\|(\boldsymbol{u}_{\text{neo}} - \boldsymbol{u}_*)\|\|_0$	-	1.24E-10	1.25E-10
$\|\|(p_{\text{neo}} - p_*)\|\|_0$	-	2.83E-02	2.83E-02
$\|\|(\boldsymbol{F}_{\text{neo}} - \boldsymbol{F}_*)\hat{\boldsymbol{g}}_1\|\|$	-	3.38E-07	3.42E-07
$\|\|(\boldsymbol{F}_{\text{neo}} - \boldsymbol{F}_*)\hat{\boldsymbol{g}}_2\|\|$	-	7.21E-07	7.33E-07
$\|\|(\boldsymbol{F}_{\text{neo}} - \boldsymbol{F}_*)\hat{\boldsymbol{g}}_3\|\|$	-	3.17E-07	3.17E-07
$\sqrt{\frac{\|\Delta\boldsymbol{u}\|^2}{\|\bar{\boldsymbol{u}}\|^2}} * 100$	-	57.39%	57.63%

Table 22 Numerical results of a growth problem with anisotropic growth modes applied along the normal or the combined sheet and normal directions in a coarse (56 tetrahedral elements) or refined (448 tetrahedral elements) LV model. The norm differences of the solution of $\boldsymbol{u}$, p, the deformation gradients $\boldsymbol{F}$ along the growth directions $(\boldsymbol{g}_1, \boldsymbol{g}_2, \boldsymbol{g}_3)$ and the difference between the geometrical differences $\Delta\boldsymbol{u}$ with respect to the geometrical changes in a `neo` material following growth in %.

(a) Anisotropic growth along normal direction in LV model

	`neo`	`ho`(56)	`ho`(448)
$\|\|(\boldsymbol{u}_{\text{neo}} - \boldsymbol{u}_*)\|\|_0$	-	7.67E-09	1.10E-09
$\|\|(p_{\text{neo}} - p_*)\|\|_0$	-	8.85E-03	2.49E-02
$\|\|(\boldsymbol{F}_{\text{neo}} - \boldsymbol{F}_*)\hat{\boldsymbol{g}}_1\|\|$	-	1.36E-04	1.11E-06
$\|\|(\boldsymbol{F}_{\text{neo}} - \boldsymbol{F}_*)\hat{\boldsymbol{g}}_2\|\|$	-	1.04E-04	4.15E-06
$\|\|(\boldsymbol{F}_{\text{neo}} - \boldsymbol{F}_*)\hat{\boldsymbol{g}}_3\|\|$	-	1.65E-04	1.50E-06
$\sqrt{\frac{\|\Delta\boldsymbol{u}\|^2}{\|\bar{\boldsymbol{u}}\|^2}} * 100$	-	141.29%	46.43%

(b) Anisotropic growth along the combined sheet and normal direction in LV model

	`neo`	`ho`(56)	`ho`(448)
$\|\|(\boldsymbol{u}_{\text{neo}} - \boldsymbol{u}_*)\|\|_0$	-	5.93E-10	6.03E-10
$\|\|(p_{\text{neo}} - p_*)\|\|_0$	-	2.45E-02	3.40E-02
$\|\|(\boldsymbol{F}_{\text{neo}} - \boldsymbol{F}_*)\hat{\boldsymbol{g}}_1\|\|$	-	7.94E-07	7.86E-07
$\|\|(\boldsymbol{F}_{\text{neo}} - \boldsymbol{F}_*)\hat{\boldsymbol{g}}_2\|\|$	-	1.10E-05	1.17E-05
$\|\|(\boldsymbol{F}_{\text{neo}} - \boldsymbol{F}_*)\hat{\boldsymbol{g}}_3\|\|$	-	1.01E-06	1.13E-06
$\sqrt{\frac{\|\Delta\boldsymbol{u}\|^2}{\|\bar{\boldsymbol{u}}\|^2}} * 100$	-	28.67%	28.90%

Appendix .1.4. Numerical Results for Personalised BiV Heart

Table 23 Numerical results of a growth problem with anisotropic growth modes applied along the fibre or sheet microstructural direction in a biventricular model. The norm differences of the solution of $\boldsymbol{u}$, p, the deformation gradients $\boldsymbol{F}$ along the growth directions $(\boldsymbol{g}_1, \boldsymbol{g}_2, \boldsymbol{g}_3)$ and the difference between the geometrical differences $\Delta\boldsymbol{u}$ with respect to the geometrical changes in a `neo` material following growth in %.

(a) Anisotropic growth along fibre direction in a biventricular model

	`neo`	`ho`
$\|\|(\boldsymbol{u}_{\text{neo}} - \boldsymbol{u}_*)\|\|_0$	-	1.15E-11
$\|\|(p_{\text{neo}} - p_*)\|\|_0$	-	6.34E-03
$\|\|(\boldsymbol{F}_{\text{neo}} - \boldsymbol{F}_*)\hat{\boldsymbol{g}}_1\|\|$	-	3.67E-08
$\|\|(\boldsymbol{F}_{\text{neo}} - \boldsymbol{F}_*)\hat{\boldsymbol{g}}_2\|\|$	-	2.99E-08
$\|\|(\boldsymbol{F}_{\text{neo}} - \boldsymbol{F}_*)\hat{\boldsymbol{g}}_3\|\|$	-	4.21E-08
$\sqrt{\frac{\|\Delta\boldsymbol{u}\|^2}{\|\bar{\boldsymbol{u}}\|^2}} * 100$	-	4.97%

(b) Anisotropic growth along sheet direction in a biventricular model

	`neo`	`ho`
$\|\|(\boldsymbol{u}_{\text{neo}} - \boldsymbol{u}_*)\|\|_0$	-	5.73E-10
$\|\|(p_{\text{neo}} - p_*)\|\|_0$	-	9.29E-03
$\|\|(\boldsymbol{F}_{\text{neo}} - \boldsymbol{F}_*)\hat{\boldsymbol{g}}_1\|\|$	-	6.28E-07
$\|\|(\boldsymbol{F}_{\text{neo}} - \boldsymbol{F}_*)\hat{\boldsymbol{g}}_2\|\|$	-	6.09E-07
$\|\|(\boldsymbol{F}_{\text{neo}} - \boldsymbol{F}_*)\hat{\boldsymbol{g}}_3\|\|$	-	1.65E-06
$\sqrt{\frac{\|\Delta\boldsymbol{u}\|^2}{\|\bar{\boldsymbol{u}}\|^2}} * 100$	-	46.16%

Table 24 Numerical results of a growth problem with anisotropic growth modes applied along the normal or the combined sheet and normal direction in a biventricular model. The norm differences of the solution of $\boldsymbol{u}$, p, the deformation gradients $\boldsymbol{F}$ along the growth directions $(\boldsymbol{g}_1, \boldsymbol{g}_2, \boldsymbol{g}_3)$ and the difference between the geometrical differences $\Delta\boldsymbol{u}$ with respect to the geometrical changes in a `neo` material following growth in %.

(a) Anisotropic growth along normal direction in biventricular model

	`neo`	`ho`
$\|\|(\boldsymbol{u}_{\text{neo}} - \boldsymbol{u}_*)\|\|_0$	-	1.71E-11
$\|\|(p_{\text{neo}} - p_*)\|\|_0$	-	1.30E-02
$\|\|(\boldsymbol{F}_{\text{neo}} - \boldsymbol{F}_*)\hat{\boldsymbol{g}}_1\|\|$	-	4.37E-08
$\|\|(\boldsymbol{F}_{\text{neo}} - \boldsymbol{F}_*)\hat{\boldsymbol{g}}_2\|\|$	-	4.20E-08
$\|\|(\boldsymbol{F}_{\text{neo}} - \boldsymbol{F}_*)\hat{\boldsymbol{g}}_3\|\|$	-	8.73E-08
$\sqrt{\frac{\|\Delta\boldsymbol{u}\|^2}{\|\bar{\boldsymbol{u}}\|^2}} * 100$	-	17.07%

(b) Anisotropic growth along the combined sheet and normal direction in biventricular model

	`neo`	`ho`
$\|\|(\boldsymbol{u}_{\text{neo}} - \boldsymbol{u}_*)\|\|_0$	-	5.59E-10
$\|\|(p_{\text{neo}} - p_*)\|\|_0$	-	7.98E-03
$\|\|(\boldsymbol{F}_{\text{neo}} - \boldsymbol{F}_*)\hat{\boldsymbol{g}}_1\|\|$	-	6.64E-07
$\|\|(\boldsymbol{F}_{\text{neo}} - \boldsymbol{F}_*)\hat{\boldsymbol{g}}_2\|\|$	-	6.27E-07
$\|\|(\boldsymbol{F}_{\text{neo}} - \boldsymbol{F}_*)\hat{\boldsymbol{g}}_3\|\|$	-	2.61E-06
$\sqrt{\frac{\|\Delta\boldsymbol{u}\|^2}{\|\bar{\boldsymbol{u}}\|^2}} * 100$	-	36.66%

Appendix .2. Supplementary Chapter 5

This section includes the additional information and results not utilised in Chapter 5.

Table 25 Summary of the pre-SAVR patient data acquired through catheterisation (pressure data), echocardiograph (EF) and dynamic computed tomography, utilised for the forward G&R problem in Chapter 5.

	SAVR 1	SAVR 2	SAVR 3	SAVR 4	SAVR 5	SAVR 6	SAVR 7
EF [%]	55	65	75	-	60	-	65
LV EDP [mmHg]	(30)	(21)	19	(39)	14	(20)	(21)
RV EDP [mmHg]	(11)	(17)	8	(21)	12	(15)	(17)
State of AV (stenosis)	severe	yes	severe presumed bicuspid AV	-	moderate	-	moderate bicuspid AV
State of MV (regurgitation)	mild	minimal	minimal	-	minimal	-	minimal
State of PV (regurgitation)	none	minimal	minimal	-	-	-	none
State of TV (regurgitation)	minimal	minimal	mild	-	minimal	-	minimal
State of LV (size & function)	normal concentric hypertrophy	normal	normal hypertrophy	-	dilated grossly normal systolic function, grade 2 diastolic dysfunction	-	normal size, normal systolic function
State of RV (size & function)	normal	normal	normal	-	dilated, mildly decreased systolic function	-	normal

Table 26 Summary of the post-SAVR patient data acquired through catheterisation (pressure data), echocardiograph (EF) and dynamic computed tomography, utilised for the forward G&R problem in Chapter 5.

	SAVR 1	SAVR 2	SAVR 3	SAVR 4	SAVR 5	SAVR 6	SAVR 7
EF [%]	-	65	65	65	60–65	55	55–60
LV EDP [mmHg]	(23)	(20)	(13)	(20)	9	(28)	(28)
RV EDP [mmHg]	(16)	(9)	(6)	(9)	6	(19)	(19)
State of AV (regurgitation)	-	none	none, possible decreased opening of 2 leaflets	none	none	none	minimal
State of MV (regurgitation)	-	moderate	minimal	minimal	mild	minimal	mild
State of PV (regurgitation)	-	none	none	-	mild	minimal	minimal
State of TV (regurgitation)	-	mild	mild	minimal	minimal	minimal	mild
State of LV (function & size)	-	normal	normal	normal	normal, grade 3 LV dysfunction	normal	normal size, systolic function
State of RV (function & size)	-	normal	normal	normal	mildly dilated	normal, grade 1 diastolic dysfunction	normal size, systolic function
Days after surgery	133	70	413	476	92	90	124
Aortic root enlargement	yes	yes	no	no	yes	no	yes

Table 27 Summary of the pre-TAVR patient data acquired through catheterization (pressure data), echocardiograph (EF) and dynamic computed tomography, utilised for the forward G&R problem in Chapter 5.

	TAVR 1	TAVR 2	TAVR 3	TAVR 4
EF [%]	70	65	65	30
LV EDP [mmHg]	31	15	19	18
RV EDP [mmHg]	28	13	11	11
State of AV (stenosis)	-	-	Bioprosthetic AVR prosthesis stenosis	severe
State of MV (regurgitation)	-	-	mild	mild to moderate
State of PV (regurgitation)	-	-	-	-
State of TV (regurgitation)	-	-	-	-
State of LV (function & size)	normal, concentric hypertrophy	small, mild hypertrophy	-	-
State of RV (function & size)	mildly dilated	normal	-	-

Table 28 Summary of the post-TAVR patient data acquired through catheterization (pressure data), echocardiograph (EF) and dynamic computed tomography, utilised for the forward G&R problem in Chapter 5.

	TAVR 1	TAVR 2	TAVR 3	TAVR 4
EF [%]	65	70	75	20-25
LV EDP [mmHg]	24	22	(13)	18
RV EDP [mmHg]	19	14	(6)	11
State of AV (regurgitation)	-	none	-	none
State of MV (regurgitation)	mild to moderate	-	-	moderate
State of PV (regurgitation)	-	-	-	-
State of TV (regurgitation)	-	-	-	mild
State of LV (function & size)	normal, hypertrophied	normal, hypertrophied	-	normal, mild hypertrophy
State of RV (function & size)	normal	-	-	
Days after surgery	143	328	280	674

Table 29 Summary of linear $\mathbb{P}^1$ tetrahedral mesh quantities of the pre- and post-SAVR models from the ED-CT images.

	SAVR 1	SAVR 2	SAVR 3	SAVR 4	SAVR 5	SAVR 6	SAVR 7
Pre-AVR mesh	90611	56968	46202	65852	76725	56366	50195
Post-AVR mesh	86854	54420	53048	59902	45481	89008	64376

Table 30 Summary of linear $\mathbb{P}^1$ tetrahedral mesh quantities of the pre- and post-TAVR models from the ED-CT images.

	TAVR 1	TAVR 2	TAVR 3	TAVR 4
Pre-AVR mesh	64740	48326	102752	98060
Post-AVR mesh	84578	73711	100069	98186

Table 31 Summary of material parameter estimation for reduced Holzapfel-Ogden constitutive model, for the isotropic material (a and b) and the anisotropic material components ($a_{\boldsymbol{f}}$ and $b_{\boldsymbol{f}}$) for the forward G&R modelling in the SAVR and TAVR patients. Identified via Klotz-curve method.

	SAVR 1	SAVR 2	SAVR 3	SAVR 4	SAVR 5	SAVR 6	TAVR 1	TAVR 2
a	2.08	0.95	0.809	0.85	0.55	0.809	1.0	0.5
b	3.0	3.0	3.0	3.0	3.0	3.0	3.0	3.0
$a_{\boldsymbol{f}}$	4.913	2.008	1.911	1.911	1.300	0.809	2.362	1.181
$b_{\boldsymbol{f}}$	3.0	3.0	3.0	3.0	3.0	3.0	3.0	3.0

Table 32 Summary of mean and standard deviation for the incompatibility metric e_{inc} within the remodelled post-AVR states following SAVR.

	SAVR 1	SAVR 2	SAVR 3	SAVR 4	SAVR 5	SAVR 6
Con	0.211 (std=0.080)	0.197 (std=0.070)	0.164 (std=0.058)	0.173 (std=0.054)	0.210 (std=0.074)	0.211 (std=0.070)
Ecc	0.251 (std=0.077)	0.207 (std=0.076)	0.179 (std=0.060)	0.159 (std=0.058)	0.185 (std=0.076)	0.192 (std=0.067)
Iso	0.200 (std=0.093)	0.203 (std=0.072)	0.170 (std=0.059)	0.156 (std=0.063)	0.187 (std=0.086)	0.207 (std=0.070)

Table 33 Summayr of mean of the incompatibility metric e_{inc} within the remodelled post-AVR states following TAVR.

	TAVR 1	TAVR 2
Con	0.183 (std=0.057)	0.217 (std=0.048)
Ecc	0.17 (std=0.053)	0.192 (std=0.050)
Iso	0.16 (std=0.066)	0.211 (std=0.049)

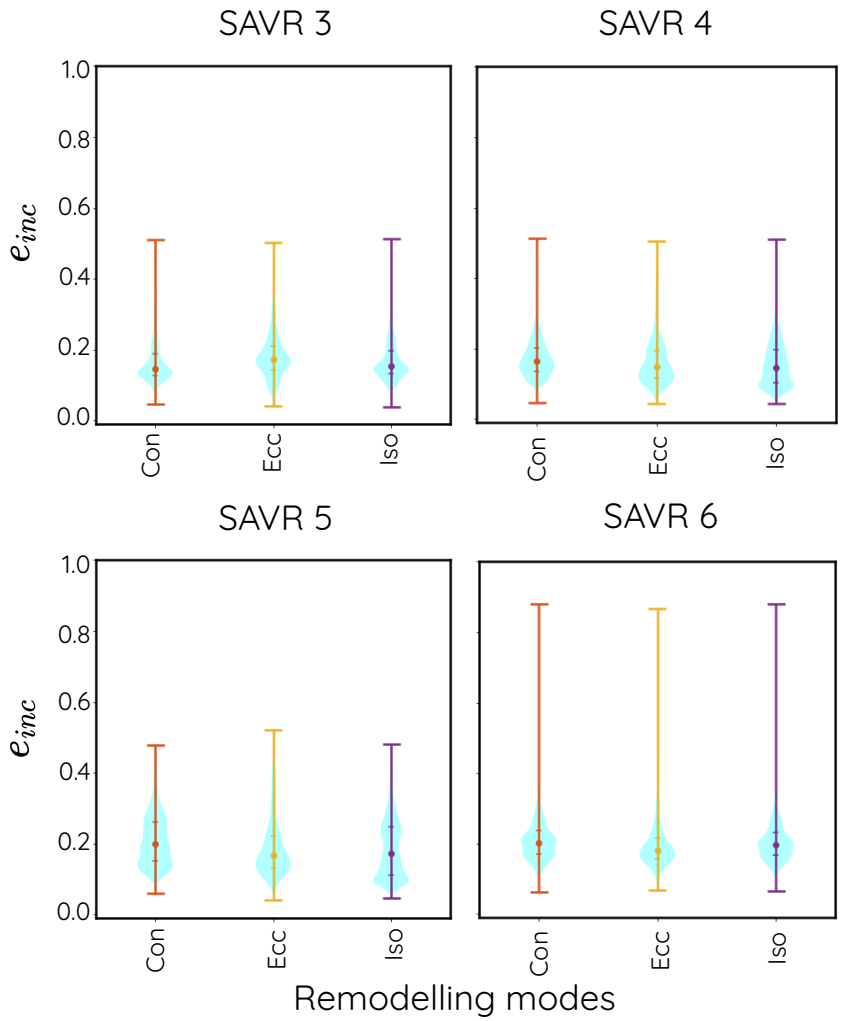

Figure 2 Summary of incompatibility metric e_{inc} within the remodelled post-AVR states following G&R in different patients. Compatibility is associated with $e_{inc} = 0$.

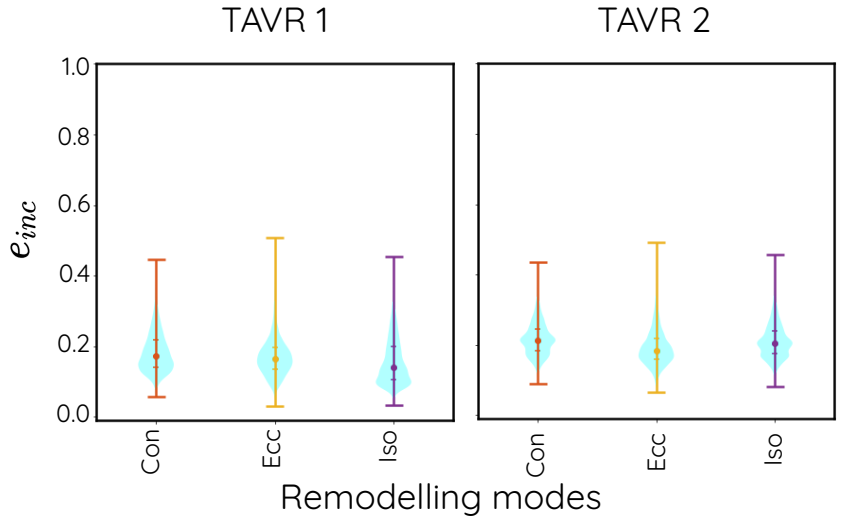

Figure 3 Summary of incompatibility metric e_{inc} within the remodelled post-AVR states following G&R in different patients. Compatibility is associated with $e_{inc} = 0$.

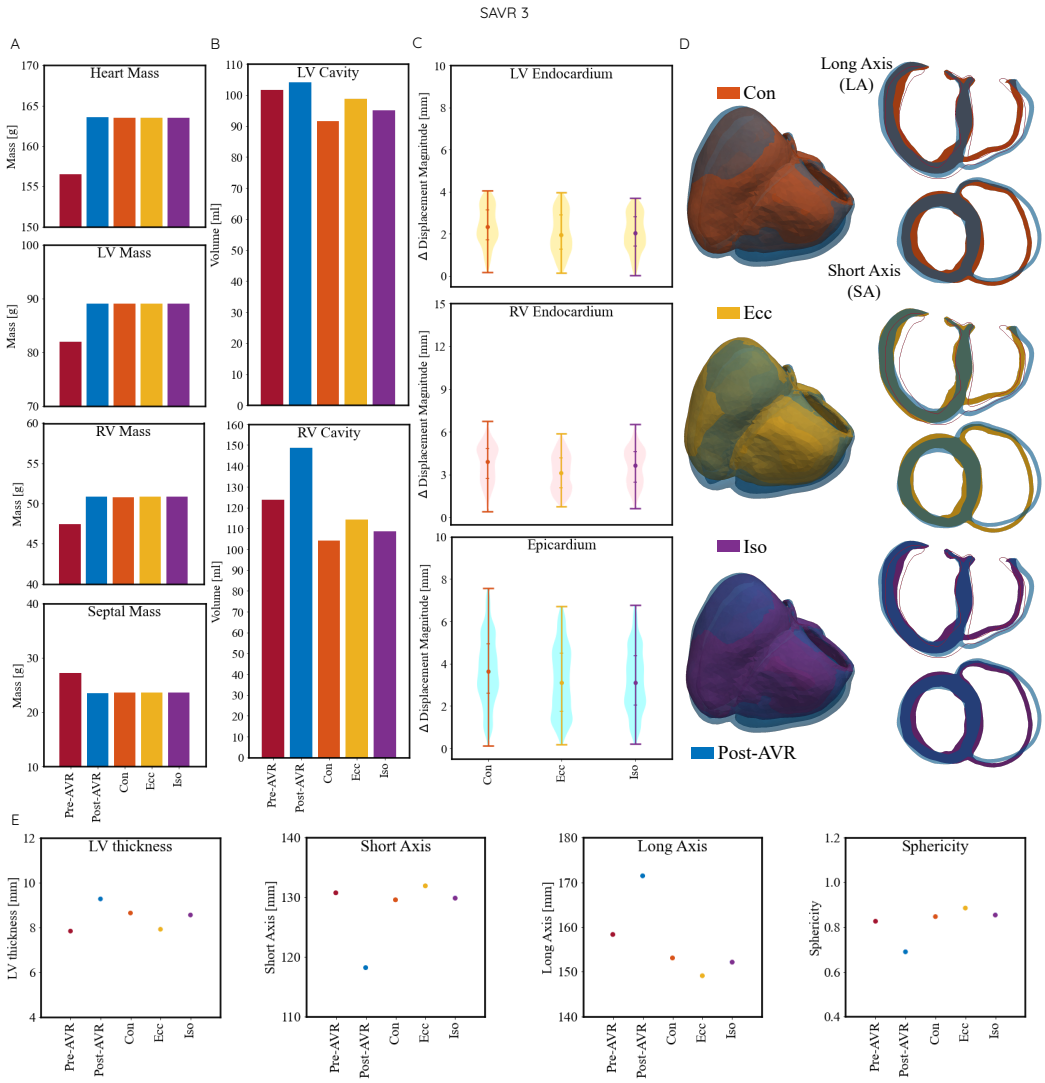

Figure 4 SAVR 3: Comparison between the Pre-, the concentric, eccentric, or isotropic adverse remodelled Post-AVR, and Post-AVR data following AVR. (A) Illustrates the mass [g] alteration of the heart (top) and within the LV (second plot from the top), the RV (third plot from the top) and the septum (bottom) related to the different models. (B) Displays the changes of the LV (top) and RV (bottom) cavity volume with respect to the model. (C) Statistical comparison of a surface registration algorithm of the LV-, RV-endocardium and the epicardium between the imaging data and the adverse growth simulation. (D) Shows the comparison of the Post-AVR data and the different models after applying one of the adverse G&R modes. On the right, the long axis (LA) cuts and short axis (SA) are visualised (red outline) as a reference for the Pre-AVR state. (D) visualises the changes of certain cardiac metrics, such as long axis length (LA), short axis (SA) diameter and LV wall thickness in [mm] and additionally the sphericity index (SI). The different colours represent the individual models, dark red: Pre-AVR model, blue: Post-AVR model, and the modelled Post-AVR concentric, eccentric and isotropic state with orange, yellow and purple, respectively.

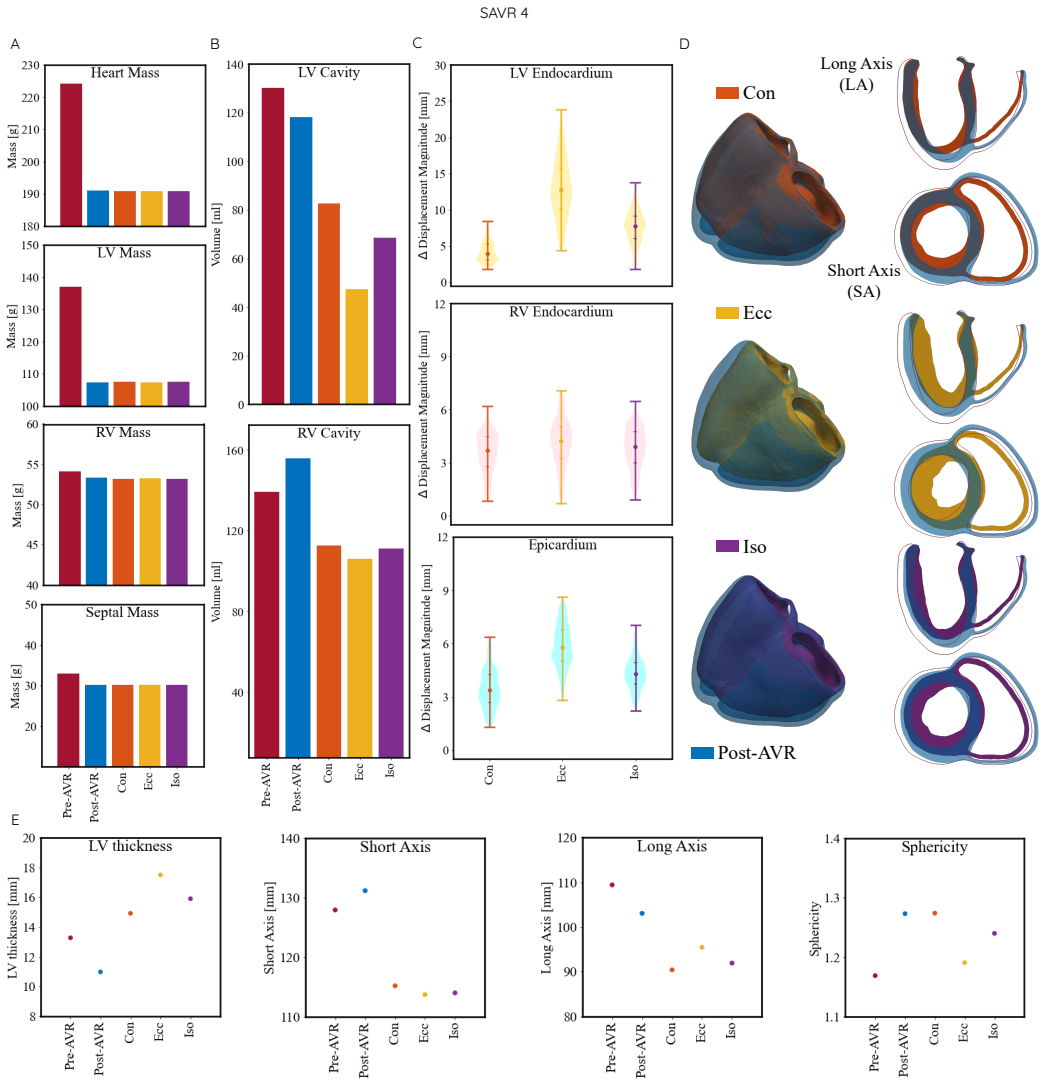

Figure 5 SAVR 4: Comparison between the Pre-, the concentric, eccentric, or isotropic reverse grown Post-AVR, and Post-AVR data following AVR. (A) Illustrates the mass [g] alteration of the heart (top) and within the LV (second plot from the top), the RV (third plot from the top) and the septum (bottom) related to the different models. (B) Displays the changes of the LV (top) and RV (bottom) cavity volume with respect to the model. (C) Statistical comparison of a surface registration algorithm of the LV-, RV-endocardium and the epicardium between the imaging data and the reverse growth simulations. (D) Shows the comparison of the Post-AVR data and the different models after applying one of the reverse G&R modes. On the right, the long axis (LA) cuts and short axis (SA) are visualised (red outline) as a reference for the Pre-AVR state. (D) visualises the changes of certain cardiac metrics, such as long axis length (LA), short axis (SA) diameter and LV wall thickness in [mm] and additionally the sphericity index (SI). The different colours represent the individual models, dark red: Pre-AVR model, blue: Post-AVR model, and the modelled Post-AVR concentric, eccentric and isotropic state with orange, yellow and purple, respectively.

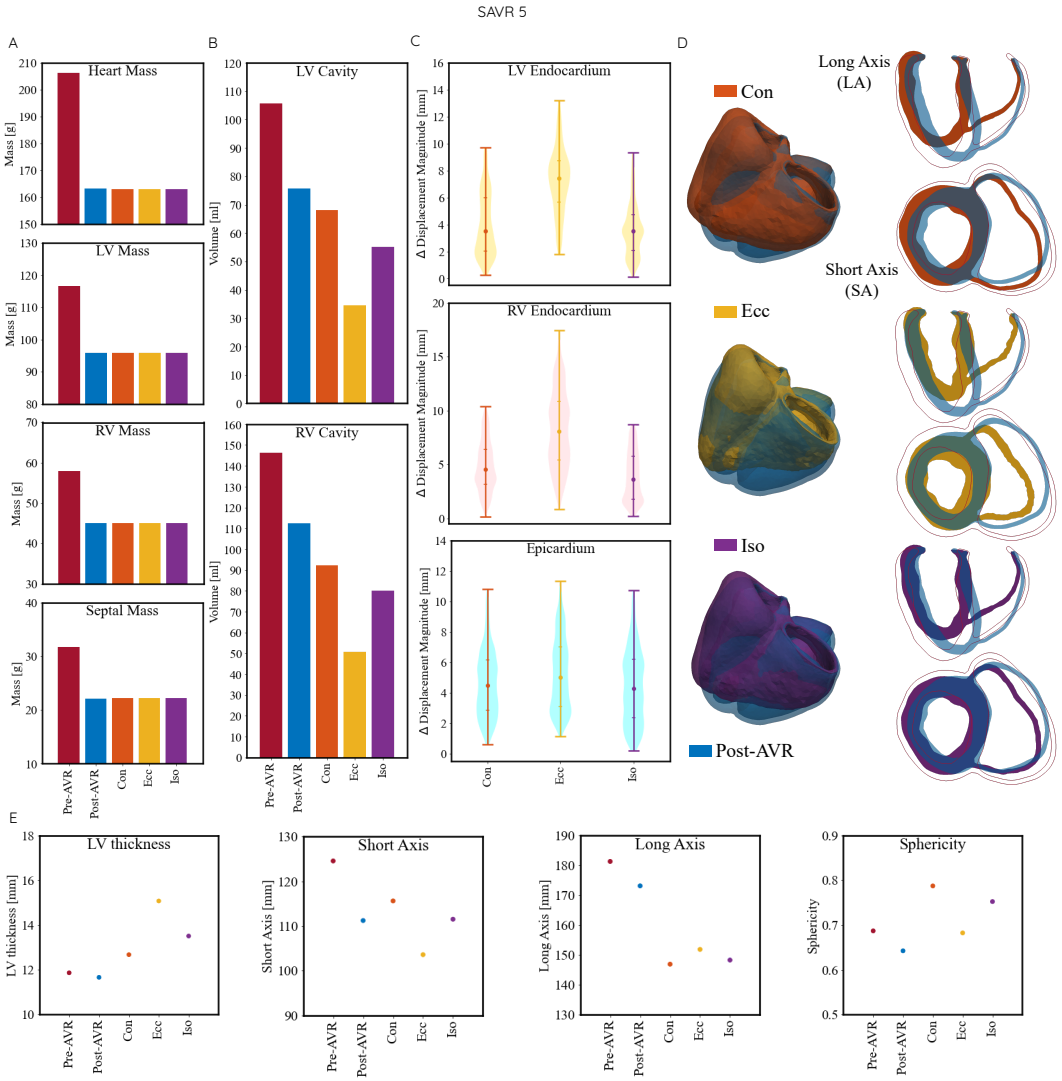

Figure 6 SAVR 5: Comparison between the Pre-, the concentric, eccentric, or isotropic reverse grown Post-AVR, and Post-AVR data following AVR. (A) Illustrates the mass [g] alteration of the heart (top) and within the LV (second plot from the top), the RV (third plot from the top) and the septum (bottom) related to the different models. (B) Displays the changes of the LV (top) and RV (bottom) cavity volume with respect to the model. (C) Statistical comparison of a surface registration algorithm of the LV-, RV-endocardium and the epicardium between the imaging data and the reverse growth simulations. (D) Shows the comparison of the Post-AVR data and the different models after applying one of the reverse G&R modes. On the right, the long axis (LA) cuts and short axis (SA) are visualised (red outline) as a reference for the Pre-AVR state. (D) visualises the changes of certain cardiac metrics, such as long axis length (LA), short axis (SA) diameter and LV wall thickness in [mm] and additionally the sphericity index (SI). The different colours represent the individual models, dark red: Pre-AVR model, blue: Post-AVR model, and the modelled Post-AVR concentric, eccentric and isotropic state with orange, yellow and purple, respectively.

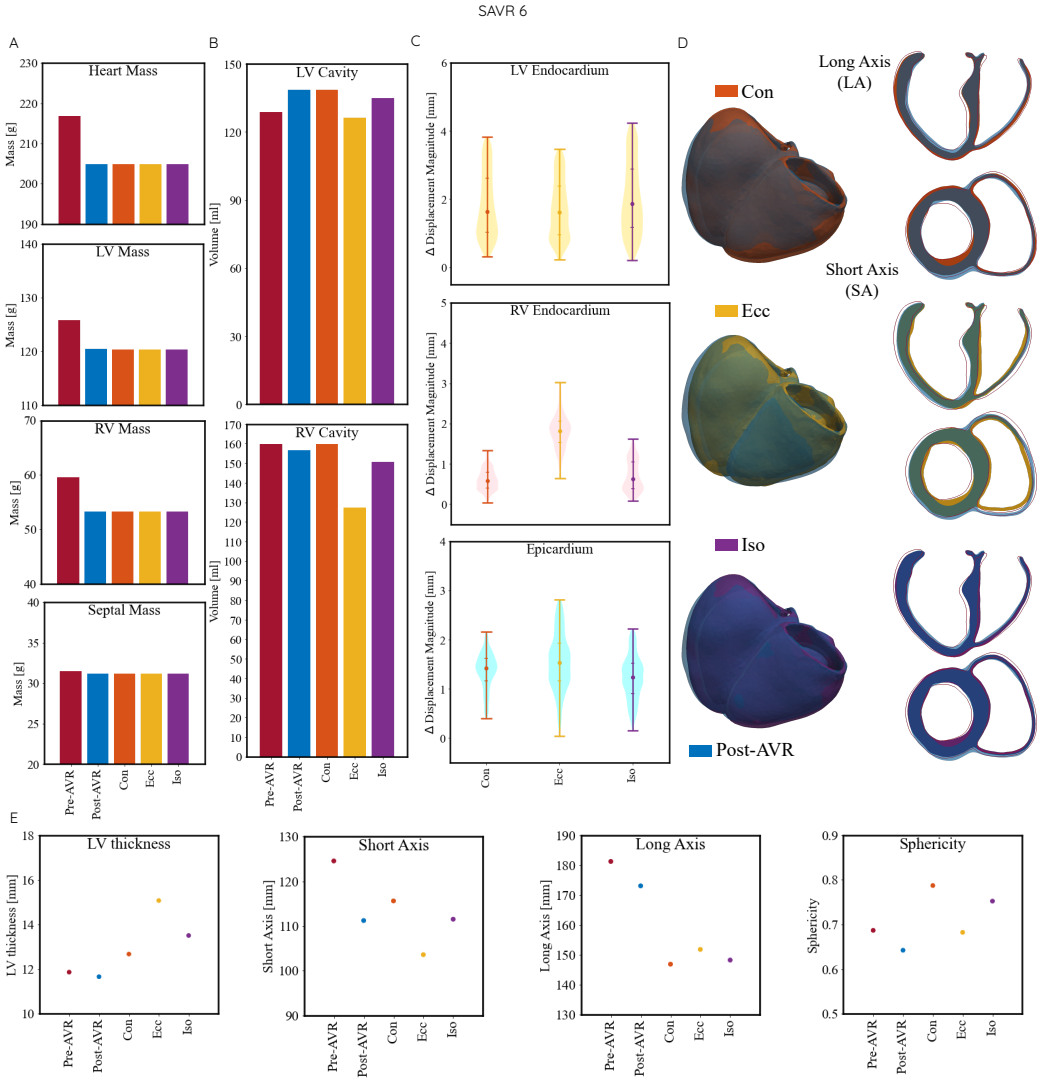

Figure 7 SAVR 6: Comparison between the Pre-, the concentric, eccentric, or isotropic reverse grown Post-AVR, and Post-AVR data following AVR. (A) Illustrates the mass [g] alteration of the heart (top) and within the LV (second plot from the top), the RV (third plot from the top) and the septum (bottom) related to the different models. (B) Displays the changes of the LV (top) and RV (bottom) cavity volume with respect to the model. (C) Statistical comparison of a surface registration algorithm of the LV-, RV-endocardium and the epicardium between the imaging data and the reverse growth simulations. (D) Shows the comparison of the Post-AVR data and the different models after applying one of the reverse G&R modes. On the right, the long axis (LA) cuts and short axis (SA) are visualised (red outline) as a reference for the Pre-AVR state. (D) visualises the changes of certain cardiac metrics, such as long axis length (LA), short axis (SA) diameter and LV wall thickness in [mm] and additionally the sphericity index (SI). The different colours represent the individual models, dark red: Pre-AVR model, blue: Post-AVR model, and the modelled Post-AVR concentric, eccentric and isotropic state with orange, yellow and purple, respectively.

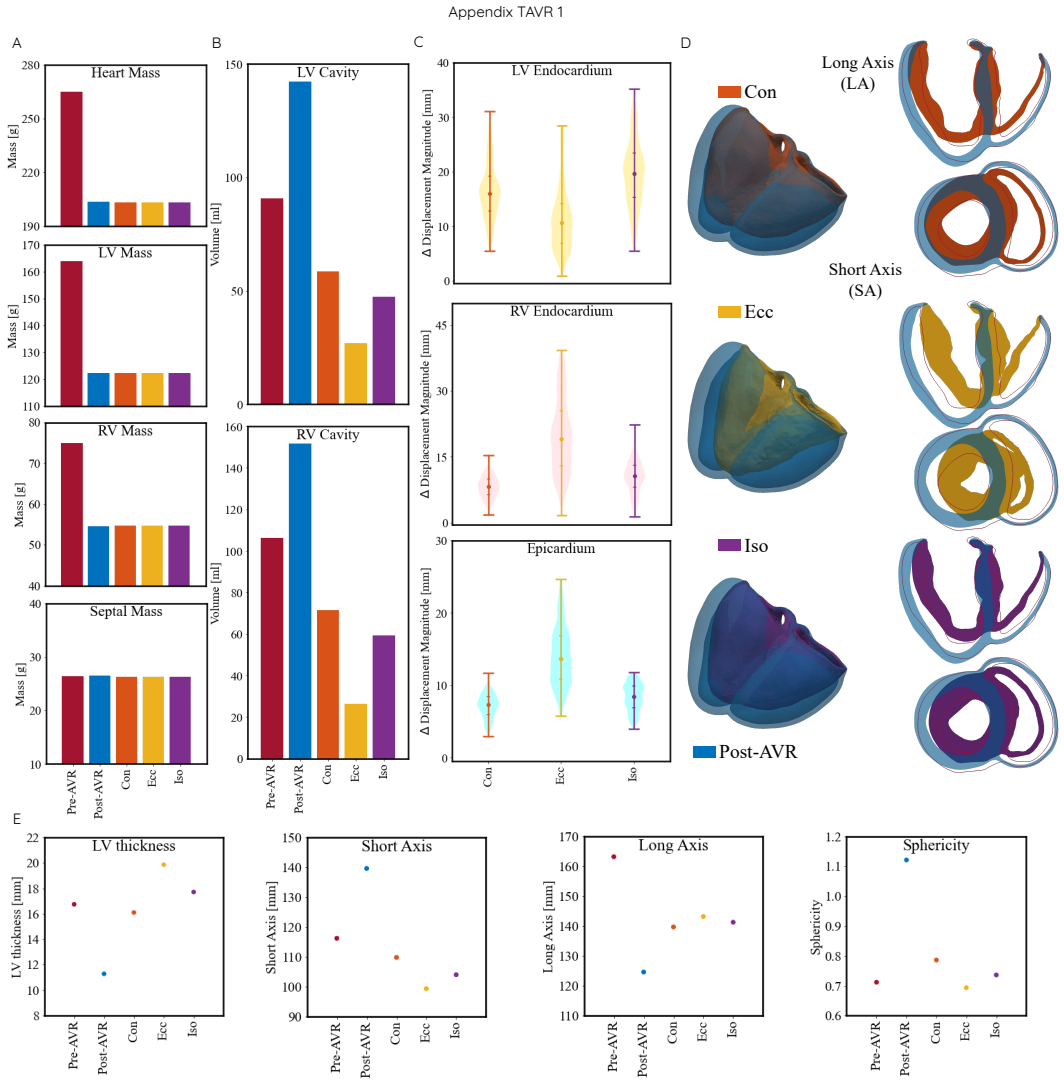

Figure 8 TAVR 1: Comparison between the Pre-, the concentric, eccentric, or isotropic reverse grown Post-AVR, and Post-AVR data following AVR. (A) Illustrates the mass [g] alteration of the heart (top) and within the LV (second plot from the top), the RV (third plot from the top) and the septum (bottom) related to the different models. (B) Displays the changes of the LV (top) and RV (bottom) cavity volume with respect to the model. (C) Statistical comparison of a surface registration algorithm of the LV-, RV-endocardium and the epicardium between the imaging data and the reverse growth simulations. (D) Shows the comparison of the Post-AVR data and the different models after applying one of the reverse G&R modes. On the right, the long axis (LA) cuts and short axis (SA) are visualised (red outline) as a reference for the Pre-AVR state. (D) visualises the changes of certain cardiac metrics, such as long axis length (LA), short axis (SA) diameter and LV wall thickness in [mm] and additionally the sphericity index (SI). The different colours represent the individual models, dark red: Pre-AVR model, blue: Post-AVR model, and the modelled Post-AVR concentric, eccentric and isotropic state with orange, yellow and purple, respectively.

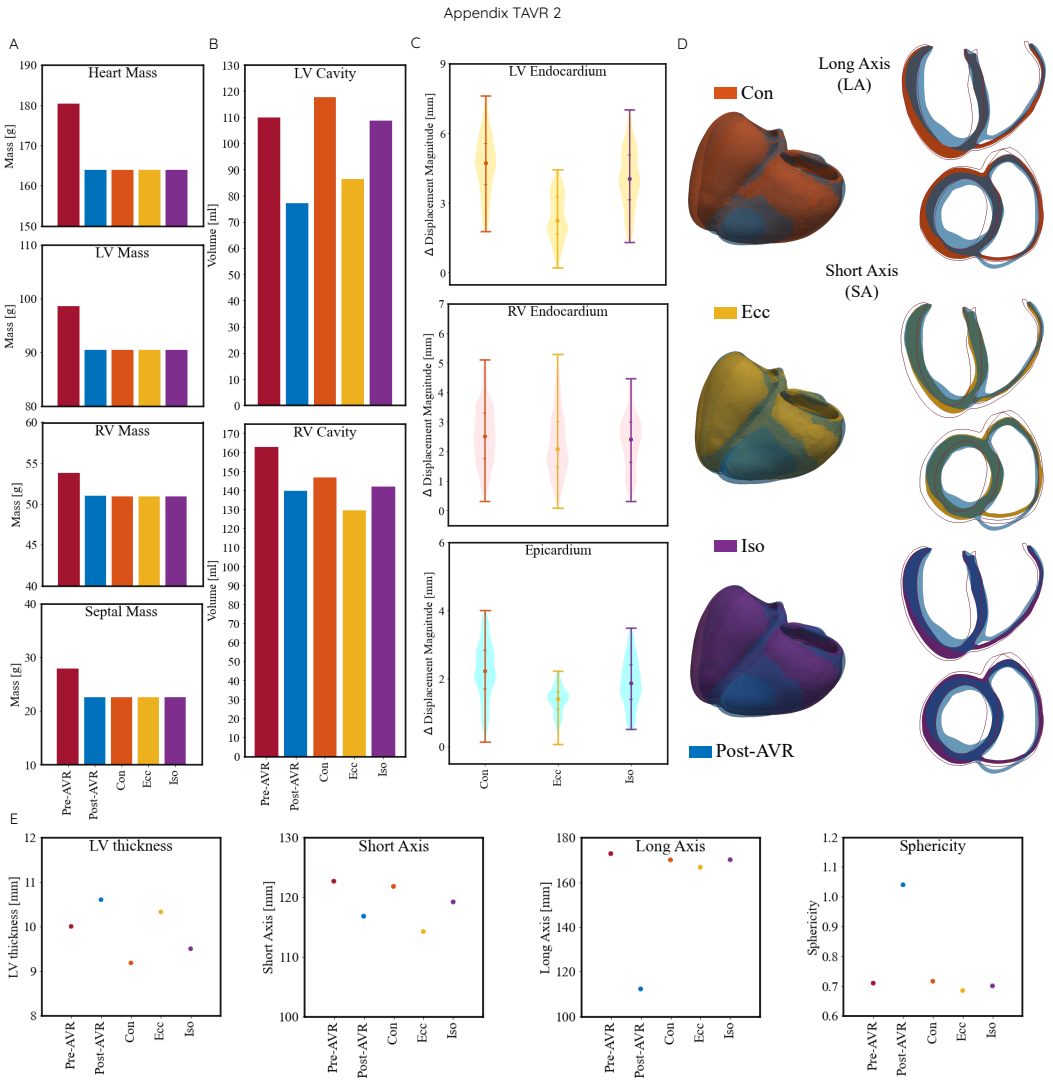

Figure 9 TAVR 2: Comparison between the Pre-, the concentric, eccentric, or isotropic reverse grown Post-AVR, and Post-AVR data following AVR. (A) Illustrates the mass [g] alteration of the heart (top) and within the LV (second plot from the top), the RV (third plot from the top) and the septum (bottom) related to the different models. (B) Displays the changes of the LV (top) and RV (bottom) cavity volume with respect to the model. (C) Statistical comparison of a surface registration algorithm of the LV-, RV-endocardium and the epicardium between the imaging data and the reverse growth simulations. (D) Shows the comparison of the Post-AVR data and the different models after applying one of the reverse G&R modes. On the right, the long axis (LA) cuts and short axis (SA) are visualised (red outline) as a reference for the Pre-AVR state. (D) visualises the changes of certain cardiac metrics, such as long axis length (LA), short axis (SA) diameter and LV wall thickness in [mm] and additionally the sphericity index (SI). The different colours represent the individual models, dark red: Pre-AVR model, blue: Post-AVR model, and the modelled Post-AVR concentric, eccentric and isotropic state with orange, yellow and purple, respectively.

Table 34 Summary of the heart mass changes following G&R: With post-AVR, and simulated G&R results (concentric, eccentric or isotropic growth) compared to the pre-AVR state in [%].

	SAVR 1	SAVR 2	SAVR 3	SAVR 4	SAVR 5	SAVR 6	TAVR 1	TAVR 2
Post	-20.5	+1.0	+4.5	-14.8	-20.9	-5.5	-23.3	-9.1
Con	-20.6	+1.0	+4.4	-14.9	-20.9	-5.5	-23.3	-9.1
Ecc	-20.7	+1.0	+4.4	-14.9	-21.0	-5.5	-23.4	-9.1
Iso	-20.6	+1.0	+4.4	-14.9	-20.9	-5.5	-23.3	-9.1

Table 35 Summary of the LV mass changes following G&R: With post-AVR data, and simulated G&R results (concentric, eccentric or isotropic growth) compared to the pre-AVR state in [%].

	SAVR 1	SAVR 2	SAVR 3	SAVR 4	SAVR 5	SAVR 6	TAVR 1	TAVR 2
Post	-35.9	-11.8	+8.8	-21.7	-17.7	-4.3	-25.4	-8.2
Con	-35.7	-11.7	+8.7	-21.6	-17.8	-4.3	-25.3	-8.3
Ecc	-35.8	-11.7	+8.7	-21.6	-17.8	-4.3	-25.4	-8.3
Iso	-35.7	-11.7	+8.7	-21.6	-17.8	-4.3	-25.3	-8.3

Table 36 Summary of the RV mass changes following G&R: With post-AVR data, and simulated G&R results (concentric, eccentric or isotropic growth) compared to the pre-AVR state in [%].

	SAVR 1	SAVR 2	SAVR 3	SAVR 4	SAVR 5	SAVR 6	TAVR 1	TAVR 2
Post	+4.4	+12.3	+7.4	-1.5	-22.3	-10.5	-27.1	-5.3
Con	+4.0	+12.3	+7.2	-1.7	-22.4	-10.4	-27.0	-5.4
Ecc	+4.1	+12.3	+7.2	-1.7	-22.4	-10.4	-27.0	-5.4
Iso	+4.1	+12.3	+7.2	-1.7	-22.4	-10.4	-27.0	-5.4

Table 37 Summary of the septal mass changes following G&R: With post-AVR data, and simulated G&R results (concentric, eccentric or isotropic growth) compared to the pre-AVR state in [%].

	SAVR 1	SAVR 2	SAVR 3	SAVR 4	SAVR 5	SAVR 6	TAVR 1	TAVR 2
Post	+19.5	+32.1	-13.5	-8.5	-30.1	-0.9	+0.5	-19.3
Con	+18.2	+31.1	-13.1	-8.6	-29.9	-1.1	-0.6	-19.1
Ecc	+18.2	+31.4	-13.2	-8.6	-30.0	-1.1	-0.6	-19.2
Iso	+18.3	+31.3	-13.1	-8.6	-29.9	-1.1	-0.6	-19.1

Table 38 Summary of the LV cavity changes following G&R: With post-AVR data, and simulated G&R results (concentric, eccentric or isotropic growth) compared to the pre-AVR state in [%].

	SAVR 1	SAVR 2	SAVR 3	SAVR 4	SAVR 5	SAVR 6	TAVR 1	TAVR 2
Post	-36.1	+37.8	+2.5	-9.1	-28.4	+7.6	+56.7	-29.9
Con	-35.2	+8.3	-9.9	-36.4	-35.6	+7.6	-35.5	+7.0
Ecc	-69.3	-2.1	-2.8	-63.6	-67.2	-1.8	-70.4	-21.4
Iso	-48.2	+8.9	-6.6	-47.2	-47.7	+4.7	-47.8	-1.1

Table 39 Summary of the RV cavity changes following G&R: With post-AVR data, and simulated G&R results (concentric, eccentric or isotropic growth) compared to the pre-AVR state in [%].

	SAVR 1	SAVR 2	SAVR 3	SAVR 4	SAVR 5	SAVR 6	TAVR 1	TAVR 2
Post	+15.5	+50.0	+20.2	+11.9	-23.2	-2.0	+42.9	-14.2
Con	+2.0	-9.7	-15.9	-19.1	-37.0	-0.1	-32.7	-9.8
Ecc	-3.5	+5.7	-7.6	-23.9	-65.3	-20.3	-75.3	-20.4
Iso	+2.9	-3.3	-12.3	-20.3	-45.3	-5.8	-44.1	-12.7

Table 40 Summary of mean and standard deviation of the displacement field as a result of registering[7] the LV endocardium surface of the predicted growth cases to the post-AVR data in [mm].

	SAVR 1	SAVR 2	SAVR 3	SAVR 4	SAVR 5	SAVR 6	TAVR 1	TAVR 2
Con	1.3 (0.6)	4.6 (1.9)	2.4 (0.9)	4.3 (1.4)	4.0 (2.4)	1.8 (0.9)	16.5 (5.2)	4.7 (1.3)
Ecc	5.4 (2.1)	6.4 (3.1)	2.1 (1.0)	13.0 (4.1)	7.3 (2.4)	1.7 (0.8)	11.4 (6.0)	2.4 (1.0)
Iso	1.2 (0.4)	5.7 (2.6)	2.1 (0.9)	7.6 (2.4)	3.6 (2.0)	2.0 (1.1)	19.6 (6.2)	4.1 (1.3)

Table 41 Summary of mean and standard deviation of the displacement field as a result of registering[7] the RV endocardium surface of the predicted growth cases to the post-AVR data in [mm].

	SAVR 1	SAVR 2	SAVR 3	SAVR 4	SAVR 5	SAVR 6	TAVR 1	TAVR 2
Con	2.1 (0.8)	5.1 (2.4)	3.8 (1.3)	3.5 (1.2)	4.8 (2.3)	0.6 (0.3)	8.2 (2.5)	2.5 (1.0)
Ecc	1.9 (0.9)	3.6 (1.5)	3.1 (1.2)	4.1 (1.4)	8.3 (3.6)	1.8 (0.4)	19.8 (8.5)	2.3 (1.1)
Iso	1.9 (0.7)	4.4 (2.0)	3.5 (1.3)	3.8 (1.2)	3.9 (2.3)	0.7 (0.4)	10.7 (3.9)	2.3 (0.9)

Table 42 Summary of mean and standard deviation of the displacement field as a result of registering[7] the epicardium surface of the predicted growth to the post-AVR data in [mm].

	SAVR 1	SAVR 2	SAVR 3	SAVR 4	SAVR 5	SAVR 6	TAVR 1	TAVR 2
Con	2.4 (0.9)	5.5 (2.0)	3.7 (1.6)	3.5 (1.1)	4.6 (2.2)	1.4 (0.4)	7.2 (1.8)	2.2 (0.8)
Ecc	3.1 (1.3)	5.5 (2.3)	3.2 (1.6)	5.8 (1.2)	5.2 (2.4)	1.6 (0.6)	14.1 (4.1)	1.4 (0.4)
Iso	1.6 (0.6)	5.4 (2.0)	3.2 (1.5)	4.3 (1.0)	4.4 (2.4)	1.2 (0.5)	8.3 (1.9)	1.9 (0.7)

Table 43 Summary of the LV thickness changes following G&R: With post-AVR data, and simulated G&R results (concentric, eccentric or isotropic growth) compared to the pre-AVR state in %.

	SAVR 1	SAVR 2	SAVR 3	SAVR 4	SAVR 5	SAVR 6	TAVR 1	TAVR 2
Post	-2.5	-19.7	+18.3	-17.3	-1.7	+4.5	-32.6	+6.0
Con	-10.1	-1.3	+10.3	+12.4	+6.9	-6.5	-3.8	-8.2
Ecc	+22.4	+10.9	+1.0	+31.8	+27.1	-2.1	+18.6	+3.3
Iso	+0.3	+1.6	+9.2	+19.8	+13.9	-4.2	+5.8	-5.0

Table 44 Summary of the short axis changes following G&R: With post-AVR data, and simulated G&R results (concentric, eccentric or isotropic growth) compared to the pre-AVR state in %.

	SAVR 1	SAVR 2	SAVR 3	SAVR 4	SAVR 5	SAVR 6	TAVR 1	TAVR 2
Post	-7.6	-3.1	-9.6	+2.5	-10.7	-1.8	+20.1	-4.8
Con	-4.2	+4.8	-0.9	-10.0	-7.2	+2.5	-5.5	-0.7
Ecc	-12.8	+8.0	+0.9	-11.1	-16.8	-0.7	-14.5	-6.9
Iso	-6.5	+6.7	-0.7	-10.9	-10.5	+1.3	-10.5	-2.8

Table 45 Summary of the long axis changes following G&R: With post-AVR data, and simulated G&R results (concentric, eccentric or isotropic growth) compared to the pre-AVR state in %.

	SAVR 1	SAVR 2	SAVR 3	SAVR 4	SAVR 5	SAVR 6	TAVR 1	TAVR 2
Post	-51.9	-31.8	+8.3	-5.8	-4.5	-37.6	-23.7	-35.0
Con	-16.8	-2.0	-3.3	-17.4	-19.0	+0.5	-14.4	-1.6
Ecc	-8.2	-0.9	-5.8	-12.7	-16.3	-0.0	-12.3	-3.5
Iso	-12.9	-0.9	-3.9	-16.0	-18.3	+0.4	-13.4	-1.6

Table 46 Summary of the LV sphericity index changes following G&R: With post-AVR data, and simulated G&R results (concentric, eccentric or isotropic growth) compared to the pre-AVR state in %.

	SAVR 1	SAVR 2	SAVR 3	SAVR 4	SAVR 5	SAVR 6	TAVR 1	TAVR 2
Post	+91.9	+42.1	-16.5	+8.9	-6.5	+57.4	+57.4	+46.5
Con	+15.2	+6.9	+2.5	+9.0	+14.6	+2.0	+10.4	+0.9
Ecc	-5.0	+8.9	+7.1	+1.9	-0.7	-0.6	-2.6	-3.5
Iso	+7.3	+7.7	+3.4	+6.1	+9.5	+0.9	+3.4	-1.3

Appendix .3. Supplementary Chapter 6

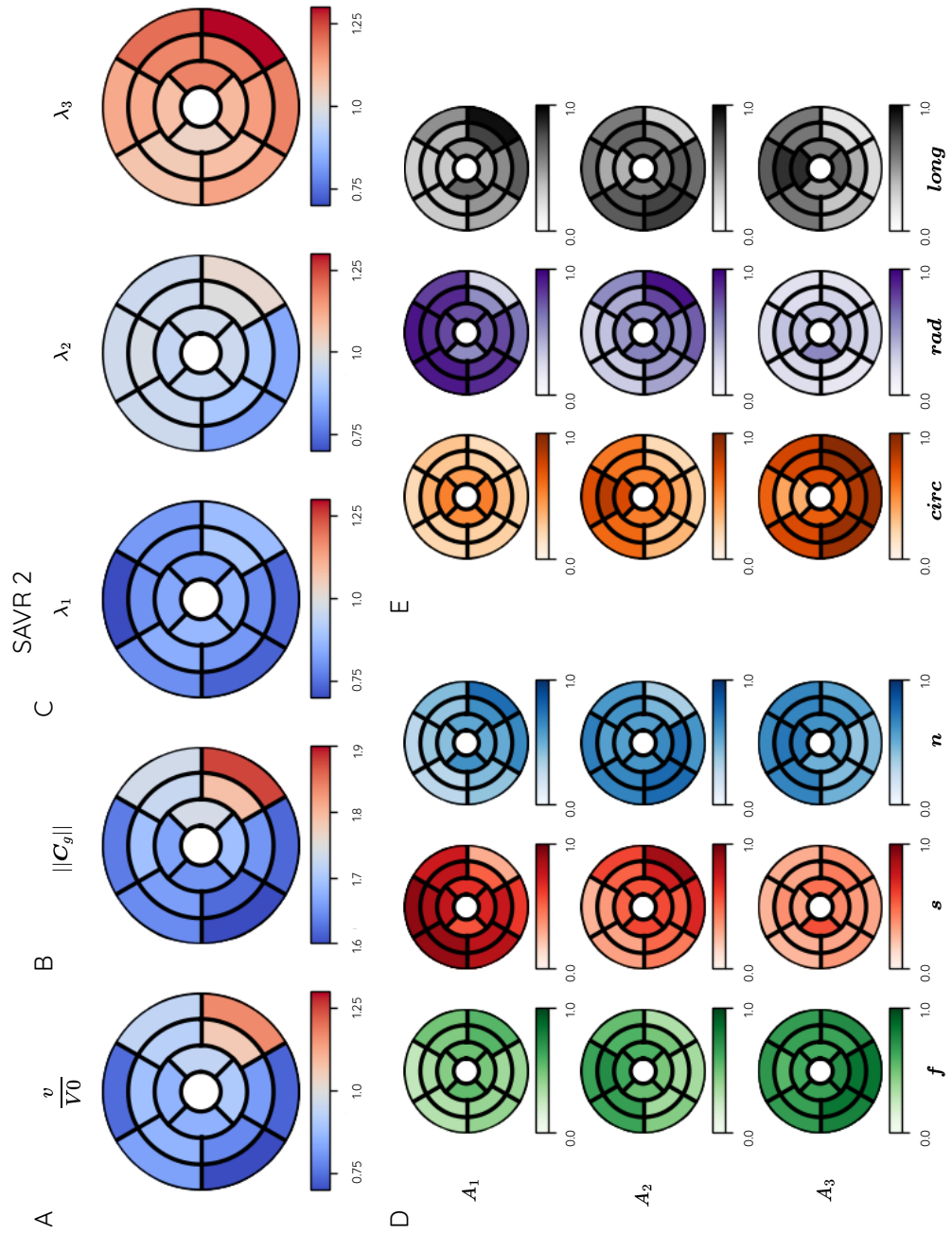

Figure 10 Adverse growth pattern analysis in SAVR 2. (A) displays the average volume ratio of the post-AVR state after adverse growth to the reference volume of the pre-AVR state across the LV. (B) illustrates the calculated mean Frobenius norm of the right Cauchy-Green growth strain tensor $\mathbf{C}_g$ within the 17 AHA segments. (C) presents the mean eigenvalues of $\mathbf{C}_g$ in ascending order within the AHA regions of the LV. Previous colour codes refer to either high (red) or low (blue) values. (D) shows the associated eigenvectors to the eigenvalues presented in (C), where a directional agreement with the fibres, sheet, or sheet-normal direction is indicated by green, red or blue, respectively. (E) shows the associated eigenvectors to the eigenvalues presented in (C), where a directional agreement with the circumferential, radial, or longitudinal direction is indicated by grey, purple or orange, respectively.

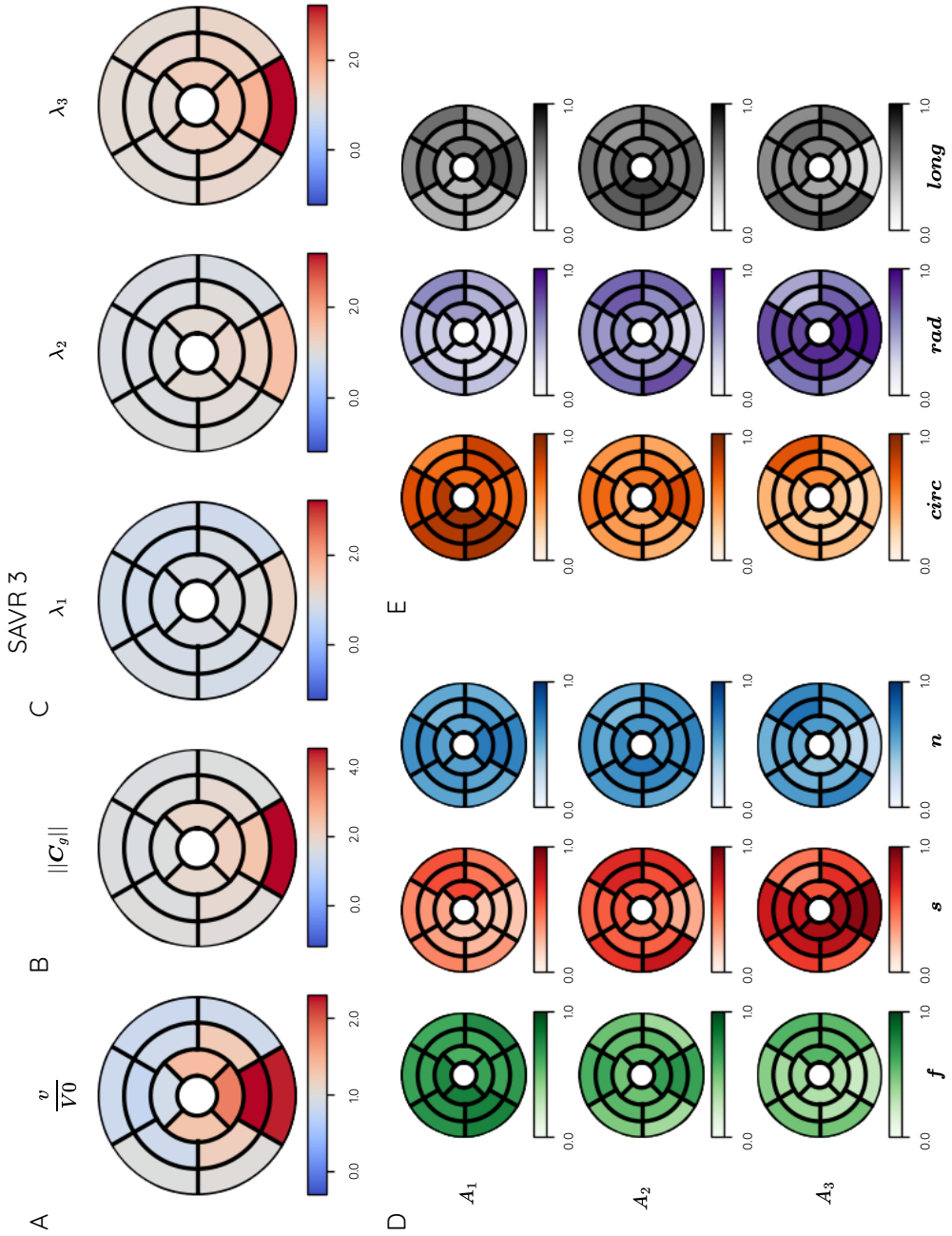

Figure 11 Adverse growth pattern analysis in SAVR 3. (A) displays the average volume ratio of the post-AVR state after adverse growth to the reference volume of the pre-AVR state across the LV. (B) illustrates the calculated mean Frobenius norm of the right Cauchy-Green growth strain tensor $\mathbf{C}_g$ within the 17 AHA segments. (C) presents the mean eigenvalues of $\mathbf{C}_g$ in ascending order within the AHA regions of the LV. Previous colour codes refer to either high (red) or low (blue) values. (D) shows the associated eigenvectors to the eigenvalues presented in (C), where a directional agreement with the fibres, sheet, or sheet-normal direction is indicated by green, red or blue, respectively. (E) shows the associated eigenvectors to the eigenvalues presented in (C), where a directional agreement with the circumferential, radial, or longitudinal direction is indicated by grey, purple or orange, respectively.

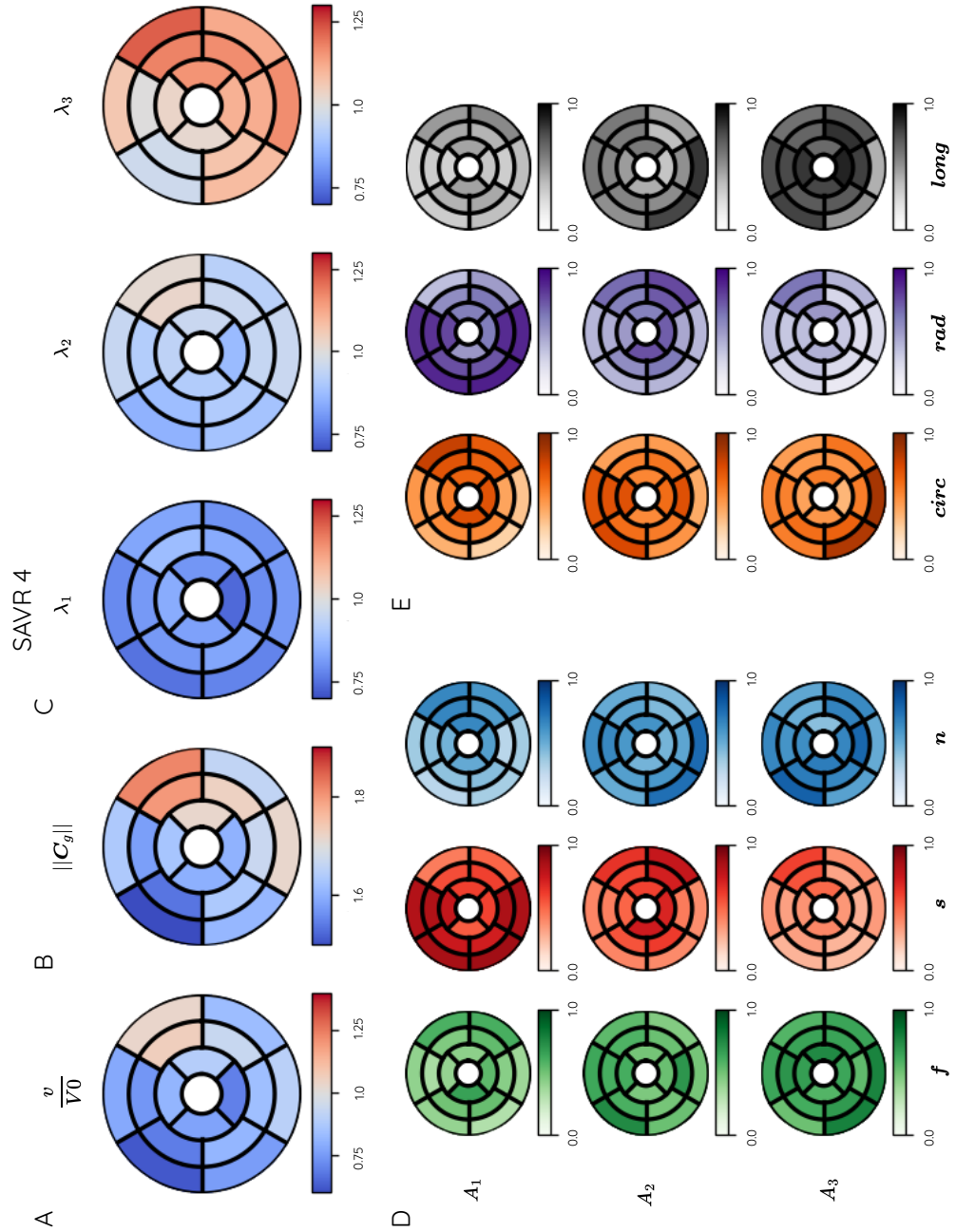

Figure 12 Reverse growth pattern analysis in SAVR 4. (A) displays the average volume ratio of the post-AVR state after reverse growth to the reference volume of the pre-AVR state across the LV. (B) illustrates the calculated mean Frobenius norm of the right Cauchy-Green growth strain tensor $\mathbf{C}_g$ within the 17 AHA segments. (C) presents the mean eigenvalues of $\mathbf{C}_g$ in ascending order within the AHA regions of the LV. Previous colour codes refer to either high (red) or low (blue) values. (D) shows the associated eigenvectors to the eigenvalues presented in (C), where a directional agreement with the fibres, sheet, or sheet-normal direction is indicated by green, red or blue, respectively. (E) shows the associated eigenvectors to the eigenvalues presented in (C), where a directional agreement with the circumferential, radial, or longitudinal direction is indicated by grey, purple or orange, respectively.

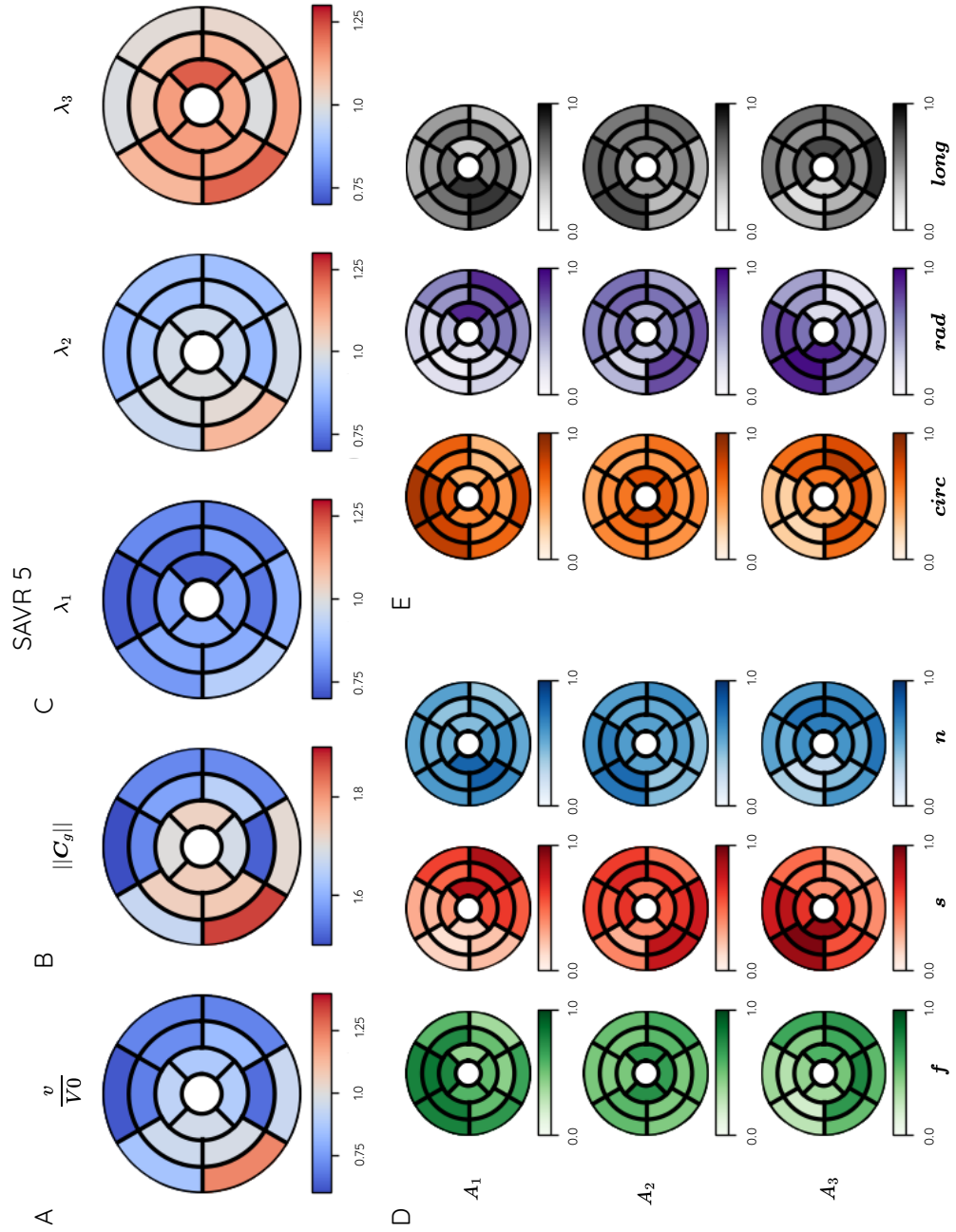

Figure 13 Reverse growth pattern analysis in SAVR 5. (A) displays the average volume ratio of the post-AVR state after reverse growth to the reference volume of the pre-AVR state across the LV. (B) illustrates the calculated mean Frobenius norm of the right Cauchy-Green growth strain tensor $\mathbf{C}_g$ within the 17 AHA segments. (C) presents the mean eigenvalues of $\mathbf{C}_g$ in ascending order within the AHA regions of the LV. Previous colour codes refer to either high (red) or low (blue) values. (D) shows the associated eigenvectors to the eigenvalues presented in (C), where a directional agreement with the fibres, sheet, or sheet-normal direction is indicated by green, red or blue, respectively. (E) shows the associated eigenvectors to the eigenvalues presented in (C), where a directional agreement with the circumferential, radial, or longitudinal direction is indicated by grey, purple or orange, respectively.

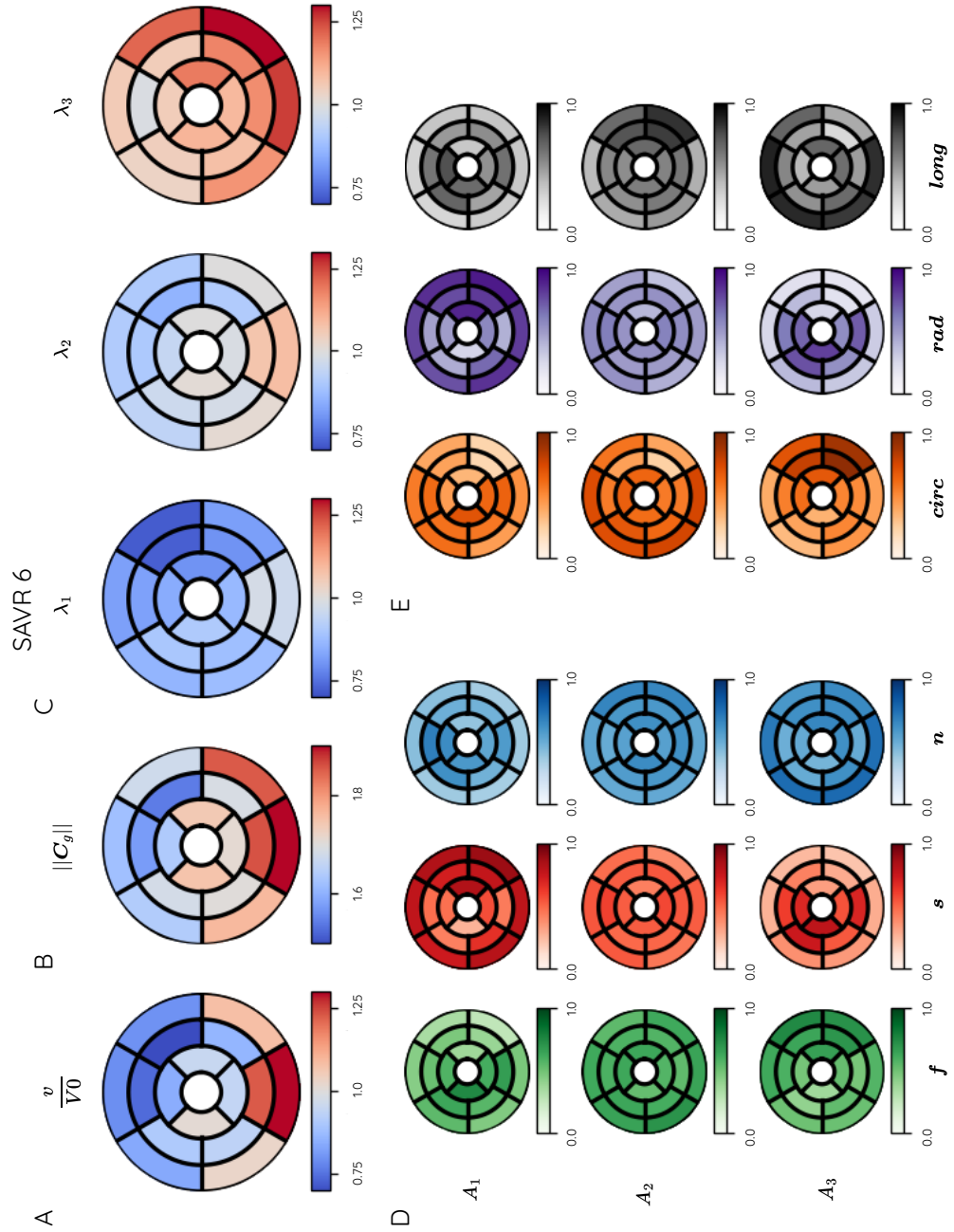

Figure 14 Reverse growth pattern analysis in SAVR 6. (A) displays the average volume ratio of the post-AVR state after reverse growth to the reference volume of the pre-AVR state across the LV. (B) illustrates the calculated mean Frobenius norm of the right Cauchy-Green growth strain tensor $\mathbf{C}_g$ within the 17 AHA segments. (C) presents the mean eigenvalues of $\mathbf{C}_g$ in ascending order within the AHA regions of the LV. Previous colour codes refer to either high (red) or low (blue) values. (D) shows the associated eigenvectors to the eigenvalues presented in (C), where a directional agreement with the fibres, sheet, or sheet-normal direction is indicated by green, red or blue, respectively. (E) shows the associated eigenvectors to the eigenvalues presented in (C), where a directional agreement with the circumferential, radial, or longitudinal direction is indicated by grey, purple or orange, respectively.

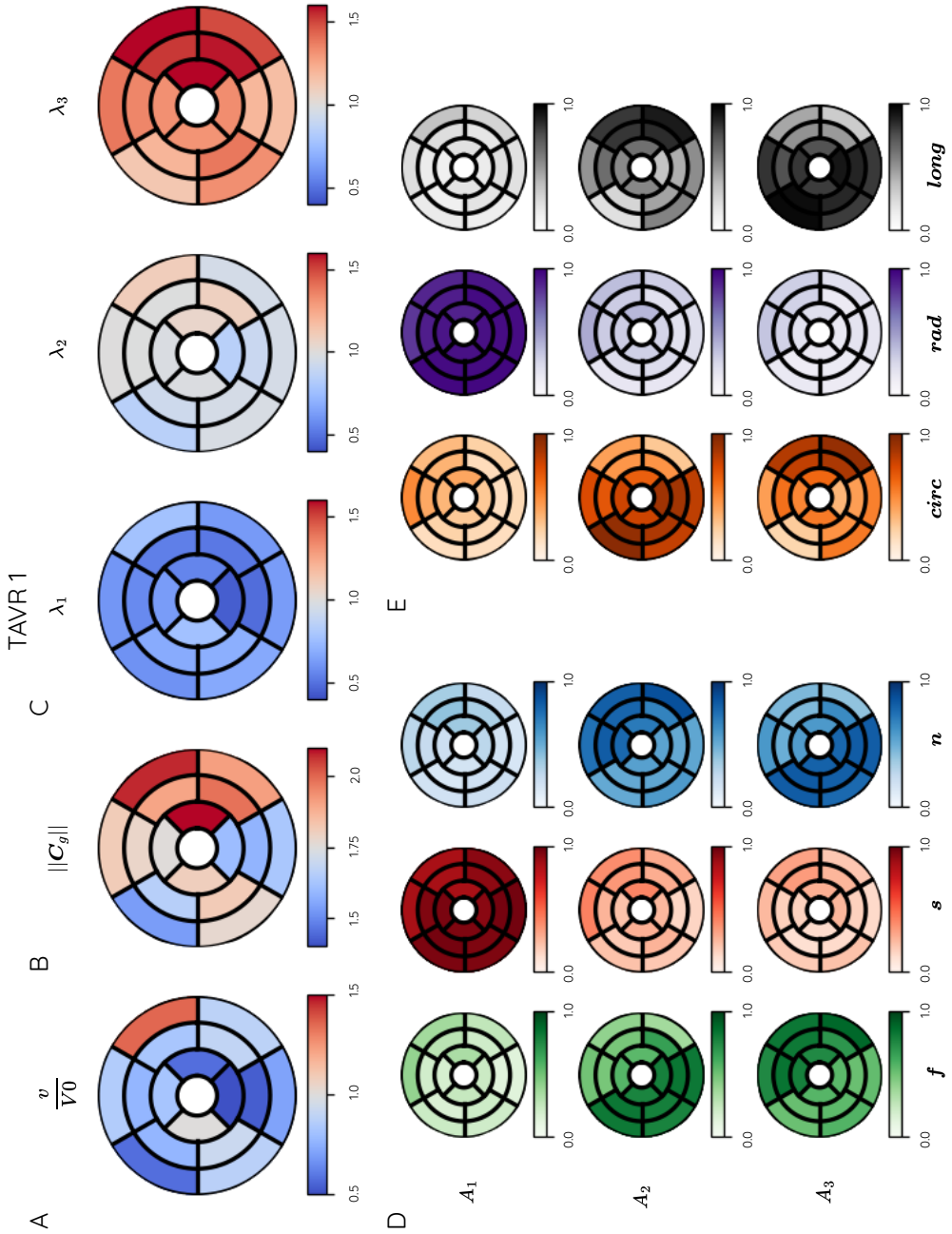

Figure 15 Reverse growth pattern analysis in TAVR 1. (A) displays the average volume ratio of the post-AVR state after reverse growth to the reference volume of the pre-AVR state across the LV. (B) illustrates the calculated mean Frobenius norm of the right Cauchy-Green growth strain tensor $\mathbf{C}_g$ within the 17 AHA segments. (C) presents the mean eigenvalues of $\mathbf{C}_g$ in ascending order within the AHA regions of the LV. Previous colour codes refer to either high (red) or low (blue) values. (D) shows the associated eigenvectors to the eigenvalues presented in (C), where a directional agreement with the fibres, sheet, or sheet-normal direction is indicated by green, red or blue, respectively. (E) shows the associated eigenvectors to the eigenvalues presented in (C), where a directional agreement with the circumferential, radial, or longitudinal direction is indicated by grey, purple or orange, respectively.

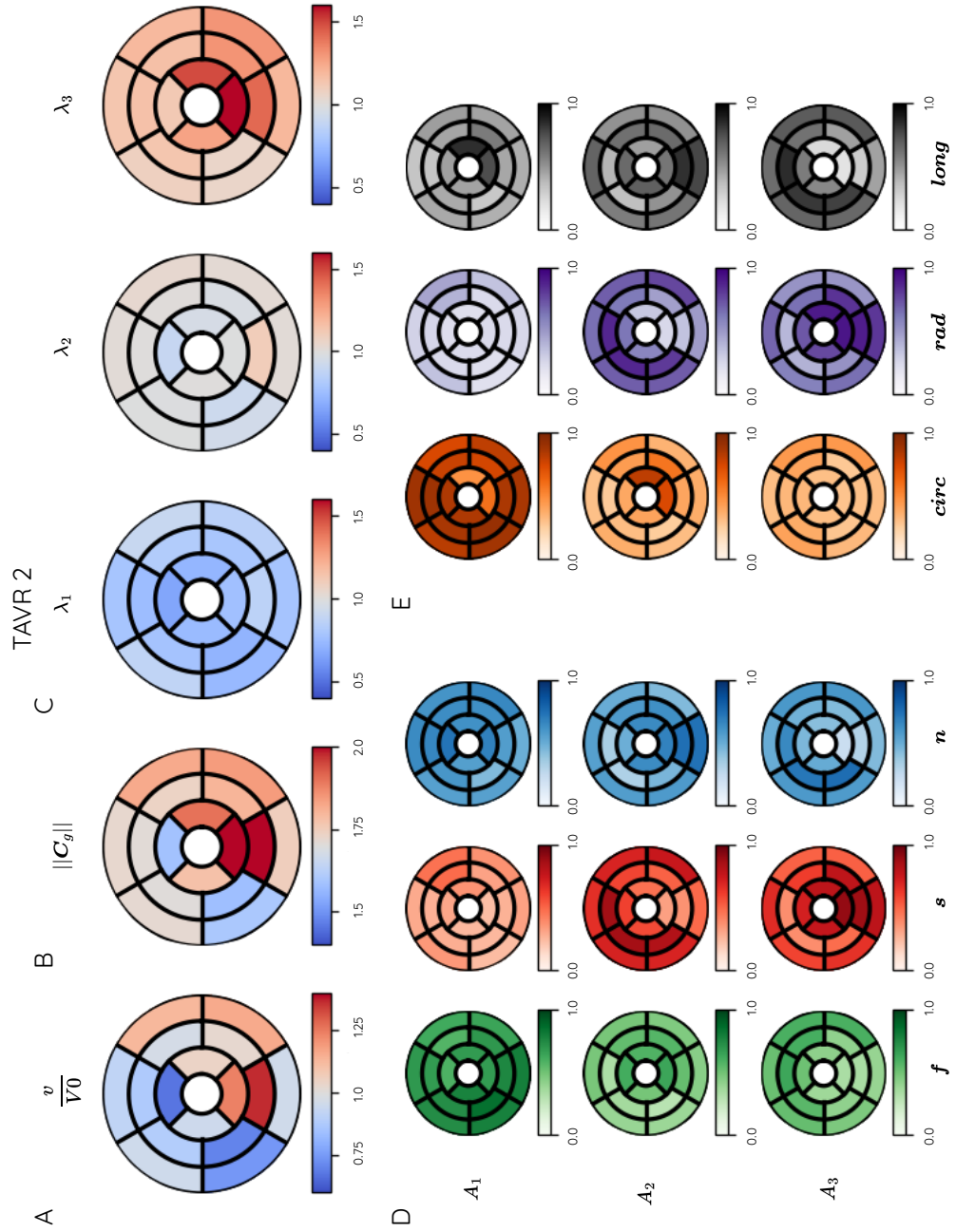

Figure 16 Reverse growth pattern analysis in TAVR 2. (A) displays the average volume ratio of the post-AVR state after reverse growth to the reference volume of the pre-AVR state across the LV. (B) illustrates the calculated mean Frobenius norm of the right Cauchy-Green growth strain tensor $\mathbf{C}_g$ within the 17 AHA segments. (C) presents the mean eigenvalues of $\mathbf{C}_g$ in ascending order within the AHA regions of the LV. Previous colour codes refer to either high (red) or low (blue) values. (D) shows the associated eigenvectors to the eigenvalues presented in (C), where a directional agreement with the fibres, sheet, or sheet-normal direction is indicated by green, red or blue, respectively. (E) shows the associated eigenvectors to the eigenvalues presented in (C), where a directional agreement with the circumferential, radial, or longitudinal direction is indicated by grey, purple or orange, respectively.

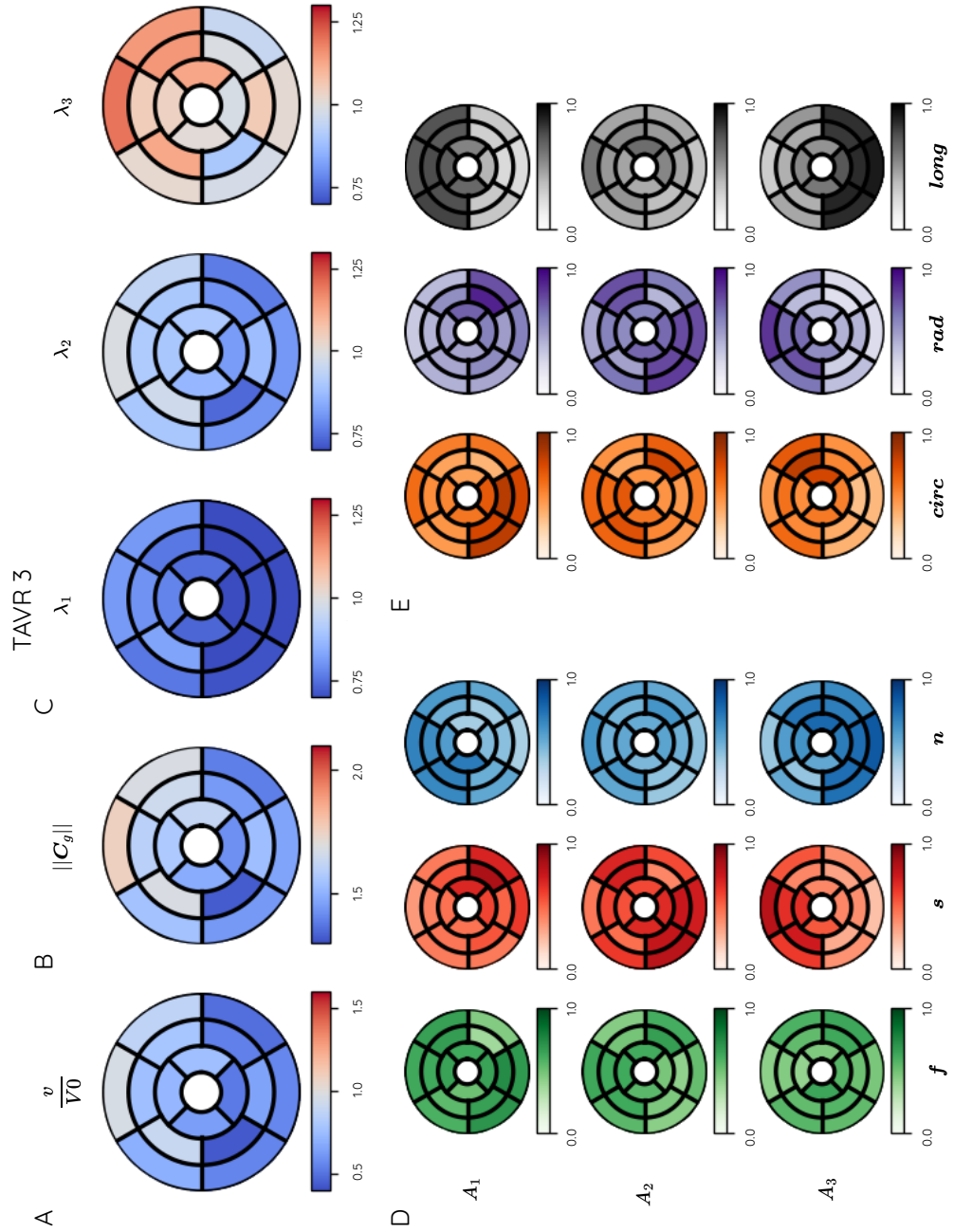

Figure 17 Reverse growth pattern analysis in TAVR 3. (A) displays the average volume ratio of the post-AVR state after reverse growth to the reference volume of the pre-AVR state across the LV. (B) illustrates the calculated mean Frobenius norm of the right Cauchy-Green growth strain tensor $\mathbf{C}_g$ within the 17 AHA segments. (C) presents the mean eigenvalues of $\mathbf{C}_g$ in ascending order within the AHA regions of the LV. Previous colour codes refer to either high (red) or low (blue) values. (D) shows the associated eigenvectors to the eigenvalues presented in (C), where a directional agreement with the fibres, sheet, or sheet-normal direction is indicated by green, red or blue, respectively. (E) shows the associated eigenvectors to the eigenvalues presented in (C), where a directional agreement with the circumferential, radial, or longitudinal direction is indicated by grey, purple or orange, respectively.

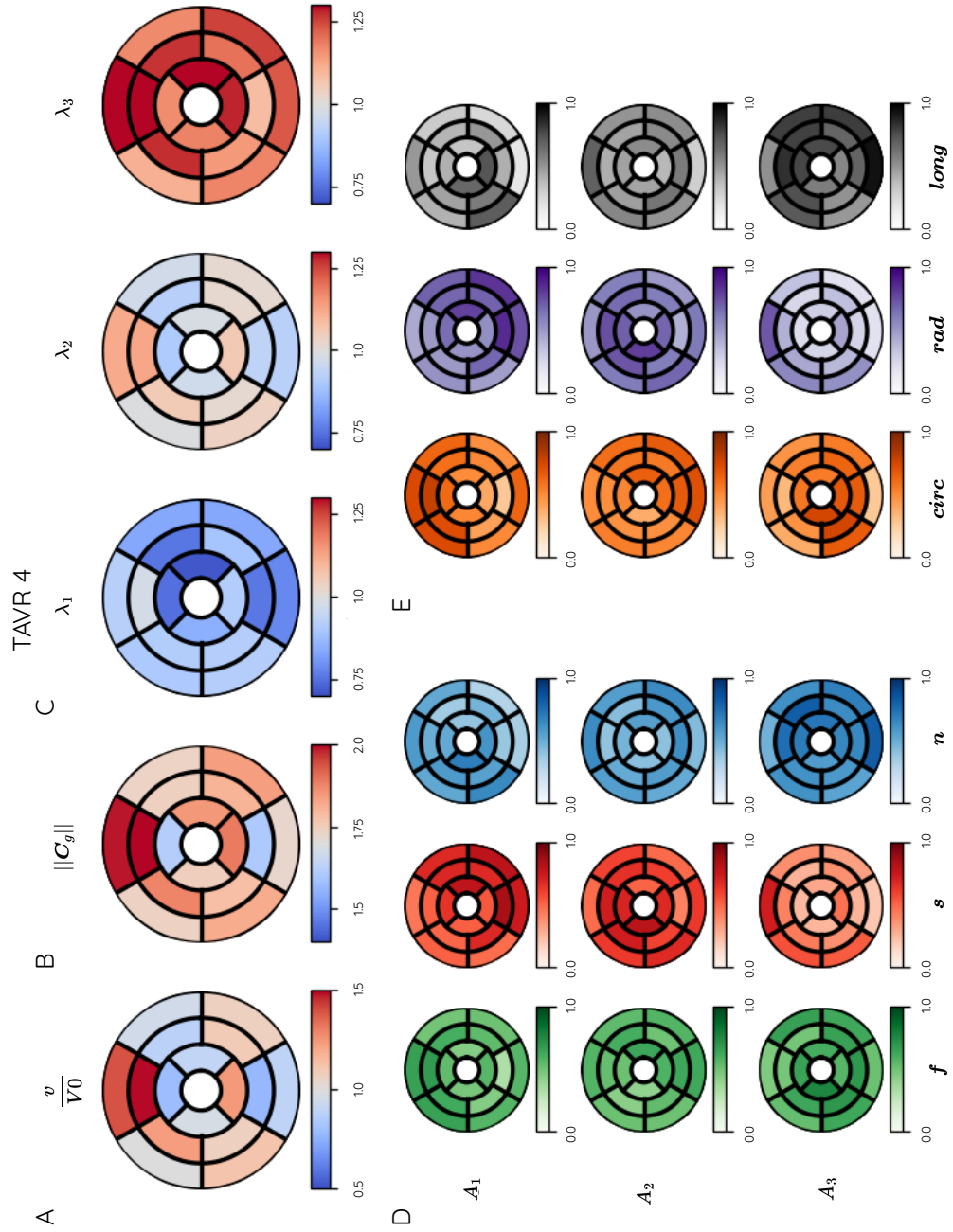

Figure 18 Reverse growth pattern analysis in TAVR 4. (A) displays the average volume ratio of the post-AVR state after reverse growth to the reference volume of the pre-AVR state across the LV. (B) illustrates the calculated mean Frobenius norm of the right Cauchy-Green growth strain tensor $\mathbf{C}_g$ within the 17 AHA segments. (C) presents the mean eigenvalues of $\mathbf{C}_g$ in ascending order within the AHA regions of the LV. Previous colour codes refer to either high (red) or low (blue) values. (D) shows the associated eigenvectors to the eigenvalues presented in (C), where a directional agreement with the fibres, sheet, or sheet-normal direction is indicated by green, red or blue, respectively. (E) shows the associated eigenvectors to the eigenvalues presented in (C), where a directional agreement with the circumferential, radial, or longitudinal direction is indicated by grey, purple or orange, respectively.

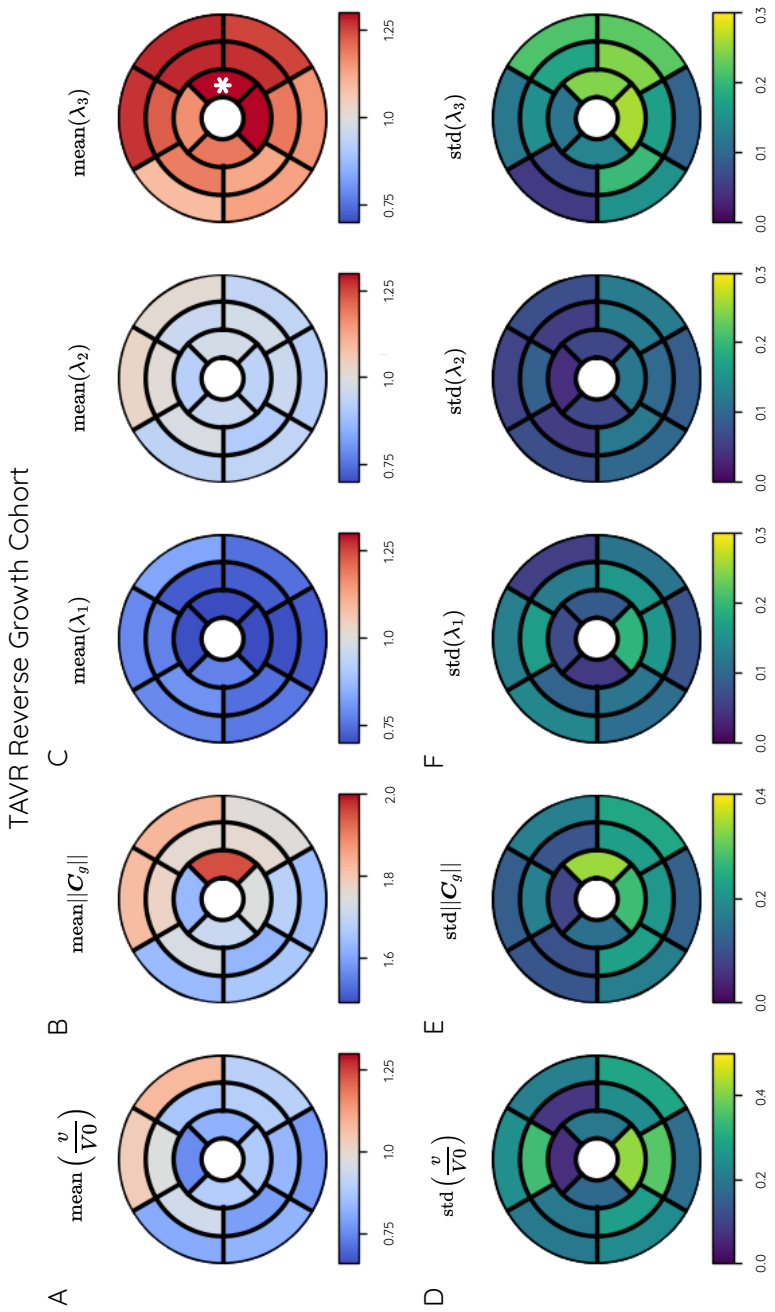

Figure 19 Reverse growth pattern analysis in TAVR patient cohort. (A) displays the mean volume ratio of the post-AVR state after reverse growth to the reference volume of the pre-AVR state across the LV. (B) illustrates the calculated mean Frobenius norm of the right Cauchy-Green growth strain tensor $\mathbf{C}_g$ within the 17 AHA segments. (C) presents the mean eigenvalues of $\mathbf{C}_g$ in ascending order within the AHA regions of the LV. Previous colour codes refer to either high (red) or low (blue) values. (E) displays the standard deviation of the volume ratio of the post-AVR state after adverse growth to the reference volume of the pre-AVR state across the LV. (F) illustrates the calculated standard deviation of the Frobenius norm of the right Cauchy-Green growth strain tensor $\mathbf{C}_g$ within the 17 AHA segments. (G) presents the standard deviation of the eigenvalues of $\mathbf{C}_g$ in ascending order within the AHA regions of the LV. Previous colour codes refer to either high (yellow) or low (dark blue) values. An asterisk in the AHA segment indicates a value higher than the upper bound of the data range.

Bibliography

[1] Abdulla, R. I., Blew, G. A., and Holterman, M. J. (2004). Cardiovascular embryology. *Pediatric cardiology*, 25:191–200.

[2] Akhtar, M. and Elliott, P. (2018). The genetics of hypertrophic cardiomyopathy. *Global cardiology science & practice*, 2018(3).

[3] Albatat, M., Finsberg, H., Arevalo, H., Sundnes, J., Bergsland, J., Balasingham, I., and Odland, H. (2022). Regional left ventricular fiber stress analysis for cardiac resynchronization therapy response. *Annals of Biomedical Engineering*, 51:1–9.

[4] Alharbi, Y., Otton, J., Muller, D., Geelan-Small, P., Lovell, N., Al Abed, A., and Dokos, S. (2020). Predicting the outcome of transcatheter mitral valve implantation using image-based computational models. *Journal of Cardiovascular Computed Tomography*, 14(4):335–342.

[5] Altenbach, H. (2018). *Kontinuumsmechanik: Einführung in die materialunabhängigen und material-abhängigen Gleichungen*. Springer Berlin Heidelberg.

[6] Amano, Y., Kitamura, M., Takano, H., Yanagisawa, F., Tachi, M., Suzuki, Y., Kumita, S., and Takayama, M. (2018). Cardiac mr imaging of hypertrophic cardiomyopathy: techniques, findings, and clinical relevance. *Magnetic Resonance in Medical Sciences*, 17:120–131.

[7] Amberg, B., Romdhani, S., and Vetter, T. (2007). Optimal step nonrigid icp algorithms for surface registration. *Proc. CVPR IEEE*, 2007 IEEE:1–8.

[8] Ambrosi, D., Ateshian, G. A., Arruda, E. M., Cowin, S. C., Dumais, J., Goriely, A., Holzapfel, G. A., Humphrey, J. D., Kemkemer, R., Kuhl, E., and Olberding, J. E. (2011). Perspectives on biological growth and remodeling. *Journal of the Mechanics and Physics of Solids*, 59:863–883.

[9] Anand, V., Adigun, R., Thaden, J., Pislaru, S., Pellikka, P., Nkomo, V., Greason, K., and Pislaru, C. (2020). Predictive value of left ventricular diastolic chamber stiffness in patients with severe aortic stenosis undergoing aortic valve replacement. *European Heart Journal-Cardiovascular Imaging*, 21(10):1160–1168.

[10] Andreasen, C., Gislason, G., Køber, L., Abdulla, J., Martinsson, A., Smith, J., Torp-Pedersen, C., and Andersson, C. (2020). Incidence of ischemic stroke in individuals with and without aortic valve stenosis: a danish retrospective cohort study. *Stroke*, 51(5):1364–1371.

[11] Aronow, W. (2017). Hypertension and left ventricular hypertrophy. *Annals of translational medicine*, 5(15).

[12] Arts, T., Bovendeerd, P., Prinzen, F., and Reneman, R. (1991). Relation between left ventricular cavity pressure and volume and systolic fiber stress and strain in the wall. *Biophysical journal*, 59(1):93–102.

[13] Arts, T., Delhaas, T., Bovendeerd, P., Verbeek, X., and Prinzen, F. (2005). Adaptation to mechanical load determines shape and properties of heart and circulation: the circadapt model. *American Journal of Physiology-Heart and Circulatory Physiology*, 288(4):H1943–H1954.

[14] Arts, T., Prinzen, F., Snoeckx, L., Rijcken, J., and Reneman, R. (1994). Adaptation of cardiac structure by mechanical feedback in the environment of the cell: a model study. *Biophysical Journal*, 66(4):953–961.

[15] Arts, T., Reneman, R., and Veenstra, P. (1979). A model of the mechanics of the left ventricle. *Annals of biomedical engineering*, 7:299–318.

[16] Arumugam, J., Mojumder, J., Kassab, G., and Lee, L. (2019). Model of anisotropic reverse cardiac growth in mechanical dyssynchrony. *Scientific reports*, 9:1–12.

[17] Asner, L., Hadjicharalambous, M., Chabiniok, R., Peressutti, D., Sammut, E., Wong, J., Carr-White, G., Razavi, R., King, A., Smith, N., Lee, J., and Nordsletten, D. (2017). Patient-specific modeling for left ventricular mechanics using data-driven boundary energies. *Comput. Method. Appl. M.*, 314:269–295.

[18] Asner, L., Hadjicharalambous, M., Chabiniok, R., Peresutti, D., Sammut, E., Wong, J., Carr-White, G., Chowienczyk, P., Lee, J., King, A., Smith, N., Razavi, R., and Nordsletten, D. (2016). Estimation of passive and active properties in the human heart using 3d tagged mri. *Biomech. Model. Mechan.*, 15(5):1121–1139.

[19] Avazmohammadi, R., Li, D., Leahy, T., Shih, E., Soares, J., Gorman, J., Gorman, R., and Sacks, M. (2018). An integrated inverse model-experimental approach to determine soft tissue three-dimensional constitutive parameters: application to post-infarcted myocardium. *Biomechanics and modeling in mechanobiology*, 17:31–53.

[20] Avazmohammadi, R., Soares, J. S., Li, D. S., Eperjesi, T., Pilla, J., Gorman, R. C., and Sacks, M. S. (2020). On the in vivo systolic compressibility of left ventricular free wall myocardium in the normal and infarcted heart. *J. Biomech*, 107(109767).

[21] Avril, S., Evans, S., and Miller, K. (2013). Inverse problems and material identification in tissue biomechanics. *Journal of the mechanical behavior of biomedical materials*, 27:129–131.

[22] Azevedo, P. S., Polegato, B. F., Minicucci, M. F., Paiva, S. A. R., and Zornoff, L. A. M. (2016). Cardiac remodeling: Concepts, clinical impact, pathophysiological mechanisms and pharmacologic treatment. *Arq. Bras. Cardiol.*, 106(1):62–69.

[23] Barreto-Chaves, M., Senger, N., Fevereiro, M., Parletta, A., and Takano, A. (2020). Impact of hyperthyroidism on cardiac hypertrophy. *Endocrine Connections*, 9(3):R59.

[24] Bauer, F., Lemercier, M., Zajarias, A., Tron, C., Eltchaninoff, H., and Cribier, A. (2010). Immediate and long-term echocardiographic findings after transcatheter aortic valve implantation for the treatment of aortic stenosis: the cribier-edwards/edwards-sapien valve experience. *J. Am. Soc. Echocardiog.*, 23(4):370–376.

[25] Bayer, J., Prassl, A., Pashaei, A., Gomez, J., Frontera, A., Neic, A., Plank, G., and Vigmond, E. (2018). Universal ventricular coordinates: A generic framework for describing position within the heart and transferring data. *Medical image analysis*, 45:83–93.

[26] Bayer, J. D., Blake, R. C., Plank, G., and Trayanova, N. A. (2012). A novel rule-based algorithm for assigning myocardial fiber orientation to computational heart models. *Ann. Biomed. Eng.*, 40(10):2243–2254.

[27] Beach, J., Mihaljevic, T., Rajeswaran, J., Marwick, T., Edwards, S., Nowicki, E., Thomas, J., Svensson, L., Griffin, B., Gillinov, A., and Blackstone, E. (2014). Ventricular hypertrophy and left atrial dilatation persist and are associated with reduced survival after valve replacement for aortic stenosis. *The Journal of thoracic and cardiovascular surgery*, 147(1):362–369.

[28] Bergström, J. (2015). *Mechanics of Solid Polymers*, chapter 4 - Continuum Mechanics Foundations, pages 131–207. William Andrew Publishing.

[29] Bernardo, B. C., Weeks, K. L., Pretorius, L., and McMullen, J. R. (2010). Molecular distinction between physiological and pathological cardiac hypertrophy: experimental findings and therapeutic strategies. *Pharmacology & therapeutics*, 128:191–227.

[30] Bols, J., Degroote, J., Trachet, B., Verhegghe, B., Segers, P., and Vierendeels, J. (2013). A computational method to assess the in vivo stresses and unloaded configuration of patient-specific blood vessels. *Journal of Computational and Applied Mathematics*, 246(8):10–17.

[31] Bonet, J. and Wood, R. D. (1997). *Nonlinear continuum mechanics for finite element analysis*. Cambridge university press, Cambridge.

[32] Bornstein, A., Rao, S., and Marwaha, K. (2021). Left ventricular hypertrophy. *StatPearls*, Internet.

[33] Bovendeerd, P. (2012). Modeling of cardiac growth and remodeling of myofiber orientation. *Journal of biomechanics*, 45(5):872–881.

[34] Bracamonte, J. H., Saunders, S. K., Wilson, J. S., Truong, U. T., and Soares, J. S. (2022). Patient-specific inverse modeling of in vivo cardiovascular mechanics with medical image-derived kinematics as input data: Concepts, methods, and applications. *Applied Sciences*, 12(8):3954.

[35] Braeu, F., Seitz, A., Aydin, R., and Cyron, C. (2017). Homogenized constrained mixture models for anisotropic volumetric growth and remodeling. *Biomechanics and modeling in mechanobiology*, 16:889–906.

[36] British Heart Foundation (2022). Global heart & circulatory diseases factsheet. `https://www.bhf.org.uk/-/media/files/research/heart-statistics/bhf-cvd-statistics-global-factsheet.pdf`. 2023–01–09.

[37] Carver, E. and Carver, B. (2012). *Medical Imaging - Techniques, Reflection and Evaluation*, chapter Ultrasound. Elsevier Health Sciences, 2 edition.

[38] Centers for Disease Control and Prevention, National Center for Health Statistics (2019). Multiple cause of death files, 1999-2017. `https://www.cdc.gov/heartdisease/valvular_disease.htm`.

[39] Cerqueira, M., Weissman, N., Dilsizian, V., Jacobs, A., Kaul, S., Laskey, W., Pennell, D., Rumberger, J., Ryan, T., and Verani, M. (2002). Standardized myocardial segmentation and nomenclature for tomographic imaging of the heart: a statement for healthcare professionals from the cardiac imaging committee of the council on clinical cardiology of the american heart association. *Circulation*, 105(4):539–542.

[40] Chagnon, G., Ohayon, J., Martiel, J. L., and Favier, D. (2017). Hyperelasticity modeling for incompressible passive biological tissues. In Payan, Y. and Ohayon, J., editors, *Biomechanics of living organs*, pages 3–30. Academic Press, New York.

[41] Cohn, J. N., Ferrari, R., and Sharpe, N. (2000). Cardiac remodeling-concepts and clinical implications: A consensus paper from an international forum on cardiac remodeling. *Journal of the American College of Cardiology*, 35:569–582.

[42] Conte, L., Fabiani, I., Pugliese, N., Giannini, C., La Carruba, S., Angelillis, M., Spontoni, P., De Carlo, M., Petronio, A., and Di Bello, V. (2017). Left ventricular stiffness predicts outcome in patients with severe aortic stenosis undergoing transcatheter aortic valve implantation. *Echocardiography*, 34(1):6–13.

[43] Costabal, F., Choy, J., Sack, K., Guccione, J., Kassab, G., and Kuhl, E. (2019). Multiscale characterization of heart failure. *Acta biomaterialia*, 86:66–76.

[44] Cowin, S. (2010). Continuum kinematical modeling of mass increasing biological growth. *International journal of engineering science*, 48(11):1137–1145.

[45] Cutugno, S., Ingrassia, T., Nigrelli, V., and Pasta, S. (2021). On the left ventricular remodeling of patients with stenotic aortic valve: A statistical shape analysis. *Bioengineering*, 8(5):66.

[46] Cyron, C. J., Aydin, R. C., and Humphrey, J. D. (2016). A homogenized constrained mixture (and mechanical analog) model for growth and remodeling of soft tissue. *Biomech. Model. Mechan.*, 15(6):1389–1403.

[47] Dahl, J., Eleid, M., Michelena, H., Scott, C., Suri, R., Schaff, H., and Pellikka, P. (2015). Effect of left ventricular ejection fraction on postoperative outcome in patients with severe aortic stenosis undergoing aortic valve replacement. *Circulation: Cardiovascular Imaging*, 8(4):e002917.

[48] Dandel, M., Potapov, E., Krabatsch, T., Stepanenko, A., Löw, A., Vierecke, J., Knosalla, C., and Hetzer, R. (2013). Load dependency of right ventricular performance is a major factor to be considered in decision making before ventricular assist device implantation. *Circulation*, 128(11_suppl_1):S14–S23.

[49] Davies, M. and Mckenna, W. (1995). Hypertrophic cardiomyopathy ? pathology and pathogenesis. *Histopathology*, 26(6):493–500.

[50] Del Bianco, F., Piero, C. F., Scacchi, S., and Fassina, L. (2018). Electromechanical effects of concentric hypertrophy on the left ventricle: a simulation study. *Computers in biology and medicine*, 99:236–256.

[51] DeVore, G. R., Klas, B., Satou, G., and Sklansky, M. (2018). 24-segment sphericity index: a new technique to evaluate fetal cardiac diastolic shape. *Ultrasound Obst. Gyn.*, 51(5):650–658.

[52] Di Donato, M., Dabic, P., Castelvecchio, S., Santambrogio, C., Brankovic, J., Collarini, L., Joussef, T., Frigiola, A., Buckberg, G., Menicanti, L., and Group, R. (2006). Left ventricular geometry in normal and post-anterior myocardial infarction patients: sphericity index and 'new'conicity index comparisons. *Eur. J. Cardio–Thorac.*, 29(Supplement_1):S225–S230.

[53] Doggrell, S. and Brown, L. (1998). Rat models of hypertension, cardiac hypertrophy and failure. *Cardiovascular research*, 39(1):89–105.

[54] Dokos, S., Smaill, B., Young, A., and LeGrice, I. (2002). Shear properties of passive ventricular myocardium. *American Journal of Physiology-Heart and Circulatory Physiology*, 283(6):H2650–H2659.

[55] Doste, R., Soto-Iglesias, D., Bernardino, G., Alcaine, A., Sebastian, R., Giffard-Roisin, S., Sermesant, M., Berruezo, A., Sanchez-Quintana, D., and Camara, O. (2019). A rule-based method to model myocardial fiber orientation in cardiac biventricular geometries with outflow tracts. *Int. J. Numer. Meth. Bio.*, 35(4):e3185.

[56] Efremidis, M., Sideris, A., Xydonas, S., Letsas, K. P., Alexanian, I. P., Manolatos, D., Mihas, C. C., Filippatos, G. S., and Kardaras, F. (2008). Ablation of atrial fibrillation in patients with heart failure: reversal of atrial and ventricular remodelling. *Hellenic J Cardiol*, 49:19–25.

[57] Ellison, G. M., Waring, C. D., Vicinanza, C., and Torella, D. (2012). Physiological cardiac remodelling in response to endurance exercise training: cellular and molecular mechanisms. *Heart*, 98:5–10.

[58] Estrada, A., Yoshida, K., Saucerman, J., and Holmes, J. (2021). A multiscale model of cardiac concentric hypertrophy incorporating both mechanical and hormonal drivers of growth. *Biomechanics and Modeling in Mechanobiology*, 20(1):293–307.

[59] Fagard, R. H. (1997). Impact of different sports and training on cardiac structure and function. *Cardiol. Clin.*, 15:397–412.

[60] Fairbairn, T., Steadman, C., Mather, A., Motwani, M., Blackman, D., Plein, S., McCann, G., and Greenwood, J. (2013). Assessment of valve haemodynamics, reverse ventricular remodelling and myocardial fibrosis following transcatheter aortic valve implantation compared to surgical aortic valve replacement: a cardiovascular magnetic resonance study. *Heart*, 99(16):1185–1191.

[61] Fan, Y., Coll-Font, J., van den Boomen, M., Kim, J. H., Chen, S., Eder, R. A., Roche, E. T., and Nguyen, C. T. (2021). Characterization of exercise-induced myocardium growth using finite element modeling and bayesian optimization. *Frontiers in Physiology*, 12.

[62] Fang, L., Ellims, A., Beale, A., Taylor, A., Murphy, A., and Dart, A. (2017). Relationships between systemic inflammation and myocardial fibrosis, diastolic dysfunction, and cardiac hypertrophy in patients with hypertrophic cardiomyopathy. *Heart, Lung and Circulation*, 26(11):S110.

[63] Fedorov, A., Beichel, R., Kalpathy-Cramer, J., Finet, J., Fillion-Robin, J.-C., Pujol, S., Bauer, C., Jennings, D., Fennessy, F., Sonka, M., Buatti, J., Aylward, S., Miller, J., Pieper, S., and Kikinis, R. (2012). 3d slicer as an image computing platform for the quantitative imaging network. *Magnetic Resonance Imaging*, 30(9):1323–1341.

[64] Fernandes, T., Baraúna, V. G., Negrão, C. E., Phillips, M. I., and Oliveira, E. M. (2015). Aerobic exercise training promotes physiological cardiac remodeling involving a set of microrna. *American Journal of Physiology-Heart and Circulatory Physiology*, 309:H543–H552.

[65] Ferreira, P., Kilner, P., McGill, L., Nielles-Vallespin, S., Scott, A., Ho, S., McCarthy, K., Haba, M., Ismail, T., Gatehouse, P., de Silva, R., Lyon, A., Parsad, S., Firmin, D., and Penell, D. (2014). In vivo cardiovascular magnetic resonance diffusion tensor imaging shows evidence of abnormal myocardial laminar orientations and mobility in hypertrophic cardiomyopathy. *Journal of Cardiovascular Magnetic Resonance*, 16(1):1–16.

[66] Finsberg, H., Balaban, G., Ross, S., Håland, T., Odland, H., Sundnes, J., and Wall, S. (2018). Estimating cardiac contraction through high resolution data assimilation of a personalized mechanical model. *Journal of computational science*, 24:85–90.

[67] Franco, F., Dubois, S. K., Peshock, R. M., and Shohet, R. V. (1998). Magnetic resonance imaging accurately estimates lv mass in a transgenic mouse model of cardiac hypertrophy. *American Journal of Physiology-Heart and Circulatory Physiology*, 274:H679–H683.

[68] Francula-Zaninovic, S. and Nola, I. (2018). Management of measurable variable cardiovascular disease'risk factors. *Current cardiology reviews*, 14(3):153–163.

[69] Frankel Cardiovascular Center University of Michigan Health (2023). Surgical aortic valve replacement savr. `https://www.umcvc.org/conditions-treatments/surgical-aortic-valve-replacement-savr`. 2023–01–30.

[70] Frey, N., Katus, H. A., Olson, E. N., and Hill, J. A. (2004). Hypertrophy of the heart: a new therapeutic target? *Circulation*, 109:1580–1589.

[71] Fuster, V., Harrington, R. A., Narula, J., and Eapen, Z. J. (2017). Section 2: Foundations of cardiovascular medicine. In Fuster, V., Harrington, R. A., Narula, J., and Eapen, Z. J., editors, *Hurst's the Heart 14th Edition: Two Volume Set*, pages 65–222. McGraw-Hill Education, United States.

[72] Gandjian, M., Verma, A., Tran, Z., Sanaiha, Y., Downey, P., Shemin, R., and Benharash, P. (2022). Influence of center surgical aortic valve volume on outcomes of transcatheter aortic valve replacement. *JTCVS open*, 11:62–71.

[73] Gao, H., Li, W., Cai, L., Berry, C., and Luo, X. (2015). Parameter estimation in a holzapfel–ogden law for healthy myocardium. *Journal of engineering mathematics*, 95:231–248.

[74] Garfinkel, A., Seidman, J., and Seidman, C. (2018). Genetic pathogenesis of hypertrophic and dilated cardiomyopathy. *Heart failure clinics*, 14(2):139–146.

[75] Garg, S., de Lemos, J., Matulevicius, S., Ayers, C., Pandey, A., Neeland, I., Berry, J., McColl, R., Maroules, C. amd Peshock, R., and Drazner, M. (2017). Association of concentric left ventricular hypertrophy with subsequent change in left ventricular end-diastolic volume: the dallas heart study. *Circulation: Heart Failure*, 10(8):e003959.

[76] Garikipati, K., Arruda, E., Grosh, K., Narayanan, H., and Calve, S. (2004). A continuum treatment of growth in biological tissue: the coupling of mass transport and mechanics. *Journal of the Mechanics and Physics of Solids*, 52(7):1595–1625.

[77] Gazzola, M., Dudte, L., McCormick, A., and Mahadevan, L. (2018). Forward and inverse problems in the mechanics of soft filaments. *Royal Society open science*, 5(6):171628.

[78] Gee, M. W., Förster, C., and Wall, W. A. (2010). A computational strategy for prestressing patient-specific biomechanical problems under finite deformation. *International Journal for Numerical Methods in Biomedical Engineering*, 26(1):52–72.

[79] Gee, M. W., Reeps, C., Eckstein, H. H., and Wall, W. A. (2009). Prestressing in finite deformation abdominal aortic aneurysm simulation. *J Biomech*, 42(11):1732–1739.

[80] Genet, M., Lee, L. C., Baillargeon, B., Guccione, J. M., and Kuhl, E. (2016). Modeling pathologies of diastolic and systolic heart failure. *Annals of biomedical engineering*, 44:112–127.

[81] Genet, M., Rausch, M., Lee, L. C., Choy, S., Zhao, X., Kassab, G. S., Kozerke, S., Guccione, J. M., and E., K. (2015). Heterogeneous growth-induced prestrain in the heart. *J. Biomech.*, 48(10):2080–2089.

[82] Gerdes, A. and Capasso, J. (1995). Structural remodeling and mechanical dysfunction of cardiac myocytes in heart failure. *Journal of molecular and cellular cardiology*, 27(3):849–856.

[83] Geske, J., Ommen, S., and Gersh, B. (2018). Hypertrophic cardiomyopathy: clinical update. *JACC: heart failure*, 6(5):364–375.

[84] Gheorghe, A. G., Fuchs, A., Jacobsen, C., Kofoed, K. F., Møgelvang, R., Lynnerup, N., and Banner, J. (2019). Cardiac left ventricular myocardial tissue density, evaluated by computed tomography and autopsy. *BMC Med. Imaging*, 19(1):1–9.

[85] Gittenberger-de Groot, A. C., Bartelings, M. M., Poelmann, R. E., Haak, M. C., and Jongbloed, M. R. (2013). Embryology of the heart and its impact on understanding fetal and neonatal heart disease. *In Seminars in Fetal and Neonatal Medicine*, 18:237–244.

[86] Gomez, A., Zou, H., Bowen, M., Liu, X., Hsu, E., and McKellar, S. (2017). Right ventricular fiber structure as a compensatory mechanism in pressure overload: a computational study. *Journal of Biomechanical Engineering*, 139(8):081004.

[87] Goodbrake, C., Goriely, A., and Yavari, A. (2021). The mathematical foundations of anelasticity: Existence of smooth global intermediate configurations. *Proceedings of the Royal Society A*, 477:20200462.

[88] Goriely, A. (2017). *The mathematics and mechanics of biological growth*, volume 45. Springer.

[89] Gotschy, A., von Deuster, C., Weber, L., Gastl, M., Schmiady, M., van Gorkum, R., Stimm, J., von Spiczak, J., Manka, R., Kozerke, S., and Stoeck, C. (2021). Cmr diffusion tensor imaging provides novel imaging markers of adverse myocardial remodeling in aortic stenosis. *Cardiovascular Imaging*, 14(7):1472–1474.

[90] Govindjee, S. and Mihalic, P. A. (1996). Computational methods for inverse finite elastostatics. *Computer Methods in Applied Mechanics and Engineering*, 136(1–2):47–57.

[91] Gradman, A. H. and Alfayoumi, F. (2006). From left ventricular hypertrophy to congestive heart failure: Management of hypertensive heart disease. *Progress in Cardiovascular Diseases*, 48:326–341.

[92] Green, E., Wakimoto, H., Anderson, R., Evanchik, M., Gorham, J., Harrison, B., Henze, M., Kawas, R., Oslob, J., Rodriguez, H., and Song, Y. (2016). A small-molecule inhibitor of sarcomere contractility suppresses hypertrophic cardiomyopathy in mice. *Science*, 351(6273):617–621.

[93] Gregor, P. and Čurila, K. (2015). Medical treatment of hypertrophic cardiomyopathy–what do we know about it today? *Cor et Vasa*, 57(3):e219–e224.

[94] Grossman, W. (1980). Cardiac hypertrophy: useful adaptation or pathologic process? *The American journal of medicine*, 69:576–584.

[95] Grossman, W., Jones, D., and McLaurin, L. (1975). Wall stress and patterns of hypertrophy in the human left ventricle. *The Journal of clinical investigation*, 56(1):56–64.

[96] Guccione, J., Moonly, S., Wallace, A., and Ratcliffe, M. (2001). Residual stress produced by ventricular volume reduction surgery has little effect on ventricular function and mechanics: a finite element model study. *The Journal of thoracic and cardiovascular surgery*, 122(3):592–599.

[97] Göktepe, S., Abilez, O. J., and Kuhl, E. (2010a). A generic approach towards finite growth with examples of athlete's heart, cardiac dilation, and cardiac wall thickening. *J. MECH PHYS SOLIDS*, 58(10):1661–1680.

[98] Göktepe, S., Abilez, O. J., Parker, K. K., and Kuhl, E. (2010b). A multiscale model for eccentric and concentric cardiac growth through sarcomerogenesis. *J. Theor. Biol.*, 265(3):433–442.

[99] Hadjicharalambous, M., Asner, L., Chabiniok, R., Sammut, E., Wong, J., Peressutti, D., Kerfoot, E., King, A., Lee, J., Razavi, R., Smith, N., Carr-White, G., and Nordsletten, D. (2017). Non-invasive model-based assessment of passive left-ventricular myocardial stiffness in healthy subjects and in patients with non-ischemic dilated cardiomyopathy. *Ann. Biomed. Eng.*, 45(3):605–618.

[100] Hadjicharalambous, M., Chabiniok, R., Asner, L., Sammut, E., Wong, J., Carr-White, G., Lee, J., Razavi, R., Smith, N., and Nordsletten, D. (2015). Analysis of passive cardiac constitutive laws for parameter estimation using 3d tagged mri. *Biomechanics and modeling in mechanobiology*, 14:807–828.

[101] Hager, S., Zhang, W., Miller, R., Lee, J., and Nordsletten, D. (2021). An exploratory assessment of focused septal growth in hypertrophic cardiomyopathy. *In Functional Imaging and Modeling of the Heart: 11th International Conference*, 11:328–339.

[102] Hajar, R. (2017). Risk factors for coronary artery disease: historical perspectives. *Heart views: the official journal of the Gulf Heart Association*, 18(3):109.

[103] Harris, C., Croce, B., and Phan, K. (2015). Aortic stenosis. *Annals of cardiothoracic surgery*, 4(1):99.

[104] Heineke, J. and Molkentin, J. (2006). Regulation of cardiac hypertrophy by intracellular signalling pathways. nature reviews molecular cell biology. *Frontiers in Physiology*, 7(8):589–600.

[105] Hieda, M., Sarma, S., Hearon Jr, C., Dias, K., Martinez, J., Samels, M., Everding, B., Palmer, D., Livingston, S., Morris, M., and Howden, E. (2020). Increased myocardial stiffness in patients with high-risk left ventricular hypertrophy: the hallmark of stage-b heart failure with preserved ejection fraction. *Circulation*, 141(2):115–123.

[106] Hill, J. A. (2003). Electrical remodeling in cardiac hypertrophy. *Trends in cardiovascular medicine*, 13:316–322.

[107] Holzapfel, G. and Ogden, R. (2003). *Biomechanics of soft tissue in cardiovascular systems*, volume 441. Springer Science & Business Media.

[108] Holzapfel, G. A. (2000). *Nonlinear Solid Mechanics: A Continuum Approach for Engineering*. John Wiley & Son, Chichester.

[109] Holzapfel, G. A., Gasser, T. C., and Ogden, R. W. (2000). A new constitutive framework for arterial wall mechanics and a comparative study of material models. *Journal of elasticity and the physical science of solids*, 61:1–48.

[110] Holzapfel, G. A. and Ogden, R. W. (2009). Constitutive modelling of passive myocardium: a structurally based framework for material characterization. *Philos. T. R. Soc. A*, 367(1902):3445–3475.

[111] Hor, K. and Trask, A. (2018). *Encyclopedia of Cardiovascular Research and Medicine*, chapter Cardiac Anatomy, Physiology, and Pathophysiology. Elsevier: Oxford.

[112] Huang, X., Deng, L., Yang, C., Lesperance, M., and Tang, D. (2019). Comparisons of patient-specific active and passive models for left ventricle in hypertrophic obstructive cardiomyopathy. *Molecular & Cellular Biomechanics*, 16:58.

[113] Huded, C., Arnold, S., Chhatriwalla, A., Saxon, J., Kapadia, S., Yu, X., Webb, J., Thourani, V., Kodall, S., Smith, C., Mack, M., Leon, M., and Cohen, D. J. (2022). Rehospitalization events after aortic valve replacement: Insights from the partner trial. *Circulation: Cardiovascular Interventions*, 15(12):e012195.

[114] Humphrey, J. D. and Rajagopal, K. (2002). A constrained mixture model for growth and remodeling of soft tissues. *Math. Mod. Meth. Appl. S.*, 12(03):407–430.

[115] Hunter, J. J. and Chien, K. R. (1999). Signaling pathways for cardiac hypertrophy and failure. *New England Journal of Medicine*, 341:1276–1283.

[116] Kalabunde, R. E. (2012). *Cardiovascular Physiology Concepts*, chapter Cardiovascular Integration, Adaptation, AND Pathophysiology. Lippincott Williams & Wilkins, 2 edition.

[117] Kalisz, K. and Rajiah, P. (2017). Computed tomography of cardiomyopathies. *Cardiovascular diagnosis and therapy*, 7:539–556.

[118] Katz, A. (2010). *Physiology of the Heart*. Lippincott Williams & Wilkins.

[119] Kay, F. U., Abbara, S., Joshi, P. H., Garg, S., Khera, A., and Peshock, R. M. (2020). Identification of high-risk left ventricular hypertrophy on calcium scoring cardiac computed tomography scans: validation in the dhs. *Circulation: Cardiovascular Imaging*, 13:e009678.

[120] Kerckhoffs, R., Omens, J., and McCulloch, A. (2012a). Mechanical discoordination increases continuously after the onset of left bundle branch block despite constant electrical dyssynchrony in a computational model of cardiac electromechanics and growth. *Europace*, 14(suppl_5):v65–v72.

[121] Kerckhoffs, R. C., Omens, J. H., and McCulloch, A. D. (2012b). A single strain-based growth law predicts concentric and eccentric cardiac growth during pressure and volume overload. *Mech. Res. Commun.*, 42:40–50.

[122] Khalique, Z., Ferreira, P., Scott, A., Nielles-Vallespin, S., Firmin, D., and Pennell, D. (2020). Diffusion tensor cardiovascular magnetic resonance imaging: a clinical perspective. *Cardiovascular Imaging*, 13(5):1235–1255.

[123] Kitai, T., Xanthopoulos, A., Nakagawa, S., Ishii, N., Amano, M., Triposkiadis, F., and Izumi, C. (2022). Contemporary diagnosis and management of hypertrophic cardiomyopathy: the role of echocardiography and multimodality imaging. *Journal of Cardiovascular Development and Disease*, 9(6):169.

[124] Klepach, D., Lee, L., Wenk, J., Ratcliffe, M., Zohdi, T., Navia, J., Kassab, G., Kuhl, E., and Guccione, J. (2012). Growth and remodeling of the left ventricle: a case study of myocardial infarction and surgical ventricular restoration. *Mechanics research communications*, 42:134–141.

[125] Klotz, S., Hay, I., Dickstein, M., Yi, G., Wang, J., Maurer, M., Kass, D., and Burkhoff, D. (2006). Single-beat estimation of end-diastolic pressure-volume relationship: a novel method with potential for noninvasive application. *Am. J. Physiol.-Heart C.*, 291(1):H403–H412.

[126] Klues, H., Schiffers, A., and Maron, B. (1995). Phenotypic spectrum and patterns of left ventricular hypertrophy in hypertrophic cardiomyopathy: Morphologic observations and significance as assessed by two-dimensional echocardiography in 600 patients. *Journal of the American College of Cardiology*, 26(7):1699–1708.

[127] Koga-Ikuta, A., Fukushima, S., Kawamoto, N., Saito, T., Shimahara, Y., and Yajima, S. (2021). Reverse remodelling after aortic valve replacement for chronic aortic regurgitation. *Interactive CardioVascular and Thoracic Surgery*.

[128] Krishnamurthy, A., Villongco, C., Chuang, J., Frank, L., Nigam, V., Belezzuoli, E., Stark, P., Krummen, D., Narayan, S., Omens, J., McCulloch, A., and Kerckhoffs, R. (2013). Patient-specific models of cardiac biomechanics. *Journal of computational physics*, 244:4–21.

[129] Kroon, W., Delhaas, T., Bovendeerd, P., and Arts, T. (2009). Computational analysis of the myocardial structure: adaptation of cardiac myofiber orientations through deformation. *Medical image analysis*, 13(2):346–353.

[130] Kuchta, M., Mardal, K. A., and Mortensen, M. (2019). On the singular neumann problem in linear elasticity. *Numerical Linear Algebra with Applications*, 26.

[131] Kuhl, E. (2014). Growing matter: a review of growth in living systems. *Journal of the Mechanical Behavior of Biomedical Materials*, 29:529–543.

[132] Kuhl, E., Garikipati, K., Arruda, E., and Grosh, K. (2005). Remodeling of biological tissue: mechanically induced reorientation of a transversely isotropic chain network. *Journal of the Mechanics and Physics of Solids*, 53(7):1552–1573.

[133] Kuhl, E. and Holzapfel, G. (2007). A continuum model for remodeling in living structures. *Journal of Materials Science*, 42:8811–8823.

[134] Lai, W., Rubin, D., and Krempl, E. (2010). *Introduction to Continuum Mechanics (Fourth Edition)*, chapter CHAPTER 5 - The Elastic Solid, pages 201–352. Butterworth-Heinemann.

[135] Lampert, B. C. (2018). *Encyclopedia of Cardiovascular Research and Medicine*, chapter Right Heart Catheterization. Elsevier: Oxford.

[136] Landmesser, U., Wollert, K. C., and Drexler, H. (2009). Potential novel pharmacological therapies for myocardial remodelling. *Cardiovascular research*, 81:519–527.

[137] Lanir, Y. (2015). Mechanistic micro-structural theory of soft tissues growth and remodeling: tissues with unidirectional fibers. *Biomechanics and modeling in mechanobiology*, 14:245–266.

[138] Lanir, Y. (2017). Fibrous tissues growth and remodeling: Evolutionary micro-mechanical theory. *Journal of the Mechanics and Physics of Solids*, 107:115–144.

[139] Lantz, J., Henriksson, L., Persson, A., Karlsson, M., and Ebbers, T. (2016). Patient-specific simulation of cardiac blood flow from high-resolution computed tomography. *Journal of biomechanical engineering*, 138(12):121004.

[140] Latorre, M. (2020). Modeling biological growth and remodeling: contrasting methods, contrasting needs. *Current Opinion in Biomedical Engineering*, 15:26–31.

[141] Lee, A., Costa, C., Strocchi, M., Rinaldi, C., and Niederer, S. (2018). Computational modeling for cardiac resynchronization therapy. *Journal of cardiovascular translational research*, 11:92–108.

[142] Lee, E. H. (1969). Elastic-plastic deformation at finite strains. *J. Appl. Mech-T ASME*, 36(1):1–6.

[143] Lee, J., Cookson, A., Roy, I., Kerfoot, E., Asner, L., Vigueras, G., Sochi, T., Deparis, S., Michler, C., Smith, N. P., and Nordsletten, D. A. (2016a). Multiphysics computational modeling in cheart. *SIAM Journal on Scientific Computing*, 38:C150–C178.

[144] Lee, L., Kassab, G., and Guccione, J. (2016b). Mathematical modeling of cardiac growth and remodeling. *Wiley Interdisciplinary Reviews: Systems Biology and Medicine*, 8(3):211–226.

[145] Lee, L. C., Genet, M., Acevedo-Bolton, G., Ordovas, K., Guccione, J. M., and Kuhl, E. (2015a). A computational model that predicts reverse growth in response to mechanical unloading. *Biomech. Model. Mechan.*, 14(2):217–229.

[146] Lee, L. C., Sundnes, J., Genet, M., Wenk, J. F., and T., W. S. (2015b). An integrated electromechanical-reversible growth heart model for simulating cardiac therapies. *Biomechanics and Modeling in Mechanobiology*, 15(4):791–803.

[147] Lee, S., Park, S., Kim, Y., Chang, S., Park, E., Kim, H., Lee, W., Lee, S., Park, S., Sohn, D., and Choe, Y. (2013). Early detection of subclinical ventricular deterioration in aortic stenosis with cardiovascular magnetic resonance and echocardiography. *Journal of Cardiovascular Magnetic Resonance*, 15(1):1–10.

[148] LeGrice, I. J., Smaill, B. H., Chai, L. Z., Edgar, S. G., Gavin, J. B., and Hunter, P. J. (1995). Laminar structure of the heart: ventricular myocyte arrangement and connective tissue architecture in the dog. *Am J Physiol-Heart C*, 269(2):H571–H582.

[149] Li, W., Gao, H., Mangion, K., Berry, C., and Luo, X. (2021). Apparent growth tensor of left ventricular post myocardial infarction–in human first natural history study. *Computers in Biology and Medicine*, 129:104168.

[150] Liew, A., Vassiliou, V., Cooper, R., and Raphael, C. (2017). Hypertrophic cardiomyopathy—past, present and future. *Journal of Clinical Medicine*, 6(12):118.

[151] Lindman, B., Clavel, M., Mathieu, P., Iung, B., Lancellotti, P., Otto, C., and Pibarot, P. (2016). Calcific aortic stenosis. *Nature reviews Disease primers*, 2(1):1–28.

[152] Losi, M. A., Nistri, S., Galderisi, M., Betocchi, S., Cecchi, F., Olivotto, I., Ballo, P., Buralli, S., D'Andrea, A., D'Errico, A., and Mele, D. (2010). Echocardiography in patients with hypertrophic cardiomyopathy: usefulness of old and new techniques in the diagnosis and pathophysiological assessment. *Cardiovascular Ultrasound*, 8:1–19.

[153] Lu, J., Zhou, X., and Raghavan, M. L. (2007). Inverse elastostatic stress analysis in pre-deformed biological structures: Demonstration using abdominal aortic aneurysms. *J Biomech*, 40(3):693–696.

[154] Lubarda, V. A. and Hoger, A. (2002). On the mechanics of solids with a growing mass. *International journal of solids and structures*, 39:4627–4664.

[155] Maillet, M., Van Berlo, J. H., and Molkentin, J. D. (2013). Molecular basis of physiological heart growth: fundamental concepts and new players. *Nature reviews Molecular cell biology*, 14:38–48.

[156] Maksuti, E., Westerhof, B., Ugander, M., Donker, D., Carlsson, M., and Broomé, M. (2019). Cardiac remodeling in aortic and mitral valve disease: a simulation study with clinical validation. *Journal of Applied Physiology*, 126(5):1377–1389.

[157] Marian, A. and Braunwald, E. (2017). Hypertrophic cardiomyopathy: genetics, pathogenesis, clinical manifestations, diagnosis, and therapy. *Circ. Res*, 121(7):749–770.

[158] Maron, B. (2002). Hypertrophic cardiomyopathy: a systematic review. *Jama*, 287(10):1308–1320.

[159] Maron, B. and Epstein, S. (1979). Hypertrophie cardiomyopathy: A discussion of nomenclature. *The American Journal of Cardiology*, 43(6):1242–1244.

[160] Maron, B. and Maron, M. (2013). Hypertrophic cardiomyopathy. *The Lancet*, 381(9862):242–255.

[161] Maron, B. and Roberts, W. (1979). Quantitative analysis of cardiac muscle cell disorganization in the ventricular septum of patients with hypertrophic cardiomyopathy. *Circulation*, 59(4):689–706.

[162] MATLAB (2020). *version 9.9.0.1524771 (R2020b)*. The MathWorks Inc., Natick, Massachusetts.

[163] Mauger, C., Gilbert, K., Suinesiaputra, A., Pontre, B., Omens, J., McCulloch, A., and Young, A. (2018). An iterative diffeomorphic algorithm for registration of subdivision surfaces: application to congenital heart disease. *Annual International Conference of the IEEE Engineering in Medicine and Biology Society (EMBC)*, pages 596–599.

[164] McGregor, J., Rahman, A., Rosanio, S., Ware, D., Birnbaum, Y., and Saeed, M. (2004). Monomorphic ventricular tachycardia: a late complication of percutaneous alcohol septal ablation for hypertrophic cardiomyopathy. *The American journal of the medical sciences*, 328(3):185–188.

[165] McMullen, J. R. and Jennings, G. L. (2007). Differences between pathological and physiological cardiac hypertrophy: novel therapeutic strategies to treat heart failure. *Clinical and experimental pharmacology & physiology*, 34:255–262.

[166] McNally, E., Golbus, J., and Puckelwartz, M. (2013). Genetic mutations and mechanisms in dilated cardiomyopathy. *The Journal of clinical investigation*, 123(1):19–26.

[167] Mehdipoor, G., Chen, S., Chatterjee, S., Torkian, P., Ben-Yehuda, O., Leon, M., Stone, G., and Prince, M. (2020). Cardiac structural changes after transcatheter aortic valve replacement: systematic review and meta-analysis of cardiovascular magnetic resonance studies. *Journal of Cardiovascular Magnetic Resonance*, 22:1–10.

[168] Menzel, A. (2007). A fibre reorientation model for orthotropic multiplicative growth: configurational driving stresses, kinematics-based reorientation, and algorithmic aspects. *Biomechanics and modeling in mechanobiology*, 6:303–320.

[169] Menzel, A. and Kuhl, E. (2012). Frontiers in growth and remodeling. *Mechanics research communications*, 42:1–14.

[170] Milićević, B., Milošević, M., Simić, V., Trifunović, D., Stanković, G., Filipović, N., and Kojić, M. (2023). Cardiac hypertrophy simulations using parametric and echocardiography-based left ventricle model with shell finite elements. *Computers in Biology and Medicine*, 157:106742.

[171] Miller, R., Kerfoot, E., Mauger, C., Ismail, T. F., Young, A., and Nordsletten, D. (2021a). An implementation of patient-specific biventricular mechanics simulations with a deep learning and computational pipeline. *Front. Physiol.*, page 1398.

[172] Miller, R., Marlevi, D., Zhang, W., Hirschvogel, M., Hadjicharalambous, M., Capilnasiu, A., Balmus, M., Hager, S., Jilberto, J., Bonini, M., and Wittgenstein, A. (2021b). *Modeling Biomaterials*, chapter Modeling Biomechanics in the Healthy and Diseased Heart, pages 141–239. Birkhäuser.

[173] Mojumder, J., Choy, J., Leng, S., Zhong, L., Kassab, G., and Lee, L. (2021). Mechanical stimuli for left ventricular growth during pressure overload. *Experimental mechanics*, 61:131–146.

[174] Mone, S. M., Sanders, S. P., and Colan, S. D. (1996). Control mechanisms for physiological hypertrophy of pregnancy. *Circulation*, 94:667–672.

[175] Morelli, C., Ingrasciotta, G., Jacoby, D., Masri, A., and Olivotto, I. (2022). Sarcomere protein modulation: The new frontier in cardiovascular medicine and beyond. *European Journal of Internal Medicine*, 102:1–7.

[176] Muraru, D., Badano, L., Peluso, D., Dal Bianco, L., Casablanca, S., Kocabay, G., Zoppellaro, G., and Iliceto, S. (2013). Comprehensive analysis of left ventricular geometry and function by three-dimensional echocardiography in healthy adults. *Journal of the American Society of Echocardiography*, 26(6):618–628.

[177] Müller, H., Noble, S., Keller, P. F., Sigaud, P., Gentil, P., Lerch, R., Shah, D., and Burri, H. (2008). Biatrial anatomical reverse remodelling after radiofrequency catheter ablation for atrial fibrillation: evidence from real-time three-dimensional echocardiograph. *Europace*, 10:1073–1078.

[178] Nagueh, S. F., Bachinski, L. L., Meyer, D., Hill, R., Zoghbi, W. A., Tam, J. W., Quiñones, M. A., Roberts, R., and Marian, A. J. (2001). Tissue doppler imaging consistently detects myocardial abnormalities

in patients with hypertrophic cardiomyopathy and provides a novel means for an early diagnosis before and independently of hypertrophy. *Circulation*, 104:128–130.

[179] Nakamori, S., Ismail, H., Ngo, L., Manning, W., and Nezafat, R. (2017). Left ventricular geometry predicts ventricular tachyarrhythmia in patients with left ventricular systolic dysfunction: a comprehensive cardiovascular magnetic resonance study. *Journal of Cardiovascular Magnetic Resonance*, 19(1):1–10.

[180] Nakamura, M. and Sadoshima, J. (2018). Mechanisms of physiological and pathological cardiac hypertrophy. *Nature Reviews Cardiology*, 15:387–407.

[181] Neff, L., Zhang, Y., Van Laer, A., Baicu, C., Karavan, M., Zile, M., and Bradshaw, A. (2022). Mechanisms that limit regression of myocardial fibrosis following removal of left ventricular pressure overload. *American Journal of Physiology-Heart and Circulatory Physiology*, 323(1):H165–H175.

[182] Nguyen, A., Schaff, H. V., Nishimura, R. A., Dearani, J. A., Geske, J. B., Lahr, B. D., , and Ommen, S. R. (2018). Determinants of reverse remodeling of the left atrium after transaortic myectomy. *The Annals of thoracic surgery*, 106:447–453.

[183] Niestrawska, J. A., Augustin, C. M., and Plank, G. (2020). Computational modeling of cardiac growth and remodeling in pressure overloaded hearts—linking microstructure to organ phenotype. *Acta biomaterialia*, 106:34–53.

[184] Nolan, D. R., Gower, A. L., Destrade, M., Ogden, R. W., and McGarry, J. P. (2014). A robust anisotropic hyperelastic formulation for the modelling of soft tissue. *Journal of the mechanical behavior of biomedical materials*, 39:48–60.

[185] Noseworthy, P., Rosenberg, M., Fifer, M., Palacios, I., Lowry, P., Ruskin, J., Sanborn, D., Picard, M., Vlahakes, G., Mela, T., and Das, S. (2009). Ventricular arrhythmia following alcohol septal ablation for obstructive hypertrophic cardiomyopathy. *The American journal of cardiology*, 104(1):128–132.

[186] Ogden, R. W. (1997). *Non-linear elastic deformations*. Dover Publications, New York.

[187] Olivotto, I., Ommen, S., Maron, M., Cecchi, F., and Maron, B. (2007). Surgical myectomy versus alcohol septal ablation for obstructive hypertrophic cardiomyopathy: will there ever be a randomized trial? *Journal of the American College of Cardiology*, 50(9):831–834.

[188] Omens, J. H. and Fung, Y. (1990). Residual strain in rat left ventricle. *Circulation Research*, 66:37–45.

[189] Omens, J. H., McCulloch, A. D., and Criscione, J. C. (2003). Complex distributions of residual stress and strain in the mouse left ventricle: experimental and theoretical models. *Biomechanics and Modeling in Mechanobiology*, 1:267–277.

[190] Omens, J. H., Vaplon, S. M., Fazeli, B., and McCulloch, A. D. (1998). Left ventricular geometric remodeling and residual stress in the rat heart. *Journal of Biomechanical Engineering*, 120:715–719.

[191] Ooms, J., Wang, D., Rajani, R., Redwood, S., Little, S., Chuang, M., Popma, J., Dahle, G., Pfeiffer, M., Kanda, B., and Minet, M. (2021). Computed tomography–derived 3d modeling to guide sizing and planning of transcatheter mitral valve interventions. *Cardiovascular Imaging*, 14(8):1644–1658.

[192] Pardo Mindán, F. and Panizo, A. (1993). Alterations in the extracellular matrix of the myocardium in essential hypertension. *European heart journal*, 14:12–14.

[193] Peirlinck, M., Costabal, F., Yao, J., Guccione, J., Tripathy, S., Wang, Y., Ozturk, D., Segars, P., Morrison, T., Levine, S., and Kuhl, E. (2021). Precision medicine in human heart modeling: Perspectives, challenges, and opportunities. *Biomechanics and modeling in mechanobiology*, 20:803–831.

[194] Peirlinck, M., Costabal, F. S., Sack, K. L., Choy, J. S., Kassab, G. S., Guccione, J. M., De Beule, M., Segers, P., and Kuhl, E. (2019). Using machine learning to characterize heart failure across the scales. *Biomechanics and modeling in mechanobiology*, 18:1987–2001.

[195] Pluijmert, M., Delhaas, T., de la Parra, A., Kroon, W., Prinzen, F., and Bovendeerd, P. (2017). Determinants of biventricular cardiac function: a mathematical model study on geometry and myofiber orientation. *Biomechanics and modeling in mechanobiology*, 16:721–729.

[196] Prakash, R. A. V. I. (1978). Determination of right ventricular wall thickness in systole and diastole. echocardiographic and necropsy correlation in 32 patients. *Heart*, 40(11):1257–1261.

[197] Prior, D. and La Gerche, A. (2012). The athlete's heart. *Heart*, 98(12):947–955.

[198] Rader, F., Sachdev, E., Arsanjani, R., and Siegel, R. (2015). Left ventricular hypertrophy in valvular aortic stenosis: mechanisms and clinical implications. *The American journal of medicine*, 128(4):344–352.

[199] Raghavan, M. L., Ma, B., and Fillinger, M. F. (2006). Non-invasive determination of zero-pressure geometry of arterial aneurysms. *Ann Biomed Eng*, 34(9):1414–1419.

[200] Rausch, M., Dam, A., Göktepe, S., Abilez, O., and Kuhl, E. (2011). Computational modeling of growth: systemic and pulmonary hypertension in the heart. *Biomechanics and modeling in mechanobiology*, 10:799–811.

[201] Rodriguez, E. K., Hoger, A., and McCulloch, A. D. (1994). Stress-dependent finite growth in soft elastic tissues. *J. Biomech.*, 27(4):455–467.

[202] Rodriguez-Gabella, T., Voisine, P., Puri, R., Pibarot, P., and Rodés-Cabau, J. (2017). Aortic bioprosthetic valve durability: incidence, mechanisms, predictors, and management of surgical and transcatheter valve degeneration. *Journal of the American College of Cardiology*, 70(8):1013–1028.

[203] Rogers, F. (2013). Aortic stenosis: new thoughts on a cardiac disease of older people. *Journal of Osteopathic Medicine*, 113(11):820–828.

[204] Rossi, M. A. and Carillo, S. V. (1991). Cardiac hypertrophy due to pressure and volume overload: distinctly different biological phenomena? *Int. J. Cardiol.*, 31(2):133–141.

[205] Saladin, K. (2006). *Anatomy and Physiology: The Unity of Form and Function*, chapter The Circulatory System: The Heart, pages 716–746. The McGraw–Hill Companies.

[206] Sato, K., Kumar, A., Jones, B., Mick, S., Krishnaswamy, A., Grimm, R., Desai, M., Griffin, B., Rodriguez, L., Kapadia, S., and Obuchowski, N. (2017). Reversibility of cardiac function predicts outcome after transcatheter aortic valve replacement in patients with severe aortic stenosis. *Journal of the American Heart Association*, 6(7):e005798.

[207] Sattar, Y. and Alraies, M. C. (2020). Ventricular aneurysm. In *StatPearls [Internet]*. StatPearls Publishing.

[208] Sawada, K. I. and Kawamura, K. (1991). Architecture of myocardial cells in human cardiac ventricles with concentric and eccentric hypertrophy as demonstrated by quantitative scanning electron microscopy. *Heart and vessels*, 6:129–142.

[209] Schein, A. and Gee, M. W. (2021). Greedy maximin distance sampling based model order reduction of prestressed and parametrized abdominal aortic aneurysms. *Advanced Modeling and Simulation in Engineering Sciences*, 8(18).

[210] Schield, R. T. (1967). Inverse deformation results in finite elasticity. *Zeitschrift für angewandte Mathematik und Physik (ZAMP)*, 18(4):490–500.

[211] Semsarian, C., Ingles, J., Maron, M., and Maron, B. (2015). New perspectives on the prevalence of hypertrophic cardiomyopathy. *Journal of the American College of Cardiology*, 65(12):1249–1254.

[212] Shenasa, M., Shenasa, H., and El-Sherif, N. (2015). Left ventricular hypertrophy and arrhythmogenesis. *Cardiac electrophysiology clinics*, 7(2):207–220.

[213] Shimizu, I. and Minamino, T. (2016). Physiological and pathological cardiac hypertrophy. *Journal of molecular and cellular cardiology*, 97:245–262.

[214] Shiojima, I., Sato, K., Izumiya, Y., Schiekofer, S., Ito, M., Liao, R., Colucci, W. S., and Walsh, K. (2005). Disruption of coordinated cardiac hypertrophy and angiogenesis contributes to the transition to heart failure. *The Journal of clinical investigation*, 115:2108–2118.

[215] Skalak, R., Zargaryan, S., Jain, R. K., Netti, P. A., and Hoger, A. (1996). Compatibility and the genesis of residual stress by volumetric growth. *Journal of Mathematical Biology*, 34:889–914.

[216] Stern, J., Markova, S., Ueda, Y., Kim, J., Pascoe, P., Evanchik, M., Green, E., and Harris, S. (2016). A small molecule inhibitor of sarcomere contractility acutely relieves left ventricular outflow tract obstruction in feline hypertrophic cardiomyopathy. *PLoS One*, 11(12):e0168407.

[217] Strocchi, M., Gsell, M., Augustin, C., Razeghi, O., Roney, C., Prassl, A., Vigmond, E., Behar, J., Gould, J., Rinaldi, C., Bishop, M., Plank, G., and Niederer, S. (2020). Simulating ventricular systolic motion in a four-chamber heart model with spatially varying robin boundary conditions to model the effect of the pericardium. *Journal of Biomechanics*, 101:109645.

[218] Taber, L. and Humphrey, J. (2001). Stress-modulated growth, residual stress, and vascular heterogeneity. *J. Biomech. Eng.*, 123(6):528–535.

[219] Taber, L. A. (1995). Biomechanics of growth, remodeling, and morphogenesis. *Appl. Mech. Rev.*, 48:487–545.

[220] Taber, L. A. and Chabert, S. (2002). Theoretical and experimental study of growth and remodeling in the developing heart. *Biomech. Model. Mechan.*, 1(1):29–43.

[221] Tamura, T., Onodera, T., Said, S., and Gerdes, A. (1998). Correlation of myocyte lengthening to chamber dilation in the spontaneously hypertensive heart failure (shhf) rat. *Journal of molecular and cellular cardiology*, 30(11):2175–2181.

[222] Teare, D. (1958). Asymmetrical hypertrophy of the heart in young adults. *Heart*, 20(1):1–8.

[223] Tham, Y. K., Bernardo, B. C., Ooi, J. Y., Weeks, K. L., and McMullen, J. R. (2015). Pathophysiology of cardiac hypertrophy and heart failure: signaling pathways and novel therapeutic targets. *Archives of toxicology*, 89:1401–1438.

[224] Toussaint, N., Stoeck, C., Schaeffter, T., Kozerke, S., Sermesant, M., and Batchelor, P. (2013). In vivo human cardiac fibre architecture estimation using shape-based diffusion tensor processing. *Medical image analysis*, 17(8):1243–1255.

[225] Treibel, T. A., Kozor, R., Schofield, R., Benedetti, G., Fontana, M., Bhuva, A. N., Sheikh, A., López, B., González, A., Manisty, C., and Lloyd, G. (2018). Reverse myocardial remodeling following valve replacement in patients with aortic stenosis. *Journal of the American College of Cardiology*, 71:860–871.

[226] Tsao, C., Aday, A., Almarzooq, Z., Anderson, C., Arora, P., Avery, C., Baker-Smith, C., Beaton, A., Boehme, A., Buxton, A., and Commodore-Mensah, Y. (2023). Heart disease and stroke statistics—2023 update: a report from the american heart association. *Circulation*, 147(8):e93–e621.

[227] Tsigkas, G., Despotopoulos, S., Makris, A., Koniari, I., Armylagos, S., Davlouros, P., and Hahalis, G. (2018). Transcatheter versus surgical aortic valve replacement in severe, symptomatic aortic stenosis. *Journal of geriatric cardiology: JGC*, 15(1):76.

[228] University of Minnesota/©Medtronic (2021). Atlas of human cardiac anatomy. `www.vhlab.umn.edu/atlas`.

[229] Usyk, T., Omens, J., and McCulloch, A. (2001). Regional septal dysfunction in a three-dimensional computational model of focal myofiber disarray. *American Journal of Physiology-Heart and Circulatory Physiology*, 281(2):H506–H514.

[230] Vahanian, A., Beyersdorf, F., Praz, F., Milojevic, M., Baldus, S., Bauersachs, J., Capodanno, D., Conradi, L., De Bonis, M., De Paulis, R., and Delgado, V. (2022). 2021 esc/eacts guidelines for the management of valvular heart disease: developed by the task force for the management of valvular heart disease of the european society of cardiology (esc) and the european association for cardio-thoracic surgery (eacts). *European heart journal*, 43(7):561–632.

[231] Valentin, A. and Holzapfel, G. (2012). Constrained mixture models as tools for testing competing hypotheses in arterial biomechanics: a brief survey. *Mechanics research communications*, 42:126–133.

[232] von Knobelsdorff-Brenkenhoff, F., Karunaharamoorthy, A., Trauzeddel, R., Barker, A., Blaszczyk, E., Markl, M., and Schulz-Menger, J. (2016). Evaluation of aortic blood flow and wall shear stress in aortic stenosis and its association with left ventricular remodeling. *Circulation: Cardiovascular Imaging*, 9(3):e004038.

[233] Wang, J., Sun, X., Xiao, M., Zhang, M., Chen, H., Zhu, C., Wang, S., and Wang, H. (2016). Regional left ventricular reverse remodeling after myectomy in hypertrophic cardiomyopathy. *The Annals of thoracic surgery*, 102:124–131.

[234] Wang, V., Lam, H., Ennis, D., Cowan, B., Young, A., and Nash, M. (2009). Modelling passive diastolic mechanics with quantitative mri of cardiac structure and function. *Medical image analysis*, 13(5):773–784.

[235] Wang, V., Young, A., Cowan, B., and Nash, M. (2013). Changes in in vivo myocardial tissue properties due to heart failure. *Functional Imaging and Modeling of the Heart: 7th International Conference*, 7:216–223.

[236] Wang, Z., Martin, B., Weickenmeier, J., and Garikipati, K. (2021). An inverse modelling study on the local volume changes during early morphoelastic growth of the fetal human brain. *Brain Multiphysics*, 2:100023.

[237] Wang, Z., Wang, V., Babarenda Gamage, T., Rajagopal, V., Cao, J., Nielsen, P., Bradley, C., Young, A., and Nash, M. (2020). Efficient estimation of load-free left ventricular geometry and passive myocardial properties using principal component analysis. *International journal for numerical methods in biomedical engineering*, 36(3):e3313.

[238] Weibel, E. (1984). *The pathway for oxygen: structure and function in the mammalian respiratory system*. Harvard University Press.

[239] Williams, L. K., Frenneaux, M. P., and Steeds, R. P. (2009). Echocardiography in hypertrophic cardiomyopathy diagnosis, prognosis, and role in management. *European Journal of Echocardiography*, 10:iii9–iii14.

[240] Wisneski, A., Wang, Y., Cutugno, S., Pasta, S., Stroh, A., Yao, J., Nguyen, T., Mahadevan, V., and Guccione, J. (2022). Left ventricle biomechanics of low-flow, low-gradient aortic stenosis: A patient-specific computational model. *Frontiers in Physiology*, 13:587.

[241] Witzenburg, C. and Holmes, J. (2018). Predicting the time course of ventricular dilation and thickening using a rapid compartmental model. *Journal of cardiovascular translational research*, 11:109–122.

[242] Witzenburg, C. M. and Holmes, J. W. (2017). A comparison of phenomenologic growth laws for myocardial hypertrophy. *Journal of Elasticity*, 129:257–281.

[243] Wolf, C., Moskowitz, I., Arno, S., Branco, D., Semsarian, C., Bernstein, S., Peterson, M., Maida, M., Morley, G., Fishman, G., Berul, C., Seidman, C., and Seidman, J. (2005). Somatic events modify hypertrophic cardiomyopathy pathology and link hypertrophy to arrhythmia. *Proceedings of the National Academy of Sciences*, 102(50):18123–18128.

[244] Wu, Q. Q., Xiao, Y., Yuan, Y., Ma, Z. G., Liao, H. H., Liu, C., Zhu, J. X., Yang, Z., Deng, W., and Tang, Q. Z. (2017). Mechanisms contributing to cardiac remodelling. *Clinical Science*, 131:2319–2345.

[245] Xu, H., Niederer, S. A., Williams, S. E., Newby, D. E., Williams, M. C., and Young, A. A. (2021). Whole heart anatomical refinement from ccta using extrapolation and parcellation. In *Functional Imaging and Modeling of the Heart*, pages 63–70. Springer, Cham, United States.

[246] Yang, H., Schmidt, L., Wang, Z., Yang, X., Shao, Y., Borg, T., Markwald, R., Runyan, R., and Gao, B. (2016). Dynamic myofibrillar remodeling in live cardiomyocytes under static stretch. *Scientific reports*, 6(1):1–12.

[247] Yarbrough, W. M., Mukherjee, R., Ikonomidis, J. S., Zile, M. R., and Spinale, F. G. (2012). Myocardial remodeling with aortic stenosis and after aortic valve replacement: mechanisms and future prognostic implications. *J. Thorac. Cardiov. Sur.*, 143(3):656–664.

[248] Yildiz, M., Oktay, A., Stewart, M., Milani, R., Ventura, H., and Lavie, C. (2020). Left ventricular hypertrophy and hypertension. *Progress in cardiovascular diseases*, 63(1):10–21.

[249] Yoshida, K. and Holmes, J. (2021). Computational models of cardiac hypertrophy. *Progress in biophysics and molecular biology*, 159:75–85.

[250] Yushkevich, P., Piven, J., Hazlett, H., Smith, R., Ho, S., Gee, J., and Gerig, G. (2006). User-guided 3d active contour segmentation of anatomical structures: Significantly improved efficiency and reliability. *NeuroImage*, 31(3):1116–1128.

[251] Zadpoor, A. (2013). Open forward and inverse problems in theoretical modeling of bone tissue adaptation. *Journal of the mechanical behavior of biomedical materials*, 27:249–261.

[252] Zamir, E. A. and Taber, L. A. (2004). Material properties and residual stress in the stage 12 chick heart during cardiac looping. *J. Biomech. Eng.*, 126:823–830.

[253] Zhuan, X. and Luo, X. (2020). Residual stress estimates from multi-cut opening angles of the left ventricle. *Cardiovascular Engineering and Technology*, 11:381–393.

[254] Zipes, D. (2018). *Braunwald's heart disease: a textbook of cardiovascular medicine*. BMH Medical Journal.